Luis Ronan Marquez Ferreira de Souza
Ana Luisa Alencar De Nicola
Harley De Nicola
Editors

Atlas of Imaging in Infertility

A Complete Guide Based in Key Images

Springer

Atlas of Imaging in Infertility

Luis Ronan Marquez Ferreira de Souza
Ana Luisa Alencar De Nicola • Harley De Nicola
Editors

Atlas of Imaging in Infertility

A Complete Guide Based in Key Images

Springer

Editors
Luis Ronan Marquez Ferreira de Souza
Associate Professor of Radiology
Universidade Federal do Triangulo Mineiro
Uberaba, MG
Brazil

Ana Luisa Alencar De Nicola
Department of Gynecology Endoscopy
Santa Casa Medical School
São Paulo, SP
Brazil

Harley De Nicola
Diagnostic Imaging Department
of UNIFESP – Federal University of São Paulo
São Paulo Hospital
São Paulo, SP
Brazil

ISBN 978-3-319-13892-3 ISBN 978-3-319-13893-0 (eBook)
DOI 10.1007/978-3-319-13893-0

Library of Congress Control Number: 2017942961

Printed on acid-free paper

This Springer imprint is published by Springer Nature
The registered company is Springer International Publishing AG
The registered company address is: Gewerbestrasse 11, 6330 Cham, Switzerland

Foreword

Over the last two generations there has been a dramatic change in reproductive patterns worldwide – mainly postponing pregnancy. In Brazilian society, as in many other developing countries, birth rates have plummeted to unprecedented levels, and the age for first pregnancies has matched European customs. What does a decrease in the ability to conceive due to oocyte aging mean, especially when it requires increasingly assisted reproductive treatments?

Within this context, considering the routine use of laparoscopy in the late 1970s, from the diagnostic work-up to follicular aspiration for *in vitro* fertilization, remarkable advances were made during the last few decades. At IVF laboratories it is possible to cryopreserve gametes and embryos with the same recovery rates, to fertilize oocytes from severe sperm conditions, or to take biopsies from embryos in order to avoid a host of genetic diseases. On a daily basis, ultrasound guidance estimates ovarian stimulation, and permits oocyte recovery or the correct embryo placement in the uterine cavity.

Imaging techniques also experienced a true revolution in evaluating the pelvic cavity with great detail and accuracy, making it possible to detect pathologies at the very early stages of pregnancy. This new approach has changed the understanding of reproduction and promoted better decisions to enhance pregnancy outcomes. Perhaps endometriosis may represent this new trend, where the precise initial diagnosis could modify the therapeutic management, but also prevent surgeries without the correct approach.

However, all these advances require the proper training of qualified professionals to correctly transmit this range of information and to put new technologies and equipment to proper use. A continuous exchange between imaging specialists and gynecologists, endocrinologists, urologists, or anyone else dealing with infertility, will promote ideal interaction for the benefit of infertile patients.

São Paulo, Brazil — Eduardo Leme Alves da Motta

About the Editors

Luis Ronan Marquez Ferreira de Souza: Graduated in Medicine from the State University of Campinas, Brazil (UNICAMP), in 2000 and has a Ph.D. in Medical Sciences (Radiology Clinic) from the Federal University of São Paulo, Brazil (UNIFESP/EPM), in 2005. He is currently an associated professor at the Federal University of Triangulo Mineiro. He has extensive diagnostic imaging experience, with a focus on abdominal and women's imaging using ultrasound, magnetic resonance imaging, and computed tomography. Member of the Brazilian College of Radiology (CBR), Radiological Society of North America (RSNA) and European Society of Gastrointestinal Radiology (ESGAR).

Ana Luisa Alencar De Nicola: Graduated in Medicine from the Bahiana Medical School of Medicine and Public Health (1994) and specialized in general ultrasound at the Training Center in Ultrassonography of São Paulo (Cetrus – 1998). She completed her residency in Gynecology and Obstertrics at the Maternity Association of São Paulo (1997). She is a member of the Brazilian College of Radiology. Currently an assistant at Gynecological Endoscopy and Endometriosis Sector, Department of Obstetrics and Gynecology, Santa Casa de São Paulo School of Medical Science. She also has extensive experience in the field of medical radiology.

Harley De Nicola: Graduated in Medicine from Lusíada University of Santos-SP (FCMS) in 1993 and completed his Ph.D. in Medical Sciences (Radiology Clinic) at the Federal University of São Paulo (UNIFESP/EPM) in 2005. Currently an assistant at the Federal University of São Paulo and coordinator of Medical Ultrasound Post-Graduate Course at I.D.I Foundation (Radiology Research and Teaching Institute at São Paulo), he also has broad experience in diagnostic imaging, with a focus on general ultrasound and interventional ultrasound. He is a member of the Brazilian College of Radiology and the Radiology Society of North America (RSNA).

Contents

Contributors

Geraldo Souza Pinho Alves Radiology Department, Hospital do Servidor Público Estadual de São Paulo (IAMSPE), São Paula, SP, Brazil

Paulo Eduardo de Aguiar Kuriki Departamento de Diagnóstico por Imagem, Universidade Federal de São Paulo, São Paulo, SP, Brazil

Leonardo Kayat Bittencourt Department of Radiology, CDPI Clinics (DASA) and Fluminense Federal University (UFF), Rio de Janeiro, RJ, Brazil

Elisa Almeida Sathler Bretas Abdominal Imaging, Department of Diagnostic Imaging, Escola Paulista de Medicina – Universidade Federal de São Paulo (EPM-Unifesp), São Paulo, SP, Brazil

César Amaral de Camargo Penteado Radiology Department, Hospital do Servidor Público Estadual de São Paulo (IAMSPE), São Paulo, SP, Brazil

Renata Chehin Ultrassonographer, Hospital Beneficencia Portuguesa de São Paulo, São Paulo, SP, Brazil

Ana Luisa Alencar De Nicola Department of Gynecology Endoscopy, Santa Casa Medical School, São Paulo, SP, Brazil

Harley De Nicola Diagnostic Imaging Department of UNIFESP – Federal University of São Paulo, São Paulo Hospital, São Paulo, SP, Brazil

Luis Ronan Marquez Ferreira de Souza Associate Professor of Radiology, Universidade Federal do Triangulo Mineiro, Uberaba, MG, Brazil

Giuseppe D'Ippolito Department of Diagnostic Imaging, Escola Paulista de Medicina – Universidade Federal de São Paulo (EPM-Unifesp), São Paulo, SP, Brazil

Jorge Elias Jr. Radiology Division of Internal Medicine Department, Ribeirão Preto Medical School of University of São Paulo, Ribeirão Preto, SP, Brazil

Paula Condé Lamparelli Elias Endocrinology and Metabology Division of Internal Medicine Department, Ribeirão Preto Medical School of University of São Paulo, São Paulo, SP, Brazil

Mariana Kefalas Oliveira Gomes Department of Materno-Infantil, Universidade Federal do Triangulo Mineiro, Uberaba, MG, Brazil

Dáfne Daniela Dias Melquiades Department of Radiology, CDPI Clinics (DASA), Rio de Janeiro, RJ, Brazil

Valdair Francisco Muglia Radiology Division of Internal Medicine Department, Ribeirão Preto Medical School of University of São Paulo, Ribeirão Preto, SP, Brazil

Osmar Cassio Saito Department of Radiology, Clinicas Hospital – University of São Paulo, São Paulo, SP, Brazil

Priscila Silveira Salvatori Abdominal Imaging, Department of Diagnostic Imaging, Escola Paulista de Medicina – Universidade Federal de São Paulo (EPM-Unifesp), São Paulo, SP, Brazil

Jacob Szejnfeld Full professor of Diagnostic Imaging Department of UNIFESP – Federal University of São Paulo, São Paulo Hospital, São Paulo, SP, Brazil

Sara Reis Teixeira Radiology Division of Internal Medicine Department, Ribeirão Preto Medical School of University of São Paulo, Ribeirão Preto, SP, Brazil

Lucas Rios Torres Abdominal Imaging, Department of Diagnostic Imaging, Escola Paulista de Medicina – Universidade Federal de São Paulo (EPM-Unifesp), São Paulo, SP, Brazil

Anatomy and Embryology

1

Mariana Kefalas Oliveira Gomes and Luis Ronan Marquez Ferreira de Souza

Anatomy of the Genital System

The female pelvis comprises organs that produce gametes and are responsible for their transport, as well as the bone and muscle support structures. The pelvis can be divided into the pelvic structure and internal and external genitalia [1, 2].

Pelvic Structure

Hip Bone

The skeleton of the pelvis is formed by the sacrum, coccyx, and the hip bones (ilium, ischium, and pubis) that previously merged to form the pubis symphysis.

The sacrum and coccyx are an extension of the backbone, resulting from the five fused sacral vertebrae; they are connected by a symphysis type of articulation that allows for some movement.

One of the key points of the sacrum is the promontory, the most prominent and anterior projection, which is located just below the bifurcation of the level of the common iliac arteries. It is an important point of reference for the insertion of a laparoscope and for sacrocolpopexy.

The two hip bones are then posteriorly articulated to the sacrococcygeal region of the spine, and previously between themselves, through the pubic symphysis, both being semi-mobile joints. A plane passing through the arched line, and the top edge of the pubic symphysis, divides the pelvis into the greater pelvis (above it) and lower pelvis (below it); this is known as the true pelvis.

M.K.O. Gomes
Department of Materno-Infantil, Universidade Federal do Triangulo Mineiro, Uberaba, MG, Brazil
e-mail: mako@terra.com.br

L.R.M.F. de Souza (✉)
Associate Professor of Radiology, Universidade Federal do Triangulo Mineiro, Uberaba, MG, Brazil
e-mail: radiologia.abdome@gmail.com

Muscles, Support Structures, and Ligaments

The muscles of the pelvis include those of the sidewall and pelvic floor (Fig. 1.1). They pass into the gluteal region in order to help thigh rotation and adduction. They include the piriformis, the internal stop valve, and the iliopsoas.

The pelvic and urogenital diaphragms form the pelvic floor. The former is a funnel-shaped fibromuscular partition that creates the primary support structure for the pelvic organs. It comprises the anus levator muscles (pubococcygeus, puborectal, and iliococcygeal) and coccyx, together with its upper and lower fascia. The loss of normal tonus of the anus levator, by direct muscle denervation or injury, results in sagging of the urogenital gap that is involved in the beginning of prolapse in females.

The muscles of the urogenital diaphragm (deep transverse perineal muscle and urethral sphincter) reinforce the front of the pelvic diaphragm, and are protected by upper and lower fascia of the urogenital diaphragm-pubovesicocervical ligament.

The urogenital diaphragm is closely related to the vagina and urethra, and an injury to the diaphragm is associated with cystocele and urethrocele.

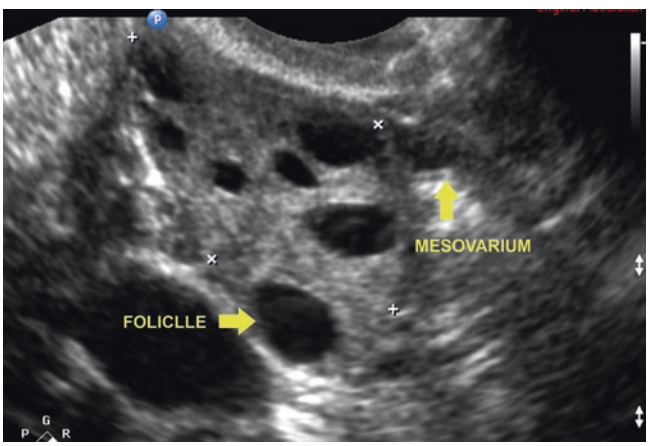

Fig. 1.1 Transvaginal ultrasound of the ovary, showing the normal anatomy

L.R.M.F. de Souza et al. (eds.), *Atlas of Imaging in Infertility*, DOI 10.1007/978-3-319-13893-0_1

Vascularization and Lymphatic Drainage

The main arteries that irrigate the pelvic structures and the organs are shown in Fig. 1.2:

(a) Median sacral artery – a single vessel located on the mid-line, emerging from the posterior part of the terminal aorta. It supplies the bone and muscular structures of the posterior pelvic wall.
(b) Internal iliac arteries (hypogastric) – originate from the common iliac arteries (terminal division of the aorta at the level of the fourth lumbar vertebra). They move down close to the ureter, and branch out into further divisions consisting of the following arteries: superior gluteal, lateral sacral, iliolumbar, and its previous division consisting of the obturator artery, internal pudendal, umbilical, superior, media and inferior bladders, rectal media, uterine, and vaginal and inferior gluteal.
(c) Ovarian arteries – originate at the ventral surface of the aorta, just below the origin of the renal vessels. They cross near the common iliac vessels; in proximity to the ureter, it departs from its course, crossing over the ureter while running superficial to the psoas muscle, and then laterally to the ureter, where it enters the pelvis as part of the infundibulopelvic ligament. They supply with blood the ovaries, fallopian tubes, and broad ligament. If the hypogastric arteries, ovarian arteries, sacral or inferior mesenteric need suturing, direct branches of the aorta will supply blood to the pelvic structures once irrigated by the hypogastric arteries.

The venous system accompanies the arteries, except for the ovarian arteries, in which the right one opens into the inferior vena cava, and the left into the left renal vein. Lymphatic drainage, however, is accomplished by lymph vessels that originate in the walls of the uterus, fallopian tubes, ovaries, and vagina, heading for the internal and external iliac, common iliac, aortic (para-aortic), and superior and profound inguinals. Among the most important lymph nodes, Cloquet's (or Rosenmüller's) can be mentioned; these are the highest of the deep inguinal lymph nodes, located at the opening of the femoral canal.

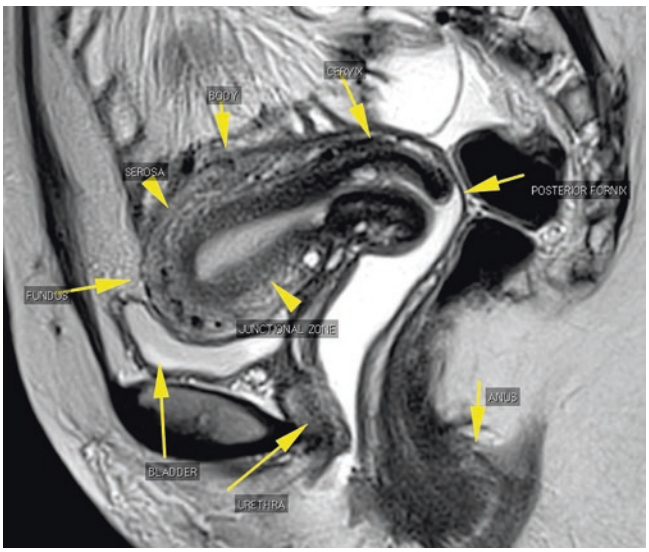

Fig. 1.2 Pelvic MRI, Sagittal TSE T2 weight, demonstrating the normal zonal anatomy of the uterus

Innervation

The pelvis is innervated by both the autonomic and somatic nervous systems.

Somatic innervation is carried by the lumbosacral plexus, which provides motor and sensory innervation to the lower wall, the pelvic and urogenital diaphragms, the perineum and the hip, and the lower extremities. The responsible nerves are the iliohypogastric, ilioinguinal, side femoral cutaneous, femoral, genitofemoral, obturator,superior and inferior gluteus, posterior cutaneous of the thigh, sciatic, and pudendal.

Autonomic innervation, however, is accomplished by the following plexus:

(a) Aortic, located laterally to the spine;
(b) Ovarian, responsible for the innervation of the ovaries, fallopian tubes and part of the broad ligament;
(c) Inferior mesenteric, which innervates the left colon, the sigmoid and rectum;
(d) Superior hypogastric or pre-sacral plexus is responsible for pelvic innervation. It is the continuation of the aortic plexus, under the peritoneum in front of the terminal aorta, the fifth lumbar vertebra and the promontory, medial to the ureters. Just below the promontory, the superior hypogastric plexus is divided into two loosely arranged nerve trunks, the hypogastric nevi. These nerves course below and laterally, to connect themselves to the inferior hypogastric plexus, a dense network of nerves and ganglia that are situated at the side wall of the pelvis, superposing the internal iliac vessels.

The inferior hypogastric plexus includes efferent, afferent (sensory), and parasympathetic fibers that emerge from the splanchnic pelvic nerves. It is divided into the bladder plexus, middle rectal plexus, and uterovaginal plexus.

Internal Genitalia

Ovary

The ovaries are a pair of gonadal structures that are suspended between the pelvic wall and the uterus by the infundibulopelvic ligament, laterally, and by the utero-ovarian ligament, medially. At the bottom, the hilar surface connects to the broad ligament by its mesentery, in a dorsal position to meso fallopian tubes and the uterine tube. Primary neurovascular structures – the ovarian arteries that supply the ovaries – reach the ovary through the infundibulopelvic ligament. The size of the ovaries are approximately 3–4 cm long, 2 cm wide, and 1 cm thick; they weigh 3–9 g.

Each ovary consists of a cortex and a medulla, and is covered by a single layer of cuboidal epithelium. The cortex consists of specialized stroma and follicles in various stages of development or regression. The medulla is located in the hilar portion and consists of fibromuscular tissue and blood vessels (Fig. 1.1).

Uterine Tubes

The uterine tubes are hollow, paired structures located in the mesofallopian tubes. They range from 7 to 12 cm in length and are about 1 cm in diameter [3]. They are divided into four parts: infundibular – terminal where the fimbriae approach the ovarian surface, aiding in the capture of gametes; ampullary – longest portion, with a more tapered diameter, and greater lateral walls; isthmic – shorter, and with thicker walls, closer to the uterine wall; and interstitial, which lies within the uterine wall, and forms the tubal ostia in the endometrial cavity (Fig. 1.3).

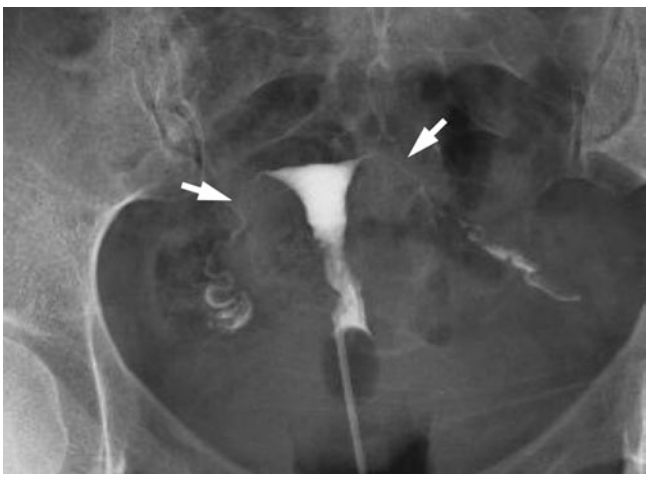

Fig. 1.3 Hysterosalpingography of a normal uterus. The *arrow* are demonstrating the uterine tubes

located in the vagina, approximately 3 cm in length, consisting of a few muscle fibers, but large amounts of connective tissue.

The uterus is lined internally by the endometrium (mucosa and submucosa), and externally by serosa, a peritoneum that covers the uterus and determines the appearance of recto-uterine and vesicouterine reflections. The smooth muscles that compose the myometrium (smooth muscle layer between the endometrium and serous) intertwine in all directions, and form four layers: submucosal stratum, vascular stratum (where the arcuate arteries are identified), supravascular stratum, and subserosal stratum.

The irrigation of the uterus is performed by the uterine arteries that direct themselves superior to the uterus, tortuously, through the lateral margin, resulting in anterior and posterior rami. They terminate with the tubal and ovarian rami (anastomosis with ovarian artery). The initial ramus of the uterine arteries are the arcuate arteries, which are divided into the radial arteries that penetrate deep into the myometrium and come from the following radial arteries: straight arterioles, that reach deep into the endometrial third (and are responsible for constant movement, not being affected by changes in the menstrual cycle), and the spiral arterioles, which reach the upper third of the endometrium and change with the menstrual cycle.

The lymphatic drainage of the body goes to the para-aortic lymph nodes, while those that drain the region of the isthmus and cervix head to the hypogastric lymph nodes, obturators, and external iliac.

Vagina

The vagina is a fibromuscular tubular organ located inferiorly between the vulvar vestibule and the uterus, located superiorly, just above the cervix. It is about 10 cm long and extends in a superposterior direction; it is 3 cm longer at the posterior wall. The spaces between the cervix and the vagina are known as the anterior, posterior, and lateral vaginal fornix. The posterior fornix is of essential importance since it is a means of easy access to the peritoneal cavity.

The vagina is linked to the side pelvic wall by fascial endopelvic connections, and to the tendinous arch (white line), which extends from the pubis to the ischial spine. This connection converts the vaginal lumen into a transverse opening, with the anterior and posterior walls in apposition; the lateral space where the two walls meet is called the vaginal sulcus. The lower vagina is slightly narrowed as it passes through the urogenital hiatus in the pelvic diaphragm; the upper vagina is more spacious.

The vaginal mucosa consists of a mucous layer of stratified squamous non- keratinized epithelium, without glands; a muscular layer of connective tissue and smooth muscle; and the adventitia, composed of endopelvic fascia that separate the lower urinary and gastrointestinal systems. Before that, the vagina is in close contact with the urethra, bladder neck, trigonal region, and posterior bladder; later, it is associated with the perineal body, anal canal, lower rectum, and posterior fornix.

The vagina is irrigated by the vaginal artery and branches that derive from the uterine arteries, rectal media, and internal pudenda. The lymphatic drainage of the lower portion of the vagina is done for femoral and inguinal lymph nodes, while the upper two-thirds drain into the hypogastric lymph nodes, obturators, and external iliac.

External Genitalia

Vulva

The vulva consists of the mons pubis, larger and smaller labia, clitoris, hymen, greater vestibular glands orifice, posterior labial commissure, para-urethral glands orifice, vaginal ostium, and urethral ostium. Its lymphatic drainage leads to the superficial inguinal lymph nodes.

Perineum

The perineum is located at the lower end of the trunk, between the buttocks. Its bony boundaries include (anteriorly) the inferior edge of the pubis symphysis, (posteriorly) the tip of the coccyx, and (laterally) the ischial spines. These reference points correspond to the pelvis output limits, and, looking at it, it is the area between the anus and the vagina, which receives the inserts of the urogenital diaphragm muscle (Fig. 1.4). It is bounded (anteriorly) by the urogenital trigones, and (posteriorly) by the anal trigone.

Urogenital Trigone

The perineal floor is composed of skin and two layers of superficial fascia. The superficial perineal compartment lies between the superficial perineal fascia and the lower fascia of the urogenital diaphragm (perineal membrane). It includes:

(a) Erectile bodies – the vestibule bulbs, which are 3 cm. highly vascularized structures,that surround the vestibule and are located under the bulbospongiosus muscle;
(b) Muscles – ischicavernous, bulbospongiosus, and perineal superficial transverse; and
(c) Vestibular glands – located on each side of the vestibule, under the rear end of the vestibule bulb. They drain the region between the hymen and labia, and their secretion helps maintain proper lubrication.

In the next depth level is the urogenital diaphragm, which contains the urethra, the vagina, two fascias, and support muscles (described above). They are located between the ischiopubic rami, covered by the triangular membrane, which complete the pelvic support.

Perineal Body

The perineal body, or central tendon perineum, is critical for the rear support of the lower portion of the anterior vaginal wall. It is a triangle-shaped structure that separates the distal portion of the anal and vaginal canals, beginning at the convergence of tendon fixations of the bulbospongiosus muscle, external anal sphincter, and perineal superficial transverse muscle. It is the central connection between the two support layers of the pelvic floor – the pelvic and urogenital diaphragms [4].

Anal Trigone

The anal trigone includes the lower end of the anal canal. The external anal sphincter that surrounds the anal trigone, and the ischiorectal fossa, are found on each side.

The ischiorectal fossa is bound, laterally, by the fascia of the internal obturator, and, medially, by the anus elevator muscles, coccyx, and anal sphincter. It is a space outlined by fascias, inferiorly located between the skin of the perineum, and, superiorly, by the pelvic diaphragm. The latter comprises the levator muscle of the anus and the coccyx.

The urinary and genital systems have a common dependency of several interdependent structures for support. The cardinal and uterosacral ligaments are condensations of the endopelvic fascia, that support the cervix and upper vagina, on the anus levator. The anterior distal vagina and the urethra are anchored to the urogenital diaphragm, and the posterior distal vagina to the perineal body. Laterally, the middle vagina is connected through the paracolpos to the tendinous arch of the upper pelvic fascia.

Embryology of the Genital System

The sex of the embryo, determined at fertilization – 46XX or 46XY – remains indistinguishable between the female and male genders in the embryonic stage. Male sexual differentiation is an active process, requiring the presence of the SRY gene, located on the short arm of chromosome Y.

For the development of internal reproductive organs, primordial germ cells derived from the primitive ectoderm, migrate from the yolk sac, by the mesentery of the hindgut to the mesenchyme of the posterior body wall, near the level of the tenth thoracic vertebra. In a sequence around the fifth week of pregnancy, the proliferation of cells in the adjacent mesonephros and coelomic epithelium are induced to form the genital ridges, medial to the mesonephros. Stem cells are the precursors of oocytes and spermatogonials.

The testicular differentiation begins around the sixth week of intrauterine life, with the presence of the testicular determining factor, present in the SRY region of the Y chromosome. By the seventh week, the degeneration of the gonadal cortex and medullary differentiation of gonads in the Sertoli region cells occur, forming the testicular cords, where the germ cells are located. Sertoli cells produce the androgen-binding protein, which maintains a high local concentration of androgens, and it will be important to form the male internal genitalia and spermatogenesis. The production of androgen will depend on the Leydig cells, formed from the mesenchyme of testicular cords, after the eighth week of pregnancy.

The ovarian differentiation, which takes place passively, 2 weeks after testicular differentiation (by the absence of the testicular determining factor), begins with the transformation to oogonia. The oogonia are surrounded by cells of the superficial epithelium (future granulosa cells), and form the primordial follicles. Oogonia enter the first meiotic division (prophase 1) as primary oocytes, at which point the development is suspended until puberty. There are six to seven million of them in the first half of pregnancy, but by undergoing intensive atresia during the second half of pregnancy, there are around one to two million at birth.

Differentiation of the Internal Genitalia

Initially, every human being has two pairs of genital ducts, which are the mesonephric (Wolffian) ducts and the paramesonephrics (Mullerian) ducts (Fig. 1.4). The Wolf ducts produce the epididymis, seminal vesicle, and vas deferens. In females, the fallopian tubes, uterus, and upper part of the vagina originate from paramesonephric ducts.

In the male embryo, Leydig cells begin to produce testosterone around the eighth week of intrauterine life, and the Sertoli cells produce the anti-Müllerian hormone (AMH); the latter causes regression of the paramesonephric ductal system. The inhibitory action of AMH on Müller canals is local and unilateral, influencing canalicular differentiation, according to the ipsilateral gonad. Thus, testosterone becomes responsible for the evolution of the mesonephric duct system, vas deferens, epididymis, seminal vesicles, and ejaculatory duct.

In the female embryo, the absence of the Y chromosome and functional testicle determines the absence of AMH, thus allowing the differentiation of paramesonephric ducts. These are formed on the sides of the mesonephric ducts; they grow caudally, and then medially to fuse the medical line. They join the urogenital sinus in the posterior urethra region, in a slight thickening known as genital tubercle.

Cranially, the Müllerian ducts open into the abdominal cavity. At the midline they come into close contact with the paramesonephric duct from the opposite side. The two ducts are separated by a septum that disappears in week 9 to form the uterine canal. With the descent of the ovaries, the first two parts develop into the uterine tubes and the caudal part fuses to form the uterine canal, giving rise to the body and cervix of the uterus. The endometrial stroma and myometrium are differentiated from the surrounding mesenchyme. There is an initial permanence of a vertical septum fusion, which disappears cranially, with full vaginal canalization between the 18th and 22nd weeks of gestation, ending the formation of the internal genitalia.

The remnants of Wolf ducts in females (present in 25% of adult women) are Morghani hydatids, paraooforo, and Gartner ducts.

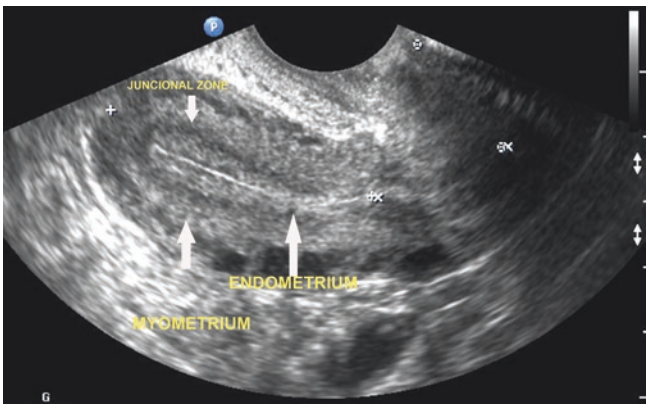

Fig. 1.4 Transvaginal ultrasound of the uterus

Differentiation of the External Genitalia

At the beginning of the fifth week of embryonic life, tissue folds are formed on each side of the cloaca, and they meet above the midline to create the genital tubercle. With the division of the cloaca by the urorectal septum and consequent formation of the perineum, these cloacal folds were previously known as the "anal folds." By the eighth week, the genital tubercle begins to grow, and at the same time labioscrotal bumps and urogenital folds emerge.

In the female embryo, the genital tubercle's growth diminishes and becomes the clitoris, and the urogenital folds become the labia minora. On the sides of the urogenital folds, another pair of dilatations develop – the labioscrotal saliences – and the labia majora develop in the absence of androgens. The final urogenital sinus originates in the vaginal vestibule, into which the urethra, the vagina, and the larger glands open. The external genitalia differentiation process will end around the 20th week in females.

The masculinization of the external genitalia takes place by the action of dihydrotestosterone – a testosterone metabolite – through the action of a 5α-reductase enzyme. Its end occurs around the 14th week of gestation. The genital tubercle creates the penis, and the labioscrotal saliences are responsible for the development of the scrotum, the urogenital folds, and the urethra.

Abnormalities in the development of the urinary and genital systems can be explained and understood after taking into account male and female embryonic development. Due to the intertwined development of these two systems, abnormalities in one may be associated with abnormalities in the other. About 10% of infants are born with some abnormality of the genitourinary system.

Development problems, apart from having a significant role in the differential diagnosis of certain clinical signs and symptoms, have special implications for reproductive life and pelvic surgery. For this reason, it is important to have basic knowledge of the embryology of the genital system.

References

1. Gardner E, Gray DJ, O'Rahilly R. Anatomia – Estudo Regional do Corpo Humano. 4th ed. Rio de Janeiro: Guanabara Koogan; 1978. p. 465–75.
2. Ribeiro LFN, Dutra PA, Gagliardo GI. Anatomia e Histologia dos Orgaos Genitais Femininos. In: SOGIMIG. Manual de Ginecologia e Obstetricia– SOGIMIG. Belo Horizonte: Coopmed; 2012. p. 3–11.
3. Sadler TW. Langman's medical embryology. 9th ed. Philadelphia: Wolters Kluwer Lippincott Williams & Wilkins; 2004.
4. Sokol ER, Genadry R, Anderson JR. Anatomia e Embriologia. In: Berek JS, editor. Berek & Novak gynecology. 15th ed. 2012. Portuguese Edition: Berek JS. Berek e Novak: tratado de ginecologia (trans Araujo CLC, Duarte TC). Rio de Janeiro: Guanabara Koogan; 2014. p. 50–88.

Part I

Imaging of Female Infertility

Polycystic Ovarian Syndrome

2

Ana Luisa Alencar De Nicola and Harley De Nicola

Introduction

Polycystic ovarian syndrome (PCOS) was first described by Stein and Leventhal [1] in 1935. They reported the pathognomonic appearance of the ovaries seen during laparotomy in seven patients with hirsutism and amenorrhea (Fig. 2.1). The histological findings after surgical resection wedge were prominent teak, fibrotic thickening of the albuginea tunic, and antral follicles in excessive numbers [1].

The involvement of the hypothalamic-pituitary axis in PCOS has been increasingly reported in other studies, when the biochemical criteria acquired are of paramount importance to its diagnosis [2]. Elevated serum levels of luteinizing hormone, testosterone, and androstenedione, in association with normal or low levels of follicle-stimulating hormone, characterize a profile associated with this pathology [3].

The pathophysiology of PCOS is not completely understood. Between 16% and 25% of healthy women may show morphology of polycystic ovaries on ultrasound without associated hormonal changes [4], and the development of PCOS requires additional factors [5, 6]. At any rate, its early diagnosis is essential for identifying the potential risk of metabolic disorders and cardiovascular diseases. Many of these patients show a resistance to insulin and hyperinsulinemia, abnormal levels of lipoproteins, and lipids and fibrynolisis changes (Scheme 2.1).

The clinical presentation is variable, but usually includes trace or anovulation, hyperandrogenism (clinical and/or laboratory,) and the appearance of polycystic ovaries. A combination of these three conditions – or all of them – may be present, so the diagnosis is a complex challenge and a controversial issue.

In 1990 at a conference on PCOS, the U.S. National Institutes of Health (NIH) recommended that the diagnostic criteria include hyperandrogenism with no other apparent causes, such as adrenal hyperplasia and ovulatory dysfunction. The morphology of polycystic ovaries in ultrasound has been considered prevalent, but not essential for diagnosis [7].

The need to redefine PCOS and to include an ultrasound aspect of polycystic ovaries in the diagnosis prompted a consensus meeting of the ASRM/ESHRE that took place in 2003 in Rotterdam. According to this new setting, the diagnosis of PCOS requires the presence of two of the following three criteria: Oligo/anovulation; hyperandrogenism (clinical and/or laboratory); and polycystic ovaries, excluding other etiologies [8]. Thus there are two definitions in the literature for PCOS (Table 2.1); at any rate, PCOS usually manifests in the early years of reproductive life and is considered the most common endocrine disorder in women. A prevalence of 6–10% is estimated, according to criteria of the NIH, and up to 15% when the Rotterdam consensus parameters are used [9].

In 2010 there was a new ASRM/ESHRE consensus meeting in Amsterdam, where special attention was paid to the diagnosis of PCOS in adolescent patients. For this group, the diagnosis of PCOS when the following three parameters are present is considered: Oligo/anovulation; hyperandrogenism (clinical and/or laboratory); and polycystic ovaries, excluding other etiologies [9].

A.L.A. De Nicola (✉)
Department of Gynaecological Endoscopy,
Santa Casa Medical School, São Paulo, SP, Brazil
e-mail: analui.nicola@terra.com

H. De Nicola
Diagnostic Imaging Department of UNIFESP – Federal University of São Paulo, São Paulo Hospital, São Paulo, SP, Brazil
e-mail: harley.nicola@terra.com.br

L.R.M.F. de Souza et al. (eds.), *Atlas of Imaging in Infertility*, DOI 10.1007/978-3-319-13893-0_2

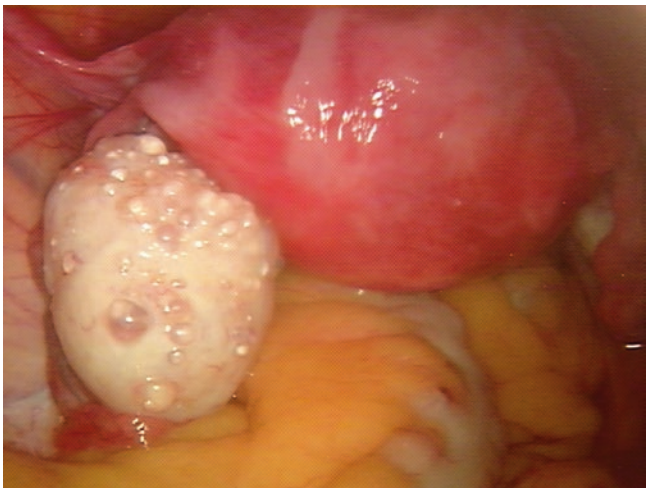

Fig. 2.1 Pathognomonic appearance of the polycystic ovary at laparotomy. Enlarged ovary with multiple small follicles (Image courtesy of Dr. Dorival Gomide Ramos)

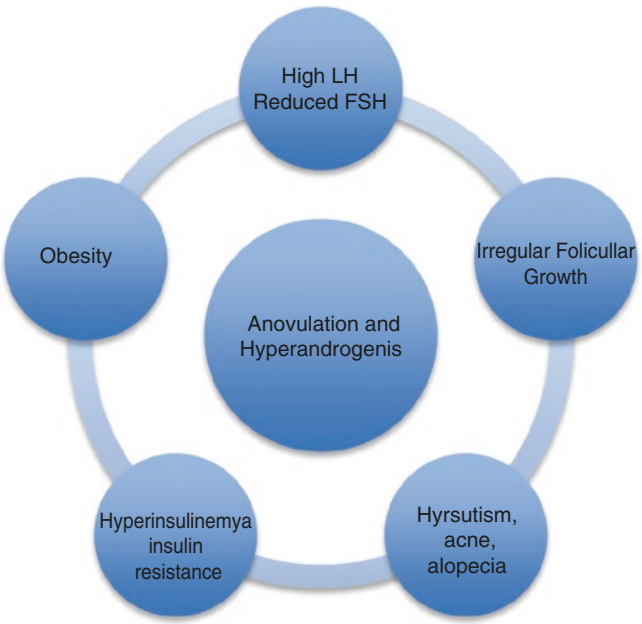

Scheme 2.1 Pathophysiology of polycystic ovary syndrome

Table 2.1 Polycystic Ovary Syndrome definitions

Authors	Criteria
NIH, 1990	Hyperandrogenism, without other causes; and oligo/anovulation
ASRM/ESHRE Rotterdam, 2003	Two of three: Oligo/anovulation Hyperandrogenism Polycystic ovary on ultrasound

Imaging Findings

The findings of ovaries with polycystic morphology can be quite common in the imaging methods of the female pelvis. In a study involving 230 women between the ages of 18 and 25, the morphology of polycystic ovaries was found on ultrasound in 74 (33%) of them [10]. About 80% of these patients had signs and symptoms of PCOS, usually moderate, while 20% did not have any hormonal or ovulatory change [4].

Pelvic ultrasound is the most commonly used method for identifying polycystic ovaries. It is easy to visualize the increased volume of ovaries with more evident stroma and multiple small follicles that make up the appearance of small cysts that are very different from the normal ovary (Figs. 2.2 and 2.3).

The transvaginal approach is the best one for identifying polycystic ovaries, mainly due to increased spatial resolution that makes a detailed assessment of the internal structures of the ovaries possible. Often an ovary that has a more homogeneous echotexture by the abdominal approach shows polycystic morphology in transvaginal examination, especially in obese patients. The detection of polycystic ovaries is virtually the same (about 78%) on transabdominal and transvaginal ultrasound ovaries [11].

In 1985, Adams et al, still using transabdominal ultrasound, defined a polycystic ovary as one that in a single cutting plane has at least 10 follicles, that is usually between 2 and 8 mm in diameter, and is distributed circumferentially around a central dense stroma [12] (Figs. 2.4, 2.5, 2.6 and 2.7) Many other studies used the Adams criteria for the diagnosis of polycystic ovaries, and one of them concluded that viewing polycystic ovaries in ultrasound could be the key to the diagnosis of PCOS in patients with signs and symptoms [13].

Over time, a number of other descriptions have been proposed to set the morphology of polycystic ovaries on ultrasound, all based on the main histologic features: excessive number of follicles, and stroma hypertrophy. The increase in ovarian volume or the stroma area, stromal hyperechogenicity, the relationship between the stromal and ovarian areas, and the relationship between the ovarian and uterine volumes were also described and the parameters were tested.

The denser ovarian stroma is an important parameter for histopathologic diagnosis [14]. In ultrasound, the ovarian stroma should theoretically be less echogenic than the myometrium [8]. The hyperechoic stroma (Fig. 2.8) had a sensitivity of 94% and specificity of 90% for the diagnosis of polycystic ovaries in a study that compared women with PCOS with a control group [15]. In a study in which the echogenicity of the stroma was measured in a formula that took into account the number of pixels per area examined, the values found in PCOS patients were not significantly different [16].

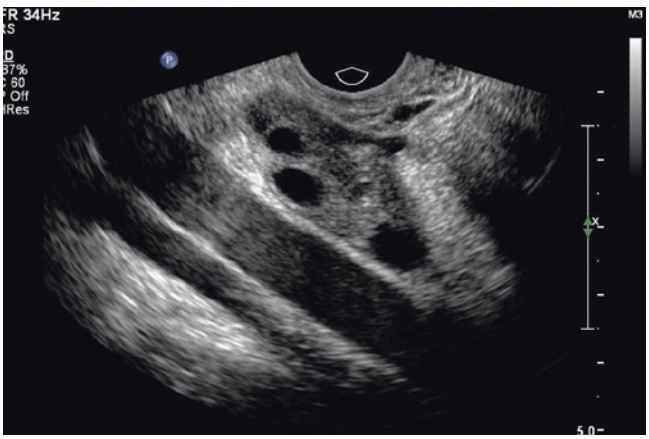

Fig. 2.2 Transvaginal sagittal image of normal ovary

Fig. 2.3 Transvaginal image of polycystic ovary. The enlarged ovary with more evident stroma and multiple small follicles that make up the appearance of small cysts

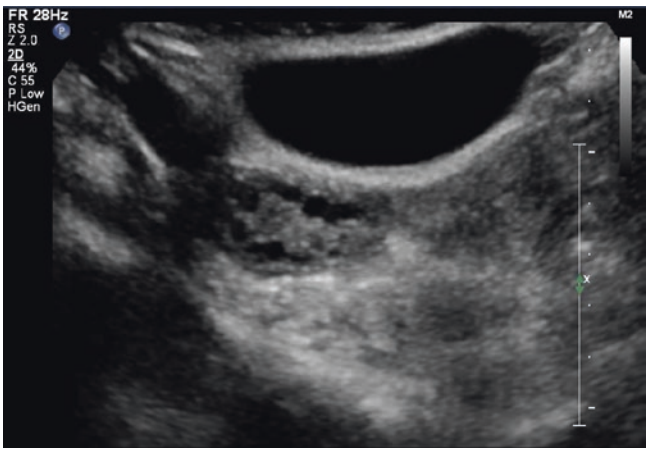

Fig. 2.4 Transabdominal image of a polycystic ovary as described by Adams: at least 10 follicles, usually from 2 to 8 mm in diameter, distributed circumferentially around a central dense stroma

Fig. 2.5 Transvaginal image of a polycystic ovary as described by Adams: at least 10 follicles, usually from 2 to 8 mm in diameter, distributed peripherally around a central dense stroma

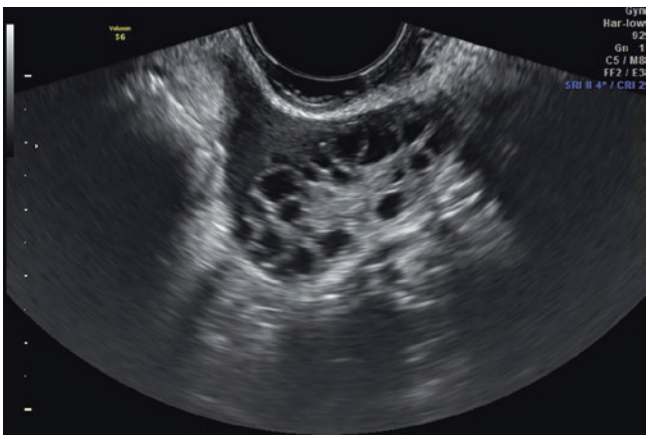

Fig. 2.6 Transvaginal image (axial view) of a polycystic ovary as described by Adams: at least 10 follicles, usually from 2 to 8 mm in diameter, distributed peripherally around a central dense stroma

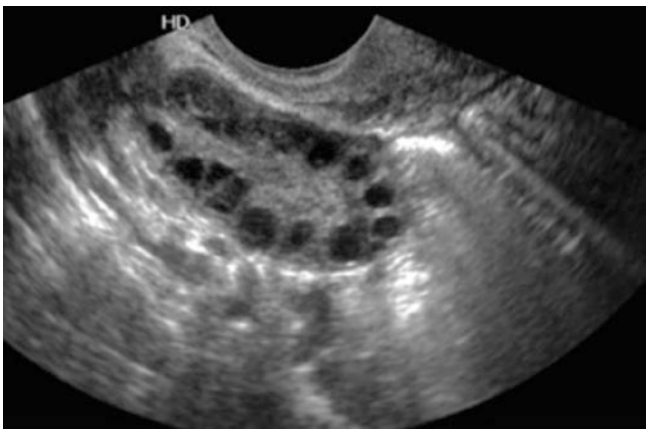

Fig. 2.7 Transvaginal image of a polycystic ovary as described by Adams: at least 10 follicles, usually from 2 to 8 mm in diameter, distributed peripherally around a central dense stroma

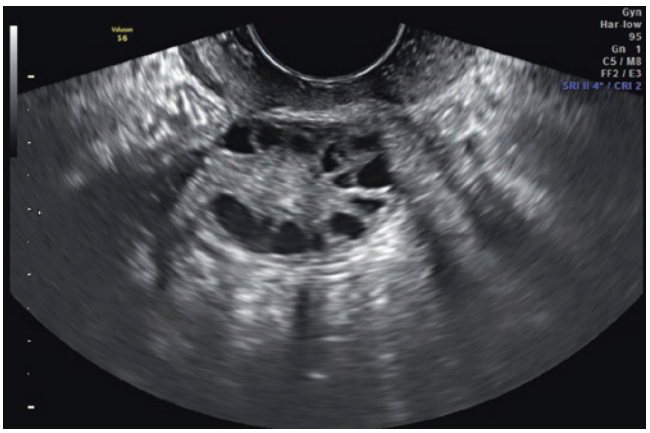

Fig. 2.8 Transvaginal B mode image of polycystic ovary shows a hyperechoic central stroma

Dopplerfluxometry

Angiogenesis is an important histological component of follicular luteinization. This neovascularization occurs by luteinizing hormone stimulation and is mediated by local production of the endothelial growth factor [17]. The intra-ovarian stromal blood flow can be seen on a colored Doppler, and is usually increased significantly in the polycystic ovaries relative to normal ovaries (Figs. 2.9 and 2.10). The intra-ovarian blood flow was observed in the early follicular phase in 88% of patients with PCOS, and in 50% of normal patients [18]. The increase in intra-ovarian stromal vascularization is also considered an important parameter for predicting the response to stimulus for in vitro fertilization [19].

Aiming to standardize and make diagnosis more reproducible, a consensus reached at the ASRM/ESHRE meeting in Rotterdam in 2003 reviewed the various parameters and defined as polycystic those ovaries that have one of the following conditions: 12 or more follicles of 2–9 mm in diameter, or an increase in volume (more than 10 cm^3) [8] (Figs. 2.11 and 2.12).

The threshold of 12 or more follicles between 2 and 9 mm was the best for the diagnosis of PCOS (sensitivity 75% and specificity 99%) [17]. The value of ovarian volume was mainly defined, because the reviewed studies rarely showed normal ovaries with more than 10 cm^3. The hypertrophy of the stroma contributes to the increase in the global ovarian volume; the latter parameter is more objective and less subject to technical variations, as interpretation from the examiner or equipment settings. They also recommend that [8]:

- The subjective impression of the examiner should not replace these parameters, except in patients who use oral contraceptives, in which case the ovarian volume can be normal and the polycystic appearance may persist.
- The arrangement of follicles, if peripheral or scattered by the stroma, does not need to be reported.
- If only one ovary meets one of the criteria, it is enough for the characterization of polycystic ovaries.
- If there is one dominant follicle (more than 10 mm in diameter) or lute body, the test must be repeated in the next cycle (Fig. 2.13).
- The patient with a morphology of polycystic ovaries on ultrasound, but is asymptomatic (no signs of hyperandrogenism or anovulation) should not be diagnosed with polycystic ovary syndrome.

As for the technique of the examination, the Rotterdam consensus orients the following standardization [8]:

- The examination should be performed by an examiner trained to use modern equipment.
- The transvaginal approach is preferred, especially in obese patients.
- The examination should be performed in the early follicular phase, between days 3 and 5 of the cycle. In cases of patients with amenorrhea or oligomenorrhea, it can be random or shortly after bleeding induced by progesterone.
- The ovarian volume is calculated using the formula for an elongated ellipse (0.5 × length × depth × thickness).
- The counting of follicles should be done in two cutting planes (Figs. 2.14 and 2.15), and the follicular measure should be the average of the diameters obtained in the three planes (longitudinal, transverse, and anteroposterior).

The definition proposed by the Rotterdam consensus is simpler and more straightforward. The main argument used by the authors is that the standardization of quantitative parameters (follicle count and volume measure) rather than qualitative (such as increased echogenicity of the stroma or increased vasculature) becomes the most assertive and most reproducible method.

In 2010, the new consensus was held in Amsterdam, which added a particularity in the consideration of ovaries with polycystic morphology on ultrasound in adolescent patients. For this group, the two characteristics should be present: 12 or more follicles from 2 to 9 mm in diameter and an increase in volume (more than 10 cm^3) [9].

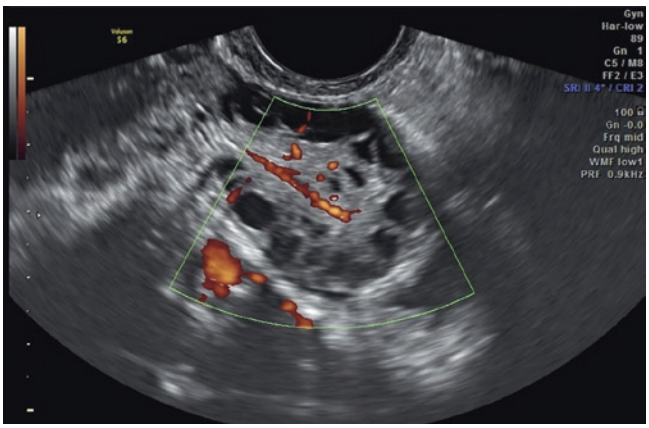

Fig. 2.9 Transvaginal Doppler sonogram of polycystic ovary shows an increased intra-ovarian stromal vascularization

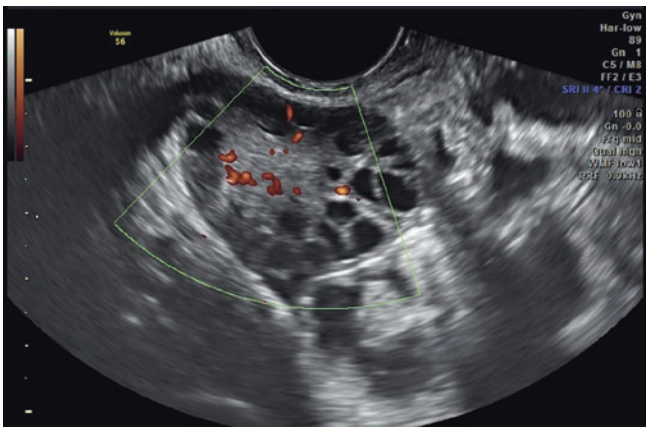

Fig. 2.10 Transvaginal Doppler sonogram of polycystic ovary shows an increased intra-ovarian stromal vascularization

Fig. 2.11 Transvaginal image of polycystic ovary as described at the Consensus meeting of ASRM/ESHRE in Rotterdam (2003). Parameters: 12 or more follicles of 2–9 mm in diameter or an increase in volume (more than 10 cm^3). The arrangement of follicles, whether peripheral or scattered by the stroma, does not need to be reported

Fig. 2.12 Transvaginal image of polycystic ovary as described at the Consensus meeting of ASRM/ESHRE in Rotterdam (2003). Parameters: 12 or more follicles of 2–9 mm in diameter or an increase in volume (more than 10 cm^3). The arrangement of follicles, whether peripheral or scattered by the stroma, does not need to be reported

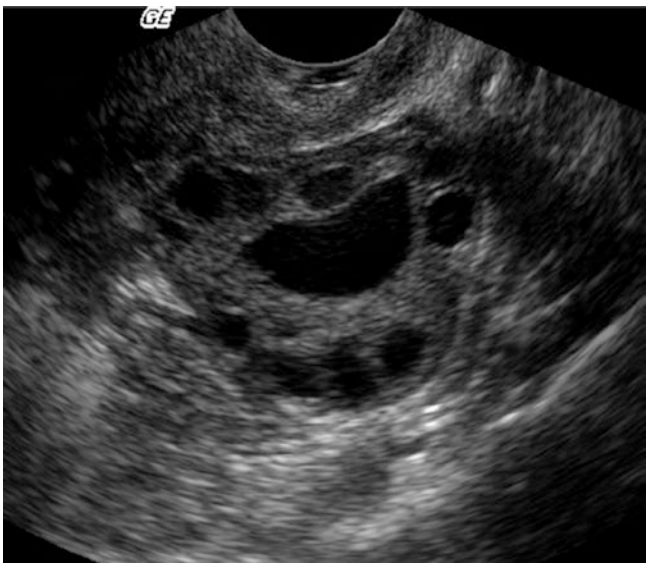

Fig. 2.13 Transvaginal image of ovary that shows 12 or more follicles and an increase in volume, but with a dominant follicle (more than 10 mm in diameter). The test must be repeated in the next cycle

Fig. 2.14 Transvaginal sagittal image of polycystic ovary. The counting of follicles should be made in two cutting planes

Fig. 2.15 Transvaginal transverse image of polycystic ovary. The same ovary showed in a sagittal image in Fig. 2.14

Policystic Ovaries vs Multifollicular Ovaries

In 1985, Adams et al described the multifollicular ovary as a normal or slightly larger ovary, with 6–10 follicles measuring between 4 and 10 mm in diameter, distributed throughout the ovary, and not circumferentially (Fig. 2.16). Different than polycystic ovaries, they do not present hypertrophy of the stroma (Fig. 2.17) and are often associated with amenorrhea by a GnRH deficiency, such as those associated with underweight women or women who experience late puberty [20]. The patients do not show signs of hyperandrogenism. A practical aspect for the differential diagnosis on ultrasound is that the multifollicular ovary loses its appearance in an ovulatory cycle, while the polycystic aspect does not.

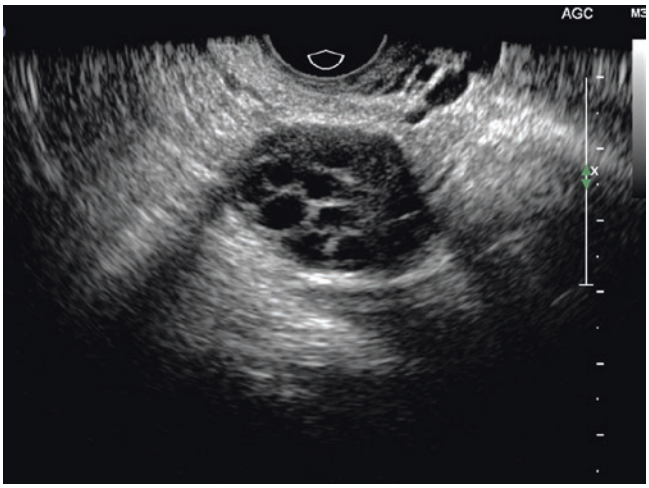

Fig. 2.16 Transvaginal image of multifollicular ovary as described by Adams. An ovary increased in size with follicles measuring between 4 and 10 mm in diameter, distributed throughout the ovary

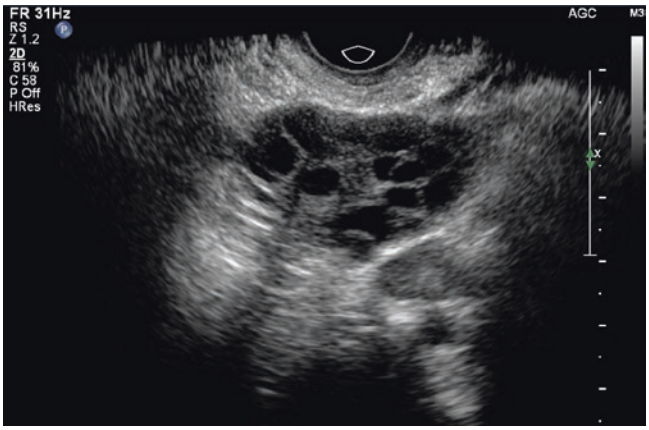

Fig. 2.17 Transvaginal image of multifollicular ovary as described by Adams. Different than a polycystic ovary, it does not present hypertrophy of the stroma

The Relationship with Endometrial Neoplasms

There is a correlation between PCOS and an increase in the risk for endometrial cancer, especially in younger patients. It is estimated that the risk of endometrial cancer is 2.7 times higher in patients with PCOS [9]. The not-antagonized hyperestrogenism and failure in endometrial shedding are the mechanisms that explain this association. There is no consensus in the application of tracing tests for endometrial cancer, but during transvaginal ultrasonography, the finding of polycystic ovaries should encourage a detailed evaluation of the endometrial echo.

References

1. Stein IF, Leventhal ML. Amenorrhea associated with bilateral polycystic ovaries. Am J Obstet Gynecol. 1935;29:181–91.
2. Rebar R, Judd HL, Yen SS, Rakoff J, Vandenberg G, Naftolin F. Characterization of the inappropriate gonadotropin secretion in polycystic ovarian syndrome. J Clin Invest. 1976;57:1320–9.
3. Franks S. Polycystic ovary syndrome. N Engl J Med. 1995;333:853–61.
4. Polson DW, Adams J, Wadsworth J, Franks S. Polycystic ovaries – a common finding in normal women. Lancet. 1988;1:870–2.
5. Lobo RA. A unifying concept for polycystic ovary syndrome. In: Chang RJ, editor. Polycystic ovary syndrome. New York: Springer; 1996. p. 334–52.
6. Lobo RA, Carmina E. The importance of diagnosing the polycystic ovary syndrome. Ann Intern Med. 2000;132:989–93.
7. Zawadzki JA, Dunaif A. Diagnostic criteria for polycystic ovary syndrome: towards a rational approach. In: Dunaif A, Givens JR, Haseltine FP, Merriam GR, editors. Polycystic ovary syndrome. Boston: Blackwell Scientific; 1992. p. 377–84.
8. Fauser B, Tarlatzis B, Chang J, et al. The Rotterdam ESHRE/ASRM-sponsored PCOS consensus workshop. 2003 consensus on diagnostic criteria and long-term health risks related to Polycystic Ovary Syndrome (PCOS). Hum Reprod. 2004;19:41–7.
9. Fauser BCJM, et al. Consensus on women's health aspects of polycystic ovary syndrome (PCOS): the Amsterdam ESHRE/ASRM-sponsored 3rd PCOS Consensus Workshop Group. Fertil Steril. 2012;97:28–38.
10. Michelmore KF, Balen AH, Dunger DB, Vessey MP. Polycystic ovaries and associated clinical and biochemical features in young women. Clin Endocrinol. 1999;51:779–86.
11. Fox R, Hull M. Ultrasound diagnosis of polycystic ovaries. Ann N Y Acad Sci. 1993;687:217–23.
12. Adams J, Polson DW, Abdulwahid N, Morris DV, Franks S, Mason HD, Tucker M, Price J, Jacobs HS. Multifollicular ovaries: clinical and endocrine features and response to pulsatile gonadotropin releasing hormone. Lancet. 1985;1375–1379.
13. Abdel Gadir A, Khatim MS, Mowa RS, Alnaser HM, Muharib NS, Shaw RW. Implications of ultrasonically diagnosed polycystic ovaries. I. Correlations with basal hormonal profiles. Hum Reprod. 1992;7:453–7.
14. Hughesdon PE. Morphology and morphogenesis of the Stein-Leventhal ovary and of so-called `hyperthecosis. Obstet Gynecol Surv. 1982;37:59–77.
15. Pache TD, Wladimiroff JW, Hop WC, Fauser BCJM. How to discriminate between normal and polycystic ovaries: transvaginal ultrasound study. Radiology. 1992;183:421–3.
16. Buckett WM, Bouzayen R, Watkin KL, Tulandi T, Tan SL. Ovarian stromal echogenicity in women with normal and polycystic ovaries. Hum Reprod. 1999;14:618–21.
17. Anasti JN, Kalantarido SN, Kimzey LM, George M, Nelson LM. Human follicle fluid vascular endothelial growth factor concentrations are correlated with luteinization in spontaneously developing follicles. Hum Reprod. 1998;13:1144–7.
18. Battaglia C, Artini PG, Genazzani AD, Sgherzi MR, Salvatori M, Giulini S, Volpe A. Color Doppler analysis in lean and obese women with polycystic ovaries. Ultrasound Obstet Gynecol. 1996;7:342–6.
19. Engmann L, Sladkevicius P, Agrawal LR, Bekir JS, Campbell S, Tan SL. Value of ovarian stromal blood flow velocity measurement after pituitary suppression in the prediction of ovarian responsiveness and outcome of in vitro fertilization treatment. Fertil Steril. 1999;71:22–9.
20. Adams J, et al. Multifollicular ovaries: clinical and endocrine features and responde to pulsatile gonadotropin releasing hormone. Lancet. 1985;2:1375–9.

Tubal Diseases

3

César Amaral de Camargo Penteado

Histerosalpingography (HSG) remains a valuable tool in the evaluation of the uterus and fallopian tubes. Radiologists should become familiar with the HSG technique and interpretation of the resulting images.

Because tubal problems are at fault in 30–40% of infertile couples, the evaluation of tubal patency is essential in the investigation of female infertility, and it should be part of every infertility investigation. With improvements in contrast media and techniques, HSG has been regarded as the most reliable test for tubal dysfunction, is much less invasive and less expensive than other procedures (such as laparoscopy), and yields valuable information about the uterine cavity and fallopian tubes.

In clinical practice, however, the number of HSG examinations has increased dramatically over the past few years. This increase is likely the result of advances in reproductive medicine, resulting in more successful in vitro fertilization procedures, as well as the trend toward women delaying pregnancy until later in life [1].

Etiology of Infertility [2]

- Male factor (40%):
  Low sperm count
  Decreased motility and/or morphology
  Autoimmunity
- Female factor (55%):
  Tubal factors (30%): partial or complete obstruction, intra- or peritubal adhesions
  Ovulatory dysfunction (30%): anovulation, luteal phase defect
  Cervix factor (10%): diminished mucus production, infected mucus, sperm antibodies
  Pelvic (peritoneal) factors: endometriosis, periadnexal adhesions, tuberculosis
  Uterine factors: anomalies, synechiae, endometritis, fibroids
  Others: serum antibodies in female, chronic vaginitis, inadequate intercourse
- No apparent etiology (5%)

Technique of Histerosalpingography and Contrast Media

This procedure is easily performed on an outpatient basis without anesthesia; this chapter explains the indications, contraindications, techniques, potential complications, and post-procedural pregnancy rates of HSG.

Because patients may experience cramping during the examination, women are advised to take a nonsteroidal anti-inflammatory or antispasmodic drug 1 h prior to the procedure. The examination should be scheduled during days 7–12 of the menstrual cycle (day 1 being the first day of menstrual bleeding). The endometrium is thin during this proliferative phase, a fact that facilitates image interpretation and should also ensure that there is no pregnancy.

The patient should be instructed to abstain from sexual intercourse from the time menstrual bleeding ends until the day of the study to avoid a potential pregnancy. If the patient has irregular menstrual cycles or there is a possibility of pregnancy, the human chorionic gonadotropin serum level is evaluated.

The patient is placed on the fluoroscopy table in the supine position. The perineum is prepared with povidone-iodine solution and draped with sterile towels, and a speculum is inserted into the vagina. The cervix is located and cleansed with povidone-iodine solution. A 5-F or 7-F HSG catheter is located in the cervical canal and the balloon is inflated fully (or to the extent that the patient can tolerate, since this maneuver may cause cramping).

C.A. de Camargo Penteado
Radiology Department, Hospital do Servidor Público Estadual de São Paulo (IAMSPE), São Paulo, SP, Brazil
e-mail: cesarpenteado@gmail.com

L.R.M.F. de Souza et al. (eds.), *Atlas of Imaging in Infertility*, DOI 10.1007/978-3-319-13893-0_3

A scout radiograph of the pelvis is obtained with the catheter in place before contrast material is instilled, and six to eight spot radiographs are obtained after the scout radiograph. The first image is taken during early filling of the uterus and is used to look for any filling defect or contour abnormality. Small filling defects are best seen at this stage.

The second image is obtained with the uterus fully distended; its shape is best evaluated at this stage, although small filling defects may be obscured when the uterus is well opacified. The third (and fourth and fifth) image is obtained to show and evaluate the fallopian tubes. The sixth image should exhibit the free intraperitoneal spillage of contrast material.

Additional spot radiographs are obtained to document any abnormality that is seen. Oblique views of the fallopian tubes may be obtained as needed, to "elongate" the tubes or displace superimposed structures. If the balloon obscured the lower uterine segment after initial placement, or migrated into this area during the study, a radiograph is usually obtained at the end of the study with the balloon deflated (Fig. 3.1a, b)

A variety of technical problems may occur, such as malfunction of the instuments used (which can be easily avoided by checking the equipment carefully before the start of study). Anatomic abnormalities, or patient discomfort can cause termination of the examination (Figs. 3.1c, 3.2 and 3.3). Complications can involve pain and discomfort, injury and bleeding, vascular intravasation (<5%), contrast material reactions [3], post-procedure infection, mortality, pregnancy radiation (Fig. 3.4).

Post-procedural pregnancy rates are not well known and have not been thoroughly investigated. Possibilities of treatment include mechanical lavage of tubes, release of peritubal adhesions, stimulation of the cilia of the tubal mucosa, alteration of the cervical mucous, and a bacteriostatic effect.

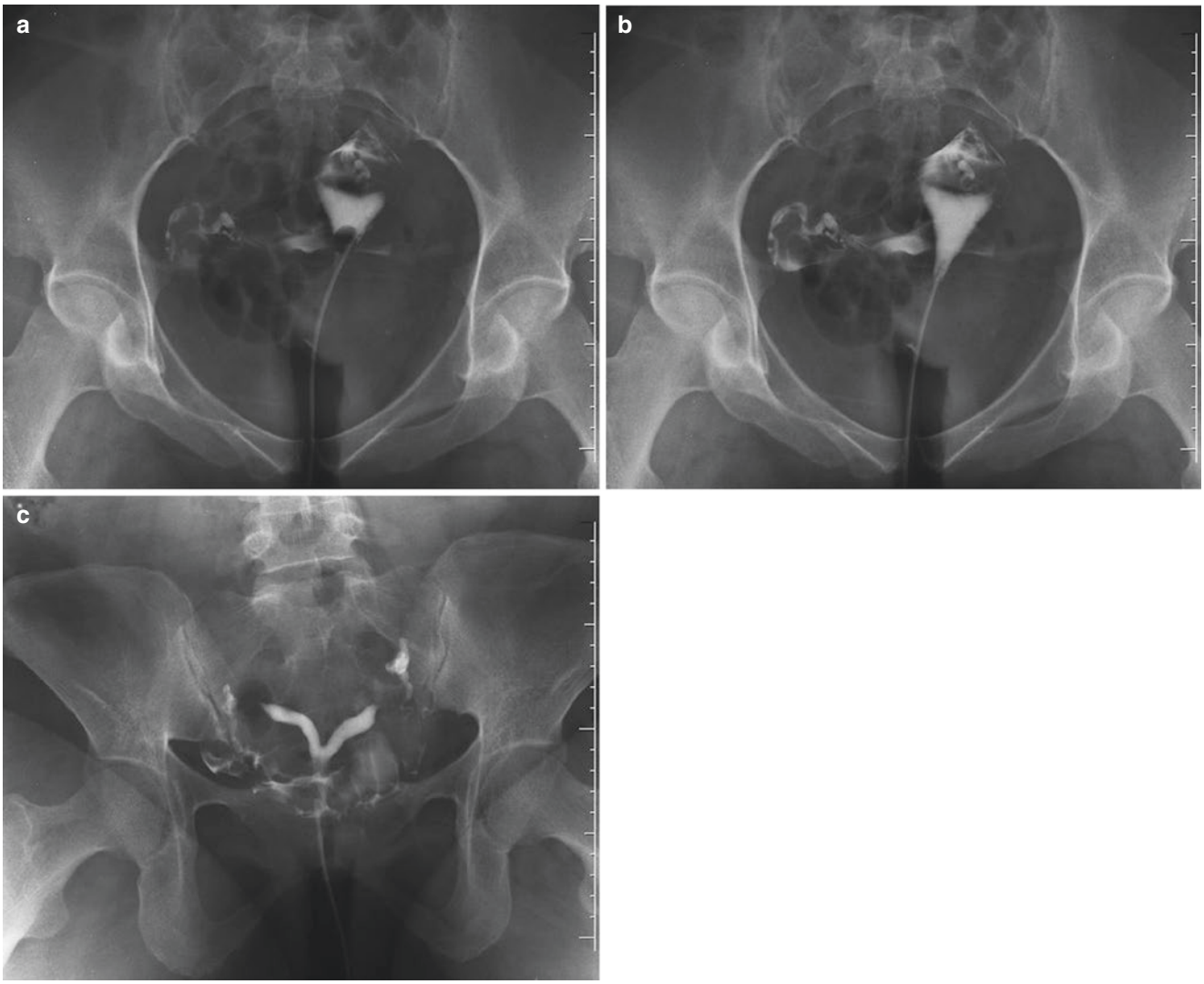

Fig. 3.1 (**a**) Balloon obscured lower uterine segment after initial placement. (**b**) balloon deflated at the end of study. (**c**) Uterine congenital anomalies, typically with a single external cervical os, can be difficult to interpret. The most common problem occurs in the complete bicornuate or septate uterus and can simulate a unicornuate uterus if the catheter is positioned into the lower uterine segment. Photo shows correct position of the catheter

Fig. 3.2 Spherical filling defect represents air bubble

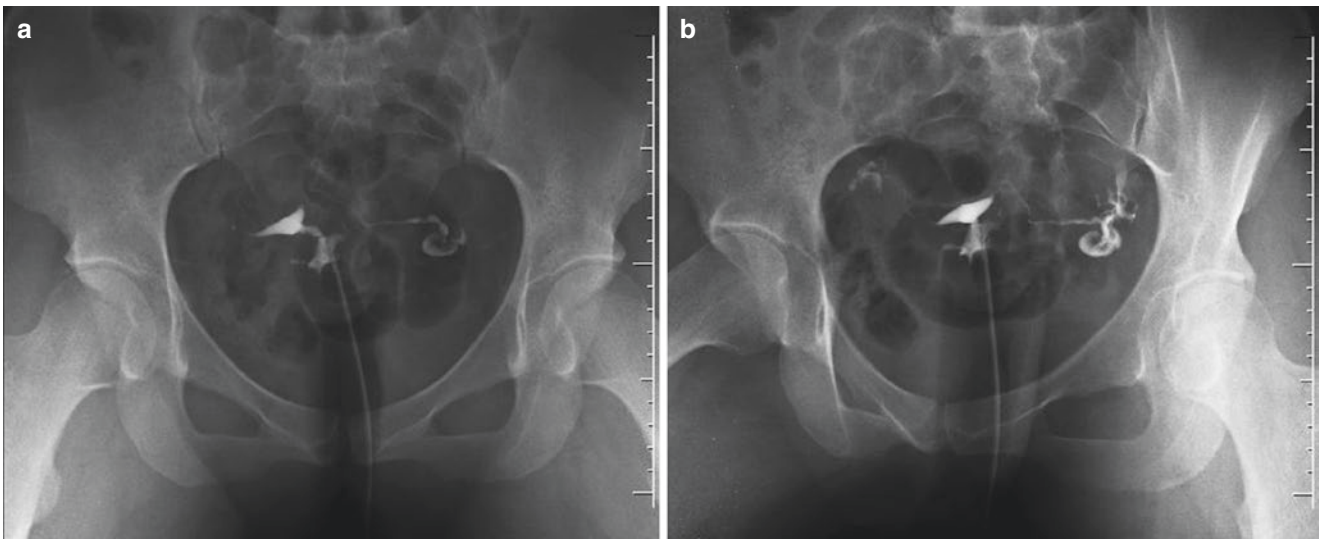

Fig. 3.3 (**a**, **b**) Right fallopian tube failed to opacify despite left tubal filling and a peritoneal spillage. Right tube is seen along with peritoneal spillage, although anatomic obstruction may be the cause. Technical problems, cornuate spasm, and mucous plugging are other considerations

Fig. 3.4 Vascular intravasation

Indications and Contraindications

- Indications for HSG
  Infertility
  Recurrent spontaneous abortions
  Postoperative evaluation following tubal ligation or reversal of tubal ligation
  Preoperative evaluation prior to myomectomy
- Contraindications for HSG
  Pregnancy
  Active pelvic infection

Radiographic Anatomy

The fallopian tubes serve as the passageway for the ovum to travel from the ovary to the uterus. They are 10–12 cm in length and course along the superior aspect of the broad ligament [5–6]. Each fallopian tube can be divided radiographically into three segments. The interstitial or cornual region is the short segment that traverses the muscular wall of the uterus; the isthmic portion is the longest of the three segments and is the narrow segment between the interstitial and ampullary regions; the ampullary portion is the widened region near the ovary [7–8]. The fimbriated part is the funnel-shaped end of the tube and is not usually seen in HSG (Figs. 3.5, 3.6, 3.7, 3.8, 3.9, 3.10 and 3.11).

Fig. 3.5 Tube segments: intramural, isthmic, ampullary

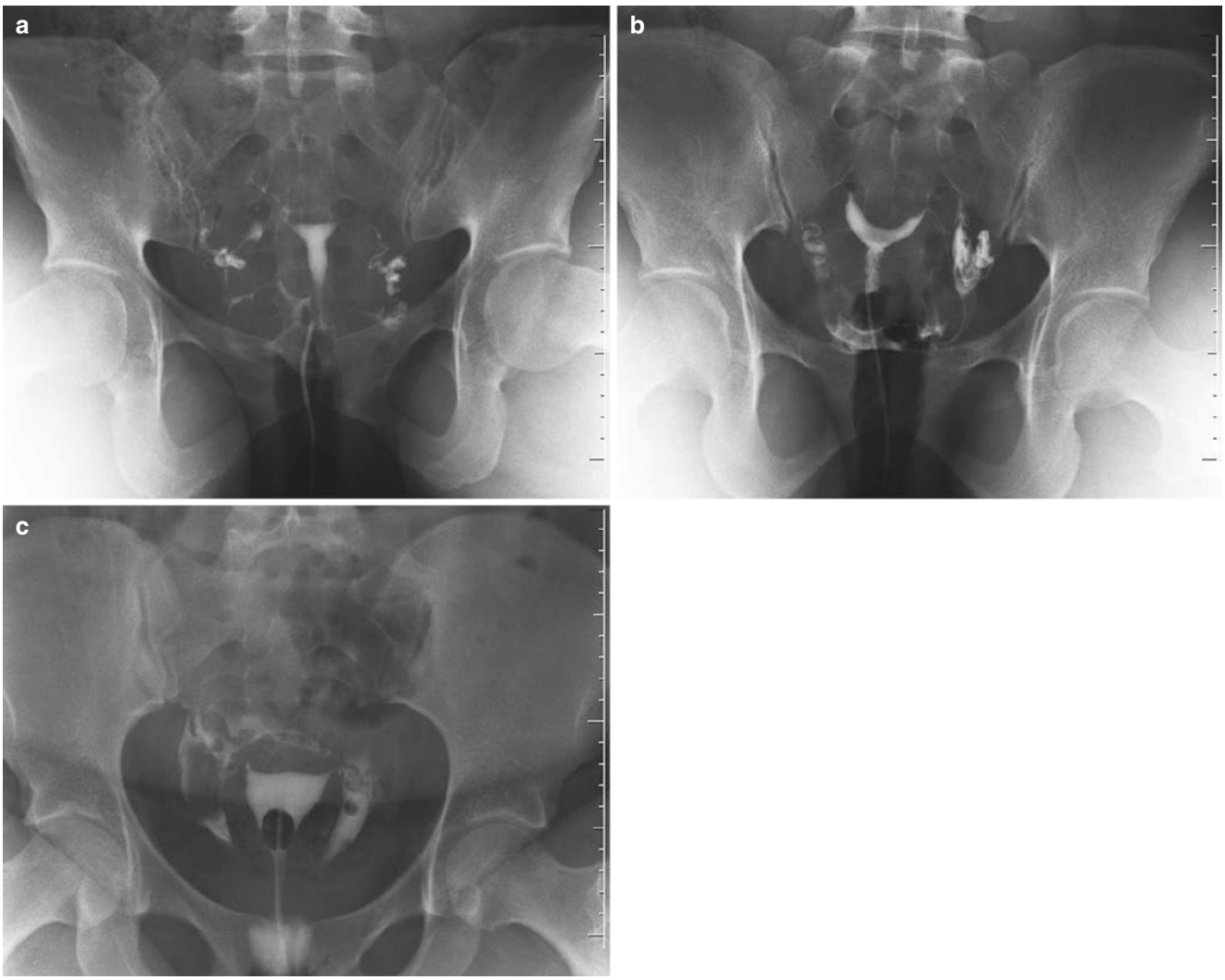

Fig. 3.6 Variants of normal uterine fundus. (**a**) straight, (**b**) concave, (**c**) convex

Fig. 3.7 Linear lucencies are seen at both corneal tubal junctions

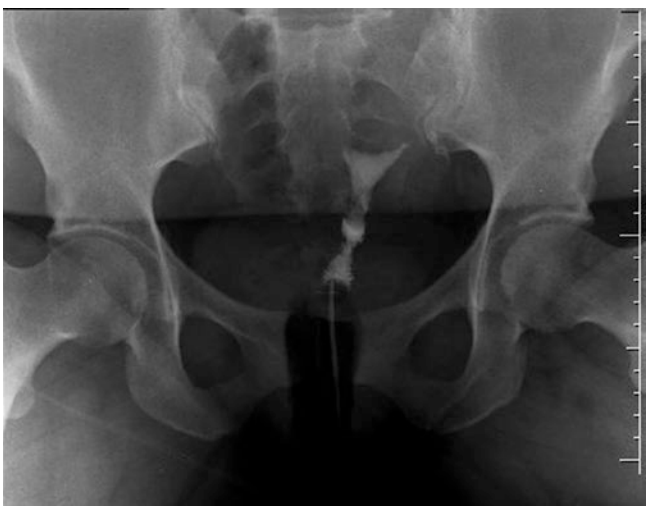

Fig. 3.8 The endocervical borders can appear serrated normally and should not be confused with endocervicitis. The mucosa of the endocervix forms small parallel folds, the plicae palmatae, to create a finely serrated margin

Fig. 3.9 Bilateral fallopian tube patency shown by intraperitoneal dispersion of contrast media

Fig. 3.11 "Clumping" – suggesting peritubal adhesions

Fig. 3.10 Spiculation of uterine cavity, when found in the upper uterus, suggests adenomyosis

General Diagnostic Principles

A. *Endocervical canal*:
Straight and long endocervical canal (Fig. 3.12)
Filling defects: polyp (Fig. 3.13)
Endocervical postoperative (diverticular-like outpunching due to cesarean section) (Fig. 3.14)

B. *Uterine cavity*: *Congenital abnormalities and uterine body abnormalities* [4]
Uterine shape: arcuate (Fig. 3.15a), bicornuate (Fig. 3.15b), unicornuate (Fig. 3.15c)
Uterine filling defects: air bubble, (Fig. 3.16a), synechiae (Fig. 3.16b), polyp/fibroid (Fig. 3.16c), neoplasm (Fig. 3.16d) (multiple irregular filling defects, possibly endometrial carcinoma with superimposed bleeding).

The uterus is a muscular sac that houses the fetus during gestation; its size varies, depending on the patient's age and parity. HSG is helpful in the evaluation of the uterine cavity only, providing indirect information about the remainder of the uterus. The uterine cavity is triangular, with the base directed cranially and the apex caudally. The cervix constitutes the most inferior aspect of the uterus and extends into the vagina. The isthmus is the uterine portion immediately above the cervix. Most of the uterus is composed of the body, or "corpus." The uppermost aspect of the uterus is the fundus, which can be concave, flattened, or slightly convex. The fallopian tubes connect to the fundus at the cornua, or lateral extremes of the base of the triangular cavity. In HSG, the uterus should look like an inverted triangle with well-defined, smooth contours. Uterine anomalies can be due to congenital abnormalities of uterine shape, luminal filling defects, or abnormalities of uterine contour [12].

C. *Tubes*: *Tubal and adnexal abnormalities*

MR hysterography with a heavily T2-weighted sequence (a procedure that is similar to MR cholangiopancreatography) has also been suggested for visualizing the fallopian tubes [9]. However, the size of the normal fallopian tube is at or below the resolution of most MR imagers [10]. Moreover, even if the tube is visualized, MR hysterography does not help assess tubal patency. The instillation of saline solution or water through an HSG catheter in conjunction with MR hysterography is possible, but this procedure has not gained wide acceptance [9].

In HSG, the fallopian tubes should appear as thin, smooth lines that widen in the ampullary portion (Fig. 3.5). The isthmic portion has been likened to a piece of spaghetti in appearance. The fallopian tubes vary in their location within the pelvis and in their degree of tortuosity. There should be free spillage of contrast material into the peritoneal cavity [11] (Figs. 3.17, 3.18, 3.19, 3.20 3.21).

Fig. 3.12 Straight and long endocervical canal

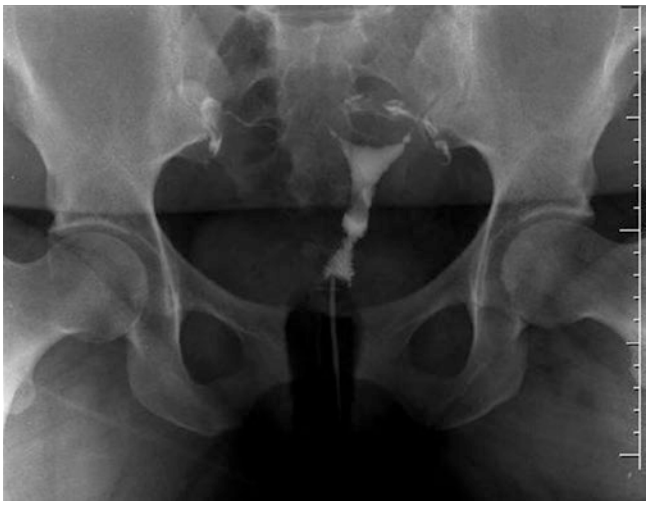

Fig. 3.13 Polyp as a filling defect

Fig. 3.14 Endocervical postoperative diverticular-like (cesarian section)

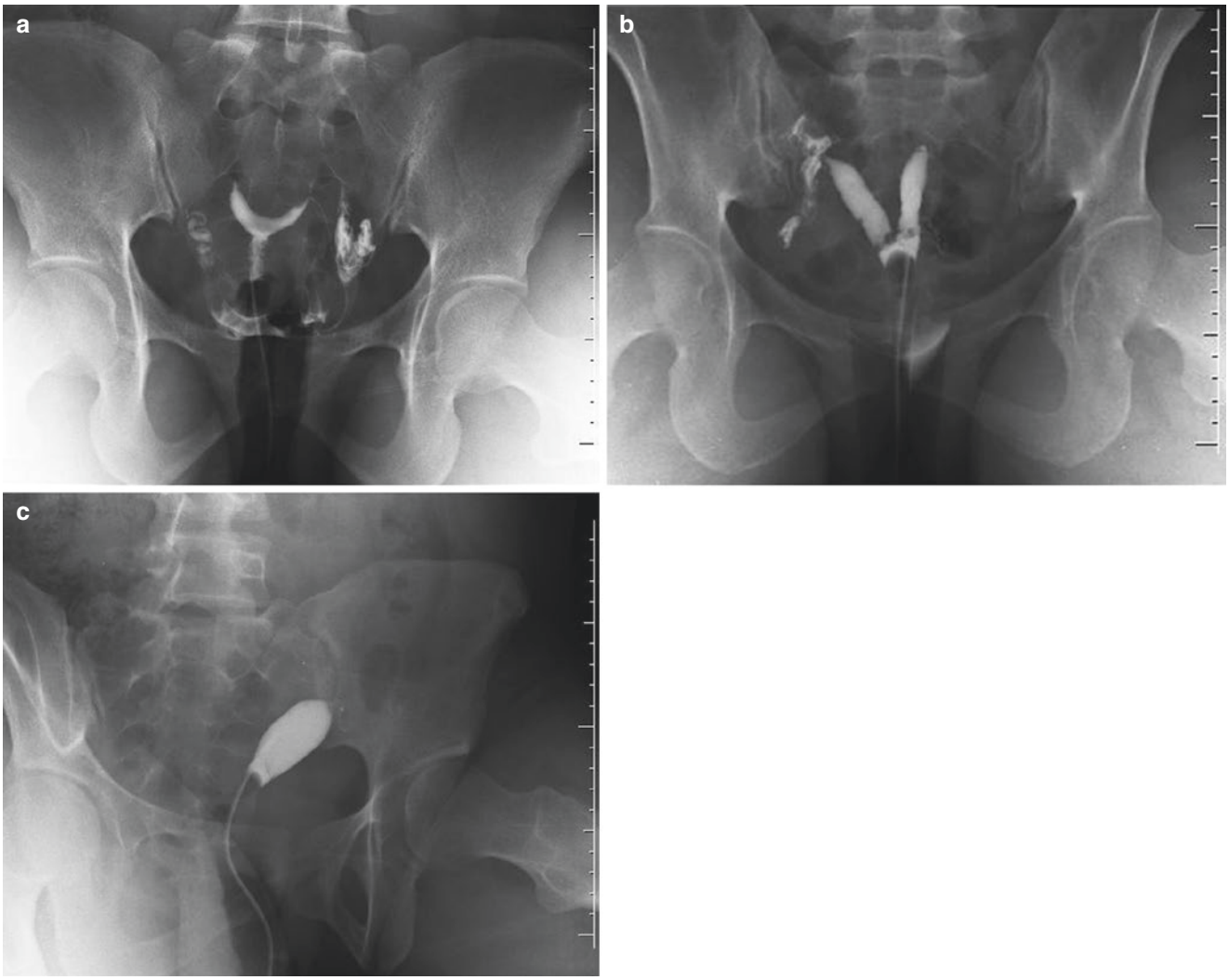

Fig. 3.15 Müllerian malformations: (**a**) arcuate uterus; (**b**) bicornuate; (**c**) unicornuate

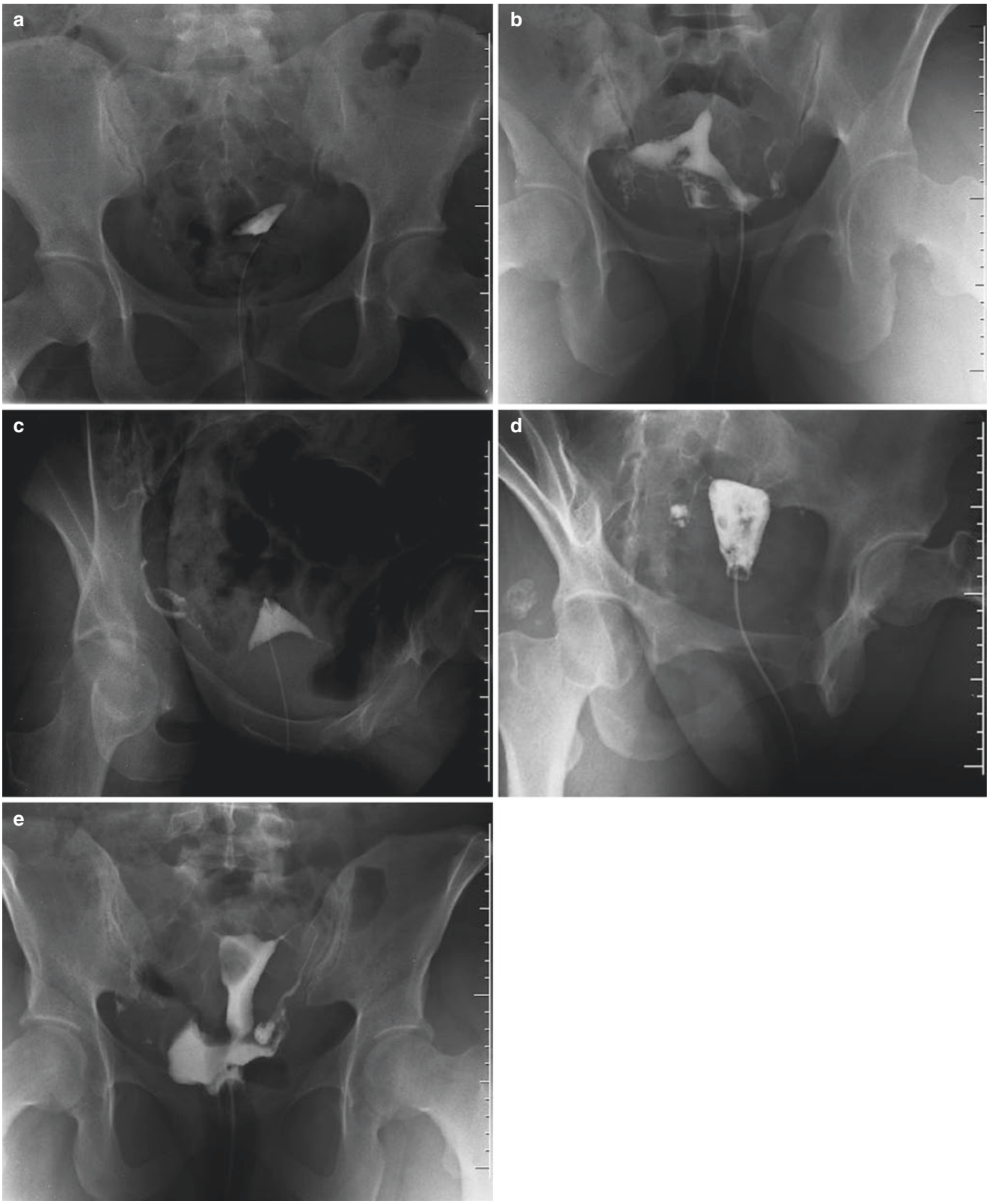

Fig. 3.16 Uterine filling defects: (**a**) air bubble; (**b**) synechiae; (**c/e**) polyp/fibroid; (**d**) neoplasm

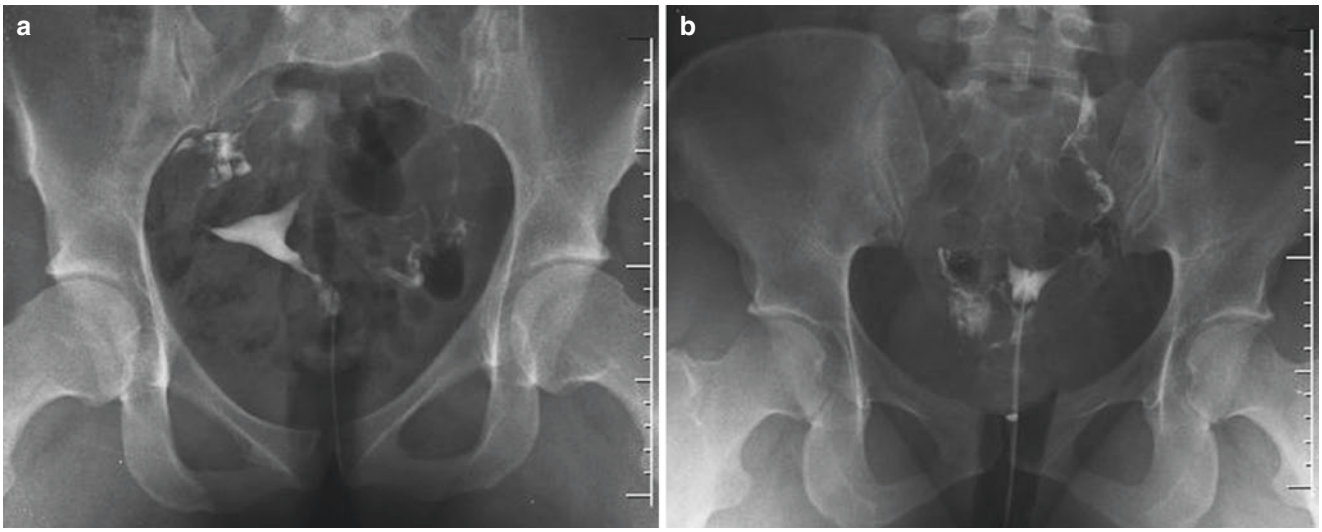

Fig. 3.17 (**a**) Right tube locates superiorly. (**b**) Left tube locates superiorly. Many variations in the course and location of the fallopian tubes were seen and should be considered normal, unless another sign associated, such as deviation from the adjacent mass

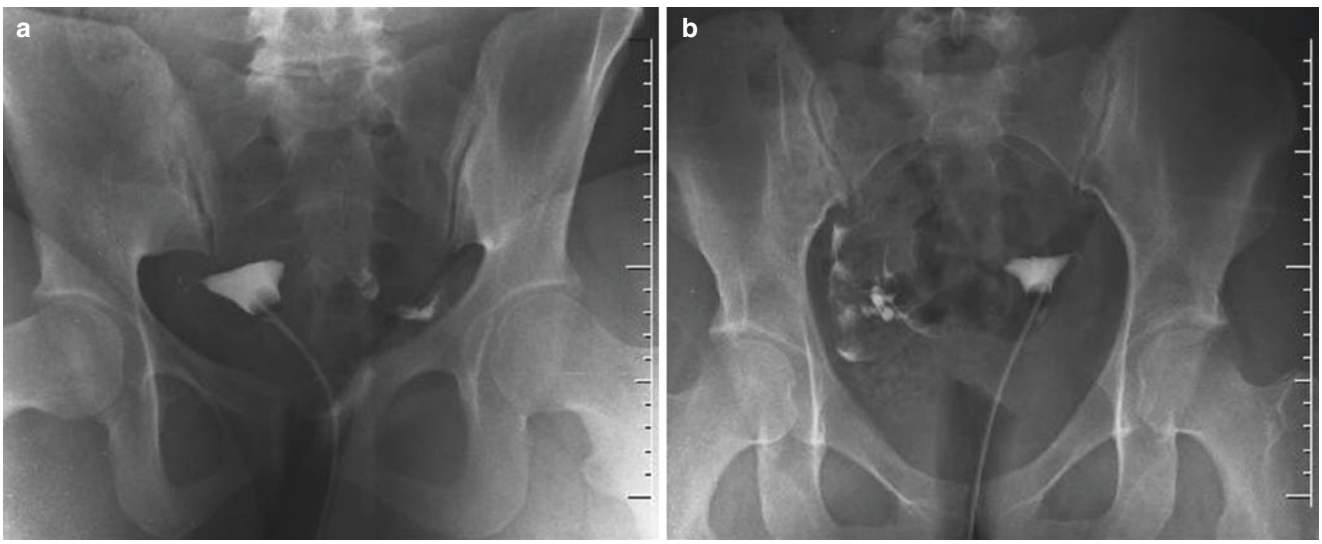

Fig. 3.18 Salpingectomy (**a**) right (**b**) left

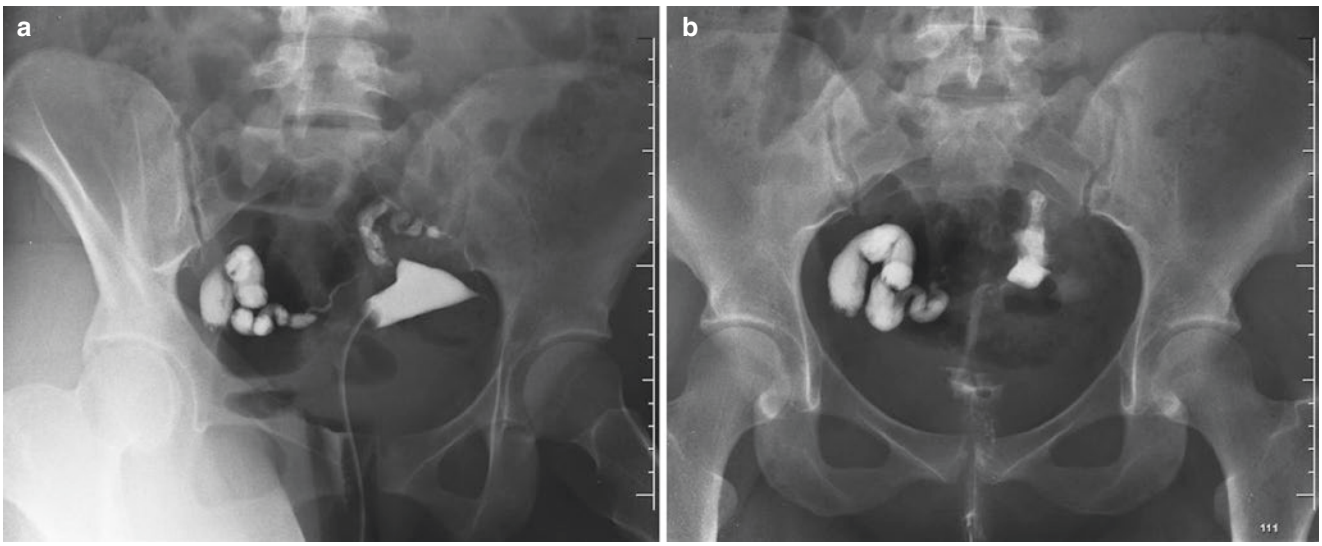

Fig. 3.19 Hydrosalpinx: (**a**) during the procedure, (**b**) showing contrast in the right fallopian tube after removing the catheter

Fig. 3.20 Polyp tubes

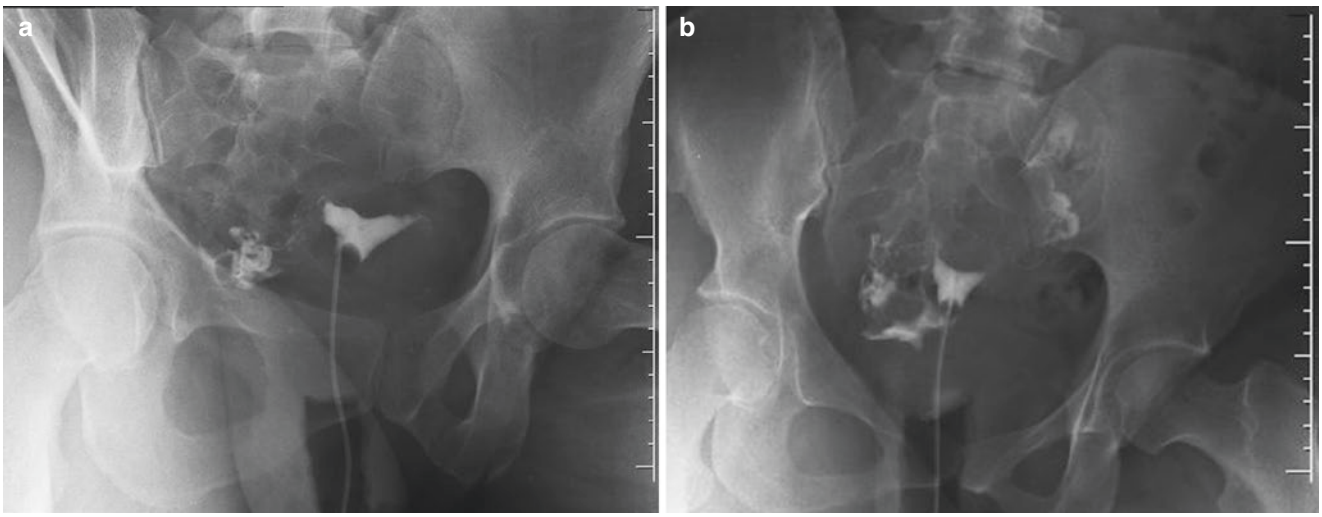

Fig. 3.21 Tubal irregularity: (**a**) salpingitis isthmica nodosa, (**b**) endometriosis

Endometriosis

Endometriosis is defined as the presence of benign endometrial implants in ectopic locations, and it may affect the fallopian tubes and adjacent peritoneum. Multiple sites may be involved, including the ovary, serosa of the uterus and tubes, pelvic peritoneum, and bowel. The pathogenesis of the disease is not known, but the most common theories are retrograde menstruation and implantation, metaplasia of multipotential ceolomic epithelium, and the lymphatic or hematogenous spread of endometrium.

Tubal endometriosis most often affects the intramural portion, although extension into other sites occurs. Endometrial nodules of varying sizes cause polypoid excrescences that compress and narrow the lumen. In the pelvic cavity, endometriosis may appear as isolated ectopic implants of endometrium, or as diffuse nodulation affecting one or more anatomic locations. The nodules are generally less than 1.0 cm in size, but can be larger in more severe cases and if endometriomas develop. Endometriosis responds to the hormonal fluctuations of the menstrual cycle with changes in appearance due to proliferation and bleeding, which incite inflammation and fibrosis; this may result in focal scarring, hemorrhagic cysts or endometriomas, or a diffuse adhesive disease involving many pelvic structures.

Endometriosis affects menstruating women,and stabilizes or regresses in menopause. Patients may be asymptomatic and the disease discovered incidentally. Symptoms depend on its sites and severity and the phase of the menstrual cycle. Patients may have pelvic, lumbar, or rectal pain, dysmenorrhea, dyspareunia, infertility, and signs of compression on adjacent organs. Symptoms usually worsen with menstruation. Endometriosis is considered to be a surgical disease because it rarely responds to medical therapy.

HSG is limited in evaluating endometriosis because tubal involvement is not common and adnexal disease is not seen directly. Tubal endometriosis may have a beaded appearance due to multiple constrictions from the endometrial deposits, which can cause occlusion. Radiographic findings were nonspecific and included dilatation, blockage, and clumping. Peritubal loculations of contrast materials were also seen, but had to be distinguished from hydrosalpinx and normal accumulations in the pelvic cavity.

References

1. Society for Assisted Reproductive Technology; American Society for Reproductive Medicine. Assisted reproductive technology in the United States: 2000 results generated from the American Society for Reproductive Medicine/Society for Assisted Reproductive Technology Registry. Fertil Steril. 2004;81(5):1207–20.
2. Meden-Vrtovec H. Ovarian aging and infertility. Clin Exp Obstet Gynecol. 2004;31(1):5–8.
3. Ott DJ, Fayez JA, Chen MYM. Techniques of hysterosalpingography. In: Ott DJ, Fayez JA, Zagoria RJ, editors. Hysterosalpingography: a text and atlas. 2nd ed. Baltimore: Williams & Wilkins; 1998. p. 11–27.
4. Troiano RN, McCarthy SM. Müllerian duct anomalies: imaging and clinical issues. Radiology. 2004;233(1):19–34.
5. Slezak P, Tillinger KG. The occurrence and significance of broad longitudinal folds in the uterine cavity at hysterography. Radiology. 1973;106:87–90.
6. Chen MYM, Zagoria RJ. Normal radiographic anatomy. In: Ott DJ, Fayez JA, Zagoria RJ, editors. Hysterosalpingography: a text and atlas. 2nd ed. Baltimore: Williams & Wilkins; 1998. p. 29–30.
7. Reis MM, Soares SR, Cancado ML, Camargos AF. Hysterosalpingo contrast sonography (HyCoSy) with SH U 454 (Echovist) for the assessment of tubal patency. Hum Reprod. 1998;13(11):3049–52.
8. Killick SR. Hysterosalpingo contrast sonography as a screening test for tubal patency in infertile women. J R Soc Med. 1999;92(12):628–31.
9. Rouanet De Lavit JP, Maubon AJ, Thurmond AS. MR hysterography performed with saline injection and fluid attenuation inversion recovery sequences: initial experience. AJR Am J Roentgenol. 2000;175(3):774–6.
10. Hagspiel KD, Altes TA, Mugler JP, Brookeman JR. Magnetic resonance hysterography and hysterosalpingography using hyperpolarized (3)He: demonstration of feasibility in an animal model. J Magn Reson Imaging. 2000;12(6):1009–13.
11. Ott DJ, Fayez JA. Tubal and adnexal abnormalities. In: Ott DJ, Fayez JA, Zagoria RJ, editors. Hysterosalpingography: a text and atlas. 2nd ed. Baltimore: Williams & Wilkins; 1998. p. 90–3.
12. Ubeda B, Paraira M, Alert E, Abuin RA. Hysterosalpingography: spectrum of normal variants and nonpathological findings. AJR Am J Roentgenol. 2001;177(1):131–5.

Pelvic Inflammatory Disease

4

César Amaral de Camargo Penteado,
Geraldo Souza Pinho Alves, and Harley De Nicola

Introduction

Pelvic inflammatory disease (PID) is an infection of the female reproductive organs (upper genital tract and the surrounding structures including the endometrium, ovaries, and fallopian tubes) [1]. PID occurs when bacteria move from the vagina and cervix upward into the uterus, ovaries, or fallopian tubes. The bacteria can lead to an abscess in a fallopian tube or ovary. Long-term problems can occur if PID is not treated promptly [1, 2].

Recurrent PID can double a woman's risk of infertility and quadruple her risk of chronic pelvic pain. PID contributes to approximately 2.5 million office visits and 125,000-150,000 hospitalizations every year. Some women with PID have only mild symptoms or no symptoms at all. Because the symptoms can be vague, women or their gynecologists or other health care professionals do not recognize many cases [3, 4].

Following are the most common signs and symptoms of PID:

- Abnormal vaginal discharge
- Pain in the lower abdomen (often a mild ache)
- Pain in the upper right abdomen
- Abnormal menstrual bleeding
- Fever and chills
- Painful urination
- Nausea and vomiting
- Painful sexual intercourse

It is believed that in up to 25% of women with lower abdominal pain admitted to emergency departments, the pain is caused by PID [2, 4, 5].

C.A. de Camargo Penteado • G.S.P. Alves
Radiology Department, Hospital do Servidor Público Estadual de São Paulo (IAMSPE), São Paulo, SP, Brazil
e-mail: cesarpenteado@gmail.com

H. De Nicola (✉)
Diagnostic Imaging Department of UNIFESP – Federal University of São Paulo, São Paulo Hospital, São Paulo, SP, Brazil
e-mail: harley.nicola@terra.com.br

Ultrasound

Ultrasonography should be the first diagnostic imaging examination to be performed in cases of suspected PID in which there are ambiguous or unexplained clinical findings or an inability to perform an adequate clinical examination. Ultrasonography is also indicated to evaluate for complications of PID, which may impact surgical vs. non-surgical management or the decision to hospitalize a patient [5–7]. US is considered to be the first-line imaging modality in the evaluation of suspected salpingitis; however, US may only show subtle abnormalities such as tubal tortuosity, wall hyperemia, and fallopian tube thickening of more than 5 mm. When they are normal in size, the fallopian tubes measure 1–4 mm in diameter and are not regularly depicted on US or CT [8–10].

MRI

MRI serves as an excellent imaging modality in cases in which the ultrasonographic findings are equivocal. In a study by Tukeva et al., the authors compared findings from MRI with sonograms and found that MRI was more accurate than ultrasonography in the diagnosis of PID [8].

Findings: The tubular structure is readily identified as cystic, with high signal intensity on T2- weighted images, which is lower than that of a pure cyst and may present a lack of internal enhancement. The signal intensity of T1-weighted images varies, depending on the protein content of the fluid. There is enhancement of the thickened fallopian tube walls and pelvic fat stranding. Although differentiating between pyosalpinx and hydrosalpinx is difficult, the thick hyper-enhancing tubal walls and surrounding inflammation serve as clues to the diagnosis. In cases of tubo-ovarian abscesses, MR imaging findings depend on the hemorrhagic and protein content of the mass. The abscess is usually hypointense at T1-weighted imaging; however, hemorrhagic or proteinaceous material can be hyperintense. A hyperintense rim

L.R.M.F. de Souza et al. (eds.), *Atlas of Imaging in Infertility*, DOI 10.1007/978-3-319-13893-0_4

along the inner wall of the abscess cavity has been described at T1-weighted imaging and is thought to correspond to granulation tissue and hemorrhage. T2-weighted imaging demonstrates a heterogeneous mass with low-signal-intensity septa, as well as hypointense linear stranding in the adjacent pelvic fat.

CT

Occasionally, CT scanning may be used as the initial diagnostic study for the investigation of nonspecific pelvic pain in a female, and PID may be found incidentally. CT scanning is very sensitive for the detection of pelvic pathology; however, it may not be as specific as sonography when an adnexal pathology must be differentiated from a tubal or ovarian one. If the diagnosis of PID is still in question, confirmation with ultrasonography is suggested.

The most common general CT findings of PID described in the literature are thickening of the uterosacral ligaments; obliteration of fascial planes; free fluid in the cul-de-sac; loss of definition of the uterine border; pelvic fat infiltration or haziness and pelvic edema; reactive lymphadenopathy; and signs of peritonitis. The uterosacral ligaments are paired structures that extend from the lower uterine segment to the mid-sacrum and are best seen on axial cross-sectional images. The normal thickness of the uterosacral ligaments is subjective and has not yet been established on CT images [11–14]. Salpingitis should be suspected at CT when the fallopian tubes are thickened, measuring more than 5 mm in axial dimension, and show enhancing walls. Associated free fluid may be depicted within the cul-de-sac. For the diagnosis of PID, the CT finding of tubal thickening was found to have a high specificity of 95% [14].

PID is often accompanied by reactive lymphadenopathy affecting the para-aortic lymphatic chain at the level of the renal hila. This lymphadenopathy is caused by the course of drainage of the ovarian and salpingian lymphatic vessels along the gonadal veins [14, 15] (Figs. 4.1, 4.2, 4.3, 4.4, 4.5, 4.6, 4.7 and 4.8).

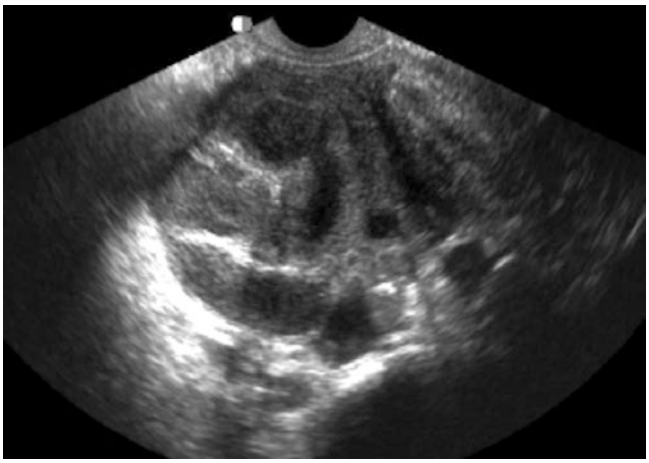

Fig. 4.1 Right adnexal region inflammatory process: ultrasound demonstrating the tortuous and dilated fallopian tube, filled with liquid, and the ovary with increased dimensions, compatible with tube and ovary abscesses. It shows up as an ill-defined adnexal tumor, containing thick liquid

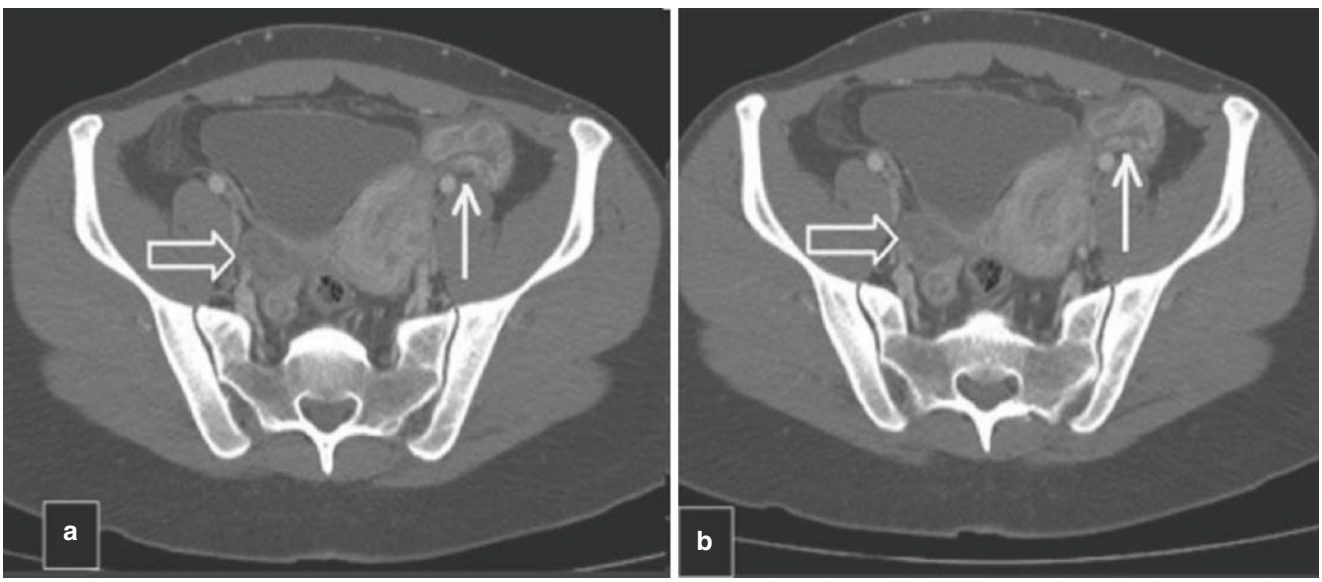

Fig. 4.2 Salpingitis: Pelvic CT, where one can observe anomalous enhancement in the left adnexal region, with a serpiginous aspect, corresponding to the wall of the tube, thickened by inflammation (*solid arrows*). A small amount of fluid surrounds it. The right ovary appears normal (*casting arrows*). (**a**, **b**) Axial sections in the venous phase of contrast injection. Salpingitis is characterized by the absence of tube dilation, but shows thickening and enhancement by contrast of tubal walls, associated with adjacent inflammatory signs. These signs manifest in the CT as a densification of adnexal fatty plans and free fluid in the pelvic cavity, as well as reactive thickening of adjacent bowels

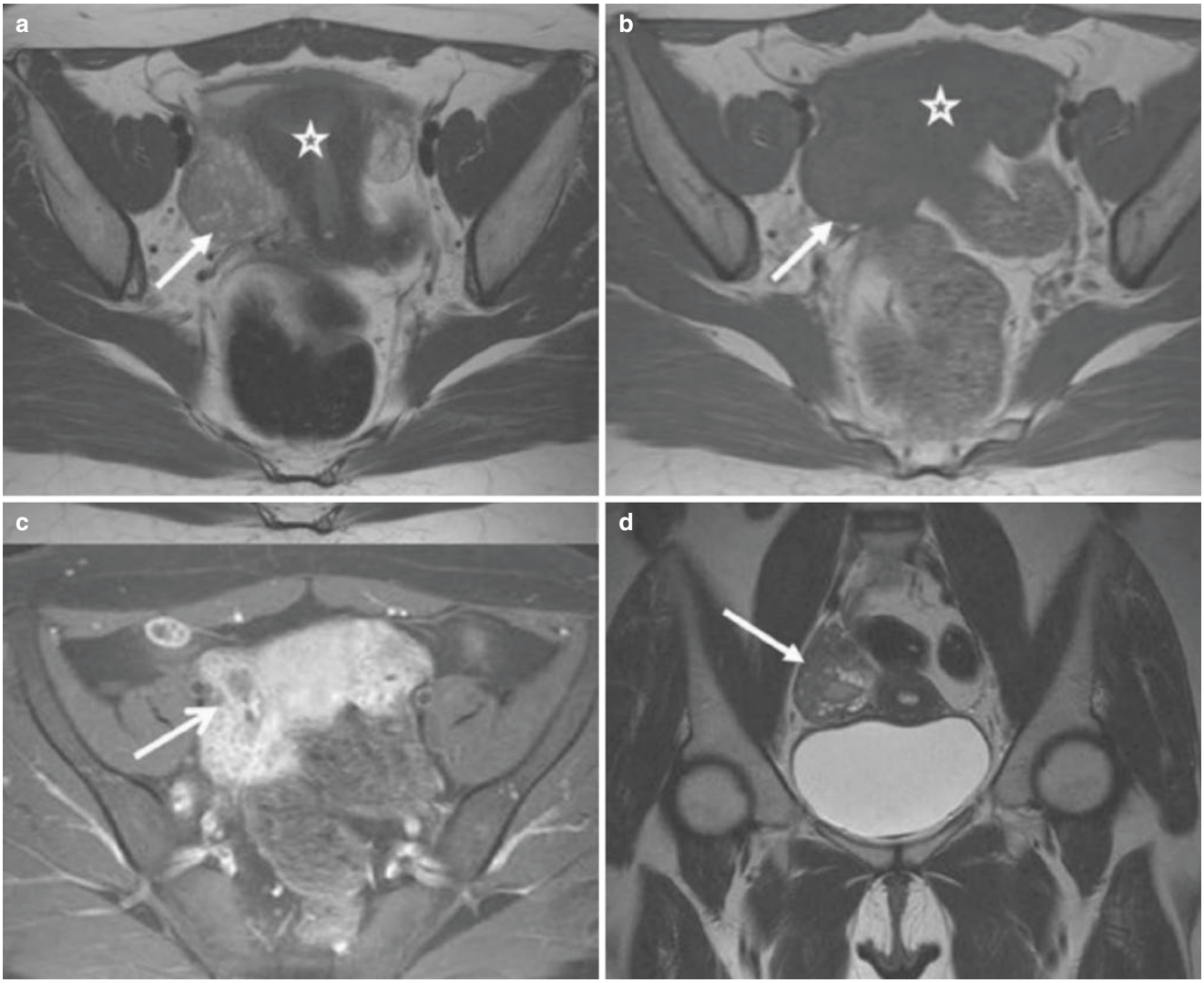

Fig. 4.3 Salpingitis: MRI of the pelvis, showing the presence of serpiginous formation in the right adnexal region (*arrows* **a**, **b**, **d**), clearly separated from the uterus (*stars* in **a**, **b**), with intense parietal enhancement, by contrast, featuring its inflammatory nature (*arrow* **c**). The aspect in **c** is highly suggestive of a fallopian tube with thickened walls. (**a**, **b**: axial T1 and T2, respectively; **c**: axial T1 with fat saturation technique, after contrast injection; **d**: coronal T2)

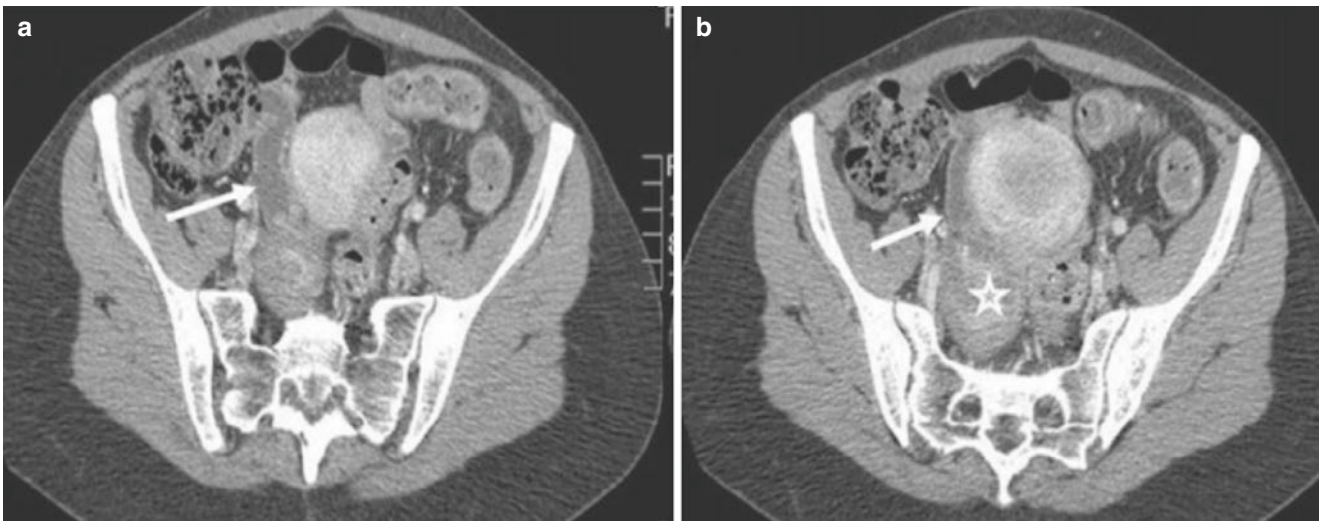

Fig. 4.4 Tubo-ovarian abcess: CT scan showing nodular formation, with heterogeneous enhancement, located in the right adnexal region, that represents the inflamed ovary (*star* **b**). The uterine tube is dilated and has parietal enhancement, indicating pyosalpinx or salpingitis (*arrows* in **a**, **b**). (**a**, **b**) Axial sections obtained in the portal phase, after the injection of contrast. Some differential diagnoses must be observed. In hydrosalpinx, unlike in pyosalpinx, tubal parietal enhancement by the contrast agent does not occur. Other diagnoses, such as appendicitis and complex adnexal masses, may make the differential diagnosis difficult

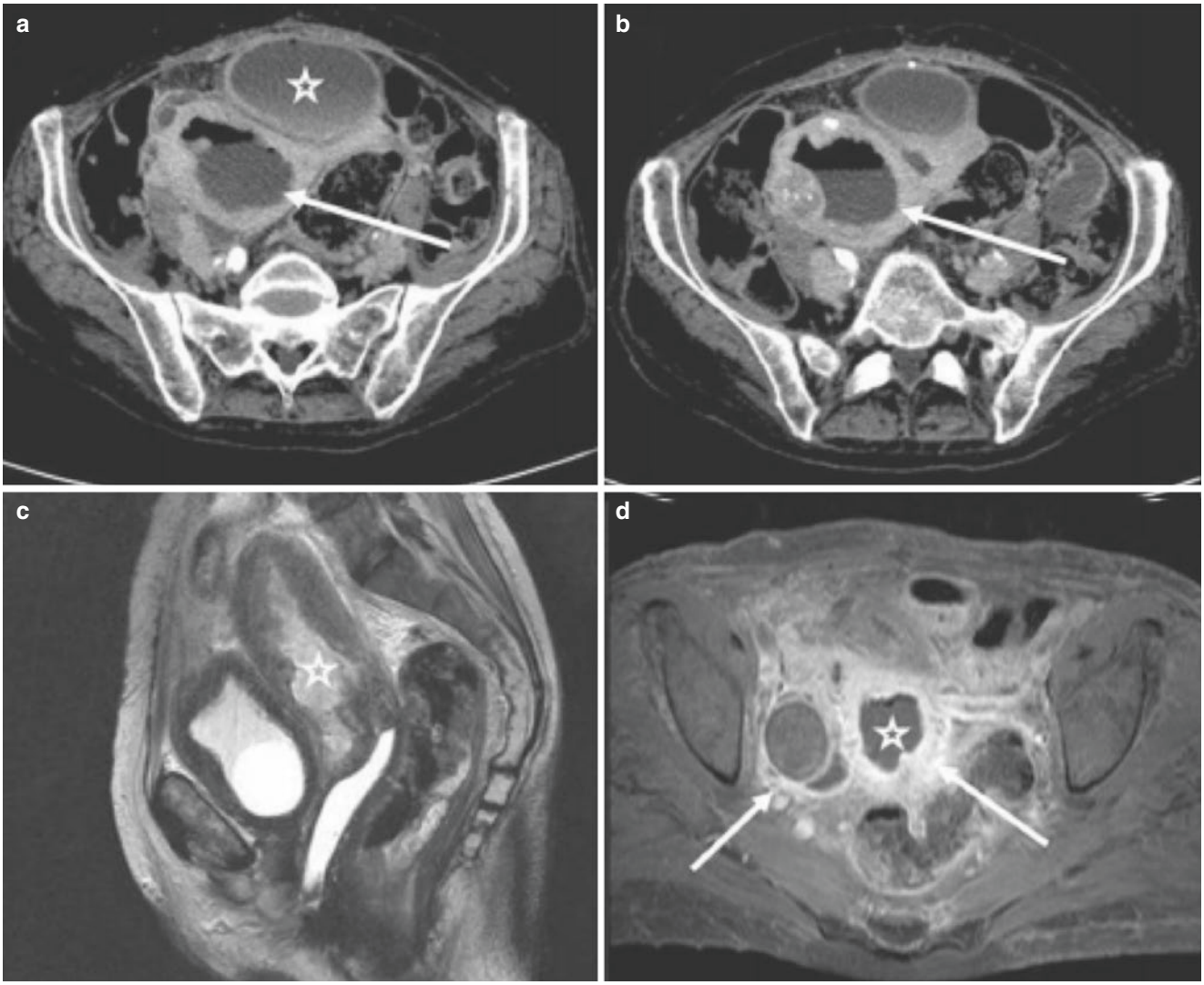

Fig. 4.5 Severe PID shown by CT (**a**, **b**) and MR (**c**, **d**). Extensive and diffuse thickening of the endometrium can be noted, with air-fluid level in the uterine cavity (*arrows* **a**, **b**). Also heterogeneous collection in front of the uterus, with thick walls, and exhibiting moderate enhancement by contrast is associated (*star* **a**). The MRI shows thick material in the uterine cavity (*stars* **c**, **d**) as well as enhancement of adnexal structures (*arrows* **d**). (**a**, **b**): axial sections obtained in the portal phase; **c**: MRI in sagittal plan, in T2; **d**: MRI in axial plan in T1, with fat saturation technique, after contrast injection. The presence of gas within the inflammatory/infectious process is not common, yet it is a very specific finding. The associated signs commonly found are mainly the thickening and enhancement of the peritoneum and uterine ligaments. There may also be involvement of adjacent structures, such as ileus, hidroureteronefrosis, and intraperitoneal abscess secondary to the rupture

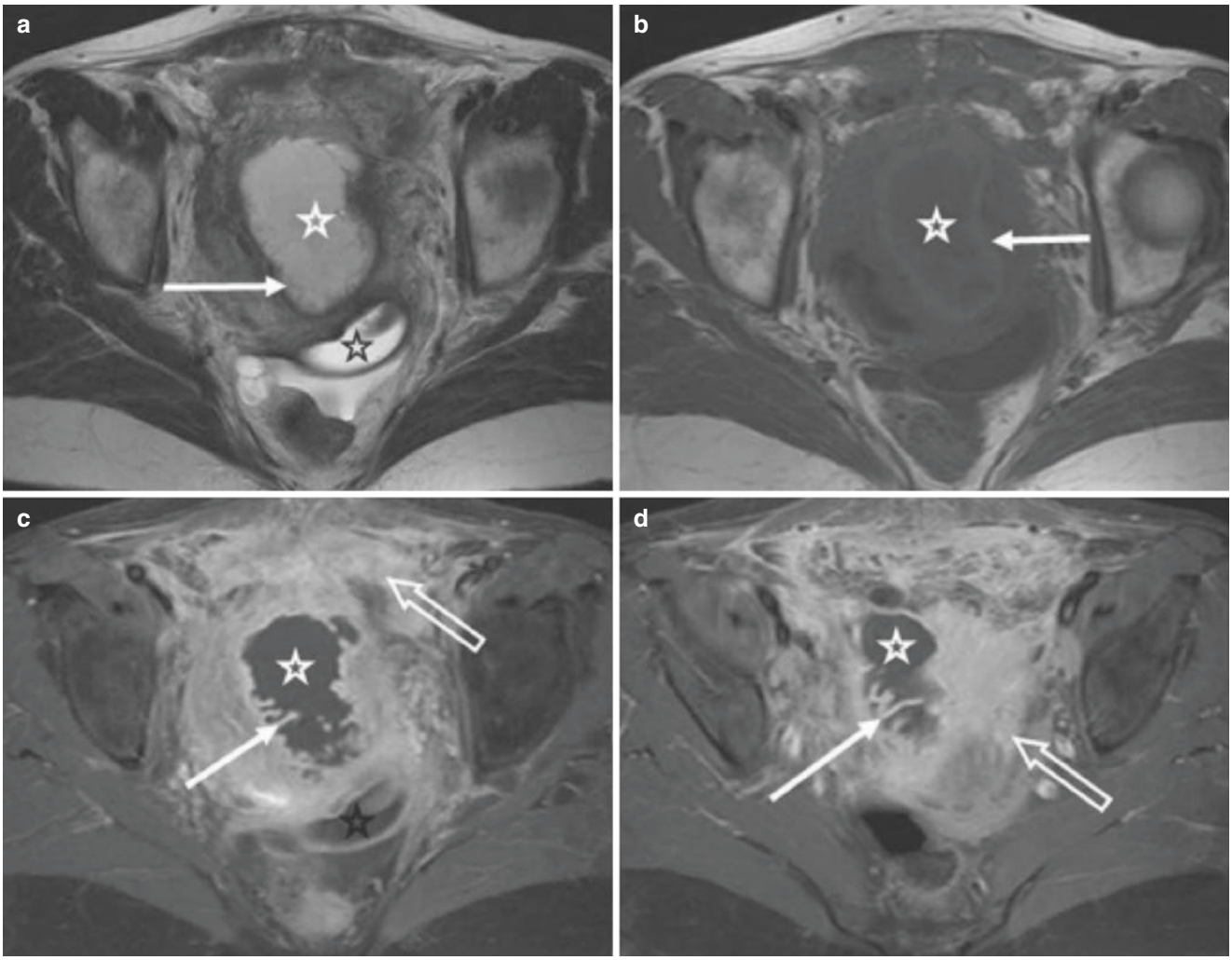

Fig. 4.6 Tubo-ovarian abcess. MRI of the pelvis showing collection (*white stars*), with thickened walls, and that feature enhancement by contrast and thin internal folds (*solid arrows* in **a**, **c**, **d**) that are compatible with a dilated tube. The wall of the formation presents high-signal intensity on T1 (*full arrow* **b**) compatible with small foci of parietal bleeding. There is still a loculated collection in the posterior fornix (*black stars* **a**, **c**) and intense enhancement of the peritoneum (*casting arrows* in **c**, **d**). (**a**, **b**) Axial plan T2 and T1 respectively; (**c**, **d**) T1 axial plan with fat saturation technique, after injection of contrast. The MRI findings depend on the hematic and protein content, with variable signals on T1-weighted sequences, depending on the amount of these components. A thin inner halo of low-signal intensity on the T1, along the inner wall of the collection, has been recently described, and assigned to the granulation tissue. The T2-weighted images show high signal, with multiple coarse internal septa, exhibiting low signal, as well as a loud signal of peritoneal fat in T2 sequences with fat saturation, corresponding to edema. These septa, along with the collection capsule, exhibit intense enhancement after contrast, associated with the enhancement of fat and abdominal structures involved

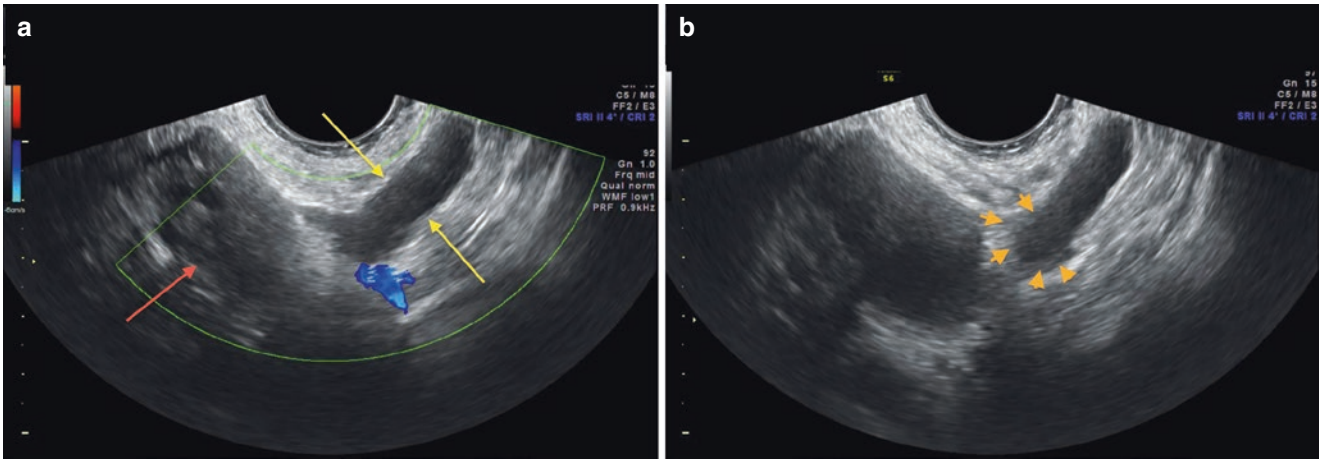

Fig. 4.7 Salpingitis to the left: (**a**) Endovaginal ultrasound, showing left tube (*yellow arrows*) as a tubular structure with thick liquid content, adjacent to the left ovary (*red arrow*). In (**b**) we can note the irregularity and thickening of the tubal wall, subsequent to inflammation (*arrowheads*)

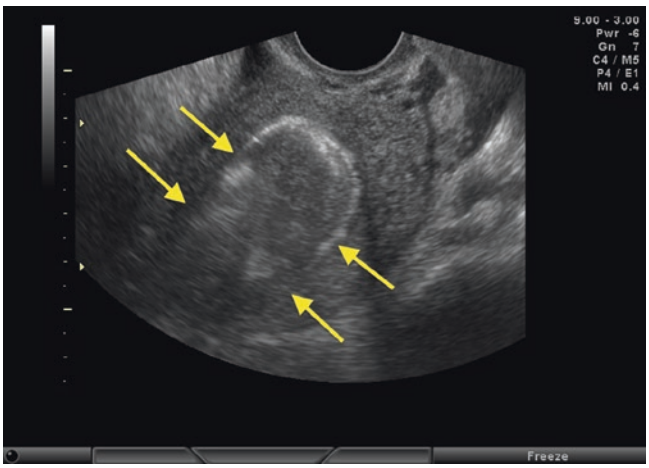

Fig. 4.8 Endometritis: Endovaginal ultrasound, in a patient with abdominal pain, vaginal bleeding and fever for 2 days. The image shows the thickened and hyperechoic endometrium, with undefined limits for the most part (between the *arrows*). The diagnosis of endometritis is often a challenging task, as signs and symptoms are non-specific and the sonographic findings are variableI; these include thickening and irregularity of the endometrium, and fluid or debris accumulated within the endometrial cavity

References

1. US National Library of Medicine, National Institutes of Health. Pelvic inflammatory disease (PID). Updated 11/29/2011. MedlinePlus. Available at http://www.nlm.nih.gov/medlineplus/ency/article/000888.htm. Accessed 9 Sept 2015.
2. Ross J. Pelvic inflammatory disease. BMJ. 2001;322(7287):658–9.
3. Beigi RH, Wiesenfeld HC. Pelvic inflammatory disease: new diagnostic criteria and treatment. Obstet Gynecol Clin North Am. 2003;30(4):777–93.
4. World Health Organization. Sexually transmitted infections. Available at http://www.who.int/mediacentre/factsheets/fs110/en/. Accessed 4 Oct 2015.
5. Golden N, Cohen H, Gennari G, Neuhoff S. The use of pelvic ultrasonography in the evaluation of adolescents with pelvic inflammatory disease. Am J Dis Child. 1987;141(11):1235–8.
6. Ozbay K, Deveci S. Relationships between transvaginal colour Doppler findings, infectious parameters and visual analogue scale scores in patients with mild acute pelvic inflammatory disease. Eur J Obstet Gynecol Reprod Biol. *2011*;156(1):105–8.
7. Thomassin-Naggara I, Darai E, Bazot M. Gynecological pelvic infection: what is the role of imaging? Diagn Interv Imaging. 2012;93(6):491–9.
8. Tukeva TA, Aronen HJ, Karjalainen PT, Molander P, Paavonen T, Paavonen J. MR imaging in pelvic inflammatory disease: comparison with laparoscopy and US. Radiology. 1999;210(1):209–16.
9. Lee MH, Moon MH, Sung CK, Woo H, Oh S. CT findings of acute pelvic inflammatory disease. Abdom Imaging. 2014;39(6):1350–5.
10. Potter AW, Chandrasekhar CA. US and CT evaluation of acute pelvic pain of gynecologic origin in nonpregnant premenopausal patients. RadioGraphics. 2008;28(6):1645–59.
11. Bennett G, Slywotzky C. Gynecologic causes of acute pelvic pain: spectrum of CT findings. RadioGraphics. 2002;22:785–0.
12. FebroniocEM,Rosas GQ, D'Ippolito G. Doença inflamatória pélvica aguda: ensaio iconográfico com enfoque em achados de tomografia computadorizada e ressonância magnética. Radiol Bras. 2012;45:345–50.
13. Agrawal A. Imaging in pelvic inflammatory disease and tubo-ovarian abscess. Available at http://emedicine.medscape.com/article/404537-overview#showall. Accessed 25 Nov 2015.
14. Revzin MV, Mathur M, Dave HB, Macer ML, Spektor M. Pelvic inflammatory disease: multimodality imaging approach with clinical-pathologic correlation. RadioGraphics. 2016;36(5):1579–96.
15. Langer JE, Dinsmore BJ. Computed tomographic evaluation of benign and inflammatory disorders of the female pelvis. Radiol Clin North Am. 1992;30(4):831–42.

Endometriosis

5

Ana Luisa Alencar De Nicola and Luis Ronan Marquez Ferreira de Souza

Introduction

Endometriosis is a chronic disease defined as the presence of tissue with histological and functional features similar to the topic endometrium, outside the uterine cavity [1]. The patient may be asymptomatic or present some symptoms, among which the most common are dysmenorrhea, dyspareunia, chronic pelvic pain, and infertility. Urinary symptoms (hematuria, dysuria) and/or gastrointestinal symptoms (hematochezia, dyschezia) may also be associated, particularly when related to the menstrual cycle [2]. The estimated prevalence is about 10% among women of reproductive age and 50% among those within infertility [3].

Three types of pelvic endometriosis are described:

- Peritoneal or superficial endometriosis
- Ovarian endometriosis
- Deep endometriosis

Physical examination may suspect the disease by identifying nodular areas in a retro-uterine space, but because of the characteristic of multiple lesions, it can be insufficient [4]. Imaging methods are currently very important for a full and detailed assessment of the disease, allowing for proper medical planning.

In the classification that is most accepted in the literature, the pelvis is divided into three sections, guided by the uterus, which is its central body.

Anterior:

- Bladder
- Ureteral meatus
- Rounded ligaments
- Serous anterior uterine
- Vesico-vaginal space

Posterior:

- Posterior uterine serosa
- Retrocervical region
- Rectovaginal septum
- Vagina
- Uterosacral ligaments
- Rectum-sigmoidean transition

Lateral:

- Ureters
- Paracolpi
- Parametrium
- Hypogastric plexus
- Broad ligaments

In addition to this, there is also abdominal involvement (subcutaneous tissue) of the diaphragm, paracolic gutters, small intestine, and the appendix. Some cases of liver and mediastinal endometriosis have also been described in the literature.

Magnetic Resonance

Magnetic resonance imaging is a non-invasive imaging and high-resolution method that allows for proper assessment of the pelvic organs, with high specificity for the diagnosis of deep endometriosis. Its main differential is the global pelvis evaluation, initially mapping the focus of affection by the disease, diagnosing possible associated diseases and stratifying the risk of surgery, thereby adding greater security to the surgical technique to be used by the gynecologist.

The MR has the following features in major injuries identified in the examination:

A.L.A. De Nicola
Department of Gynaecologic Endoscopy, Santa Casa Medical School, São Paulo, SP, Brazil
e-mail: analui.nicola@terra.com

L.R.M.F. de Souza (✉)
Associate Professor of Radiology, Universidade Federal do Triangulo Mineiro, Uberaba, MG, Brazil
e-mail: radiologia.abdome@gmail.com

L.R.M.F. de Souza et al. (eds.), *Atlas of Imaging in Infertility*, DOI 10.1007/978-3-319-13893-0_5

Morphology

- *Subperitoneal nodes*: Characterized by the formation of oval lesions that usually invade from the external to the internal layer, going through the peritoneal or extraperitoneal locations, such as the bladder, sigmoid and rectum (Fig. 5.1).
- *Cloak or confluent*: Infiltrative, most often identified in uterine serous, with obliteration of the anterior and posterior recesses (Fig. 5.2).
- *Ligament thickening*: Defined with more than 5 mm, associated with heterogeneous signal, adhesion, and distortion of usual pelvic architecture (Fig. 5.3).

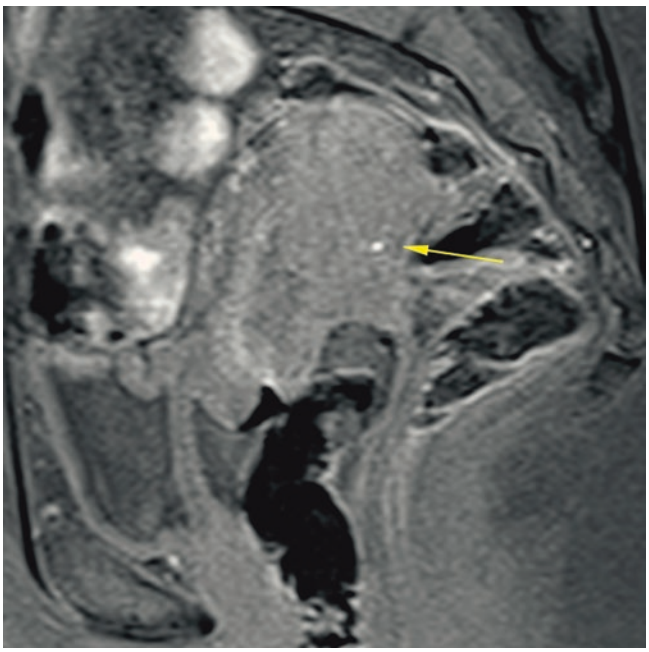

Fig. 5.1 Sagittal, SE, weighted in T1 with fat saturation. In this image, a small focus of active endometriosis can be observed (*arrow*) in the posterior uterine serous

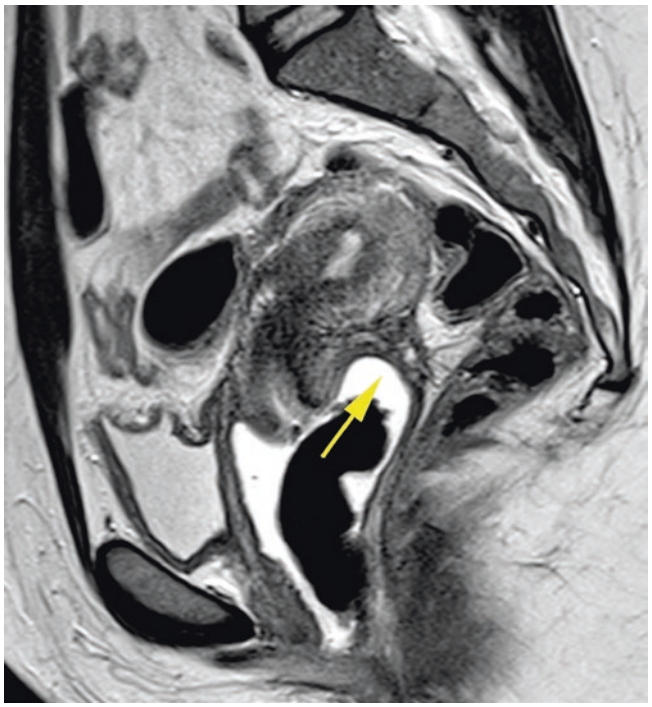

Fig. 5.2 Sagittal, TSE, T2 weighting. In this case, an endometriosis focus can be observed "in mantle" (*arrow*), involving the posterior vaginal fornix and obliterating the recto-uterine recess

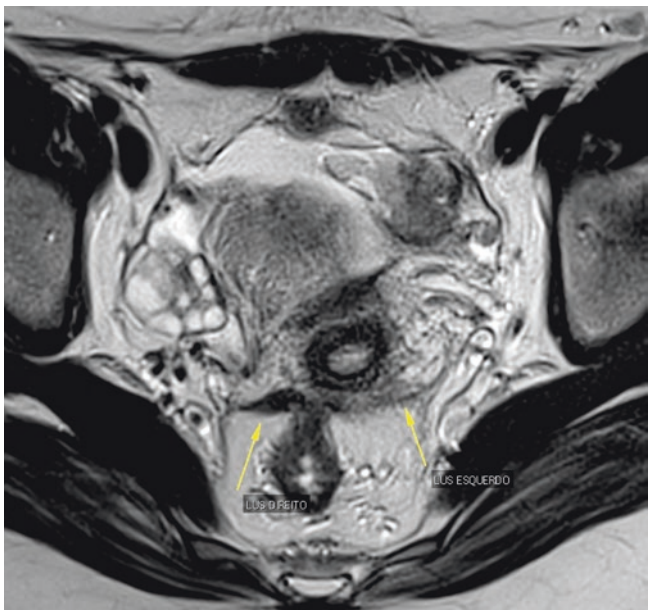

Fig. 5.3 Axial TSE, T2 weighting. Note the asymmetry between the utero-sacral ligaments (*arrows*), the right one being thicker and heterogeneous

Signal (On Sequences Weighted in T2)

- *Low signal*: Typically *fibrous*, with small amount of glandular tissue that tends to cause hemorrhaging. They can be highlighted by the contrast due to their association with the inflammatory process (Fig. 5.4).
- *High signal*: With predominance of *glandular tissue*, more unusual (Fig. 5.5).
- *Mixed*: An infrequent sign, with small bleeding spots, and with characteristic hypersignal.

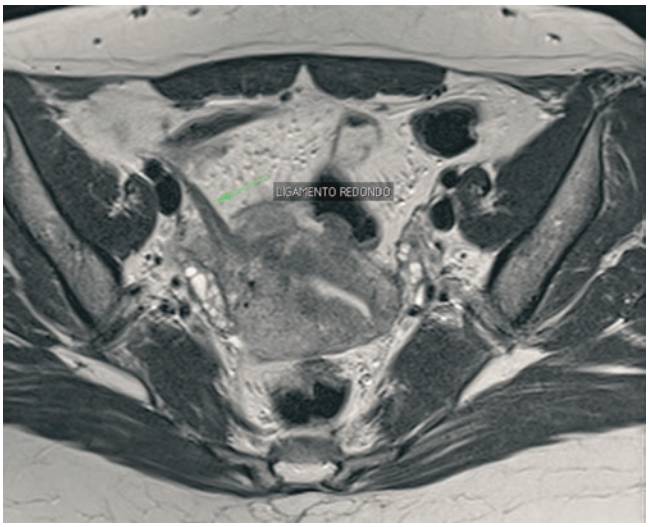

Fig. 5.4 Axial TSE T2 weighting. Asymmetry and heterogeneity of the round ligament to the right can be identified (*arrow*)

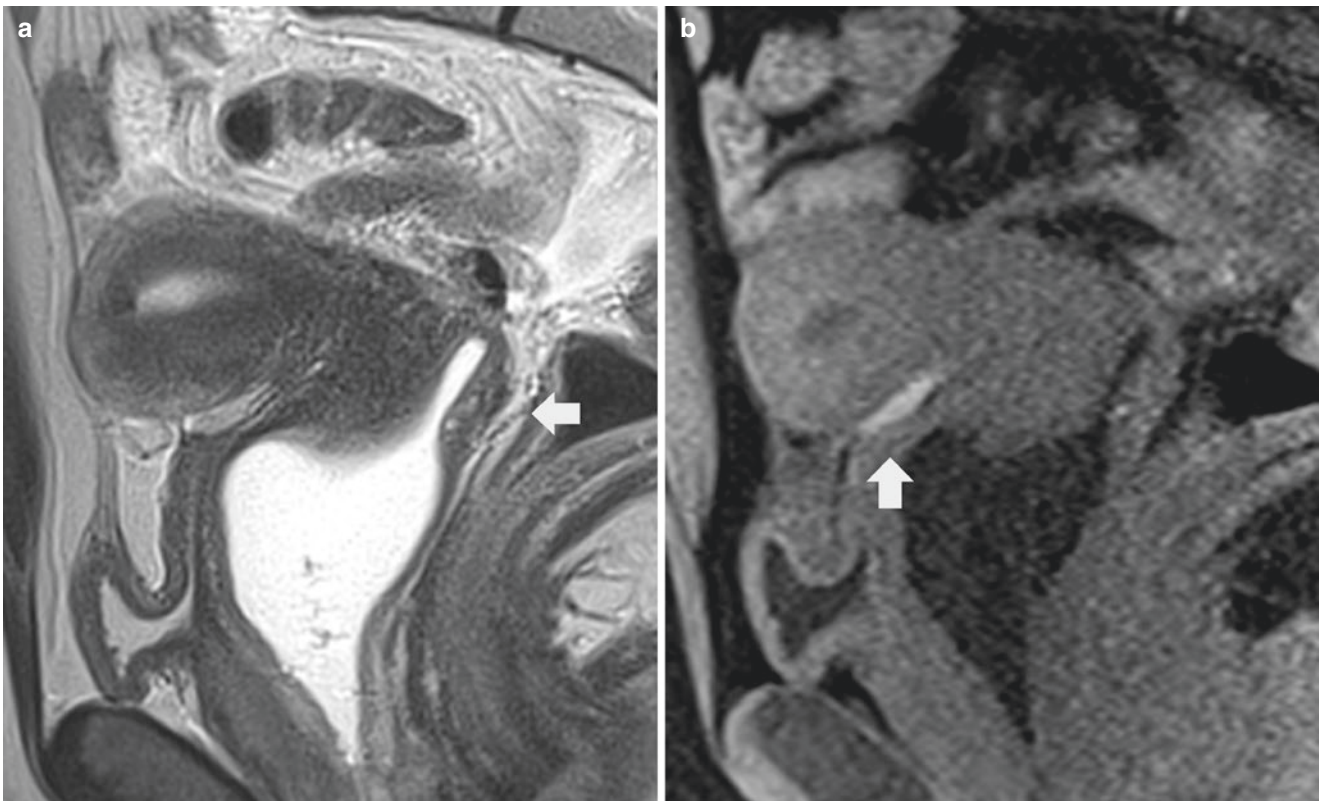

Fig. 5.5 (**a**) Sagittal, TSE, T2 weighting. In this image, the engagement of the posterior wall of the vagina can be seen, with focal thickening and heterogeneity of the signal (*arrow*). (**b**) In this figure, involvement of the vesico-uterine recess can be characterized (*arrow*), with high signal, inferring activity

Contrast

The use of contrast is discussed in the literature; those opting for its use claim that it is particularly useful for:

- Identifying associated inflammatory processes (peritoneal enhancement) (Fig. 5.6);
- Characterizing complex masses or associated tumors (nodular enhancement); and
- Better identification of skin implants, allowing greater definition of intramuscular nodes in the pelvic wall (Fig. 5.7a,b).

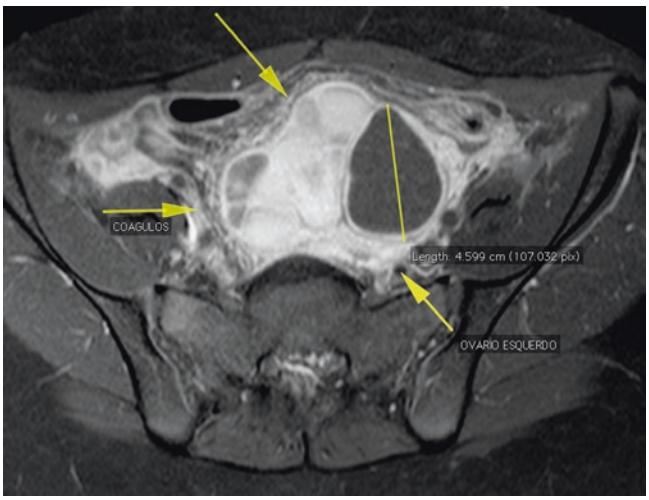

Fig. 5.6 Axial, SE, T1 weighted, with fat saturation and post contrast. Notice how in this case the use of contrast allowed to identify the extent of the inflammatory commitment by the pelvis, characterized by the contrast enhancement extending from the pelvic walls, with clots in the right adnexal region

Key Features of Magnetic Resonance Exams

- Detailed description of the main injury
- Number of lesions
- Lesions in atypical locations
- Ovarian injury or associated tubal injury
- Ureter assessment, ovarian artery, and obstruction identification
- Assessing the risk of associated malignancy
- Quantifying the number of adhesions and their locations
- Other associated diseases

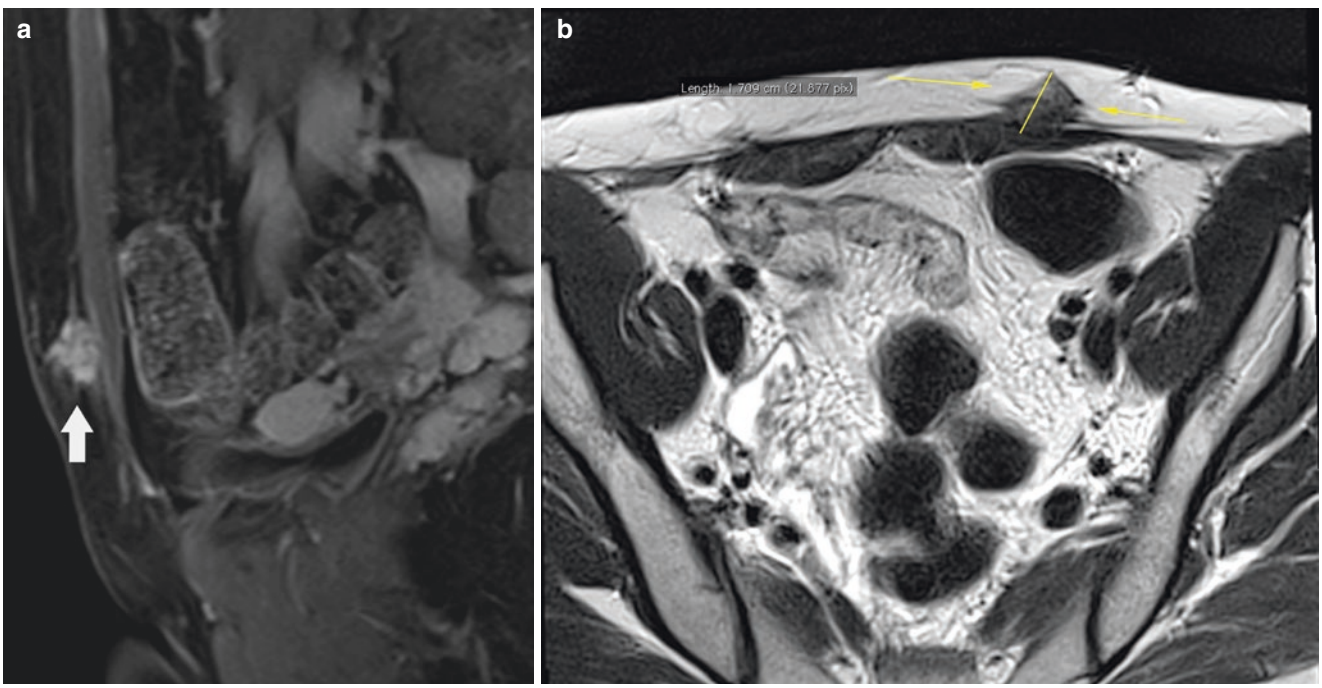

Fig. 5.7 (**a**) Sagittal, SE, weighted in T1, with fat saturation. In the figure, one of the indications for the use of contrast can be observed to better identify the focus of endometriosis in the pelvic wall, which is enhanced by contrast, because of the associated inflammation. (**b**) Axial, TSE, T2 weighting. Note the endometriosis focus on the pelvic wall to the left, and notice how difficult the delimitation of its posterior margins are, with the anterior aponeurosis of the abdominal rectum, thus favoring the use of contrast

Pelvic Endometriosis Imaging Findings

Superficial Endometriosis

Superficial endometriosis lesions are composed of peritoneal implants, generally up to 10 mm long, and adhesions secondary to the inflammatory process. Their most frequent location is the Douglas pouch and the broad ligaments.The diagnosis is still made by direct observation of lesions via laparoscopy or biopsy. Transvaginal ultrasound has no diagnostic value in this form of the disease. Adhesions may eventually be found by ultrasound, but is not specific [5].

Finding an impairment in the abdominal wall in MR occurs in less than 2% of the endometriosis cases, yet it is considered the most common location outside the pelvic cavity. The cyclic pain related to menstrual flow is important information from the clinical examination, with palpable lesions in 96% of the cases. The lesion at its greatest diameter, the depth of the abdominal wall invasion, and its relation to anatomical markers, must be described.

Ovarian Endometriosis

The morphological aspect of ovarian endometriosis is seen as small implants or hemorrhagic cysts limited by an endometrial epithelium, i.e., the endometriomas [5].

The identification of small hyperechoic foci, distributed on the ovarian surface (Figs. 5.8 and 5.9), was assigned to endometriosis in some publications [6]. More recent studies have shown that hyperechoic ovarian foci are common in transvaginal ultrasounds and may correspond to various histological findings, including small inclusion cysts, hemosiderin, calcifications, and small, dense cortical nodules [7]; thus it is a non-specific signal.

Ovarian endometriosis is often associated with dense adhesions in the pelvis, either in the ovarian fossa or in other places, among them the uterosacral ligaments, the retro-cervical space, or rounded ligaments [8]. Ultrasound is of great value for diagnosing adherence processes because it is a dynamic test in which the ovaries' mobility can be tested in real time. For this, the examiner can use one hand by abdominally compression and/or gently press the transducer vaginally.

The ovaries may be fixed in the posterior or anterior compartment to the uterus (no sliding maneuvers) and painful to touch by the transducer (Figs. 5.10, 5.11, 5.12, and 5.13). When bilateral, both ovaries may be medianized and there may be adhesions between them, commonly in the retro-uterine region (the so-called "Kissing-ovaries." [9] (Figs. 5.14 and 5.15).

Endometriomas have a brownish content and are therefore known as chocolate cysts. This hemorrhagic content is an essential criterion in ultrasound diagnosis, providing a typical sonographic appearance: a rounded cyst containing internal fine echoes with low echogenicity of homogeneous appearance, known as the "frosted glass" aspect (Figs. 5.16, 5.17, 5.18, and 5.19) [10]. It is estimated that this characteristic is present in about 95% of endometriomas [10].

Hyperechoic parietal foci can be seen in more than 30% of endometriomas and can be a useful criterion for their distinction because they are rarely seen in other benign ovarian cysts [11] (Figs. 5.20 and 5.21). Therefore, a cyst with thin internal echoes, homogeneous and hypoechoic, with no other signs of malignancy, is 32 times more likely to be an endometrioma than another anexial mass [11]. Septacan also be found in endometriomas, giving them a multilocular aspect [11] (Figs. 5.22 and 5.23).

Denser areas of the content or intracystic bleeding may appear as fixed parietal hyperechoic nodularity that can simulate solid malign projections and cause doubts [9]. Amplitude Doppler can help show the absence of flow in cystic content [12] (Figs. 5.24, 5.25, 5.26 and 5.27). Endometriomas' walls are usually thin and smooth and are clearly visible, but can rarely be true papillary projections resulting from inflammation, necrosis, or even endometriosis focus pericystic proliferation.

Transvaginal ultrasound showed a positive predictive value of 91% for the diagnosis of endometriomas [13]. In this same study, the positive predictive value was 97%, when the endometrioma had a classic look (rounded cyst, regular margins, thin and smooth walls, homogeneous smooth internal fine echoes, and hypoechoic), and 70% for those with an atypical appearance (anechoic, internal septa, irregular margins, or solid projections) [13]. Most often we see atypical endometriomas in the oldest diseases; they are more associated with adhesion processes (Figs. 5.28, 5.29, 5.30, and 5.31).

The multicentric study (IOTA) evaluated 3511 patients with adnexal masses, of which 713 were endometriomas; ultrasonography showed 81% sensitivity and 97% specificity for their diagnosis [8]. The true positive cases were more often represented by unilocular cysts with "frosted glass" content than any other category of Axial mass [8].

In magnetic resonance imaging, the endometrioma typically manifests as a hyperintense lesion (the same signal or stronger than fat) in sequences weighted in T1, with a tendency to hypointensity (usually with hyperintense foci, causing the shading effect on sequences weighted in T2) (Figs. 5.32 and 5.33).

This aspect of the image reflects the chronicity of endometrioma, which has very "thick" hematic content, due to the high concentration of intracystic methemoglobin and other proteins, which promotes shortening of T2 relaxation time. Large endometriomas may contain multiple thin septa and often present levels with blood (Fig. 5.34).

Complex lesions, mainly represented by large cystic formations and located in the ovaries, present an often parietal solid component, and this makes it difficult to characterize the tumor mass, requiring correlation with contrasted phase, to exclude malignant transformation (endometrioid carcinoma). The differential diagnosis for endometrioma on ultrasound includes hemorrhagic luteum cyst, cystadenoma, hematosalpinx or pyosalpinx, abscess, dermoid lesion, and ovarian cancer. All these lesions may have thick content (blood, mucus corpus) that eventually present a "frosted glass" on ultrasound [9].

The hemorrhagic corpus luteum cyst, because it is more recent and has the greatest amount of hemorrhage, usually has a more heterogeneous appearance with echogenic are as intermingled with liquid content, or with thin echogenic lines corresponding to fibrin networking aspect. This heterogeneous pattern in grayscale, unlike the homogeneous and hypoechoic pattern of endometriomas, is usually the best parameter for differentiation (Figs. 5.35, 5.36, 5.37, and 5.38). Doppler can also be helpful by showing the abundant classic peripheral vascular halo of the luteum cyst, while endometriomas usually have little and peripheric vascularization [12] (Figs. 5.39 and 5.40). Hemorrhagic cysts are usually present in the second phase of the cycle, associated with endometrium of a secretory aspect, and are absorbed spontaneously. The ultrasound control 5-6 weeks later can, therefore, demonstrate their regression.

Tubal dilatation, mainly hematosalpinx, usually has a serpiginosum aspect and is more tubular (Fig. 5.41). The transducer pressure may help demonstrate the non-ovarian origin (Fig. 5.42).

Dermoid lesions are most commonly characterized by the presence of solid echogenic tissue, with posterior acoustic attenuation (a feature characteristic of fat) or calcifications. However, some cysts with thick liquid-liquid levels can be difficult to differentiate between dermoid and endometrioma injury [7]. Some authors argue that at endometrioma, the supernatant content is usually hypoechoic (more liquid blood) and the deposited layer is hyperechoic (thicker or heavier blood or clots), while in dermoids the supernatant part is often hyperechoic (fat that is not deposited) [14, 15] (Fig. 5.43).

Ovarian cancer is often characterized by the presence of solid, vascularized areas [8, 9, 10, 12]. However,sometimes the,endometrioma can simulate neoplastic lesions, especially those with atypical aspects, as well as malignant lesions, and can be confused with endometriomas. In the multicentric study (IOTA), ultrasonography showed a false positive rate of 12% for the diagnosis of endometriomas, among which most were benign lesions, but 1% of them were malignant [8]. Most of the malignant tumors were found in patients aged 50 or older who were already post-menopausal [8].

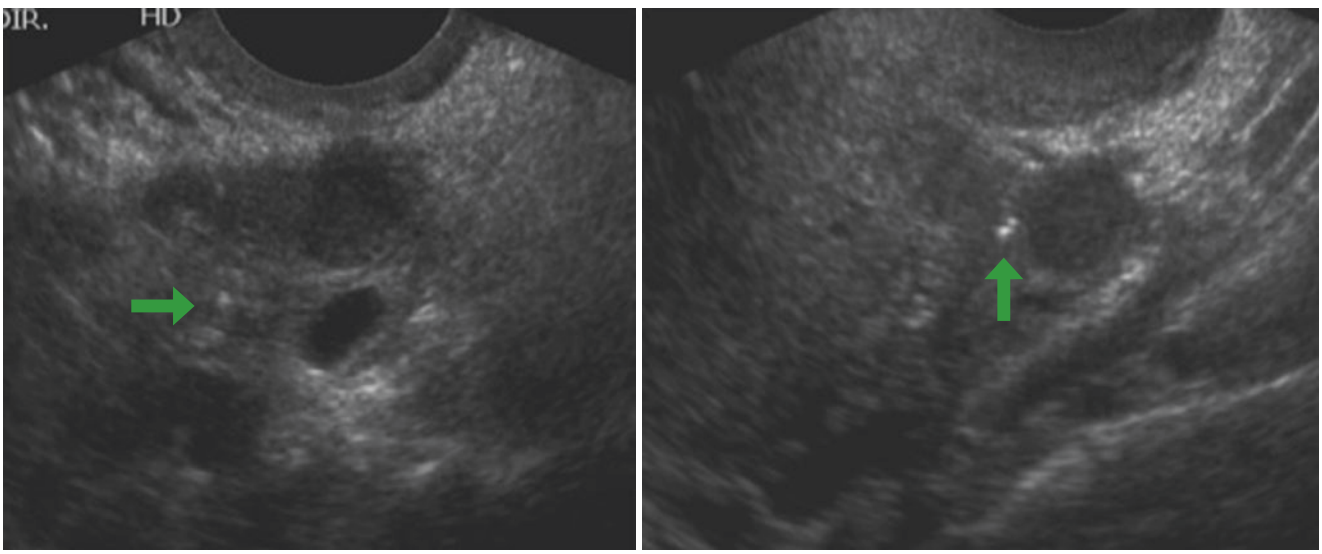

Figs. 5.8 and 5.9 Transvaginal sonogram showing echogenic foci (*arrows*) in an ovary

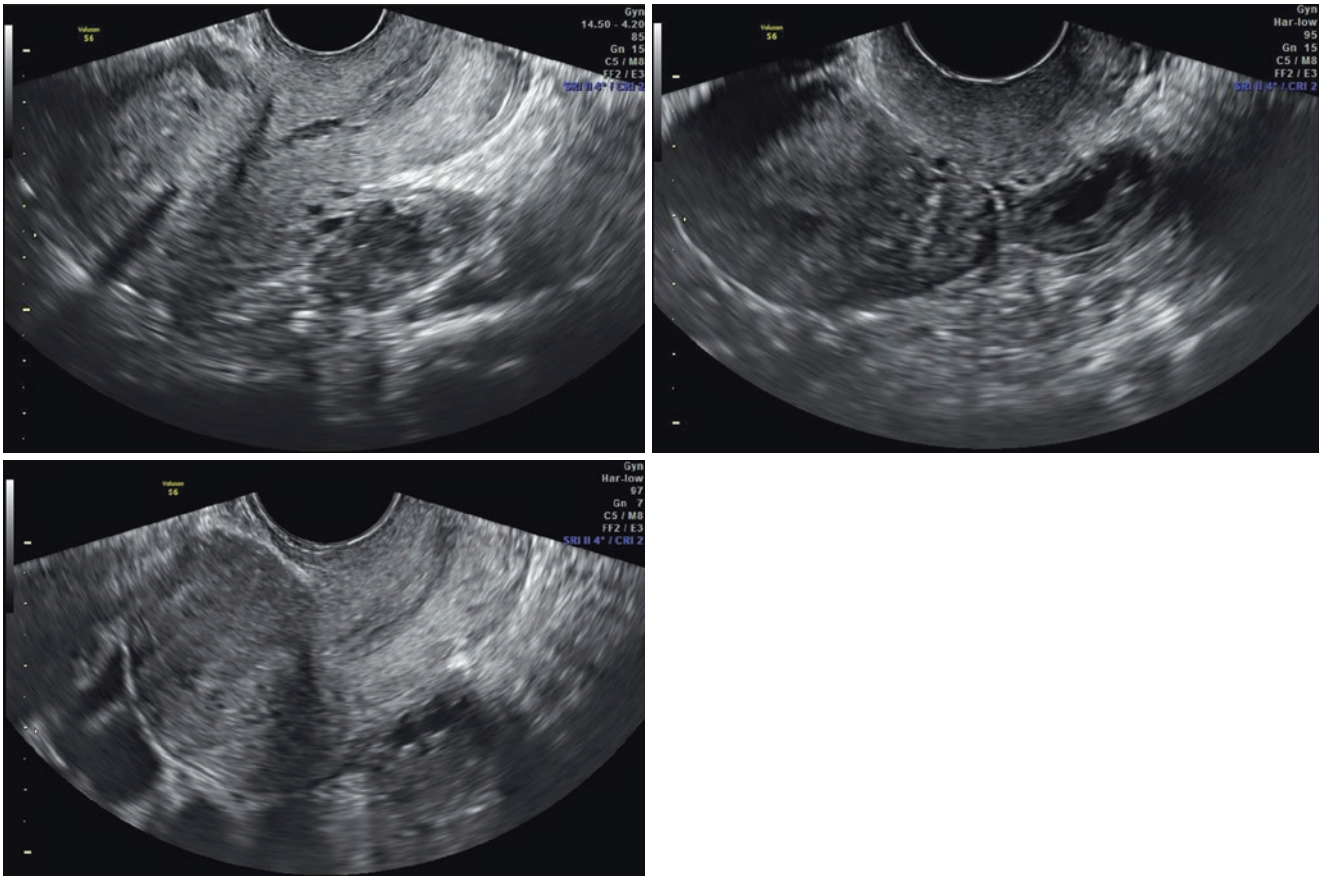

Figs. 5.10, 5.11, and 5.12 Transvaginal sagittal image: ovaries fixed at posterior uterine wall

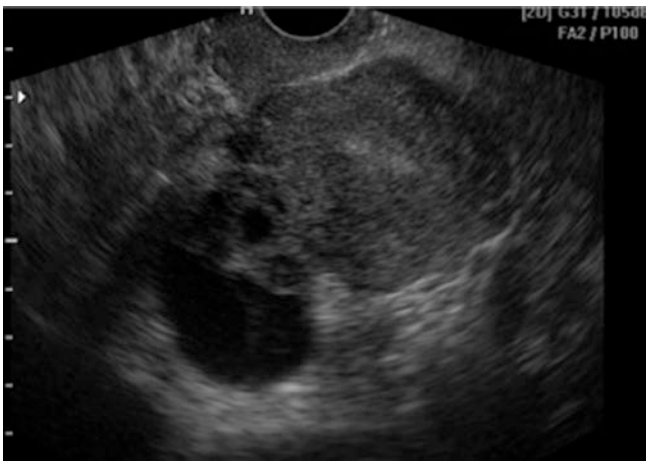

Fig. 5.13 Transvaginal sagittal image ovary fixed to the anterior uterine wall

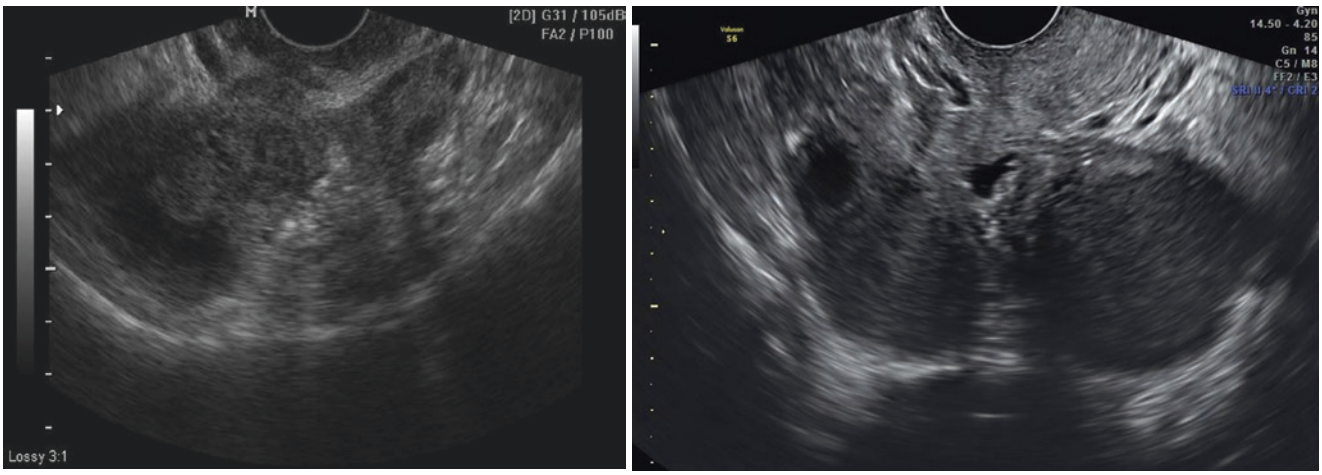

Figs. 5.14 and 5.15 Transvaginal transverse image: fixed ovaries in the posterior pelvic compartment ("Kissing ovaries")

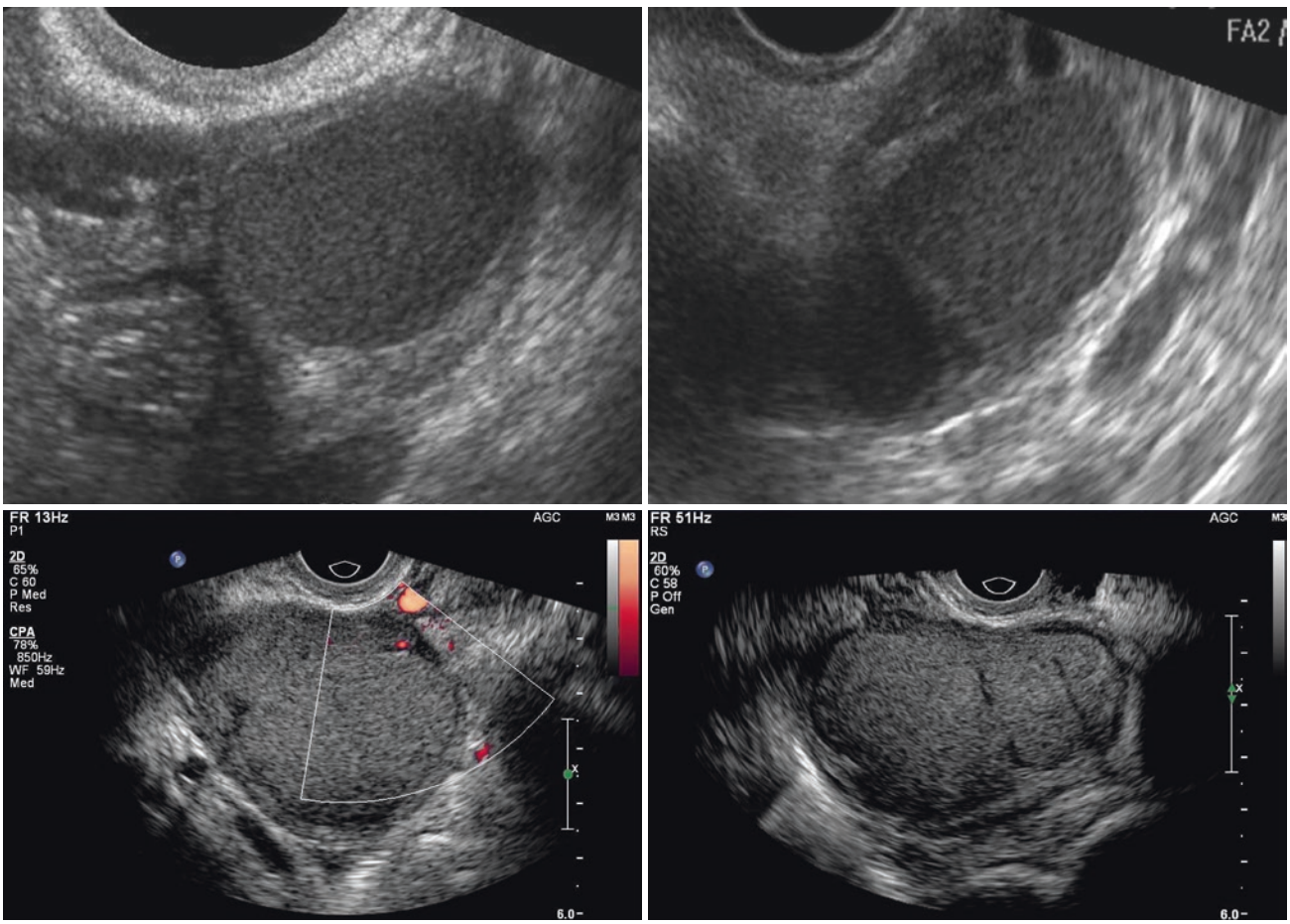

Figs. 5.16, 5.17, 5.18, and 5.19 Ovarian classic endometriomas: Well-circumscribed rounded cyst with low-level internal echoes

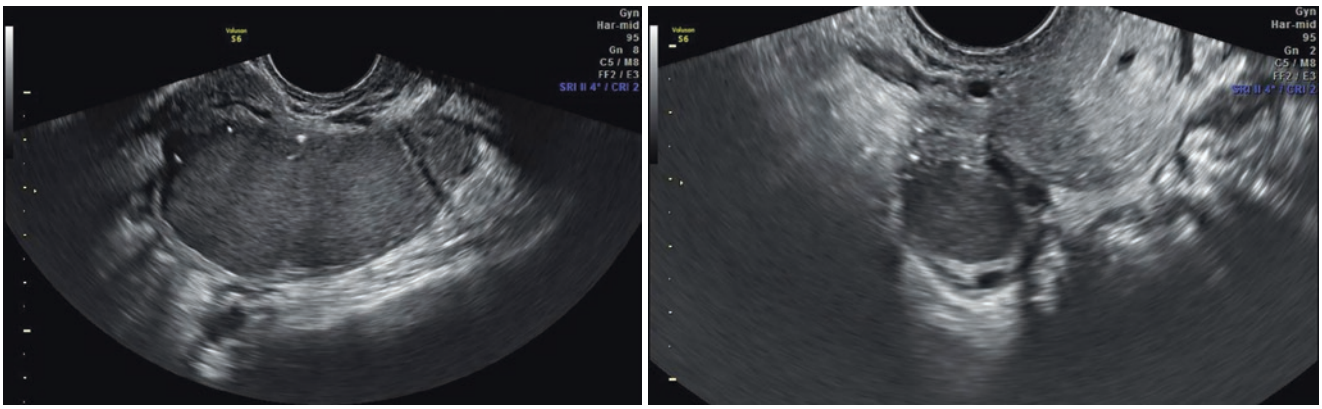

Figs. 5.20 and 5.21 Ovarian endometriomas with hyperechoic foci on the edge

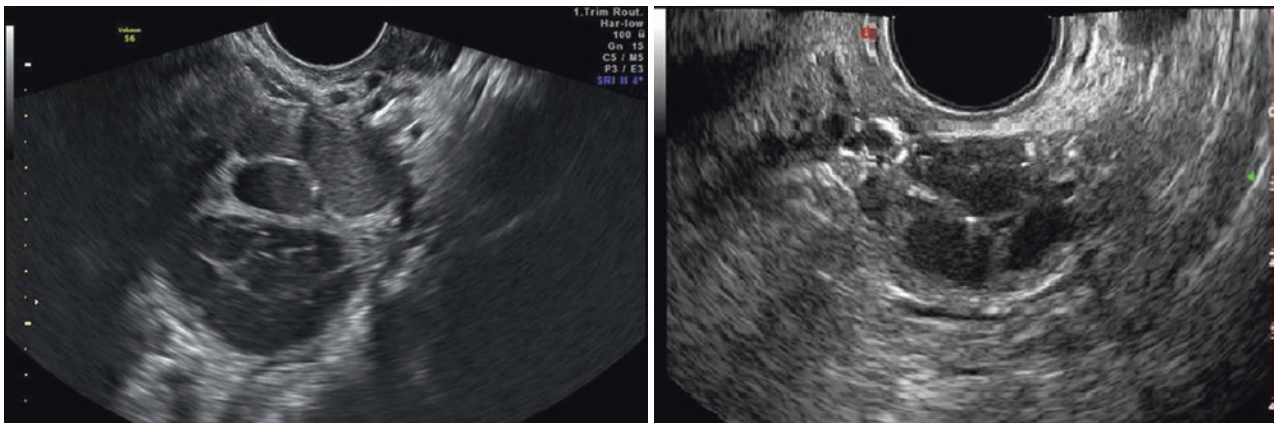

Figs. 5.22 and 5.23 Ovarian Endometrioma with internal septations (multiloculated)

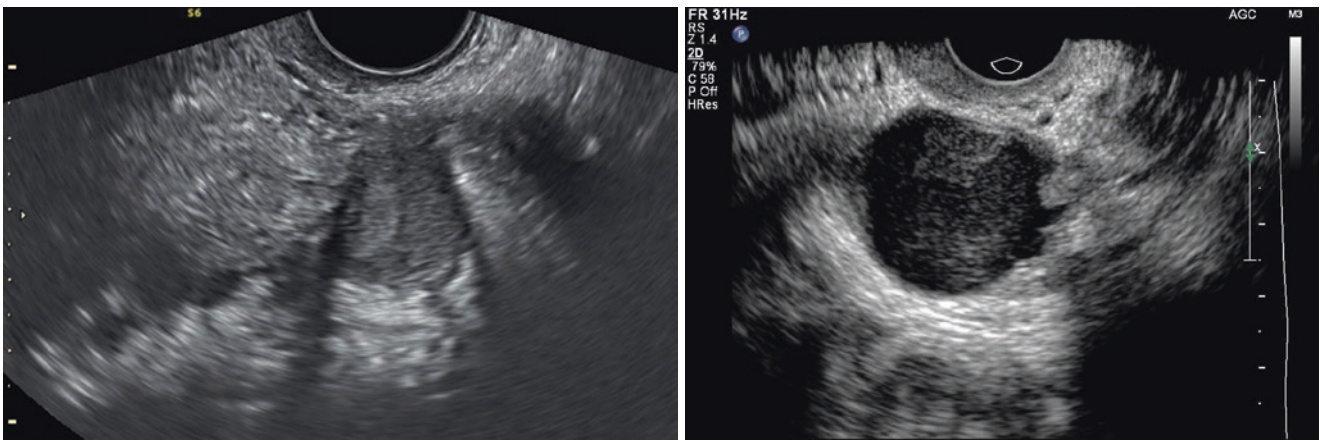

Figs. 5.24 and 5.25 Ovarian Endometrioma with focal wall nodularity (marginal clumped echoes with concave margins)

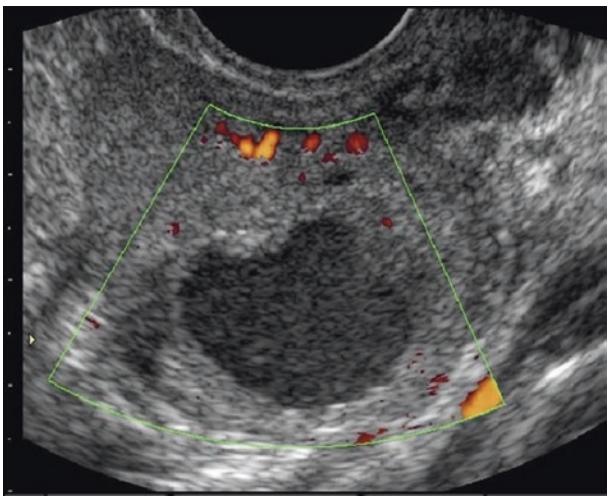

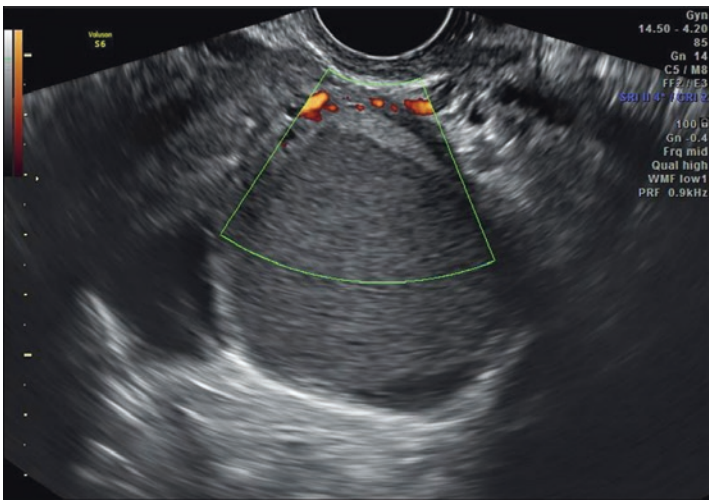

Figs. 5.26 and 5.27 Doppler sonography of ovarian endometrioma: No flow in the focal wall nodularity (retracting clot)

Fig. 5.28 Left ovary firmly attached to the posterior wall of the uterus with endometrioma of thick and hyperechoic walls (atypical appearance)

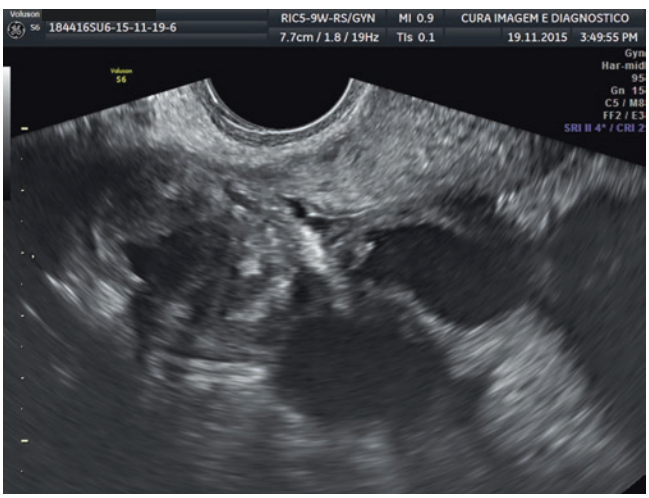

Fig. 5.29 Transverse view of right and left ovaries fixed to the posterior uterine cervix ("Kissing ovaries"). Classic endometriomas of the left ovary and atypical appearance of endometrioma on the right ovary (thick wall and solid hyperechoic projections)

Fig. 5.30 Transverse view of right and left ovaries fixed to the posterior uterine cervix ("Kissing ovaries"). Atypical appearance of endometrioma on the right ovary (as a solid hyperechoic nodule with small cysts)

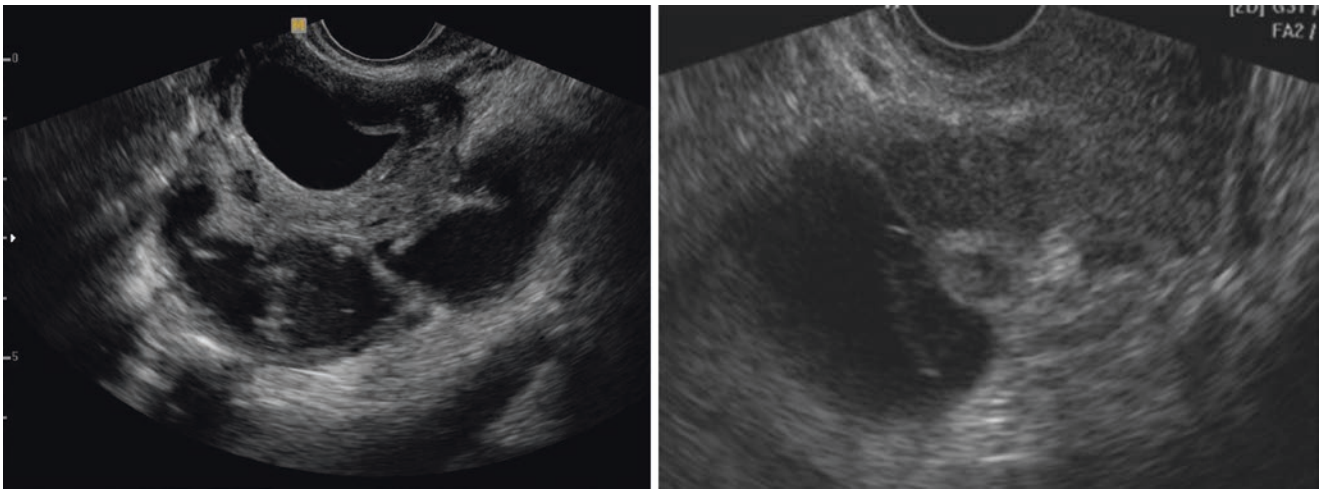

Fig. 5.31 Transvaginal transverse view: Right ovary fixed at cervix with atypical appearence of endometrioma (look like an exophytic solid nodule)

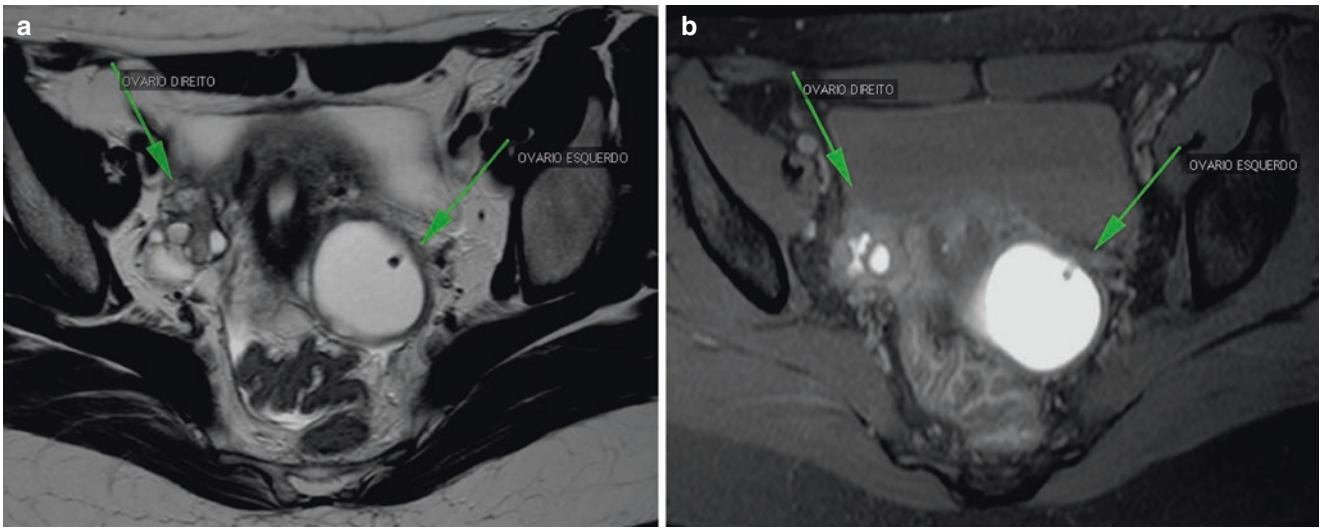

Fig. 5.32 (**a**) Axial, TSE, T2 weighting. Note in this case the low signal of the ovaries, predominantly to the right. The largest cyst on the left shows predominantly high signal, but decreases gradually and has slightly thickened walls. (**b**) Axial, SE, T1 weighting, with fat saturation, the characteristic high signal of the endometriomas can be observed

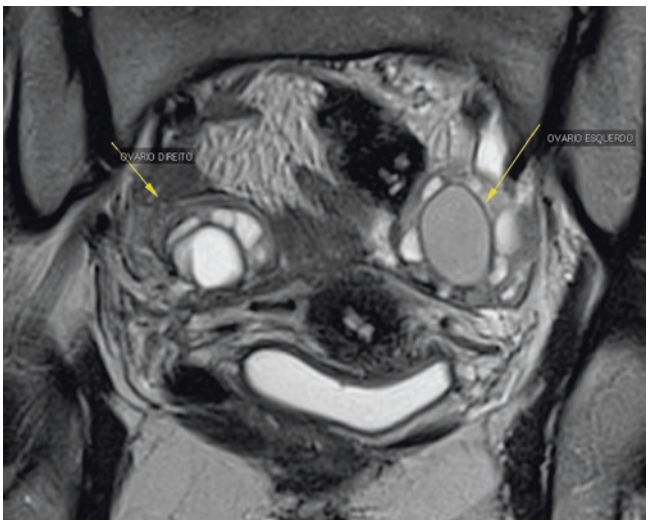

Fig. 5.33 Coronal, TSE, T2 weighting. In the left ovarian, notice the aspects already described for ovarian endometrioma (*arrow*)

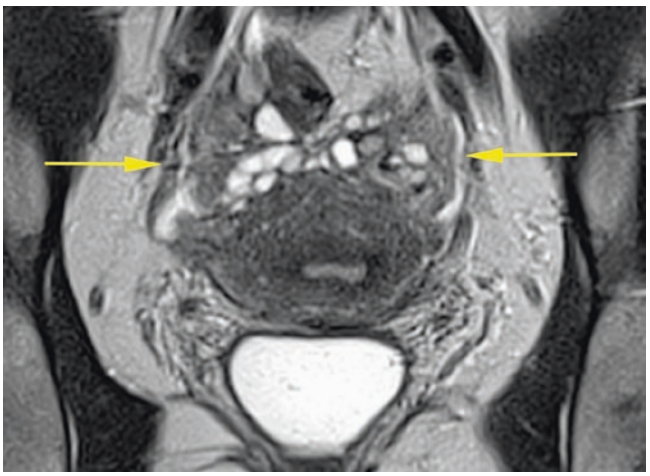

Fig. 5.34 Coronal, TSE, T2 weighting. In this image, the ovaries are near the middle line, due to the adhesion process that usually affects the pelvis – more precisely, the broad ligaments. This signal (Pseudo fusion of the ovaries) was initially described in laparoscopy tests as "Kissing ovaries"

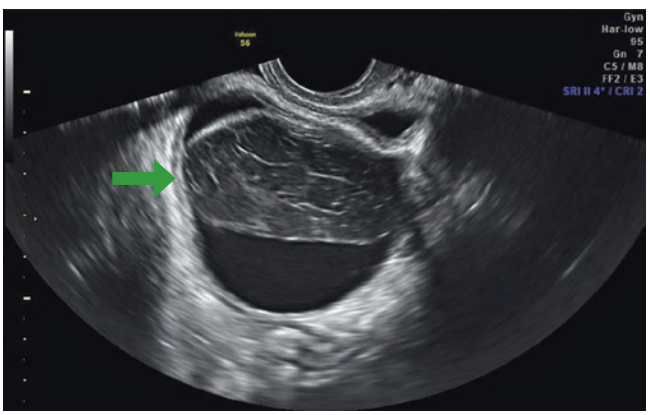

Fig. 5.35 Hemorrhagic cyst of the right ovary. Transverse endovaginal sonogram reveals fibrinous strands (*arrow*) and low-level internal echoes

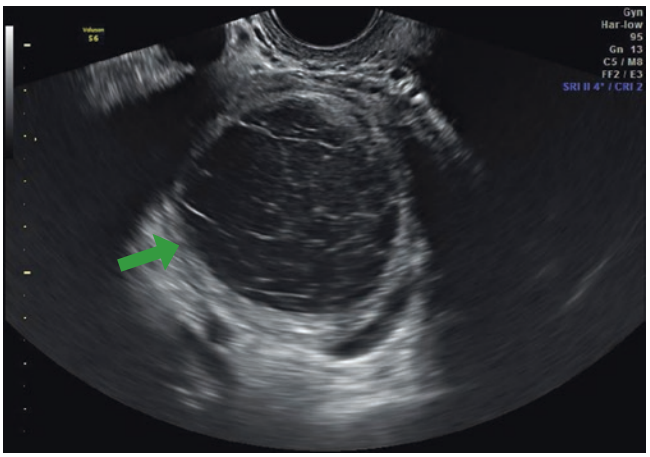

Fig. 5.36 Hemorrhagic cyst of the left ovary. Transverse endovaginal sonogram reveals fibrinous strands (*arrow*) and low-level internal echoes

Fig. 5.37 Ovarian endometrioma of the left ovary: well-circumscribed rounded cyst with low-level internal echoes without fibrinous strands

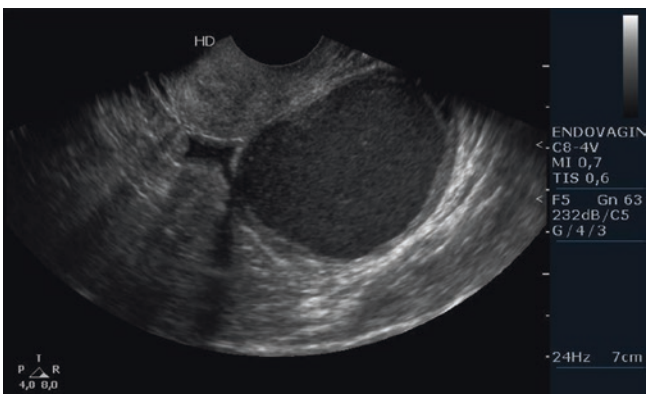

Fig. 5.38 Transvaginal transverse view: Ovarian endometrioma of the left ovary. Well-circumscribed rounded cyst with low-level internal echoes without fibrinous strands

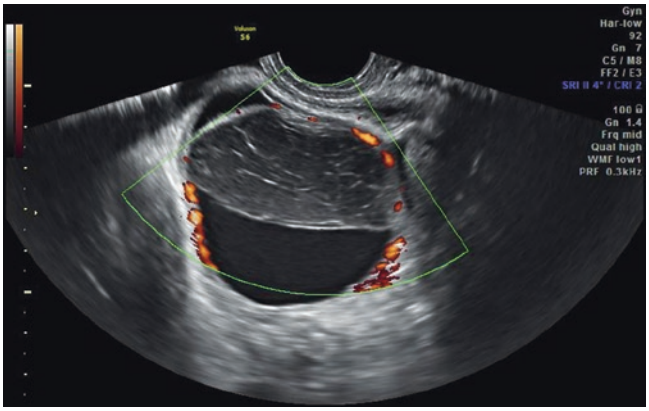

Fig. 5.39 Transvaginal sonogram of the ovary: Hemorrhagic cyst on color Doppler sonography shows a dense halo of confluent vessels surrounding the cyst

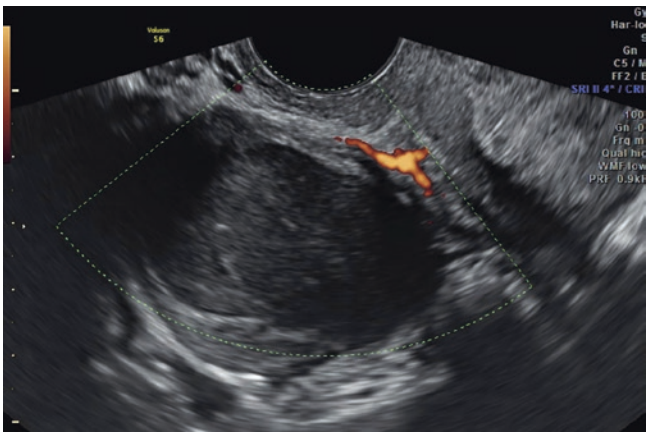

Fig. 5.40 Transvaginal sonogram of the right ovary: Endometriotic cyst with low vascularization on color Doppler sonography

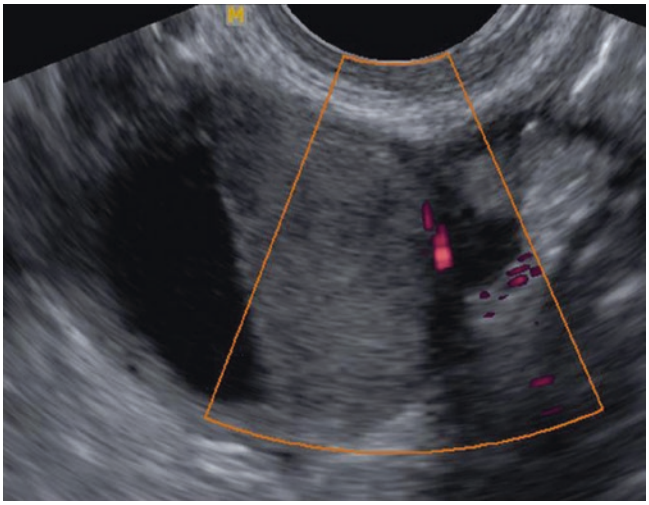

Fig. 5.41 Endometrioma with fluid layer. Transvaginal image shows an endometrioma with layering echogenic material. The supernatant fluid layer is hypoechoic

Fig. 5.42 (**a**) Axial, SE, T1 weighting, with fat saturation. Here, a tubaria collection to the right can be observed (*arrow*), which features high signal, compatible with hematic content. This same image in (**b**) transvaginal ultrasound is presented as the usual hydrosalpinx, emphasizing the value of supplementation with Magnetic Resonance (**c**) Sagittal, TSE, T2 weighting, where the liquid level/erythrocyt can be identified (*arrow*)

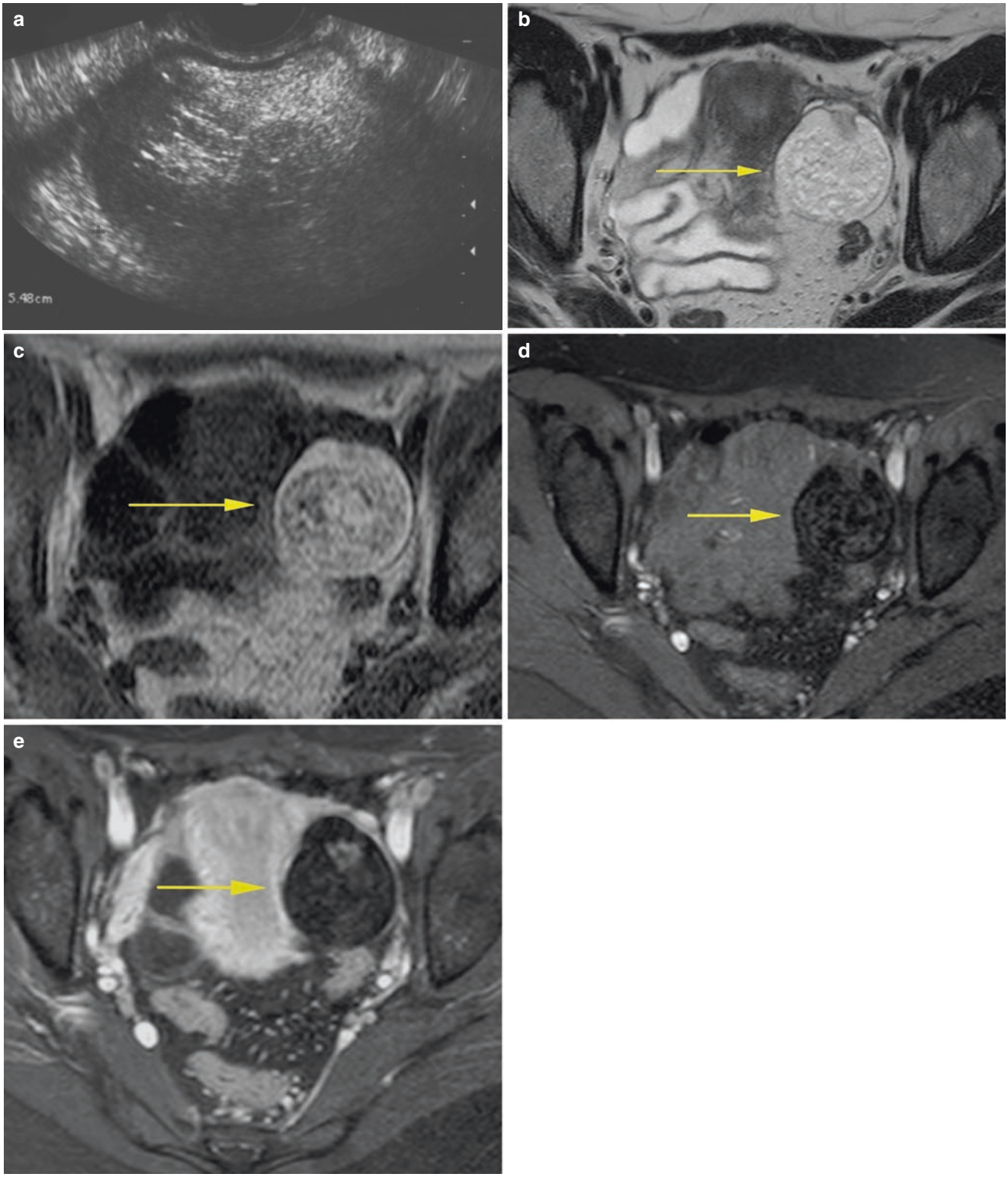

Fig. 5.43 (**a**) Dermoid cyst. Transvaginal image shows a dermoid cyst. The hyperechoic component (supernatant fat) tends to be located superiorly. (**b**) Axial TSE, T2 weighting. Predominantly cystic and heterogeneous lesion in the left ovary, which has well-defined contours. (**c**) Axial, SE, T1 weighted. The sign of the lesion is high, which may correspond to fat or blood. (**d**) Axial SE, T1 weighted, with fat saturation. The lesion has its saturated signal compatible with fat, inferring the diagnosis of teratoma. Compare with the endometrioma of Fig. 5.8b. (**e**) Axial, SE, T1 weighted, with fat saturation and after contrast. The peripheral nodular enhancement is where the promontory is, focus of the origin of the entire lesion

Deep Endometriosis

Deep endometriosis (DE), also called "infiltrative," it is the one that infiltrates the retroperitonial space more than 5 mm. [15]. It is characterized by the presence of endometrial implants, fibrosis, and sub-peritonial muscle hyperplasia; the most frequently affected sites are the uterosacral ligaments, the rectosigmoid, the vagina, and the bladder [15, 16].

DE is often multifocal, thereby affectng many places in the pelvis. Lesions of the posterior compartment of the pelvis (retro-uterine space, uterine torus, utero-sacral ligaments, vagina, and rectum-sigmoid) are much more common, but may be associated with those of the anterior pelvic compartment (vesico-uterine recess, round ligaments, and bladder). About 90% of DE cases involve the posterior compartment, and between 8% and 10% the anterior compartment [17].

In routine transvaginal ultrasound, the identification of ovarian endometriosis, especially when associated with adhesions, is an important DE marker. The presence of the Kissing ovaries sign is related to an increased risk of profound endometriosis, especially with intestinal involvement (Figs. 5.44 and 5.45) and tube obstruction [18].

The transvaginal ultrasound done with protocol for endometriosis mapping has proven to be an excellent method for detailed DE diagnosis, especially intestinal endometriosis [19, 20]. In a study of systematic review and meta-analysis, the method showed 91% sensitivity and 98% specificity for the diagnosis of intestinal endometriosis [19]. The protocol includes prior bowel preparation, possibly vaginal distension with ultrasound gel, and further evaluation of iliac fossas with a linear transducer. In the ultrasound, due to muscle hyperplasia, lesions are usually hypoechoic, not vascularized as in colored Doppler, and sometimes nodular and sometimes with irregular thickening, or in plates, according to the affected anatomical structure [5].

Fig. 5.44 Transvaginal transverse image shows the ovaries attached to each other. Note the rectum between them infiltrated by hypoechoic nodule with small cyst (intestinal deep endometriosis)

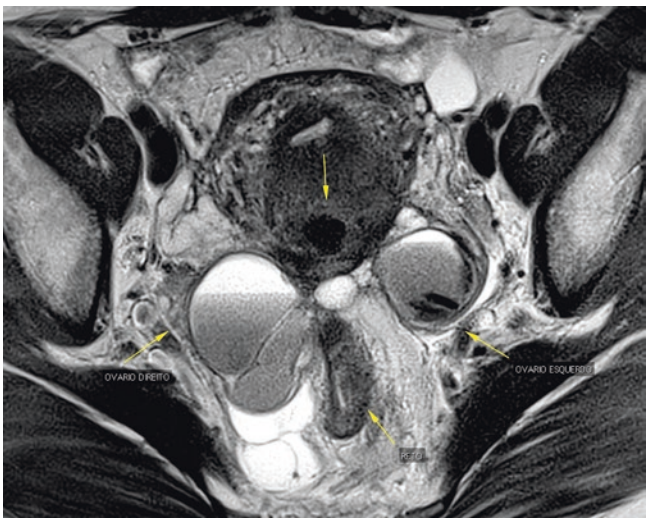

Fig. 5.45 Axial, TSE, T2 weighting. Similar to Fig. 5.10, the medianization or retraction of the ovaries to the middle line is present, with bilateral endometriomas, which form the liquid/erythrocyt level. There is also a retraction of the rectum by the adhesion process that commits the posterior compartment of the pelvis

Uterosacral Ligament Endometriosis

The uterosacral ligaments (USL) are formed by fibromuscular tissue, and compose the peri-cervical ring, with fibers that surround the cervix and upper vagina. They act as a support system that connects the vagina and the cervix to the sacrum, at the fourth vertebra.

The uterosacral ligaments and uterine torus (small peritoneal thickening posterior to the cervix, between the insertion of the uterosacral ligaments) are the sites most frequently affected by DE [21]. The involvement of the uterosacral ligaments can be unilateral or orbilateral and may appear on ultrasound as a hypoechoic thickening area, usually arcuate, or as a nodular area with speckled contours (Figs. 5.46, 5.47, 5.48, and 5.49). The normal uterosacral ligament is not usually identified on ultrasound, but when it is changed, it is thickened and becomes evident, especially when compared to the normal contralateral [22] (Figs. 5.50 and 5.51). In practice, the lesions of the uterosacral ligament occupy the *paracervical space* and may involve important structures in this location, such as ureters or the hypogastric nerve. The lesions of the uterine torus or those situated posterior to the cervix and in the midline are called *retrocervical space* lesions (Figs. 5.52 and 5.53).

In the MR, the ligament (LUS) is almost always well defined and slightly hypointense on T2. Its maximum thickness should not exceed 4 mm. The frequency of the involvement tends to be asymmetrical, predominantly the left one. If the injury extends to its sacral part, it can cause pain symptoms such as back pain. When it shows this heterogeneous signal, it is usually secondary to associated glandular tissue (Fig. 5.54).

The retrocervical region is an extraperitoneal space delimited by the posterior fornix, uterosacral ligaments, and rectovaginal septum. The involvement by endometriosis is most common in a median location; it begins with a small, irregular lump, with low signal and indistinct margins. They show enhancement by contrast and tend to converge to cloak in more advanced forms (Figs. 5.55 and 5.56).

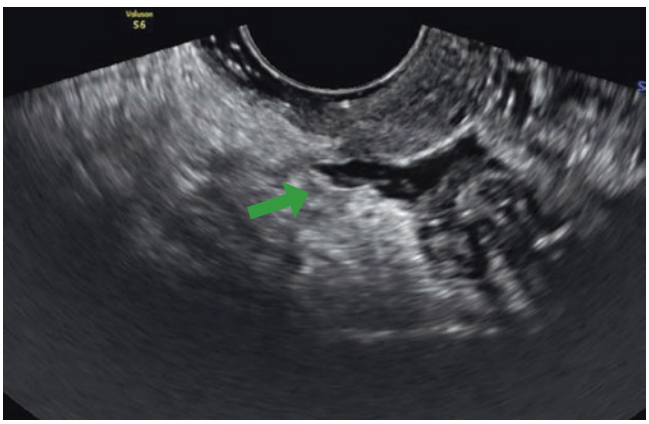

Fig. 5.46 Transvaginal transverse image shows a right uterosacral ligament thickness and hypoechoic with arciform appearance (*arrows*)

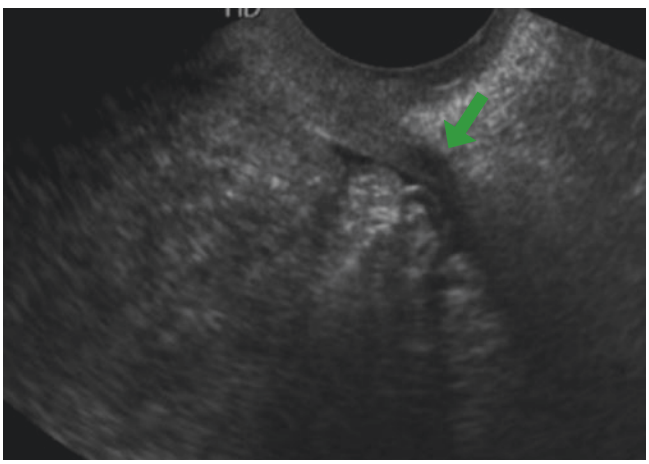

Fig. 5.47 Transvaginal oblique image shows thickened and hypoechoic left uterosacral ligament with arciform appearance (*arrows*)

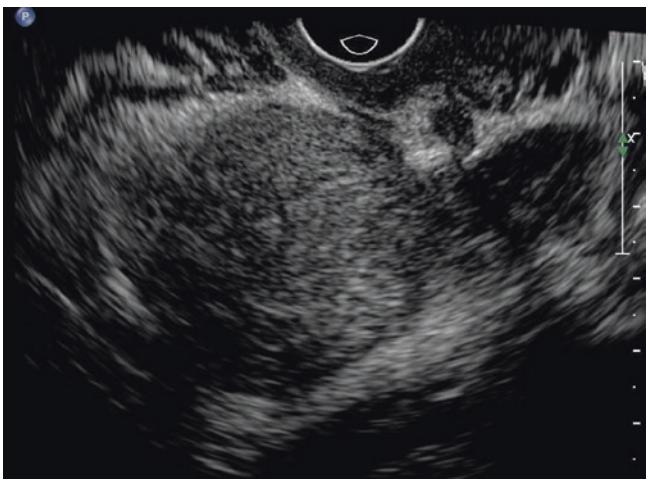

Fig. 5.48 Transvaginal transverse image shows a left utero-sacral ligament visible with a hypoechogenic nodule with irregular margins in the proximal part, near the insertion on the cervix

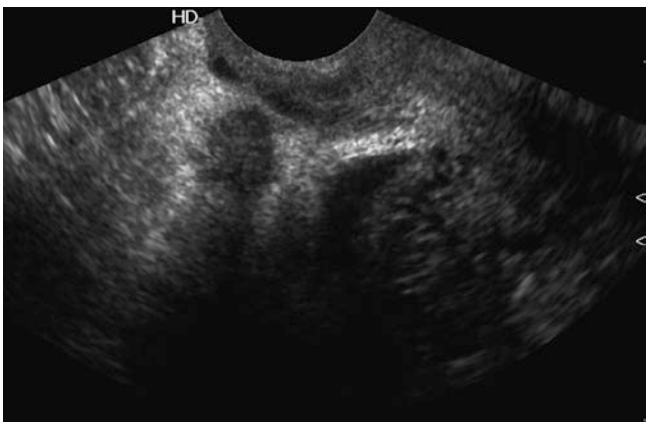

Fig. 5.49 Transvaginal oblique image shows a right utero-sacral ligament visible with a hypoechogenic nodule with irregular margins in the medial part, near the insertion on the cervix

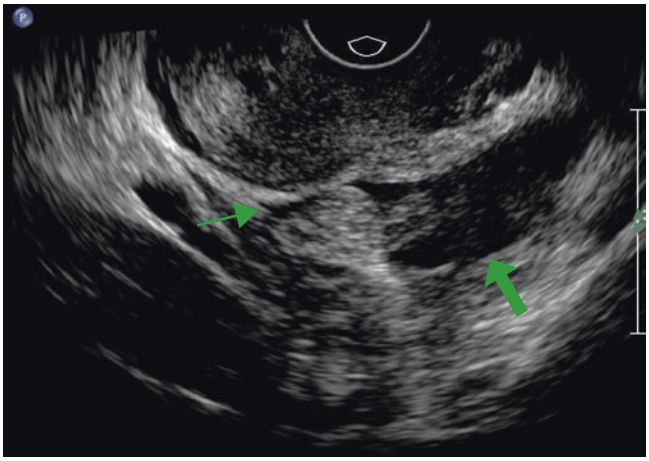

Fig. 5.50 Transvaginal transverse image shows a left utero-sacral ligament visible with a hypoechogenic linear thickening with regular margins (*arrow*). Compare it with a normal right utero-sacral (*arrowhead*)

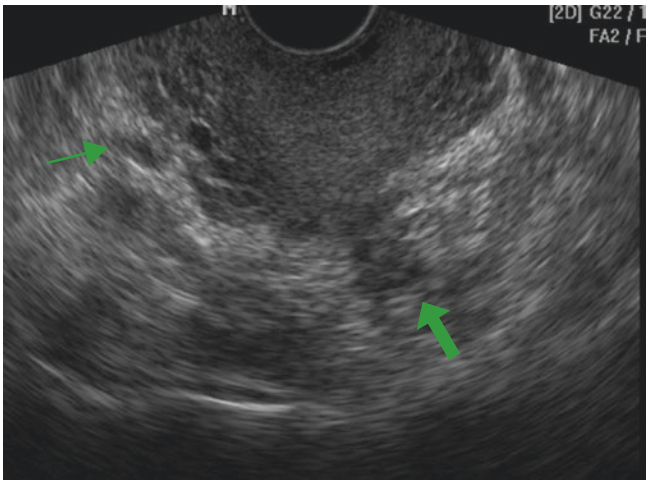

Fig. 5.51 Transvaginal transverse image shows a left utero-sacral ligament visible with a hypoechogenic linear thickening with a small cyst and regular margins (*arrow*). Compare with a normal right utero-sacral (*arrowhead*)

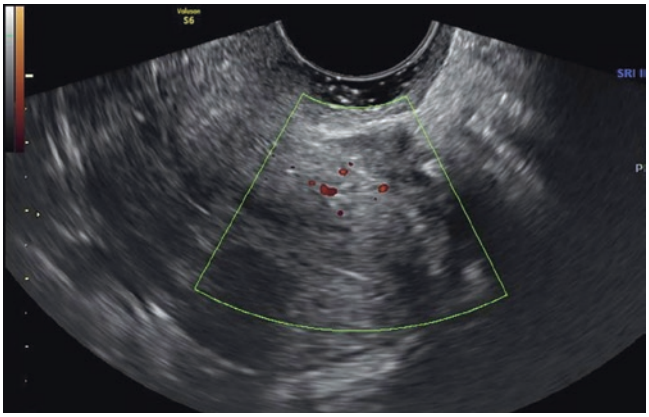

Fig. 5.52 Transvaginal sagittal image shows a long hypoechogenic thickening fixed at the posterior uterine wall (posterior subperitoneal space). No vascularization on color Doppler sonography

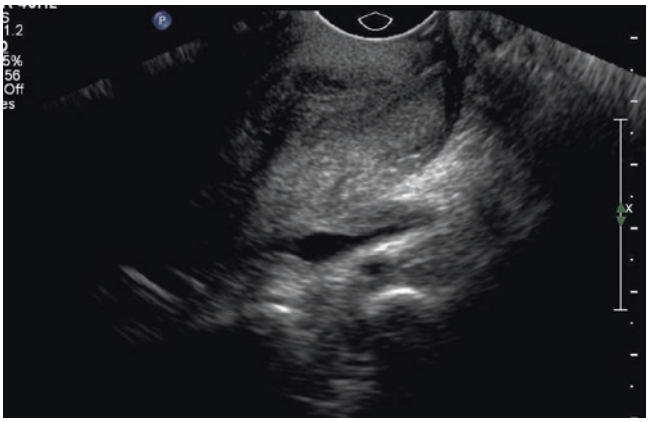

Fig. 5.53 Transvaginal sagittal image shows a long hypoechogenic thickening fixed at posterior cervix wall (posterior subperitoneal space)

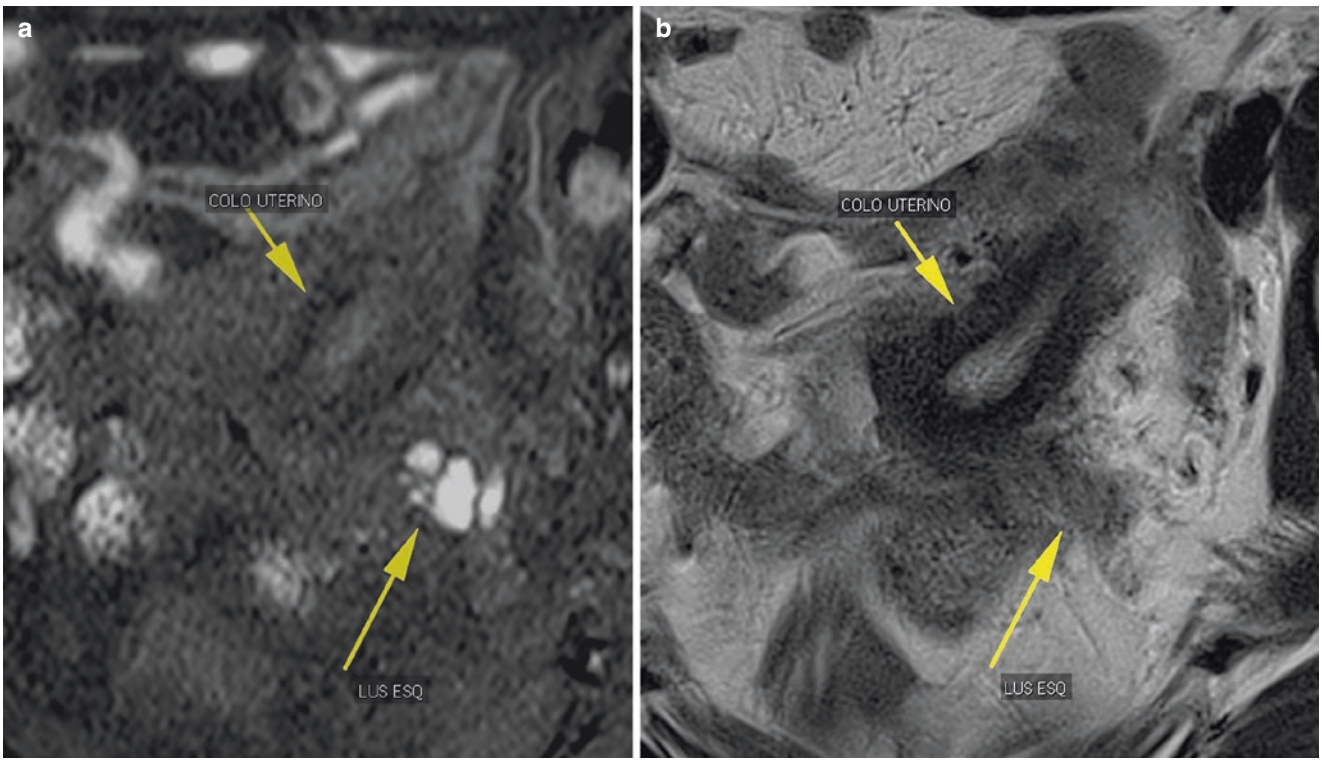

Fig. 5.54 (**a**) Axial, SE, T1 weighting, with fat saturation. In this case, active endometriosis foci can be identified in the left uterosacral ligament (*arrows*). (**b**) Axial, TSE, T2 weighting. The same as seen on (**a**); however, now it is in a sequence weighted in T2

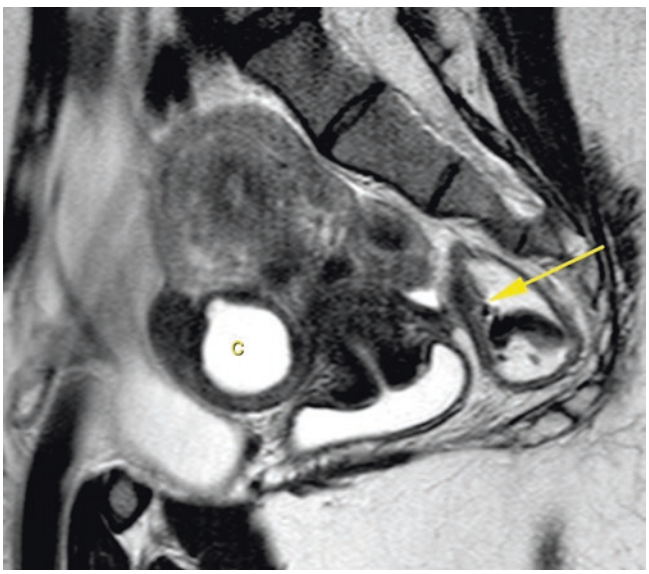

Fig. 5.55 Sagittal, TSE, T2 weighting. The adhesion process of the posterior compartment can be observed, obliterating the rectouterine recess, by a hypointense band, joining the posterior uterine serous with the anterior rectal wall (*arrow*). Cystic adenomyosis is also identified (*C*)

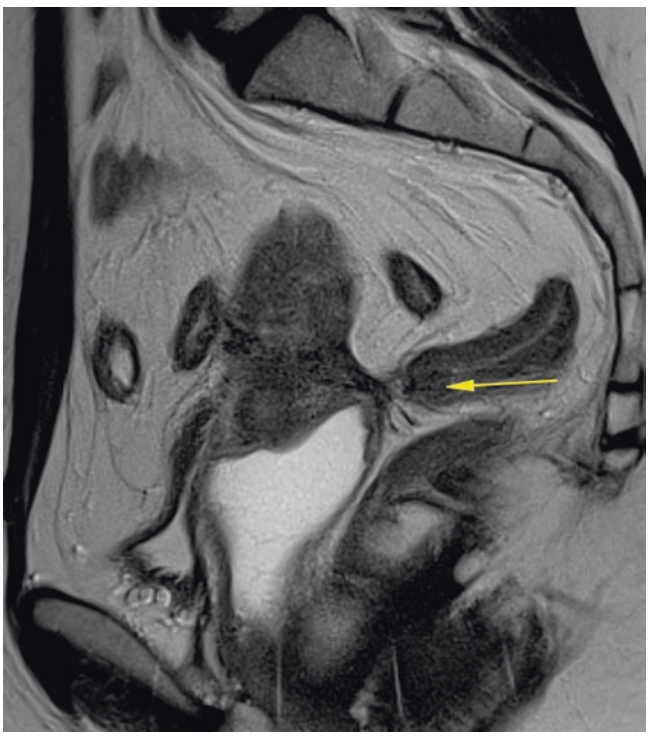

Fig. 5.56 Sagittal, TSE, T2 weighting. Adhesions processes are observed at the posterior compartment, partially obliterating the recto-uterine recess, by hypointense band, joining the posterior uterine serous with the rectum (*arrow*)

Vaginal and Rectovaginal Septum Endometriosis

The rectovaginal septum is a layer of sub-peritoneal connective tissue, lower in the posterior vaginal wall and the anterior wall of the rectum. It allows sliding between them. When affected by endometriosis, besides examining whether ureter and hypogastric nerve involvement are seen in the MR, the extent of anus muscle elevator should also be investigated (Fig. 5.57).

Vaginal involvement by endometriosis is usually secondary to infiltration from retrocervical lesions. They usually appear as thick areas or small nodes, usually with internal cystic areas that can sometimes infiltrate the mucous membrane (Figs. 5.58, 5.59, and 5.60). The introduction of vaginal gel greatly facilitates the evaluation of the vaginal fornix [23].

Isolated rectovaginal septum endometriosis is very rare; usually its involvement is secondary to a Douglas bag lesion that grows in the caudal direction. Characterized in ultrasound by a hypoechoic nodule with speckled margins, it is located posterior to the vagina in its middle third [5] (Fig. 5.61).

The vagina has walls that should have a thickness of less than 3 mm in MR exams, with intense enhancement by contrast. And since the involvement in the vaginal wall as a nodule is seldom prevalent, it is more often related to the extension of another region.

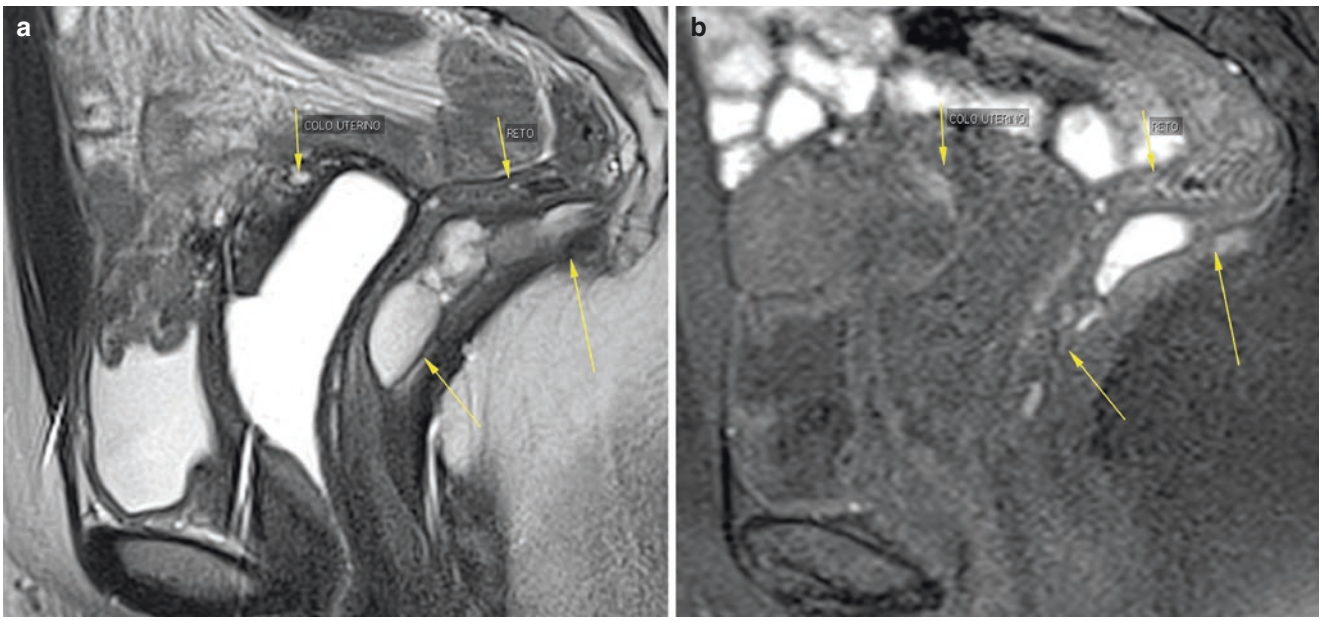

Fig. 5.57 (**a**) Sagittal, TSE, T2 weighting. Adhesions process of the posterior compartment are observed, with pre-sacral collection that features liquid level of intermediate and mixed signal. (**b**) Sagittal, SE, T1 weighting. The collection in this sequence has high signal, compatible with hematic content, inferring endometriosis, in an unusual location

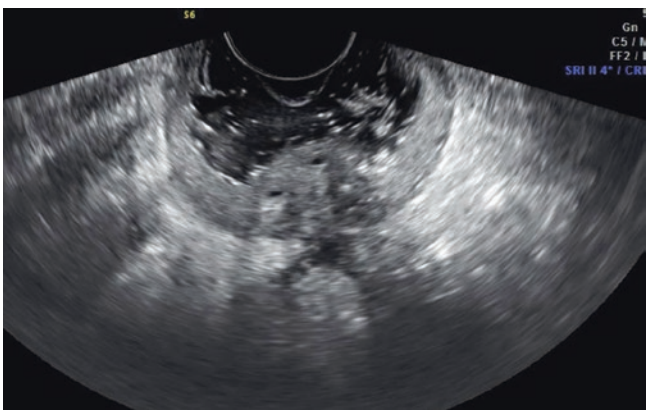

Fig. 5.58 Transvaginal transverse image shows posterior vaginal fornix thickened, with round cystic anechogenic areas. The vagina was distended by ultrasound gel

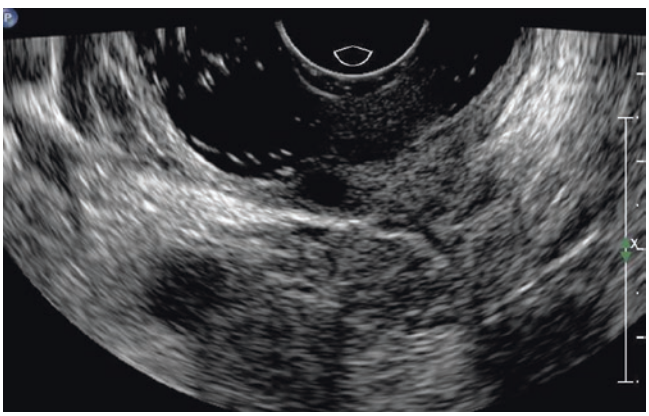

Fig. 5.59 Transvaginal transverse image shows posterior vaginal fornix thickened, with round cystic anechogenic areas. The vagina was distended by ultrasound gel

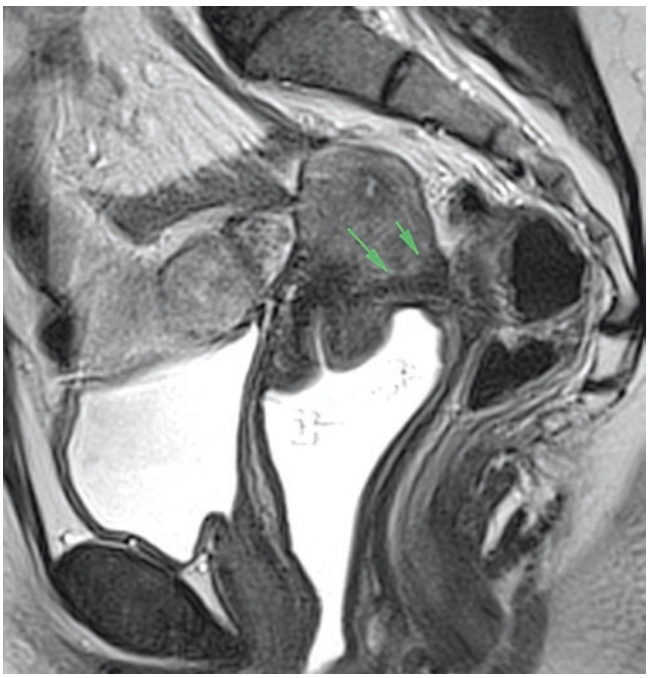

Fig. 5.60 Sagittal, TSE, T2 weighting. A hypointense band is observed, which extends from the uterine torus, compromising the anterior wall of the rectum and the posterior vaginal wall, with obliteration of the posterior fornix and the posterior vaginal fornix

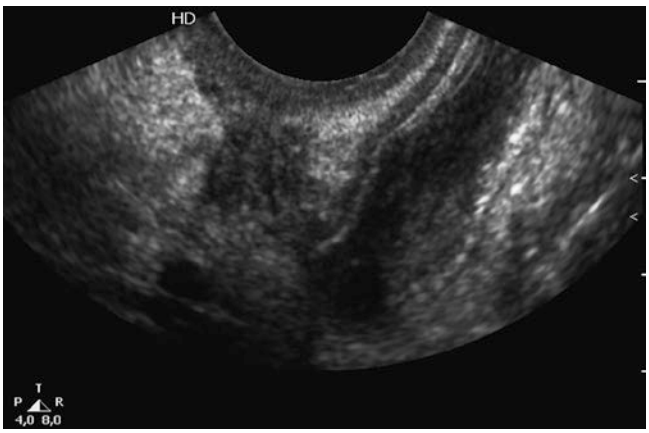

Fig. 5.61 Deep endometriosis of the rectovaginal septum. Transvaginal sagittal view shows the space between rectum and vagina (under the peritoneum) occupied by a hypoechogenic solid nodule with irregular margins

Intestinal Endometriosis

Intestinal endometriosis is one of the most severe forms of DE. Its diagnosis is extremely important for proper treatment planning. About 90% of bowel nodules affect the rectum-sigmoid; the other 10% can affect the ileum, cecum and appendix [24]. The former are seen by transvaginal ultrasound, and the latter during abdominal evaluation, using the high frequency linear transducer.

In transvaginal ultrasound with bowel preparation, the normal rectal wall has a first thin echogenic line corresponding to serous, followed by the muscle hypoechoic, with a thickness of less than 3 mm, and then the submucosa, which also appears hyperechoic, and the mucosa, hypoechoic [9]. Initially, the DE lesion affects the serous and progressively infiltrates the muscle, where it usually forms a nodule (Figs. 5.62 and 5.63). It rarely reaches the mucosa. Intestinal endometriosis is defined as that which infiltrates the muscular layer itself, so the involvement of only the serous is considered an adherence process [25] (Figs. 5.64 and 5.65).

A very common ultrasonographic aspect is the retrocervical fixed hypoechoic nodule that infiltrates the wall of the rectum-sigmoid [9] (Figs. 5.66 and 5.67). It is important in these cases to test the mobility of the structures by gently squeezing the probe between the cervix and the rectum in order to confirm the adhesion and block the posterior sac [9].

In about 40% of cases, DE infiltrates the intestine in more than one place [26] (Fig. 5.68). The transvaginal ultrasonography with bowel preparation is able to identify the number of intestinal lesions, their sizes, the depth of infiltration on parietal layers, *circumferential engagement of the strap, and also the distance from the anal surround*, which are very important parameters for surgical planning [23, 27].

The lesions in the rectum and sigmoid are initially identified as nodules on the MR, then forming an adhesion process that can lead to stenosis and obstruction. It is important to describe the lesion size (>3 cm) if the engagement is greater than 40% of the circumference of the loop, if there is wall invasion, mild stenosis, and the distance from the anal surround (if greater than 6 cm, it may have peritoneal extension) (Figs. 5.69 and 5.70).

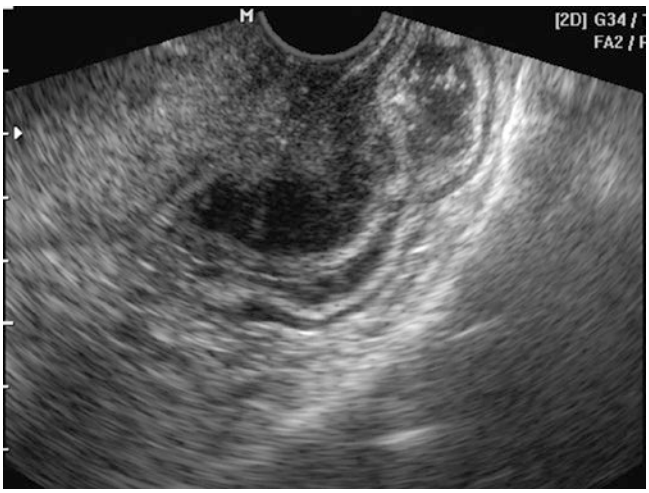

Fig. 5.62 Transvaginal sagittal image shows a hypoechogenic nodule penetrating the rectal anterior wall until the internal muscularis layer. The lesion effaced the normal adipose plane lying between the rectum and the uterus

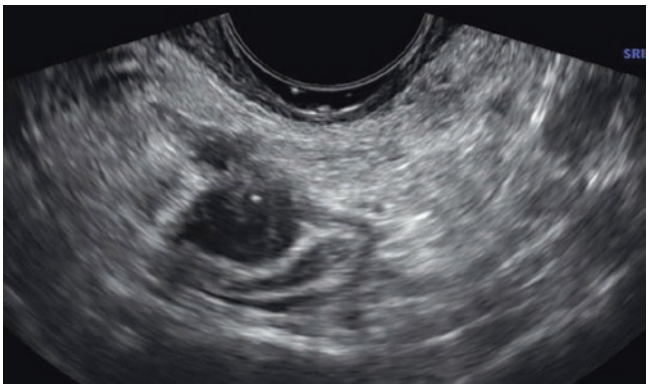

Fig. 5.63 Transvaginal transverse image of a rectum/sigmoid colon shows a hypoechogenic nodule penetrating the anterior wall until the internal muscularis layer

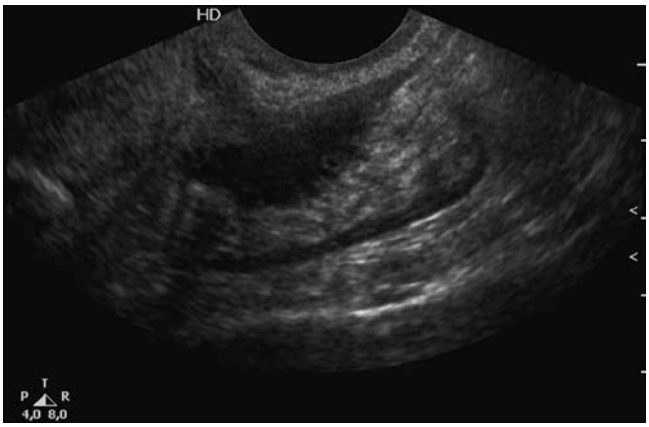

Fig. 5.64 Transvaginal sagittal image shows a hypoechogenic nodule penetrating into the rectal anterior wall until the internal muscularis and points of submucosa layer. The lesion effaced the normal adipose plane lying between the rectum and the uterus

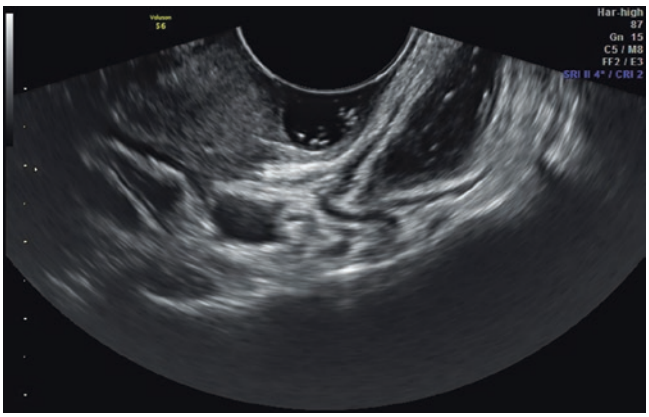

Fig. 5.65 Transvaginal sagittal image shows a hypoechogenic thickening fixed at the serosa layer of the rectal anterior wall. The normal aspect of the muscularis propria layer is preserved

Fig. 5.66 Transvaginal transverse image shows a hypoechogenic nodule on the subperitonial posterior space with a nodule penetrating into the rectal anterior wall until the internal muscularis layer

Fig. 5.67 Transvaginal sagital image shows a hypoechogenic thickening fixed on the cervix posterior wall with a nodule penetrating into the rectal anterior wall until the internal muscularis layer

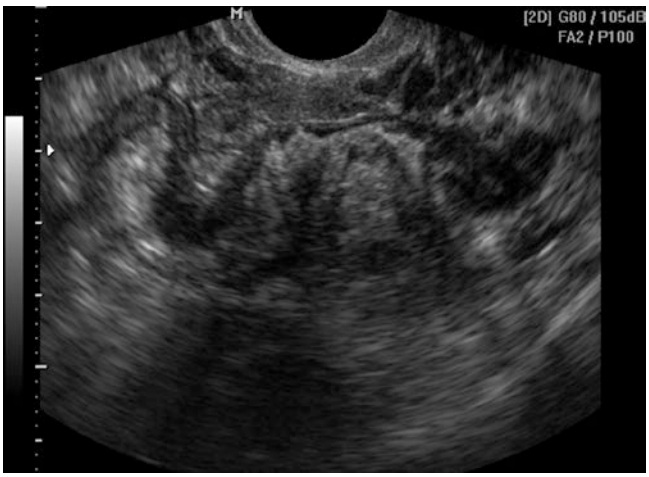

Fig. 5.68 Transvaginal sagittal image shows two hypoechogenic nodules at the anterior wall of the rectum/sigmoid colon until the internal muscularis layer

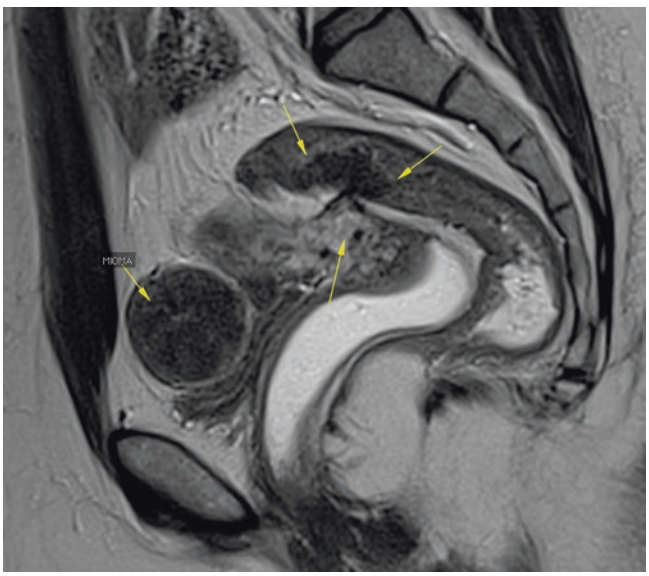

Fig. 5.69 Sagittal, TSE, T2 weighting. In this image, we can identify a large nodule in the anterior serosal of the rectal wall, formed together with an adhesion process that extends itself from the posterior uterine serosa (*arrows*). An anterior subserosal myoma is also identified

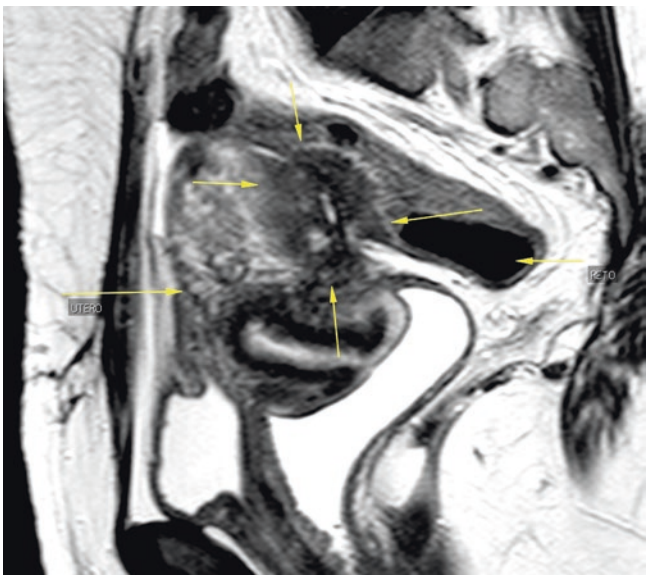

Fig. 5.70 Sagittal, TSE, T2 weighting. Note the extensive commitment of the posterior compartment of the pelvis (*arrows*), with hypointense lesion "in mantle", involving the posterior wall of the uterus, invading the myometrium and extending itself to the anterior wall of the rectum, with complete obliteration of the posterior compartment of the pelvis

Vesico-Uterine Recess and Bladder Endometriosis

To properly assess the vesico-uterine space, a moderate bladder filling is needed. Lesions usually appear as thickenings in plates attached to the anterior uterine wall and the uterine insertion of the rounded ligaments (Figs. 5.71 and 5.72).

When there is already infiltration of the posterior bladder wall, it is usually in the midline, closer to the vesical dome, and rarely near the trigon. The ultrasonographic appearance translates into hypoechoic nodules, commonly containing small internal cystic areas, with loss of echogenic line integrity of the serous, with the appearance of organ infiltration "from the outside to the inside" [28, 29] (Figs. 5.73 and 5.74).

In the anterior compartment, multifocal identification engagement is more frequent, with lateral extension of the round ligaments, anterior to the vesical ceiling and posterior vesical wall. For this analysis, the patient should begin the MR preferably with an empty bladder.

The bladder wall is formed by three predominant layers: adventitia, detrusor (muscle), and the mucous membrane. The bladder is compromised in 11% of the cases of severe endometriosis [30]; its main limits are vesico-uterine spaces, retropubic (Retzius), and vesico-vaginal.

A lesion that can simulate vesical involvement by endometriosis at the MR is the median umbilical ligament, which is previous and superior set in the vesical ceiling. It is a fibrous cord, urachus trace (Fig. 5.75).

Another lesion that can simulate vesical endometriosis is the diverticulum of the urachus, which may show a hypersign on T1 with fat saturation, simulating endometriosis.

The endometriosis implant affects the bladder as an isolated injury, predominantly involving the muscle layer. It presents as a hypointense and irregular nodule, with a heterogeneous signal, in the posterior wall and vesical superior surface, and is prone to invasion in the vesico-uterine recess (Figs. 5.76 and 5.77).

It is important to assess the following in the MR images:

- Miometrial impairment
- Mucosa/submucosa impairment
- Distance of the ureteral meatus
- Size of the ureteral meatus

The ureter is more often affected in the distal third, is one-sided, and more related to the left side.

Fig. 5.71 Transvaginal transverse image shows a small hypoechogenic nodule with cystic area in the vesicouterine pouch, without bladder involvement

Fig. 5.72 Transvaginal transverse image shows a hypoechogenic thickening with cystic area in the vesicouterine pouch, at the left round ligament uterine insertion. There are no bladder involvement signs

Fig. 5.73 Transvaginal sagittal image shows a bladder involvement. Note the hypoechoic nodule within the posterior wall of the bladder in front of the vesicouterine pouch

Fig. 5.74 Transvaginal transverse image shows a bladder-deep endometriosis. Note two hypochoic nodules within the posterior wall of the bladder

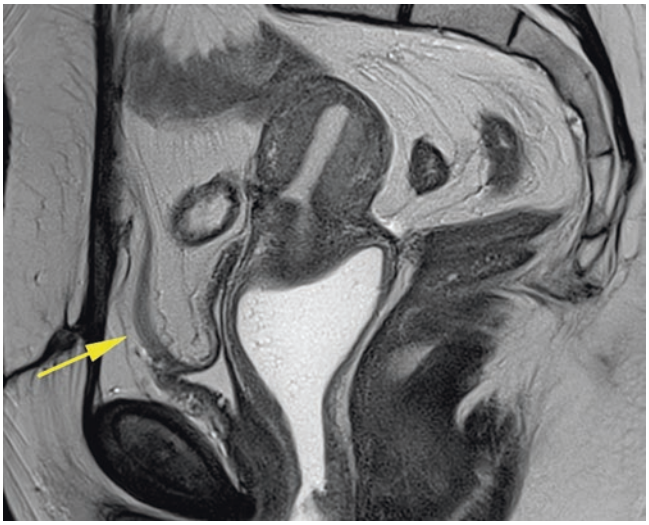

Fig. 5.75 Sagittal, TSE, T2 weighting. The median umbilical ligament (*arrow*) can be identified in this image. This ligament is an embryological remainder. When presents more focal nodularitty with smaller dimensions, may have an image aspect similar to a bladder focal lesion, such as endometriosis

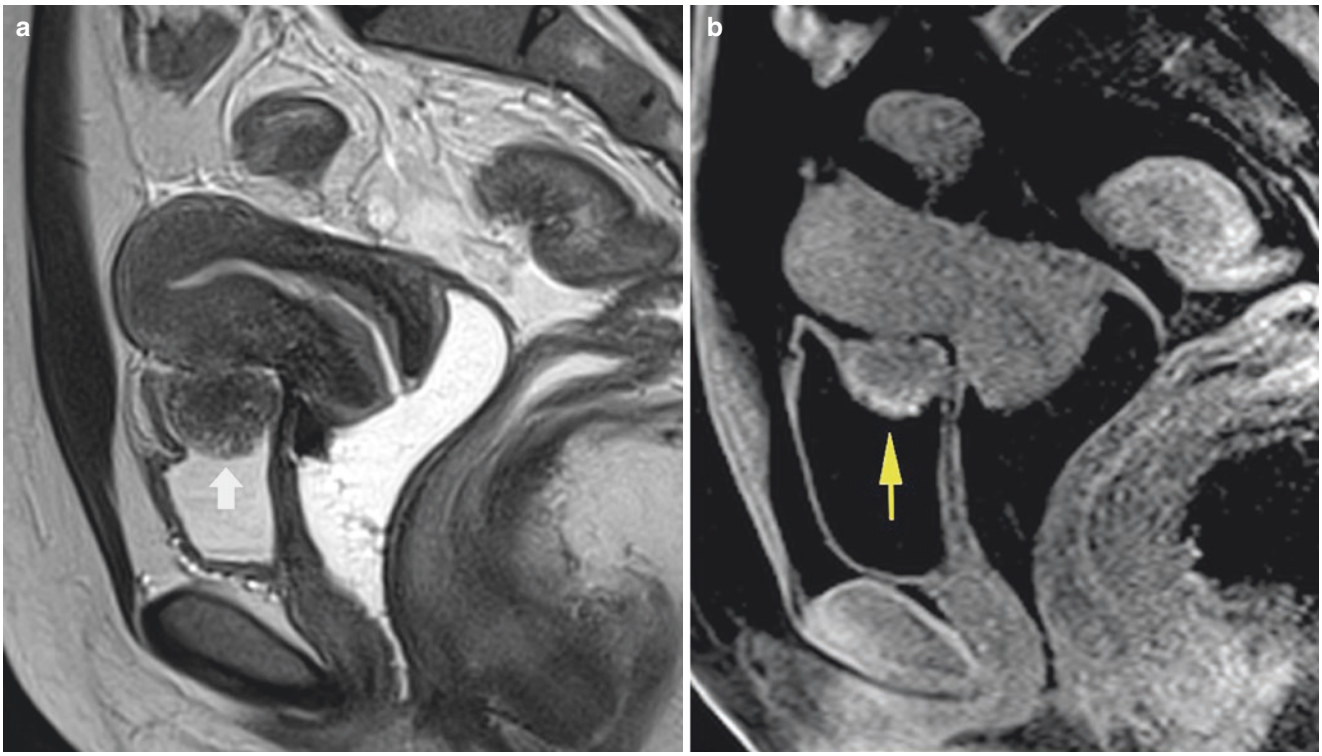

Fig. 5.76 (**a**) Sagittal, TSE, T2 weighting. Note that the white arrow shows a nodular focal lesion of the top of the bladder with heterogeneous signal. The picture is very similar to an intravesical tumor. note, however that there is obliteration of the vesico uterine space, with extension up to the previous uterine serous, implying the possibility of endometriosis. (**b**) Same image (*arrow*), now in SE sequence, T1 weighting, with fat saturation

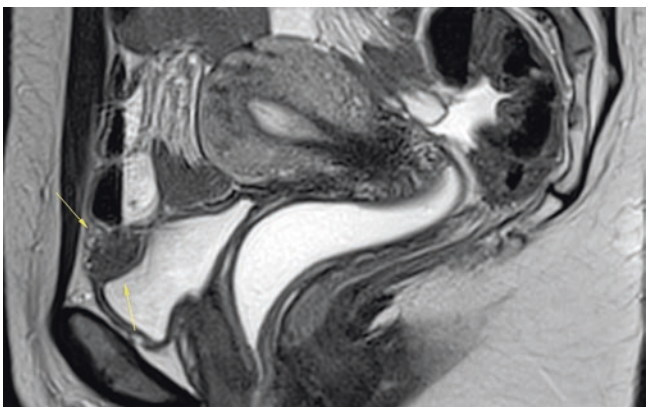

Fig. 5.77 Sagittal, TSE, T2 weighting. Another case of bladder endometriosis with a focal mass in the anterior and top of the bladder (*arrow*)

Myometrium Endometriosis (Uterine Serous)

In the posterior myometrium, local affection in MR can be variable; however, it is always peripheral, which helps differentiate adenomyosis, and which initially has central involvement. When they present cloak morphology, they tend to follow the uterine serous, with varying degrees of myometrial penetration. In addition to the diameters in the MR reports, the depth of myometrial involvement and its distance to the uterine cavity must be described [29] (Figs. 5.78 and 5.79).

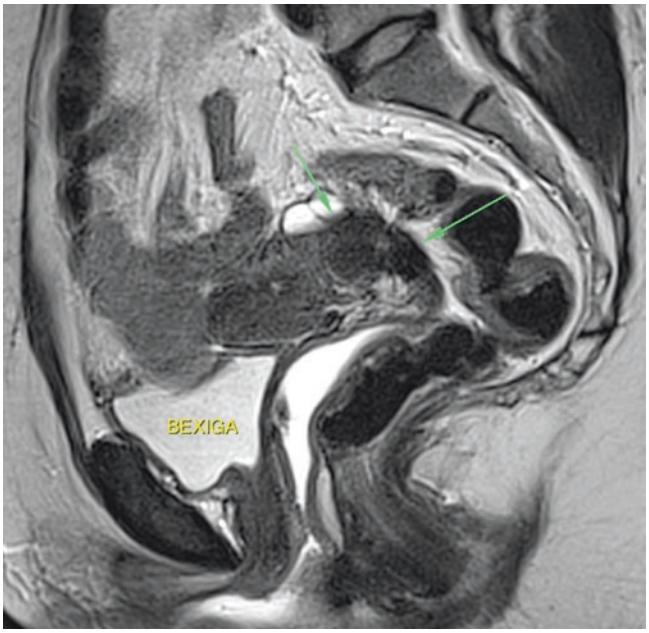

Fig. 5.78 Sagittal, TSE, T2 weighting. Note in this case, a similar lesion to Fig. 5.20, with involvement of the posterior uterine serosa, space obliteration, and myometrial invasion (*arrows*)

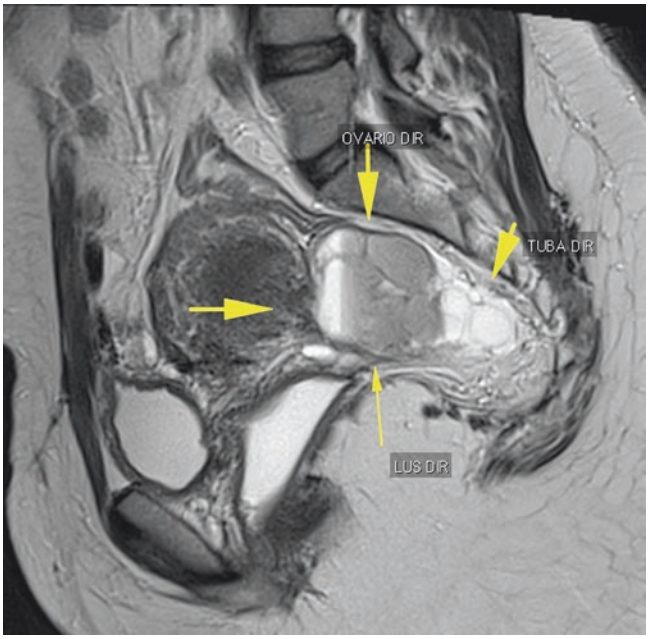

Fig. 5.79 Sagittal, TSE, T2 weighting. In this case, the uetrine commitment is deeper and lateral, extending the adhesion process of the posterior uterine serosa into the lateral compartment, involving the right ovary, the sacrum uterine ligament (LUS DIR), and forming a hydro/hematosalpinx with the distal tubal fimbriae (TUBA DIR)

Endometriosis in the Lateral Compartment

The paracolpi and parametrium are located between the leaflets of the broad ligament, consisting of cellular connective tissue and the parametrium delimits the lateral uterine borders; the paracolpi delimits the distal third of the vagina. Signal similar to fat appears in the MR, except in the region of the transition from the cervix with the vaginal vault, where small, hypointense, thin beams come from the cardinal ligament, which is another uterine-supporting structure (Fig. 5.80).

Its impairment is almost always secondary to the extension of another affected site; these can be uterosacral ligaments, rectovaginal septum, or the retrocervical region. Whenever there is parametrial involvement, the extent to the uterine artery has to be assessed; this may compromise surgical planning.

The hypogastric nerve is composed of complex upper and lower hypogastrics, next to the uterosacral ligaments and medial to the ureters. The impairment generally extends to the lateral and posterior pelvic wall [29, 30].

The pelvic floor can be surrounded by an extension of the affection of the broad ligaments, and may involve the anus muscle elevator in the midline or lateral anus. Involvement of perineal membrane endometriosis is rarely found in the episiotomy scar.

Fig. 5.80 Coronal, TSE, T2 weighting. In this figure, we have the envolvment and invasion of the right parametria, with an arching position of the broad right ligament (*arrows*)

References

1. Sampson JA. Perforating hemorrhagic (chocolate) cysts of the ovary, their importance and especially their relation to pelvic adenomas of endometrial type. Arch Surg. 1921;3:245.
2. Fedele L, Parazzini F, Bianchi S, et al. Stage and localization of pelvic endometriosis and pain. Fertil Steril. 1990;53:155–8.
3. Meuleman C, Vandenabeele B, Fieuws S, Spiessens C, Timmerman D, D'Hooghe T. High prevalence of endometriosis in infertile women with normal ovulation and normospermic partners. Fertil Steril. 2009;92:68–74.
4. Chapron C, Dubuisson JB, Pansini V, et al. Routine clinical examination is not sufficient for diagnosing and locating deeply infiltrating endometriosis. J Am Assoc Gynecol Laparosc. 2002;9(2):115–9.
5. Maubon A, Bazot M. Imagerie de léndométriose. Journal de Gynécologie Obstétrique et Biologie de la Reproduction. 2007;36(2):129–34.
6. Kerr L, Gabas F, Machado F, Cukie r E. Transvaginal diagnosis of diffuse endometriosis. J Ultrasound Med. 2002;21(suppl):S13.
7. Brown DL, Frates MC, Muto MG, Welch WR. Small echogenic foci in the ovaries: correlation with histologis findings. J Ultrasound Med. 2004;23(2):307–13.
8. Van Holsbeke C, Van Calster B, Guerriero S, et al. Imaging in gynaecology: how good are we in identifying endometriomas? Facts Views Vis Obgyn. 2009;1(1):7–17.
9. Savelli L. Transvaginal Sonography for the assessment of ovarian and pelvic endometriosis: how deep is our understanding? Ultrasound Obstet Gynecol. 2009;33(5):497–501.
10. Alcazar JL, Laparte C, Jurado M, Lopez-Garcia G. The role of transvaginal ultrasonography combined with color velocity imaging and pulsed Doppler in the diagnosis of endometrioma. Fertil Steril.1997;67:487–91.
11. Patel M, Feldstein VA, Chen DC, Lipson SD, Filly RA. Endometriomas: diagnostic performance of US. Radiology. 1999;210:739–45.
12. Guerriero S, Ajossa S, Mais V, Risalvato A, Lai MP, Melis GB. The diagnosis of endometriomata using color Doppler energy imaging. Hum Reprod. 1998;13:1691–5.
13. Dogan MM, Ugur M, Soysal SK, Soysal ME, Ekici E, Gokmen O. Transvaginal sonographic diagnosis of ovarian endometrioma. Int J Gynaecol Obstet. 1996;52:145–9.
14. Jain K. Endometrioma with calcification simulating a dermoid on sonography. J Ultrasound Med. 2006;25:1237–41.
15. Asch E, Levine D. Variations in appearance of endometriomas. J Ultrasound Med. 2007;26:993–1002.
16. Cornillie FJ, Oosterlynck D, Lauweryns JM, Koninckx PR. Deeply infiltrating pelvic endometriosis: histology and clinical significance. Fertil Steril. 1990;53:978–83.
17. Chapron C, Fauconnier A, Vieira M, Barakat H, Dousset B, Pansini V, Vacher-Lavenu MC, Dubuisson JB. Anatomical distribution of deeply infiltrating endometriosis: surgical implications and proposition for a classification. Hum Reprod. 2003;18:157–61.
18. Ghezzi F, Raio L, Cromi A, Duwe D, Beretta P, Butarelli M, Mueller MD. "Kissing ovaries": a sonographic sign of moderate to severe endometriosis. Fertil Steril. 2005;83(1):143–7.
19. Hudelist G, English J, Thomas AE, Tinelli A, Singer CF, Keckstein J. Diagnostic accuracy of transvaginal ultrasound for non-inasive diagnosis of bowel endometriosis: systematic review and meta-analysis. Ultrasound Obstet Gynecol. 2011;37:257–26.
20. Piketty M, Chopin N, Dousset B, Millischer-Bellaische AE, Roseau G, Leconte M, Borghese B, Chapron C. Preoperative work-up for patients with deeply infiltrating endometriosis: transvaginal ultrasonography must definitely be the first-line imaging examination. Hum Reprod. 2009;24:602–7.
21. Bazot M, Malzy P, Cortez A, Roseau G, Amouyal P, Darai E. Accuracy of transvaginal sonography and rectal endoscopic sonography in the diagnosis of deep infiltrating endometriosis. Ultrasound Obstet Gynecol. 2007;30:994–1001.
22. Bazot M, Thomassin I, Hourani R, Cortez A, Darai E. Diagnostic accuracy of transvaginal sonography for deep pelvic endometriosis. Ultrasound Obstet Gynecol. 2004;24:180–5.
23. Guerriero S, Ajossa S, Gerada M, D'Aquila M, Piras B, Melis GB. "Tenderness-guided" transvaginal ultrasonography: a new method for the detection of deep endometriosis in patients with chronic pelvic pain. Fertil Steril. 2007;88:1293–7.
24. De Cicco C, Corona R, Schonman R, Mailova K, Ussia A, Koninckx P. Bowel resection for deep endometriosis: a systematic review. BJOG. 2011;118:285–91.
25. Chapron C, Bourret A, Chopin N, Dousset B, Leconte M, Amsellem-Ouazana D, de Ziegler D, Borghese B. Surgery for bladder endometriosis: long-term results and concomitant management of associated posterior deep lesions. Hum Reprod. 2010;25:884–9.
26. Chapron C, Chopin N, Borghese B, Foulot H, Dousset B, Vacher-Lavenu MC, Vieira M, Hasan W, Bricou A. Deeply infiltrating endometriosis: pathogenetic implications of the anatomical distribution. Hum Reprod. 2006;21:1839–45.
27. Goncalves MO, Podgaec S, Dias Jr JA, Gonzalez M, Abrao MS. Transvaginal ultrasonography with bowel preparation is able to predict the number of lesions and rectosigmoid layers affected in cases of deep endometriosis, defining surgical strategy. Hum Reprod. 2010;25:665–71.
28. Fedele L, Bianchi S, Raffaelli R, Portuese A. Pre-operative assessment of bladder endometriosis. Hum Reprod. 1997;12:2519–22.
29. Brandao A. Atlas de ressonancia em endometrioses profunda:correlacao com laparoscopia. 1st ed. Rio de Janeiro: Revinter; 2014.
30. Whitman GJ, Mc Govern FJ. Endometriosis of the bladder detected by pelvic ultrasonography. J Ultrasound Med. 1994;13:115–7.

Leiomyoma and Cavitary Lesions

6

Harley De Nicola and Jacob Szejnfeld

Introduction

Leioyomas (fibroids or myomas) are the most common tumors of the uterus, occurring in 5–77% of women, depending on the method of diagnosis used. These benign masses occur in 20–50% of reproductive-age women [1].

Myomas arise from genetic alterations in a single myome trial cell and thus are often described as clonal [2]. Although estrogen may stimulate myoma development and growth, myomas may also grow when circulating estrogen levels are low, possibly because ovarian and adrenal androgens can be converted to estrogens by aromatase activity within myoma cells [3].

Whereas most women with uterine myomas are asymptomatic, many may have significant symptoms, including pelvic and abdominal pain and excessive bleeding. Other symptoms of myomas may result from their imposition on adjacent organs such as the bladder (urinary frequency) or rectum (tenesmus).

Although uterine myomas can be identified in approximately 5–10% of infertile women, only 2–3% of infertility cases can be attributed to the effects of myomas when all other causes are excluded [2–4]. In a prospective cohort study of women with otherwise unexplained infertility, 11% of women with myomas conceived without intervention compared with 25% of those without myomas and 42% of women who underwent laparoscopic myomectomy [5].

Myomas can adversely affect fertility through several mechanisms:

- Displacement of the cervix that may reduce exposure to sperm
- Obstruction of the proximal fallopian tubes
- Disordered uterine contractility
- Endometrial inflammation or secretion of vasoactive substances
- Disruption of the endometrium and implantation due to atrophy or venous ectasia over or opposite a submucous myoma [1, 2]

Some authors suggests that the location of the fibroids may matter: women with subserosal fibroids do not seem to be less fertile than women with no fibroids; however, women with submucosal fibroids (with or without intramural fibroids) had decreased fertility and increased pregnancy loss compared to women with no fibroids [6, 7].

Infertility is rarely caused by myomas, but when it happens it is associated with a submucous myoma or a markedly distorted, enlarged endometrial cavity that interferes with normal implantation or with sperm transportation. Severe displacement of the cervix is also capable of adversely affecting sperm deposition. Intramural myomas may cause obstruction or dysfunction of the tubal ostia or intramural portion of the tubes. For patients undergoing *in vitro* fertilization, distortion of the endometrial cavity by myomas is associated with decreased pregnancy rates and spontaneous abortion rates in up to 50% of cases. Uterine myomas have also been implicated in recurrent pregnancy loss [2, 6, 7].

MRI

MRI can provide details about fibroid size, location, signal intensity, and enhancement characteristics. Because uterine fibroids are sharply demarcated from surrounding myometrium by a pseudocapsule of light areolar tissue or compressed myometrial tissue, precise measurements can be made with three-planar MRI on T2-weighted images.

H. De Nicola (✉)
Diagnostic Imaging Department of UNIFESP – Federal University of São Paulo, São Paulo Hospital, São Paulo, SP, Brazil
e-mail: harley.nicola@terra.com.br

J. Szejnfeld
Full professor of Diagnostic Imaging Department of UNIFESP – Federal University of São Paulo, São Paulo Hospital, São Paulo, SP, Brazil

L.R.M.F. de Souza et al. (eds.), *Atlas of Imaging in Infertility*, DOI 10.1007/978-3-319-13893-0_6

Fibroids typically are well-defined masses of low signal intensity on T2-weighted images and enhanced after administration of contrast material. A less common group are those showing high-signal intensity on T2-weighted images, thought to represent hypercellular fibroids, composed of compact smooth muscle cells without intervening collagen.

As they increase in size, fibroids may undergo hyaline degeneration, resulting in a low-signal intensity on T2-weighted images. Findings indicating hemorrhagic degeneration may depend on how much time has gone by since degeneration, but usually hemorrhagic degeneration is seen as high signal intensity on T1-weighted images within the entire fibroid and lack of enhancement after administration of contrast material [8, 9].

Ultrasound

Ultrasound (US) is usually the initial investigation for examining the female pelvis. Transvaginal scans are more sensitive for the diagnosis of small fibroids; however, both transabdominal and transvaginal scans should be performed.

Transabdominal views are often of limited value in obese patients. Ultrasonography is highly operator-dependent, and in skilled hands, fibroids as small as 5 mm can be detected on transvaginal US [10].

Uterine fibroids most often appear on ultrasound as concentric, solid, hypoechoic masses. This appearance results from the prevailing muscle, which is observed at histologic examination. These solid masses absorb sound waves and therefore cause a variable amount of acoustic shadowing.

Even non-calcified fibroids often show a degree of posterior acoustic shadowing, although this is of course more marked in calcified fibroids.

Degenerate fibroids may have a complex appearance, with areas of cystic change. Doppler findings typically show circumferential vascularity; however, necrotic fibroids or fibroids that have undergone torsion will show absence of flow [11, 12].

Subserosal Myomas

Subserosal myomas typically develop on the outer uterine wall. The growth of a subserosal fibroid tumor will put additional pressure on the surrounding organs. Therefore, symptoms of subserosal myomas do not usually include abnormal or excessive menstrual bleeding or interfere with a women's normal menstrual flow or fertility.

Intramural Myomas

Intramural myomas typically develop within the uterine wall and expand from there. These uterine fibroids are the most common. This type of fibroid tumor can also cause "bulk symptoms" such as excessive menstrual bleeding, which can cause prolonged menstrual cycles, clot passing, and pelvic pain that is caused by the additional pressure placed on surrounding organs by the growth of the fibroid, which consequently can cause frequent urination and pressure.

Pedunculated Myomas

Pedunculated uterine myomas occur when a fibroid tumor grows on a stalk, resulting in pedunculated subserosal fibroids. These fibroids can grow on the outside of the uterine wall. Symptoms associated with pedunculated fibroid tumors include pain and pressure as the fibroids can sometimes twist on the stalk.

Submucosal Myomas

The least common of the various types of fibroid tumors are submucosal fibroids; these develop just under the lining of the uterine cavity. Large submucosal fibroid tumors may increase the size of the uterine cavity and can block the fallopian tubes, which can cause complications with fertility. Some fibroid tumors don't produce any symptoms at all, while others can be severely symptomatic.

Submucous fibroids are usually clearly visible, separate from the endometrium at transvaginal ultrasound, but can be difficult to differentiate from polyps. Sonohysterography is a technique in which sterile saline is instilled into the uterine cavity via a transcervical catheter while performing an ultrasound scan. This method allows better visualization of the endometrium and has been shown to be more accurate than traditional TV USG in detecting submucous fibroids and in differentiating them from polyps. The likelihood of polyps seems to be greater when there is a combination of an intact endometrial-myometrial interface, a single vessel, an acute angle, and homogeneous echogenicity [13].

The classification of submucosal myomas can be useful when considering therapeutic options or surgical approaches. The most widely used system categorizes the leiomyomas into three subtypes, according to the proportion of the lesion's diameter that is within the myometrium, usually as determined by saline infusion sonography or hysteroscopy [14]. The FIGO (International Federation of Gynecology and Obstetrics) system for classification of causes of abnormal uterine bleeding in reproduction-age women uses the same system for categorization of submucous leiomyomas, but adds a number of other categories, including type-3 lesions that abut the endometrium without distorting the endometrial cavity [15]. In addition, this system allows categorizing the relationship of the leiomyoma outer boundary with the uterine serosa, a relationship that is important when evaluating women for resectoscopic surgery. Thus, a European Society

of Gynecological Endoscopy (ESGE) type-2 leiomyoma that reaches the serosa is considered to be a type-2-5 lesion and therefore is not a candidate for surgery [16] (Figs. 6.1, 6.2, 6.3, 6.4, 6.5, 6.6, 6.7, 6.8, 6.9, 6.10, 6.11, 6.12, 6.13, 6.14, 6.15, 6.16, and 6.18).

The ESGE and the expanded FIGO classification systems are relatively simple and provide a framework for both research and clinical medicine, leaving investigators and clinicians to add, as deemed appropriate, other variables such as size, number, and location of the leiomyomas in the uterine wall. Many of these limitations have been incorporated into another classification system that has been designed to take into account four criteria:

- Myometrium invasion (same as the ESGE/FIGO system for submucous lesions) – proportion of the local endometrial surface area occupied by the base of the myoma
- The largest diameter of the myomas
- Location (Table 6.1) [17].

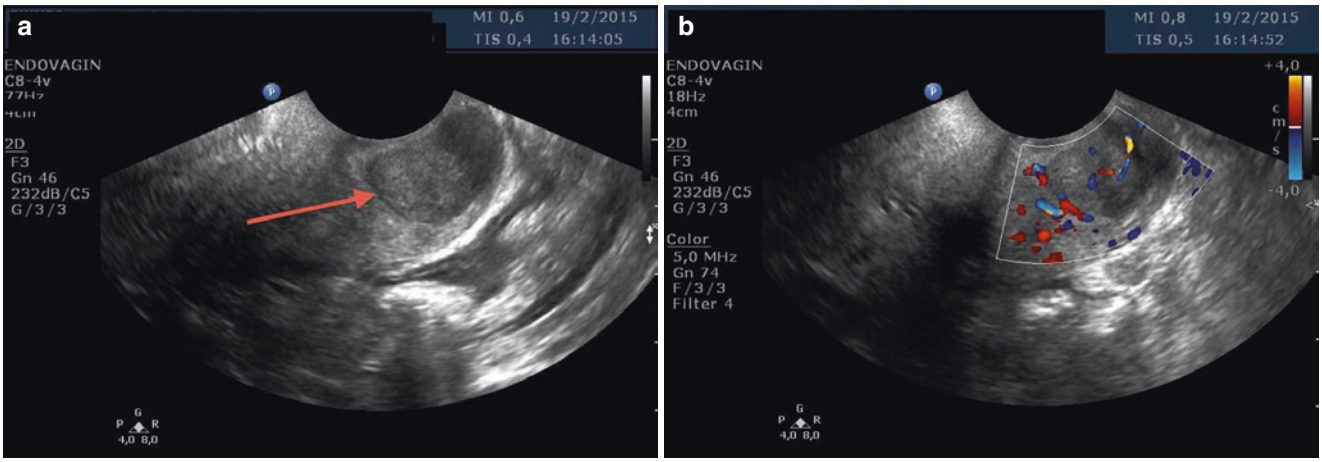

Fig. 6.1 (**a**) Longitudinal section, showing hypoechoic and intramural myoma in the posterior region of the cervix (*red arrow*), compressing the cervical canal. (**b**) Color Doppler showing central and peripheral vasculature in the myoma

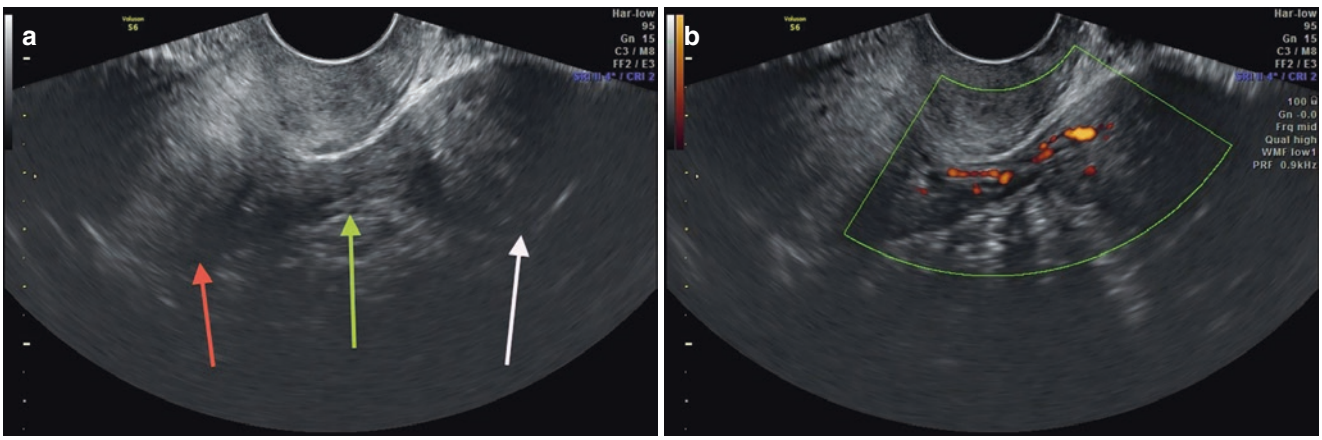

Fig. 6.2 (**a**) Axial ultrasound section, showing uterine body (*red arrow*), pedicle myoma in the left adnexal region (*white arrow*) and its respective pedicle (*green arrow*). (**b**) Power Doppler showing vascularization in vascular pedicle of the myoma

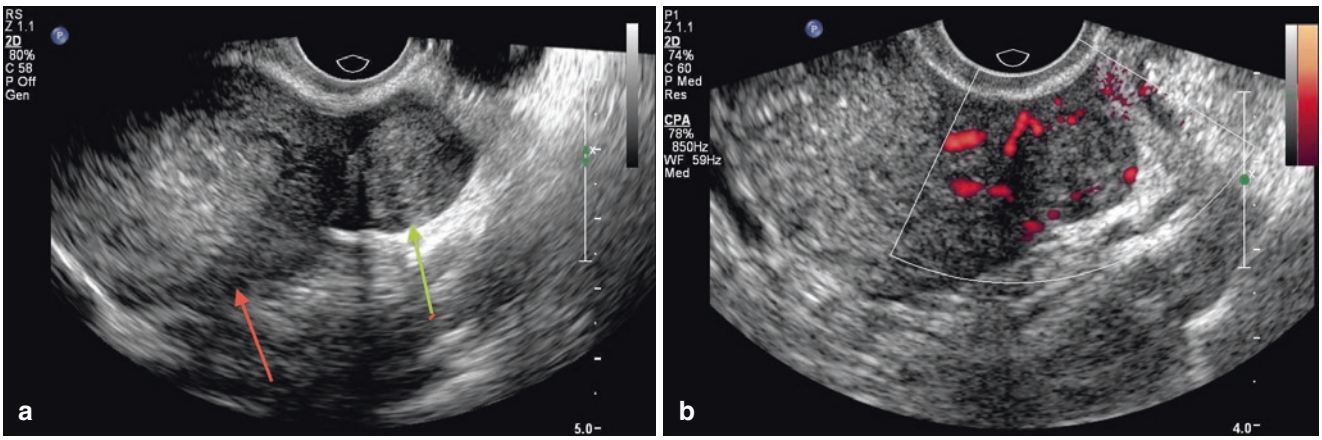

Fig. 6.3 (**a**) Axial ultrasound section of the uterine body (*red arrow*), showing subserosal nodule in the left side wall that compresses the proximal portion of the left uterine tube (*green arrow*). (**b**) Power Doppler showing sparse vascularity within the myoma

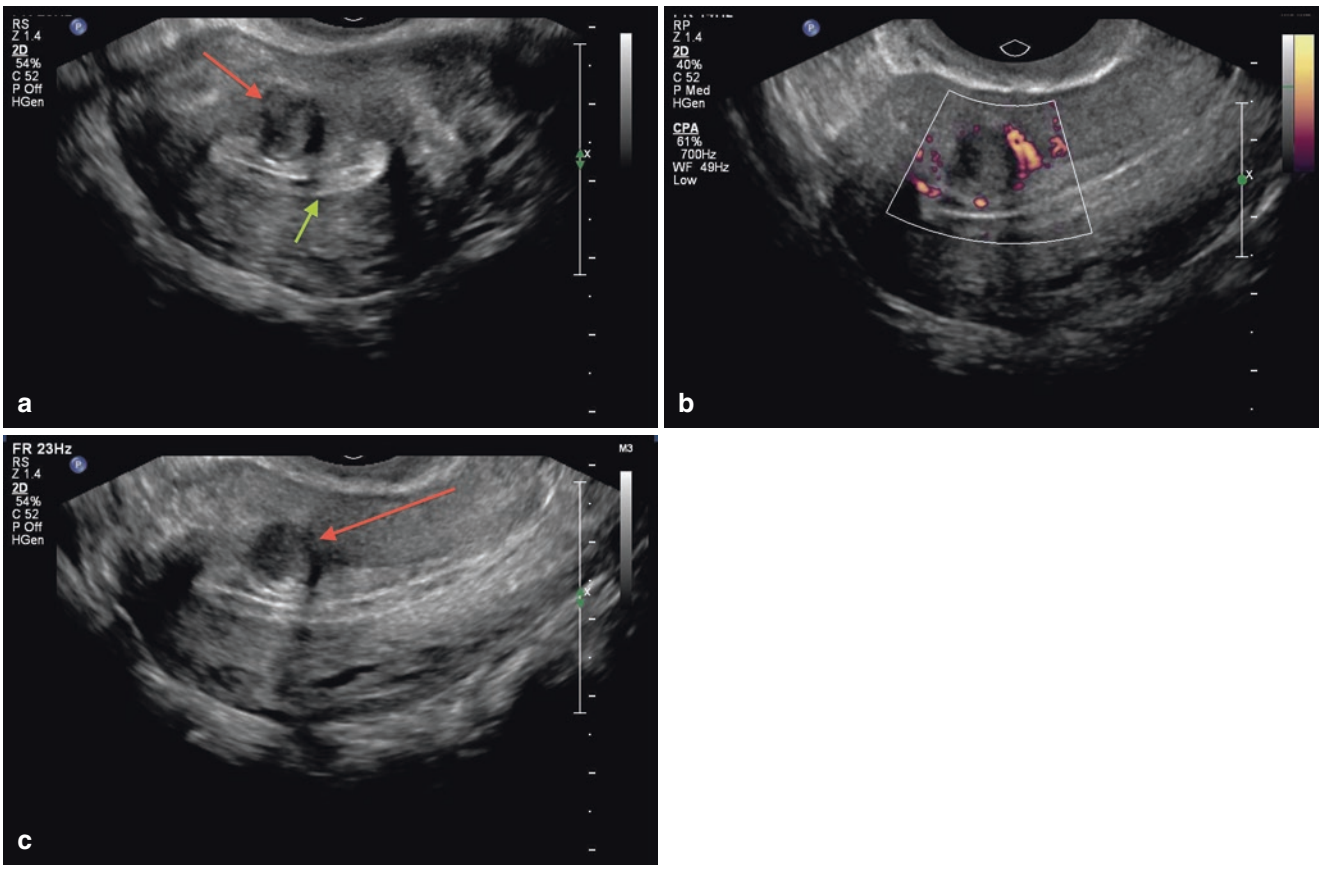

Fig. 6.4 (**a**) Axial ultrasound section of the uterine fibroid, showing myoma (*red arrow*) with submucosal component, less than 50%, and mostly with intramural component. The *green arrow* indicates the endometrial echo. (**b**) Longitudinal ultrasound section of the uterus, showing peripheral vascularization in the myoma, in a study with power Doppler. (**c**) Same myoma (*red arrow*) in longitudinal section, showing greater intramural than submucosal component. Note the narrowing of the anterior portion of the endometrium

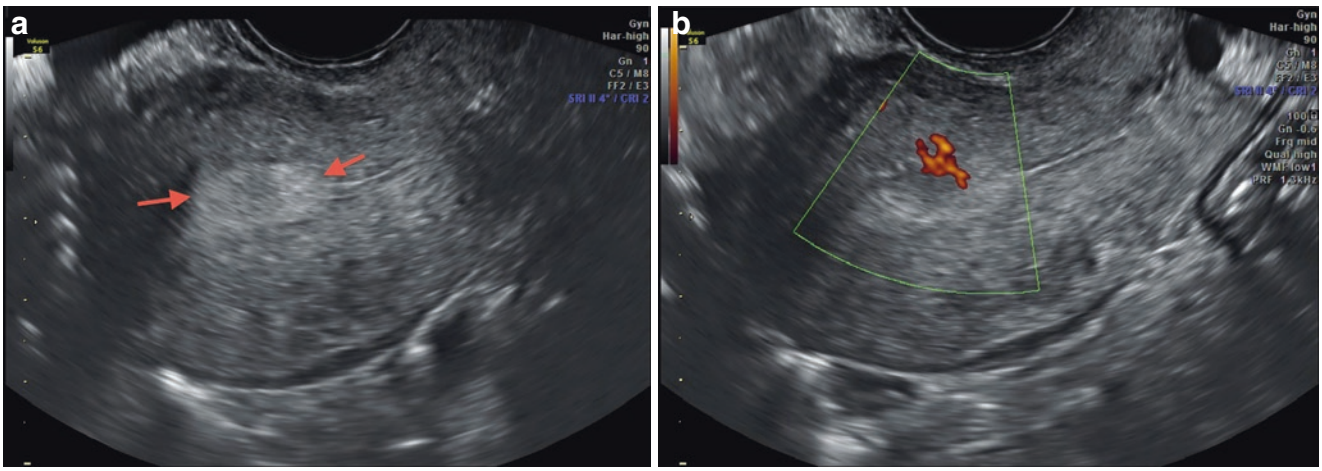

Fig. 6.5 (**a**) Longitudinal ultrasonographic section of the uterus, showing, between the *arrows*, oval and hyperechoic focal thickening of the endometrial echo, compatible with polyp. (**b**) Power Doppler demonstrating vascular pedicle in the polyp

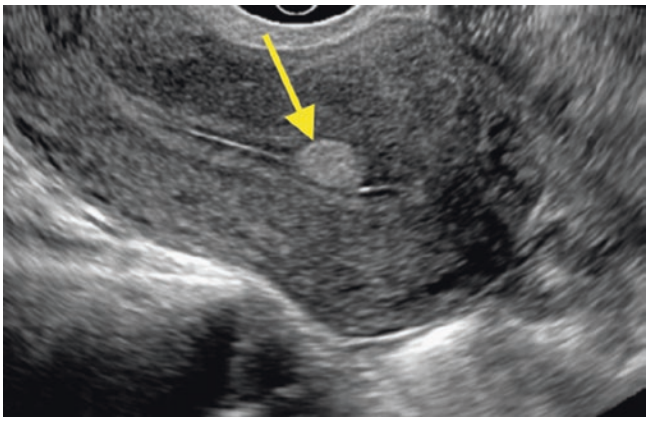

Fig. 6.6 Longitudinal section of retroverted uterus. The *yellow arrow* shows oval and hyperechoic image, in endometrial echo, compatible with polyp. Notice the previous endometrial bulging

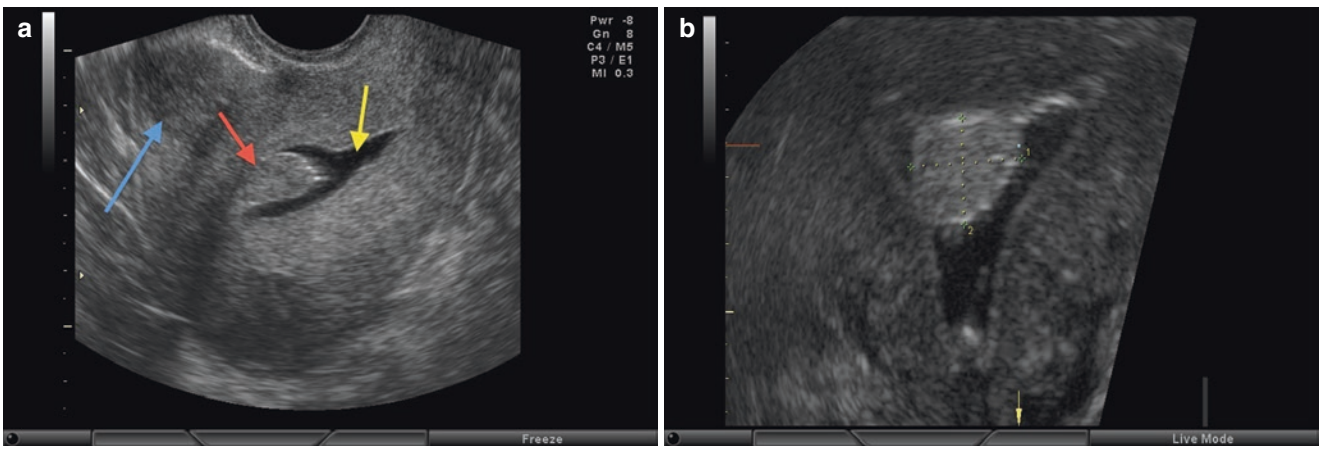

Fig. 6.7 (**a**) Hysterosonography: Longitudinal ultrasound section of the uterus. The *blue arrow* shows a previous subserosal myoma. The *yellow arrow* shows anechoic fluid in the endometrial cavity (saline solution infused) that works as a contrast, allowing better identification of the endometrial polyp (*red arrow*). Notice the clear delineation between the endometrium and myometrium. (**b**) Same hysterosonography, showing the polyp in coronal section, in 3-D ultrasound, with measures between the calipers

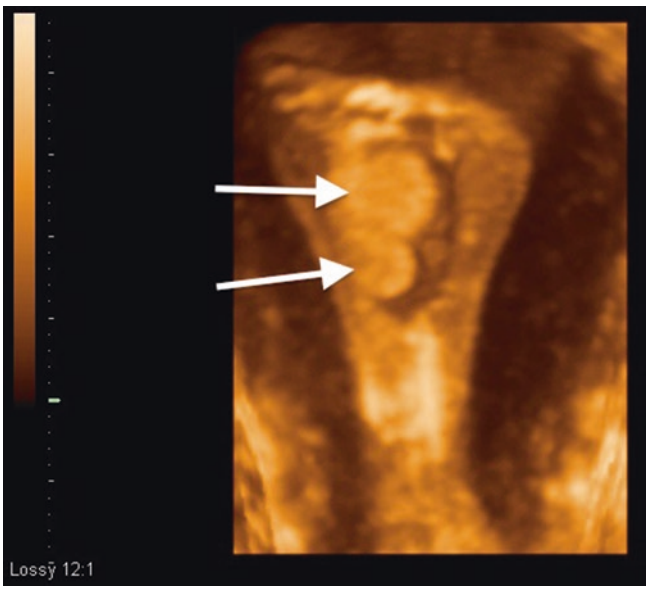

Fig. 6.8 Coronal section, in 3-D ultrasound. The picture shows the endometrial cavity, with a small amount of liquid. The *white arrows* show two adjacent nodes, compatible with polyps. The good delimitation between the endometrium and the myometrium is evident

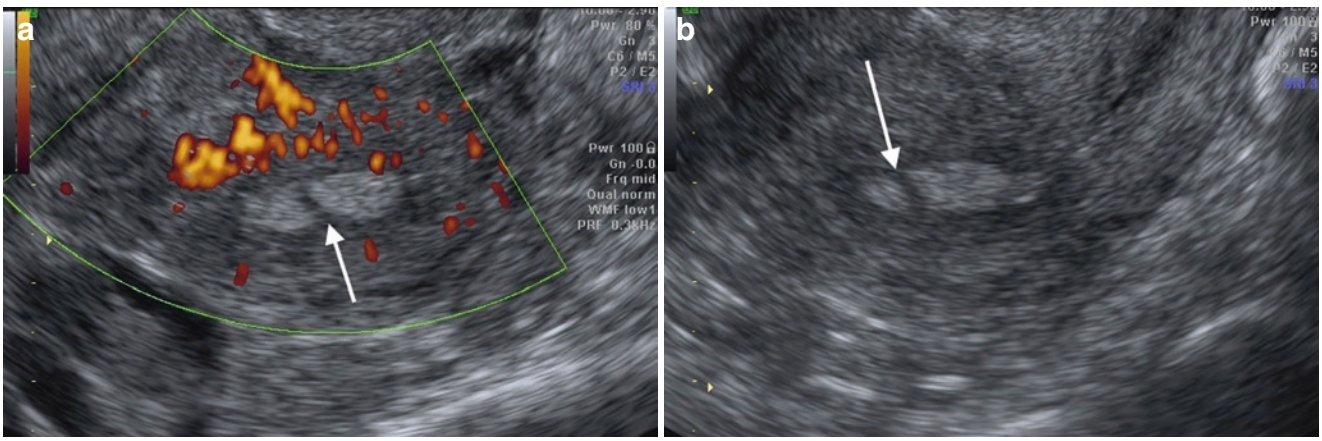

Fig. 6.9 (**a**, **b**) Asherman's Syndrome (also known as "uterine synechiae") is a condition characterized by the presence of scarring or fibrosis within the uterine cavity. In general, uterine synechiae are caused by damage to the lining of the uterus, such as curettage after abortion (most common), endometritis, intrauterine surgery, and radiotherapy; these can cause infertility, recurrent miscarriages, and menstrual disorders. The prognosis for success in pregnancy after the removal of uterine adhesions is associated with the type and severity of synechiae. Endometrial synechiae have excellent prognoses. On the other hand, the fibrous synechiae can only be undone with resection or laser, and have a high rate of recurrence after resection, making the prognosis of pregnancy much worse. The *white arrows* show the presence of thin, hypoechoic tissue "dividing" the endometrial echo (synechiae) in a 32-year-old patient with difficulty getting pregnant after curettage

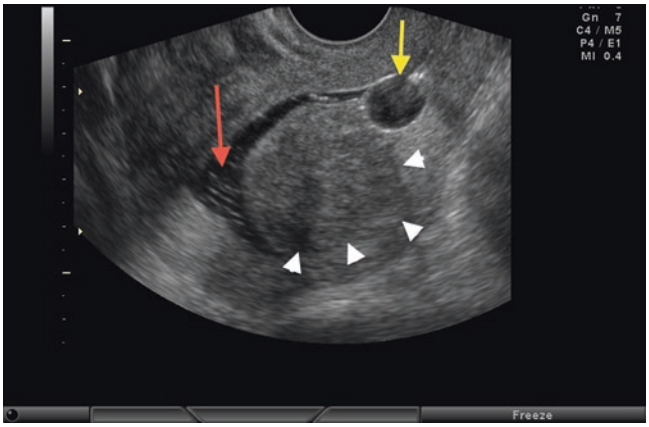

Fig. 6.10 Hysterosonography, showing longitudinal section of the uterus. The *yellow arrow* indicates the catheter balloon used. The *red arrow* shows liquid infused into the endometrial cavity. The *heads of white arrows* show a large submucosal nodule (myoma). Note that – unlike the polyps – the endometrial interface with the myometrium is poorly defined due to the presence of the nodule

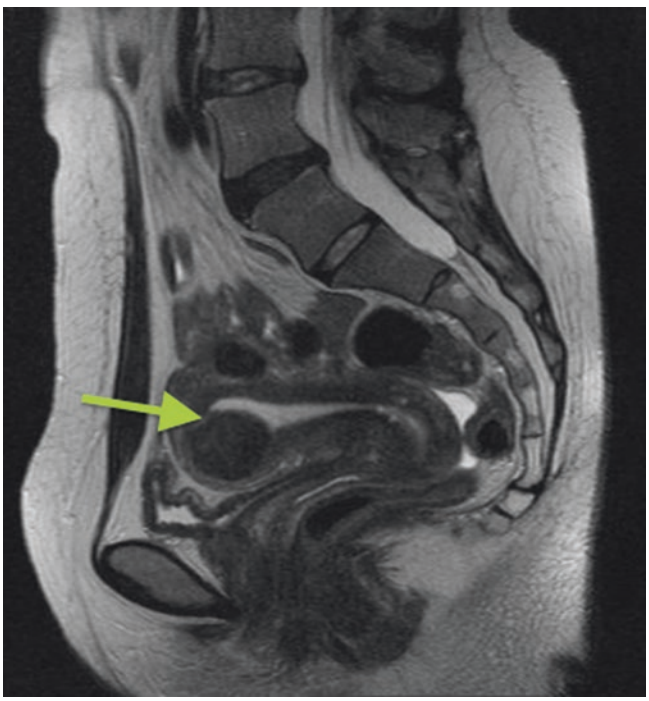

Fig. 6.11 MRI of the pelvis, sagittal, T2 weighted, showing uterine nodule with hyposignal (*arrow*), presenting intramural and submucosal component

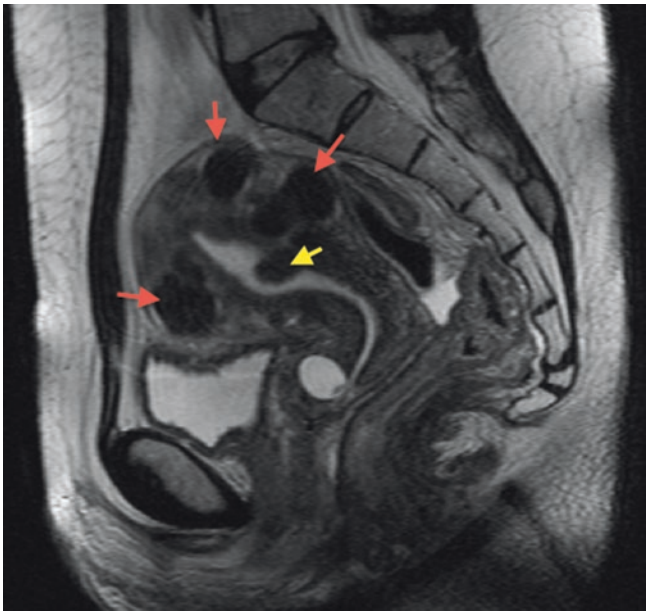

Fig. 6.12 MRI of the pelvis, sagittal, T2 weighted, showing various uterine nodules with hyposignal, which are subserosal and intramural, and one is submucosal

Fig. 6.13 MRI of the pelvis, sagittal, T2 weighted, showing uterine nodule with hyposignal (*arrow*) with intramural and submucosal component; however, it is more heterogeneous than in the previous examples due to small areas of cystic degeneration. The higher the amount of muscle fibers, the more hypointense it is on T2

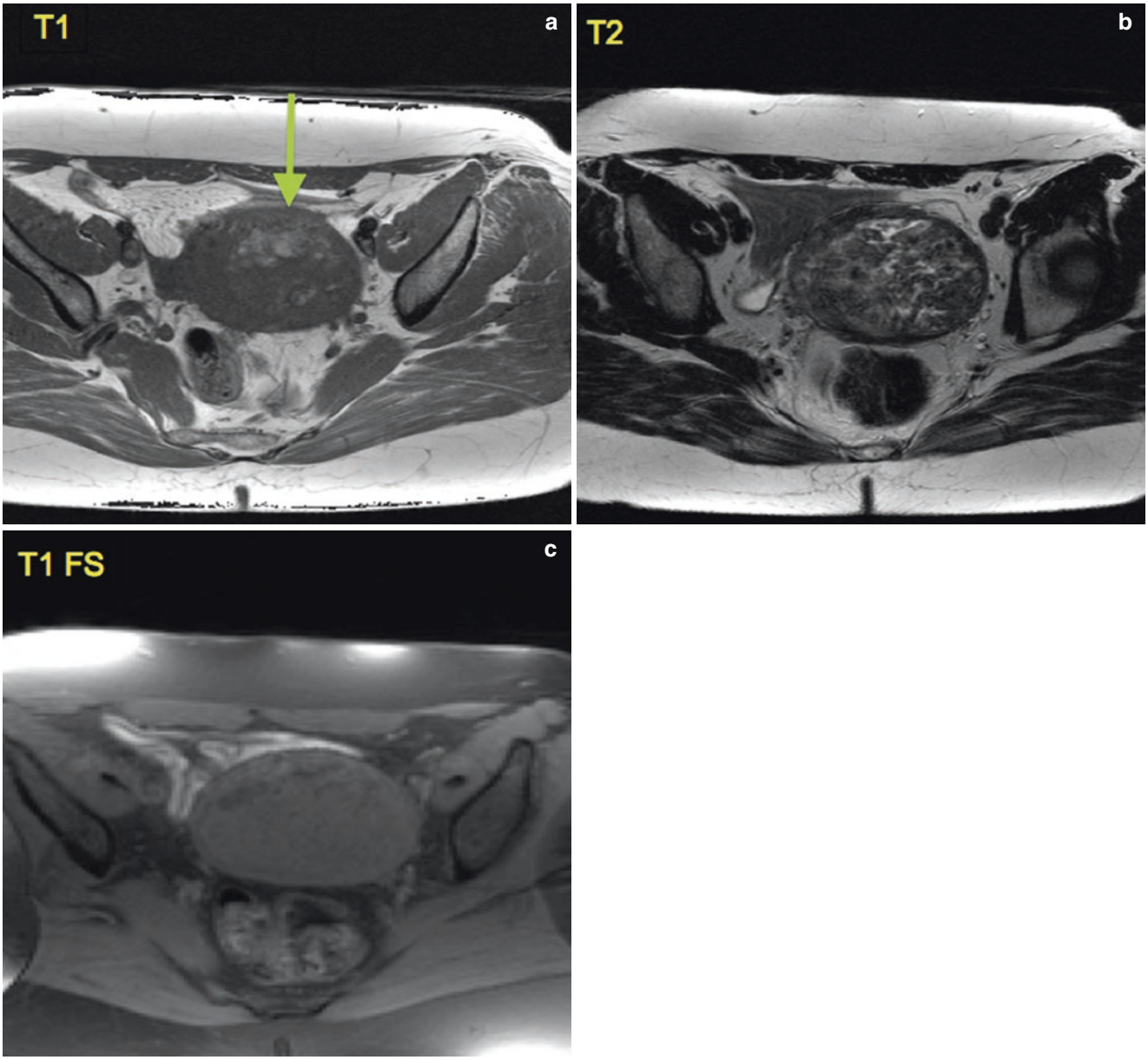

Fig. 6.14 Axial sections of the pelvis MRI, showing a heterogeneous uterine nodule (*arrow*), and with low signal, in images weighted in T1 (**a**), T2 (**b**) and with loss of signal in T1 FS (fat saturation – image (**c**)). This pattern is characteristic of fatty degeneration (lipoleiomyoma)

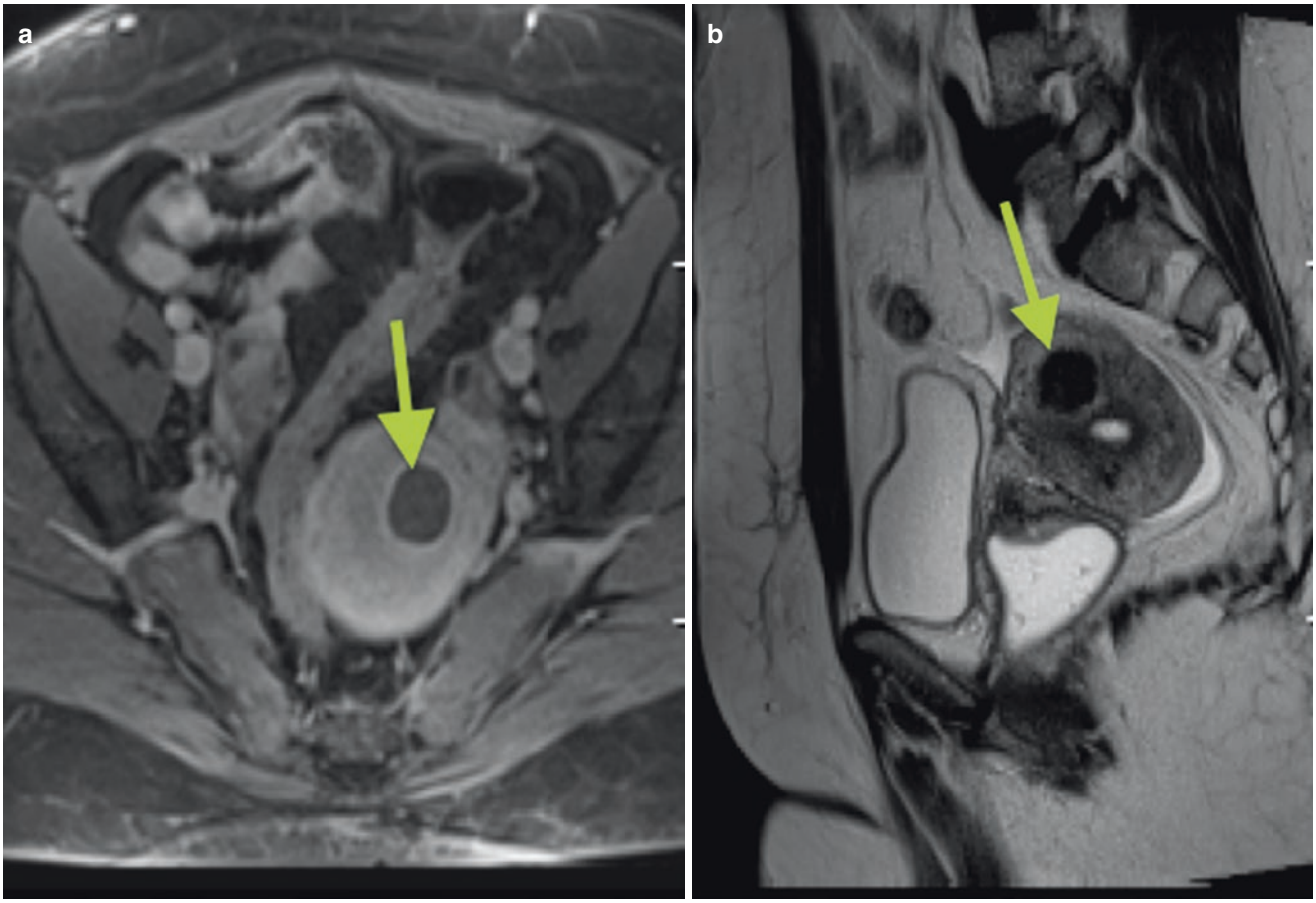

Fig. 6.15 Calcified myoma: (**a**) MRI of the pelvis, axial, T1 weighted, in post-contrast, showing intramural uterine nodule (*arrow*) that is hypointense, with a hyperintense halo around it. (**b**) Same nodule, with sagittal image weighted in T2

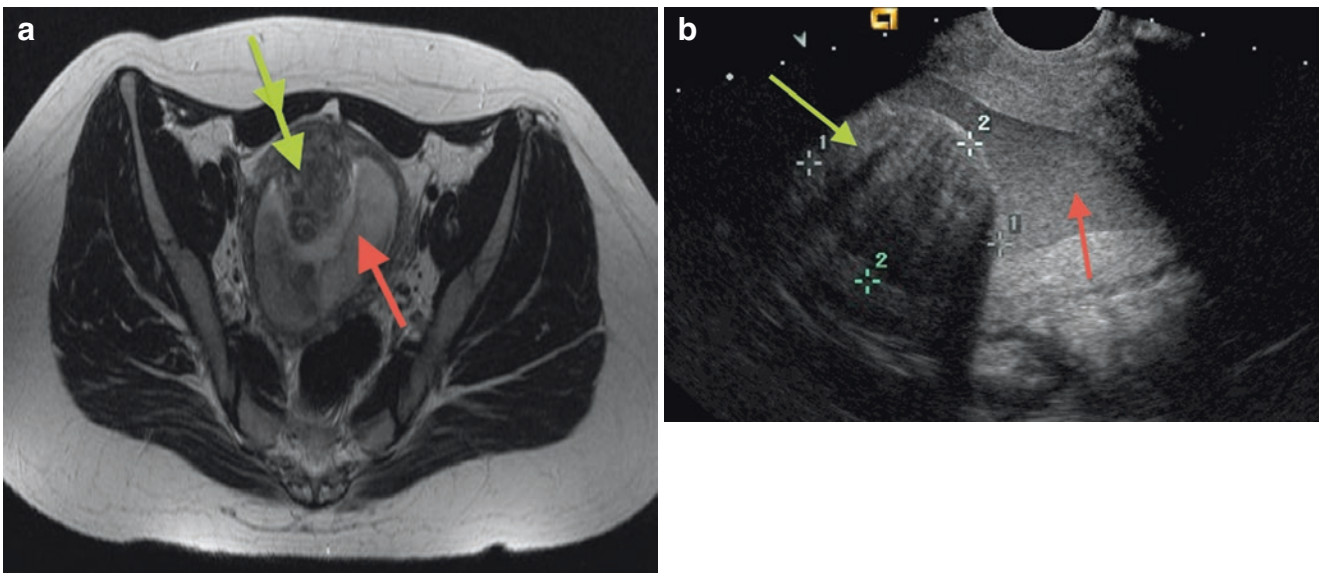

Fig. 6.16 Submucosal and intramural myoma (*green arrows*), and uterine cavity (*red arrow*), filled with thick liquid. In (**a**) MRI of the pelvis, axial section of image weighted in T2, showing heterogeneous uterine nodule, with hyposignal. In (**b**) ultrasound image of the same case

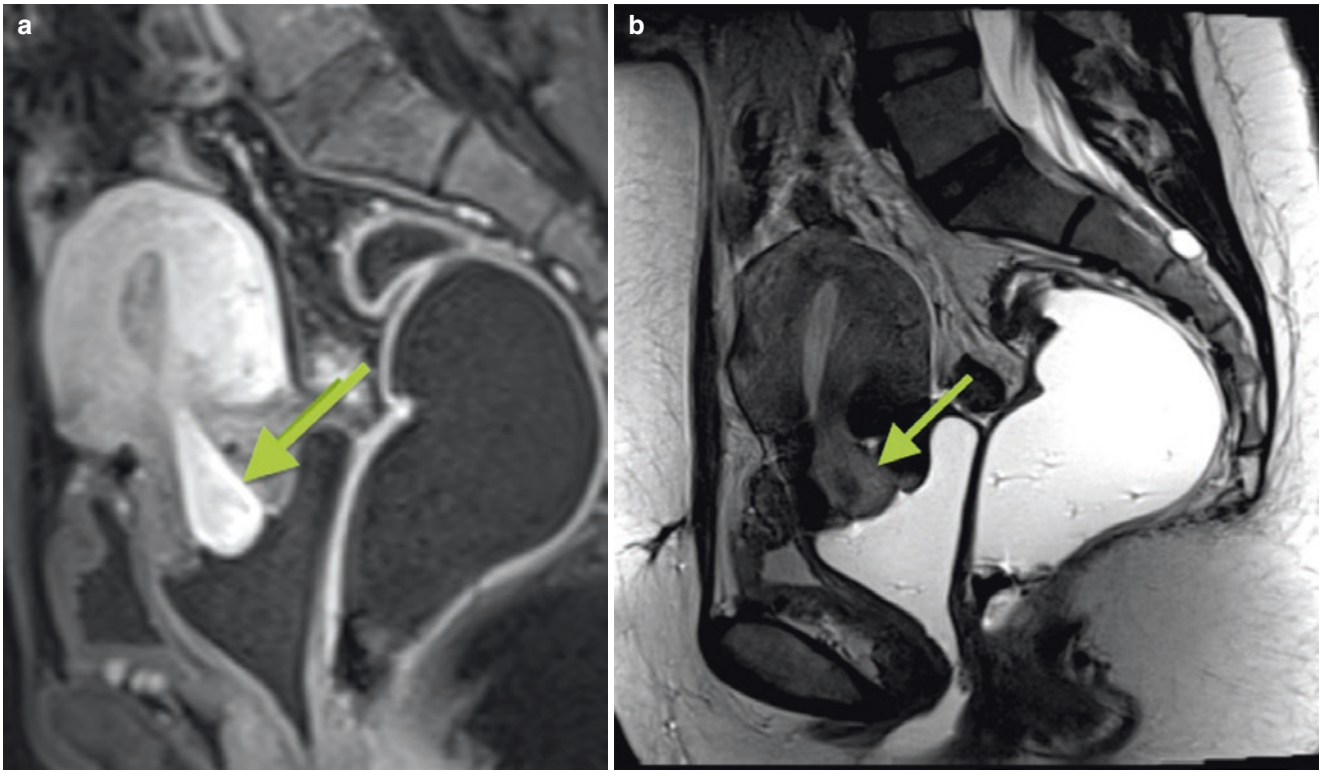

Fig. 6.17 Submucosal myoma. (**a**) Pelvic MRI, weighted in T1 after contrast injection (sagittal section), showing nodule with hypersignal (*arrow*), occupying endocervical canal, and extrauterine portion. (**b**) Same nodule, with image weighted in T2. Note the lump continuity with the myometrium

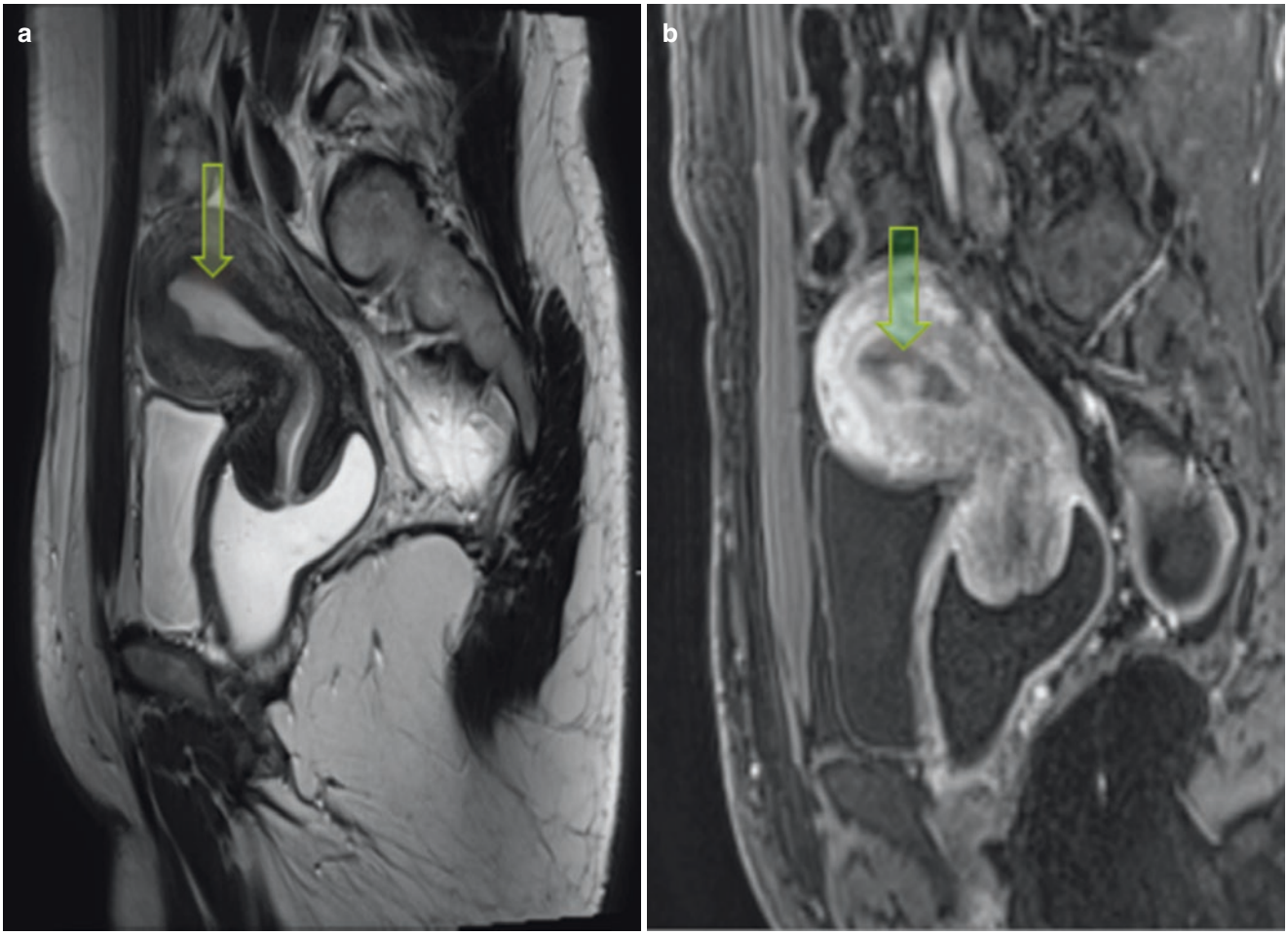

Fig. 6.18 Endometrial polyp. (**a**) MRI of the pelvis, sagittal, T2 weighted. The polyp image is very subtle, appearing as an isointense enhancement (*arrow*) that may have a more heterogeneous center. (**b**) Same polyp, in T1-weighted image

Table 6.1 Presurgical classification of SM myomas

Points	Penetration of myometrium		Largest myoma diameter		Extension of myoma base to endometrial cavity surface		Location along uterine wall (thrid)		Lateral wall (+1)
0	0		<2 cm		<1/3		Lower		
1	<50%		2–5 cm		<1/3 to 2/3		Middle		
2	>50%		>5cm		>2/3		Upper		
Total score	_____	+	_____	+	_____	+	_____	+	_____

Modified from Lasmar et al. [17]

References

1. Fibroids in infertility – consensus statement from ACCEPT (Australasian CREI Consensus Expert Panel on Trial evidence). Aust N Z J Obstet Gynaecol.2011;51:289–95.
2. ASRM Practice Committee. Myomas and reproductive function. FertilSteril.2008;90(Suppl 3):125–30.
3. Rein MS, Friedman AJ, Barbieri RL, Pavelka K, Fletcher JA, Morton CC. Cytogenic abnormalities in uterine leiomyomata. Obstet Gynecol. 1991;77:923–6.
4. Buttram Jr VC, Reiter RC. Uterine leiomyomata: etiology, symptomatology, and management. Fertil Steril. 1981;36:433–5.
5. Donnez J, Jadoul P. What are the implications of myomas on fertility? A need for a debate? Hum Reprod. 2002;17:1424–30.
6. Farquhar C. Do uterine fibroids cause infertility and should they be removed to increase fertility? BMJ. 2009;338:b126.
7. Sunkara SK, Khairy M, El-Toukhy T, Khalaf Y, Coomarasamy A. The effect of intramural fibroids without uterine cavity involvement on the outcome of IVF treatment: a systematic review and meta-analysis. Hum Reprod. 2010;25:418–29.
8. Fennessy F, Tempany C. Focused ultrasound ablation of uterine leiomyomas. In: Fielding J, Brown D, Thurmond A, editors. Gynecologic imaging. Philadelphia: W. B. Saunders; 2011. p. 584–9.
9. Fennessy F. MRI of benign female pélvis. 2013;ARRS Categorical Course. www.arrs.org/shopARRS/products/s13p_sample.pdf.
10. Sue W, Sarah S-B. Radiological appearances of uterine fibroids. Indian J Radiol Imaging. 2009;19(3):222–31.
11. Minsart AF, Ntoutoume Sima F, Vandenhoute K, Jani J, Van Pachterbeke C. Does three-dimensional power Doppler ultrasound predict histopathological findings of uterine fibroids? A preliminary study. Ultrasound Obstet Gynecol. 2012;40(6):714–20.
12. Callen PW, editor. Ultrasonography in obstetrics and gynecology. 5th ed. Philadelphia: Saunders Elsevier; 2007.
13. Bhaduri M, et al. Sonohysterography for discriminating polyps from fibroids. J Ultrasound Med. 2014;33:149–54.
14. WamstekerK,EmanuelMH, deKruifJH. Transcervical hysteroscopic resection of submucous fibroids for abnormal uterine bleeding: results regarding the degree of intramural extension. Obstet Gynecol. 1993; 82:736–40 (II-2).
15. MunroMG, CritchleyHO, BroderMS, Fraser IS. The FIGO Classification System ("PALM-COEIN") for causes of abnormal uterine bleeding in non-gravid women in the reproductive years, including guidelines for clinical investigation. Int J Gynaecol Obstet. 2011;113:3–13 (N/A).
16. American Association of Gynecologic Laparoscopists (AAGL): Advancing Minimally Invasive Gynecology Worldwide. AAGLpractice report: practice guidelines for the diagnosis and management of submucous leiomyomas. *J Minim* Invasive Gynecol. 2012;19(2):152–71.
17. LasmarRB, BarrozoPR, DiasR, OliveiraMA. Submucous myomas: a new presurgical classification to evaluate the viability of hysteroscopic surgical treatment–preliminary report. J Minim Invasive Gynecol. 2005;12:308–11 (II-2).

Adenomyosis

7

Ana Luisa Alencar De Nicola and Luis Ronan Marquez Ferreira de Souza

Definition and Clinical Findings

Adenomyosis is defined as a benign invasion from the endometrium into the myometrium, producing a diffuse increase in the uterus, showing under a microscope non-neoplastic endometrial glands and stroma surrounded by hypertrophic and hyperplastic myometrium [1]. Siegler and Camilien [2] define adenomyosis as the presence of endometrial and corium glandular cells on more than 2.5 mm from the *endometrium-myometrium interface*.

Adenomyosis affects women over age 30, predominantly from 40-50. It usually manifests clinically with dysmenorrhea, dyspareunia, and menometrorrhagia, which are non-specific symptoms that are also common in other pelvic conditions, such as myoma, endometriosis, endometrial polyps, and dysfunctional uterine bleeding [3, 4]. The physical examination only shows positive findings when there is already an increase in uterine volume [3, 4].

The prevalence of adenomyosis, according to a hysterectomy series published in the literature, varies from 5% to 70% [5]. This great variation occurs to a large extent because there is no correlation between the histological parameters used by pathologists for this diagnosis [5]. In the same uterus, incidence varied between 31% and 62%, depending on the number of biopsies that were performed [1]. The risk factors for adenomyosis are a) previous hysteroscopic surgery, and b) multiparity [6].

For many years, the diagnosis of adenomyosis was found only in the hysterectomy after surgery, usually in patients in their 30s and 40s who were symptomatic and most of the time with constituted offspring [7]. The introduction of imaging methods in the study of the pelvis allows an earlier diagnosis of adenomyosis, with excellent accuracy, and has brought with it the prospect of evaluating its impact on clinical symptoms, including infertility [8].

The relationship between adenomyosis and infertility has been much researched nowadays, due to frequent findings of adenomyosis in younger patients, and is often associated with endometriosis and infertility [8, 9]. More recent studies have shown concordance between adenomyosis and endometriosis, from 27% and even up to 70% of the cases [8, 10]. Changes in uterine peristalsis are considered one of the hypotheses of the pathophysiology of adenomyosis, and can also be one of the causes of infertility, due to irregular transport of gametes [9].

Classification

From the pathological point of view, adenomyosis can be classified as superficial (when it reaches the inner third of the myometrium), or deep (when it reaches the two outermost thirds of the myometrium) [11]. It is classified as diffuse if it affects all the walls of the uterus, and focal when it only affects a wall. For the diffuse one, the differential diagnosis is done with uterine myomatosis, and the focal form (adenomyomas) with the myomas.

The association between adenomyosis and other uterine disease is quite common. In a study, the association with other pelvic abnormalities was present in 82.5% of the cases [12]. In another publication, concomitance with uterine fibroids was seen in 38.5%, and with endometrial hyperplasia in 30.8% of the cases that were studied [13].

Image Findings

Pelvic imaging methods used for diagnosis are both transvaginal ultrasonography and magnetic resonance imaging. Both methods are dependent on the examiners, and MR

A.L.A. De Nicola
Department of Gynecology Endoscopy, Santa Casa Medical School, São Paulo, SP, Brazil
e-mail: analui.nicola@terra.com

L.R.M.F. de Souza (✉)
Associate Professor of Radiology, Universidade Federal do Triangulo Mineiro, Uberaba, MG, Brazil
e-mail: radiologia.abdome@gmail.com

L.R.M.F. de Souza et al. (eds.), *Atlas of Imaging in Infertility*, DOI 10.1007/978-3-319-13893-0_7

today is considered the method of choice in cases of clinical suspicion [3, 14, 15]. It has a sensitivity of 70–86% and a specificity of 86–93% [3].

For the diagnosis of adenomyosis on ultrasound, it is very important that the examiner pay attention to clinical information. A brief anamnesis, therefore, should always be performed. Transvaginal ultrasound, when performed by an experienced examiner, can have great diagnostic accuracy with sensitivity rates of 65 % and specificity of 97.5% [3]. In a group of patients with endometrial menometrorrhagia, without endometrial changes or myomas, the rates obtained were 80.9% of sensitivity, 100% of specificity, and 82.6% of accuracy [3]. While in a group of unselected patients who would undergo hysterectomies, the sensitivity of ultrasound was only 38.4% [12].

Various image signals associated with adenomyosis are described in the literature, and it is common to find several of them concurrently. The most important are:

Indistinct Endometrial-myometrial Junction

The loss of definition in the endometrial-myometrial transition is the characteristic sign of adenomyosis [5] (Fig. 7.1). Whether in focal areas or in a diffuse way, the presence of this uncertainty is an important parameter for the diagnosis (Figs. 7.2 and 7.3). The precise classification of the endometrium can be difficult in these situations, sometimes simulating endometrial thickening [1] (Figs. 7.4 and 7.5). MRI can confirm the diagnosis [3] (Fig. 7.6 a, b).

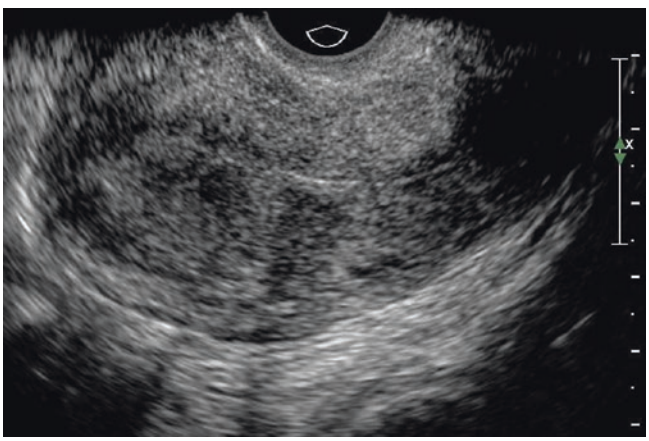

Fig. 7.1 Transvaginal sagittal image of the uterus shows heterogeneous echotexture in which the border from the endometrium is diffusedly blurred with respect to the myometrium

Fig. 7.2 Transvaginal sagittal image of the uterus shows heterogeneous echotexture in focal area at anterior wall where the edge of the endometrium is difficult to distinguish sonographically from the adjacent myometrium

Fig. 7.3 Transvaginal sagittal image of the uterus shows heterogeneous echotexture with poor definition of endometrium myometrial junction diffusedly

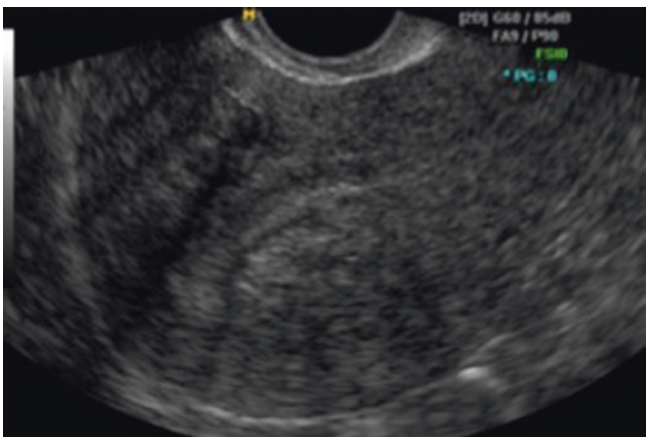

Fig. 7.4 Transvaginal sagittal image of the uterus shows heterogeneous myometrium appearance, especially on the posterior wall where hyperechoic areas with cysts mimic endometrial thickening

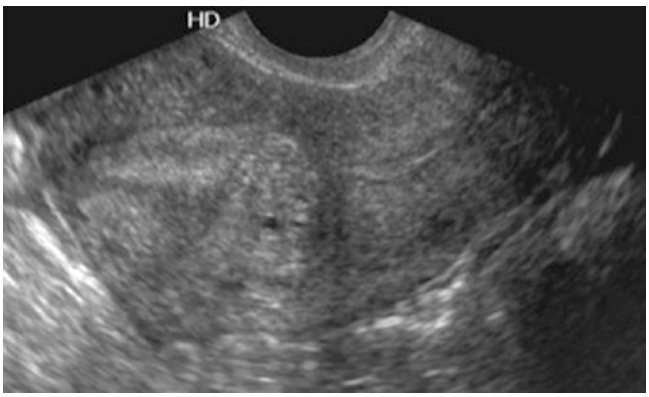

Fig. 7.5 Transvaginal sagittal image of the uterus shows heterogeneous myometrium appearance in focal area at posterior wall where hyperechoic areas with cysts mimic endometrial focal thickening

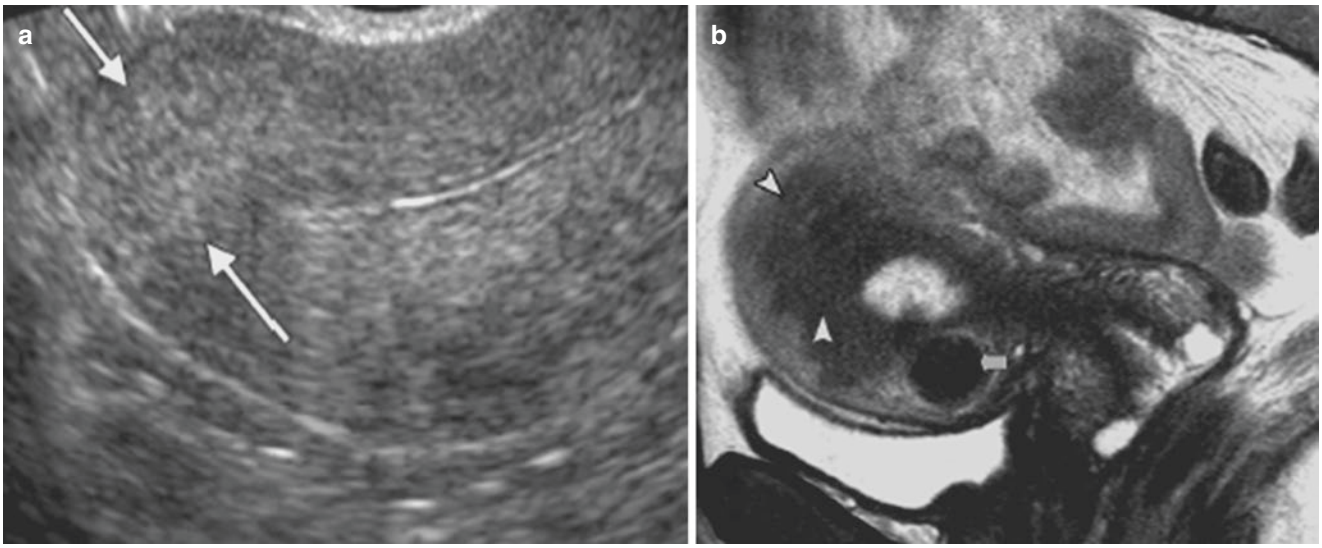

Fig. 7.6 (**a**) Transvaginal ultrasonography. In the fundus, an area of focal heterogeneity can be seen, without significant volume or morphology changes. (**b**) Sagittal, TSE, T2 weighting. The area identified in the fundus corresponds to a focal thickening of the junctional zone (*arrowheads*). There is also a uterine myoma (*arrow*) that was also identified in the US

Increase in Uterine Volume

Adenomyosis is a common cause of increased uterine volume [16]. Usually, the body is enlarged and presents a rounded shape – that is, it acquires a globular aspect [3] (Figs. 7.7, 7.8 and 7.9). This aspect, in the absence of focal lesions, is closely associated with adenomyosis, and for some authors it is considered a parameter with high sensitivity indexes for the diagnosis [13, 14].

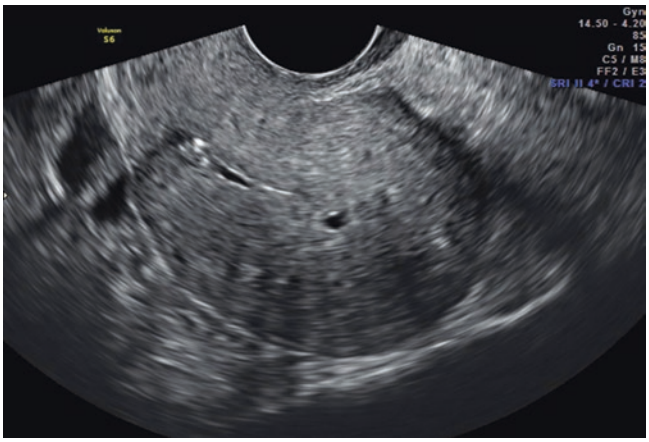

Fig. 7.7 Transvaginal sagittal image shows a globular-appearing uterus, mottled heterogeneous texture, and small cystic area

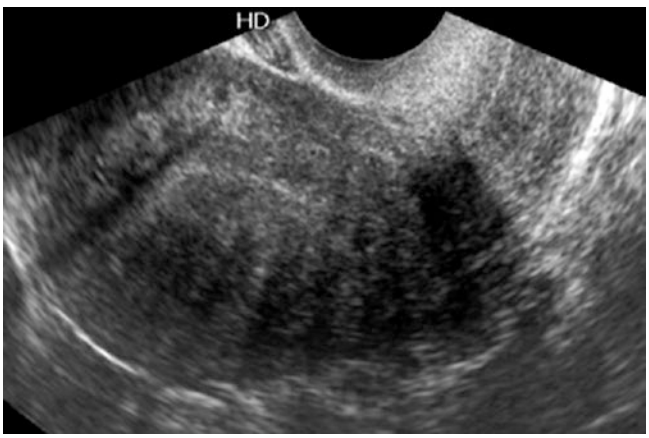

Fig. 7.8 Transvaginal sagittal image shows a globular-appearing uterus. The shape of the uterine fundus was rounded and more spherical in configuration without focal lesions

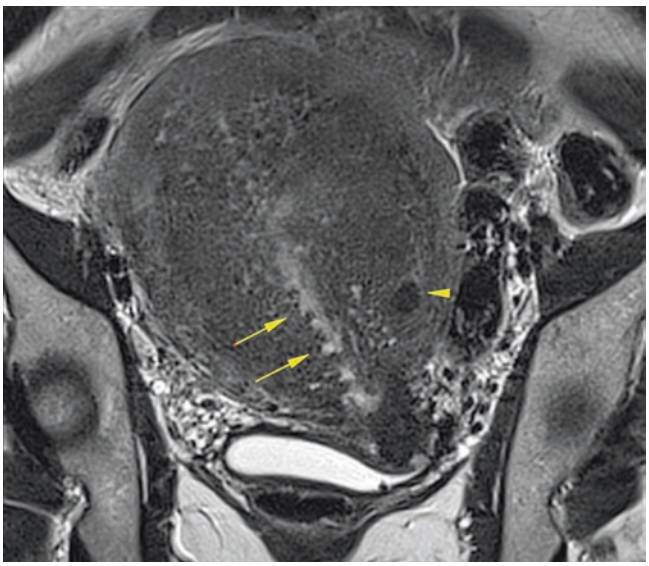

Fig. 7.9 Coronal oblique, TSE, T2 weighting. Apart from the thickening and heterogeneity of the myometrium, endometrial striations, which are adenomyosis characteristics, can also be identified (*arrows*). A small myoma (*arrowhead*) and volumetric increase can be identified as well

Asymmetrical Thickening of the Uterine Walls

Disproportion between the thickness of the uterine walls (anterior and posterior), is usually associated with adenomyosis [11] (Figs. 7.10, 7.11, 7.12, and 7.13). For some authors, this signal can increase the method specificity [12].

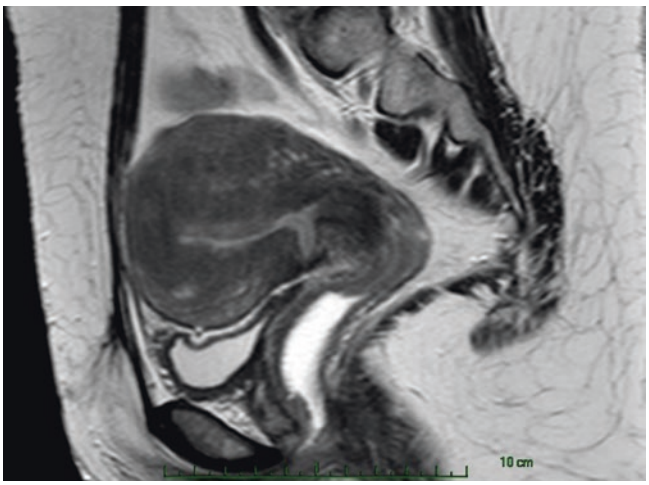

Fig. 7.10 Sagittal, TSE, T2 weighting. In this case, a diffusely low myometrium signal can be observed, secondary to the *thickening of the junctional zone with uterine volume increase and "globular" morphology*, secondary to the asymmetry of the body walls promoted by a reactional hypertrophy of the myometrium

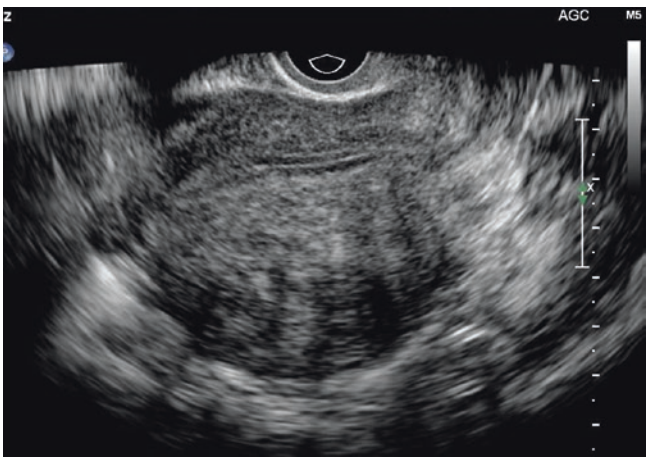

Fig. 7.11 Transvaginal sagittal image shows a globular asymmetric uterus (the posterior wall is enlarged with respect to anterior) and heterogeneous myometrium without leiomyomas

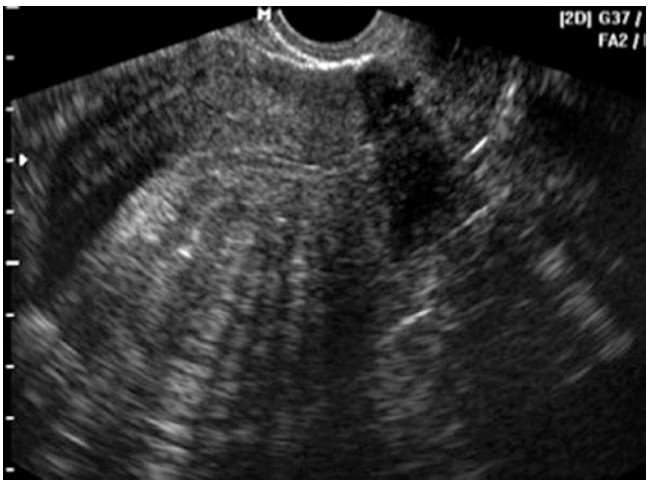

Fig. 7.12 Transvaginal sagittal image shows a globular asymmetric, enlarged uterus with the posterior wall enlarged with respect to the anterior, heterogeneous myometrium, and poor definition of endometrium-myometrial junction

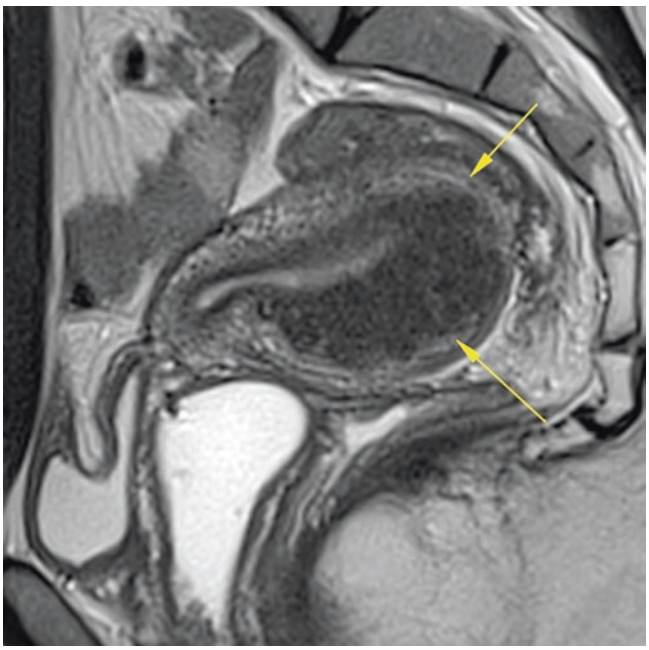

Fig. 7.13 Sagittal, TSE, T2 weighting. This figure also shows the engagement of the rear body wall by focal adenomyosis (*arrows*), *with thickening of the junctional zone and asymmetry of the body walls*

Heterogeneous Appearance of the Myometrium

One of the most frequent signs of adenomyosis is the heterogeneous appearance of the myometrium, usually characterized by predominantly hypoechoic areas that affect normal stratification. It was present in 84% of positive cases in a study of histopathological correlation [6] (Figs. 7.14, 7.15, 7.16, and 7.17). These heterogeneous areas, more hypoechoic, can be focal, with ill-defined margins or compromising the organ diffusely [4] (Figs. 7.18a, b, 7.19, and 7.20). It is very important to identify this textural change because it manifests itself even before the increase in uterine volume.

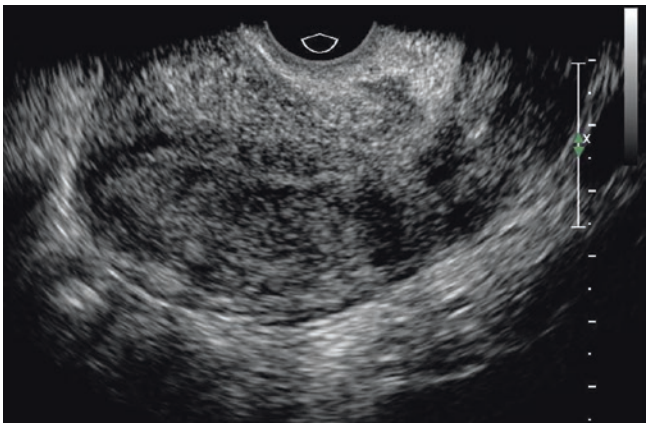

Fig. 7.14 Transvaginal sagittal image shows a uterus with markedly heterogeneous myometrium (indistinctly defined hypoechoic myometrial areas) and poor definition of endometrium myometrial transition diffusedly

Fig. 7.15 Transvaginal sagittal image shows a uterus with markedly heterogeneous myometrium and poor definition of endometrium myometrial transition in focal area of uterine fundus

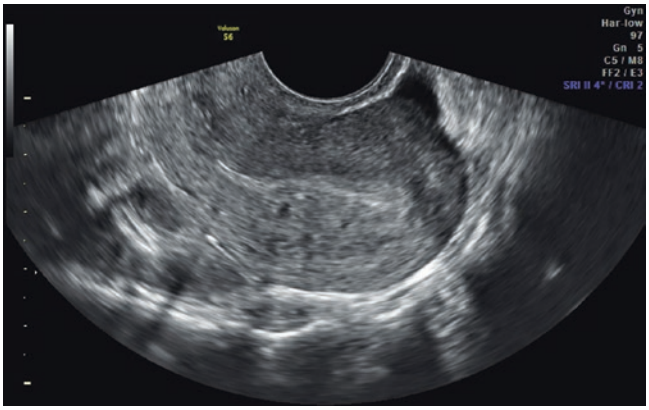

Fig. 7.16 Transvaginal sagittal image shows a uterus with heterogeneous echotexture in focal area at anterior wall. Note the poor definition of the endometrium myometrial junction and the small cystic areas associated

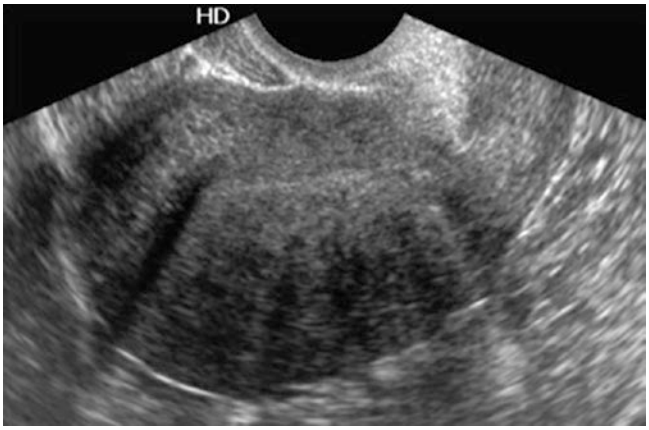

Fig. 7.17 Transvaginal sagittal image shows a uterus with diffused heterogeneous echotexture. Note the hypoechogenicity, global appearance, and poor definition of the associated endometrium myometrial junction

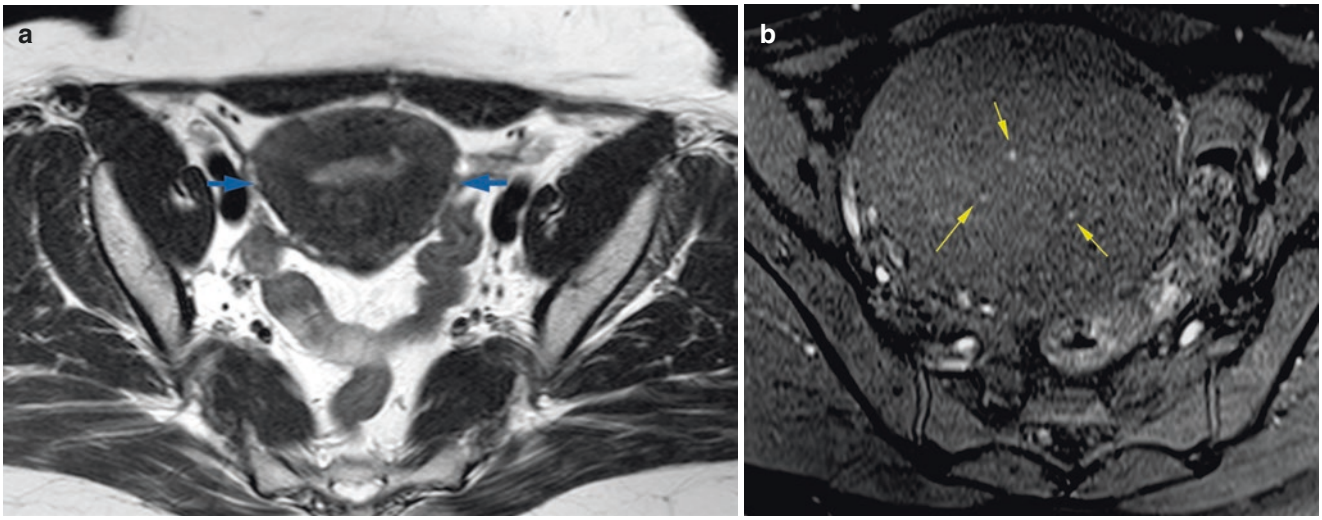

Fig. 7.18 (**a**) Axial, TSE, T2 weighting. *Signal of the myometrium diffusely reduced*, secondary to the adenomyosis (*arrows*), with no significant associated increase in volume, compatible with original shape. (**b**) Axial, SE, T1 weighted, with fat saturation. Note the *hyperintense foci* promoted by hematic content, in the myometrial cysts (*arrows*)

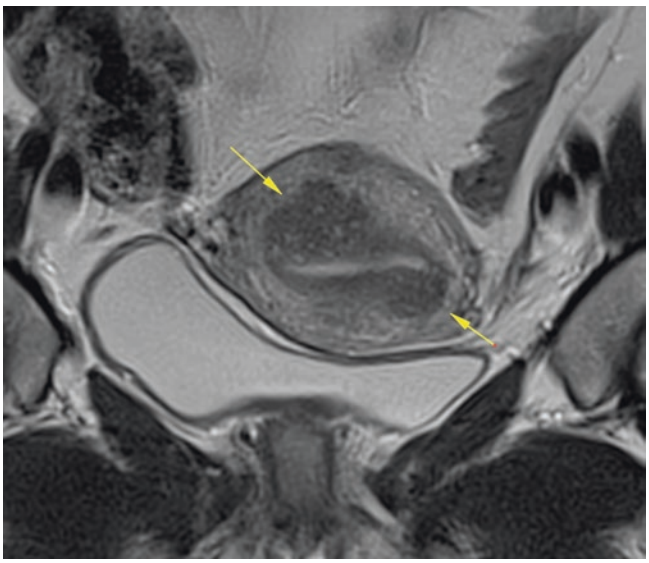

Fig. 7.19 Coronal, TSE, T2 weighting. Note the focal thickening of the junctional zone, compatible with adenomyosis (*arrows*) involving both uterine walls

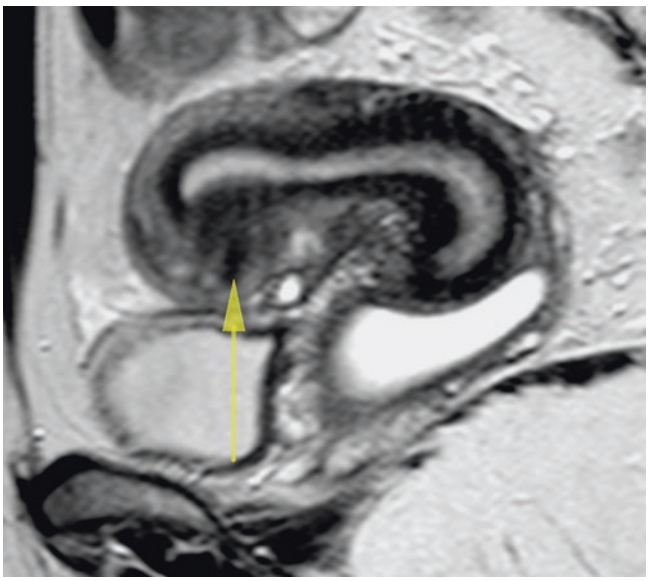

Fig. 7.20 Sagittal, TSE, T2 weighting. In this case, an adenomyosis focus can be observed in the anterior body wall, with *body asymmetry* by the greater volume in the anterior (*arrow*)

Cystic Myometrial Areas

The presence of anechoic areas, initially described as small intramiometrial lakes measuring between 1 and 3 mm, is associated with adenomyosis. When it was present, in the midst of heterogeneous myometrial areas, in patients without myomas or endometrial changes, it showed a diagnostic sensitivity of 81% in a study [17]. Currently called myometrial cysts, they are generally rounded, they are between 1 and 5 mm in size, and they are considered by some authors to be one of the most sensitive signs for the diagnostis of adenomyosis [3]. These cysts probably correspond to expansions of ectopic endometrial glands [13] (Figs. 7.21 and 7.22).

MR shows rounded foci ranging from 2-7 mm in diameter, with an average of 3 mm, surrounded by myometrial tissue. It is considered the main direct signal in the diagnosis of adenomyosis. They can provide high signal on T1-weighted sequences, depending on the phase of the secondary cycle to micro-hemorrhages (Fig. 7.18 a, b).

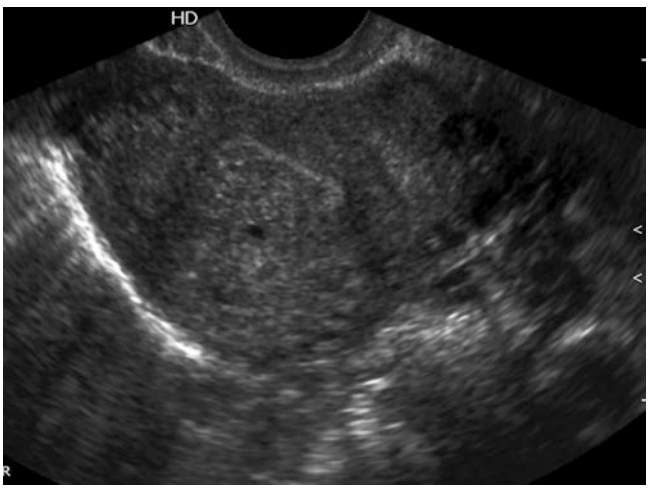

Fig. 7.21 Transvaginal transverse image of the fundus of the uterus shows a mottled heterogeneous appearance with a small cystic area in the posterior wall

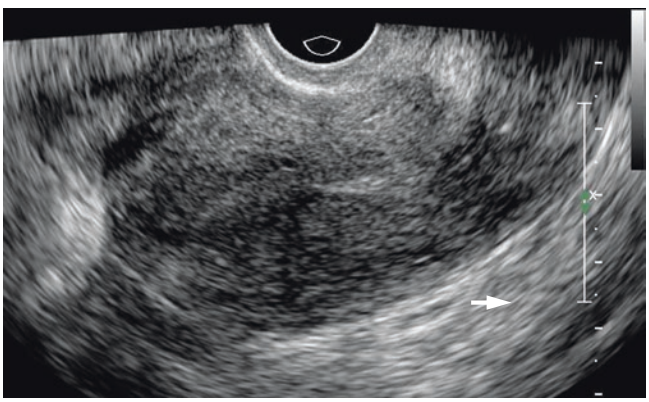

Fig. 7.22 Transvaginal sagittal image of the uterus shows a mottled heterogeneous appearance with small cystic areas in the posterior and anterior wall (*arrow*)

Echogenic Endometrial Striations

In some cases of adenomyosis, sub-endometrial echogenic linear images are formed, such as striations, transversely crossing the myometrium (Figs. 7.23 and 7.24). The finding of these striations or sub-endometrial echogenic nodules and asymmetry in the thickness of the walls showed high specificity for the diagnosis of adenomyosis, when correlated with histopathologic study [12]. Even alone, the sub-endometrial striations were considered, in another study, as the parameter with better specificity indexes, positive predictive value, and the most useful one for the differential diagnosis of adenomyosis and other diseases, especially uterine fibroids [11]. In MR, they have less significance when compared with the thickness of the junctional zone and detecting of myometrial cysts [13] (Fig. 7.9).

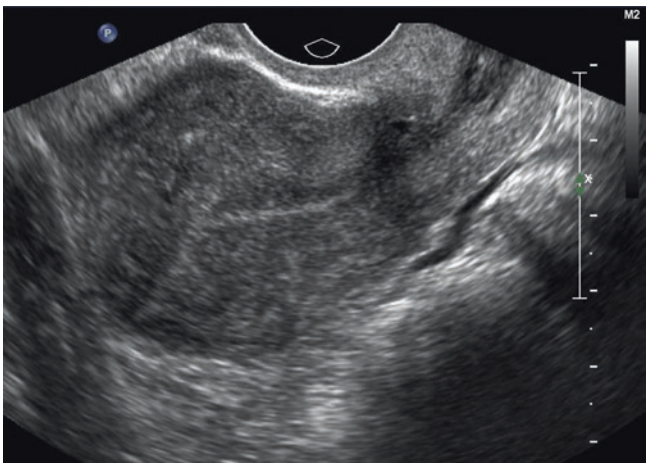

Fig. 7.23 Transvaginal sagittal image of the uterus shows myometrial hyperechoic striations as a radiate pattern of thin hyperechoic line penetrating into the myometrium from the endometrium. The myometrium is heterogeneous with poor definition of the endometrium myometrial junction and small cysts associated

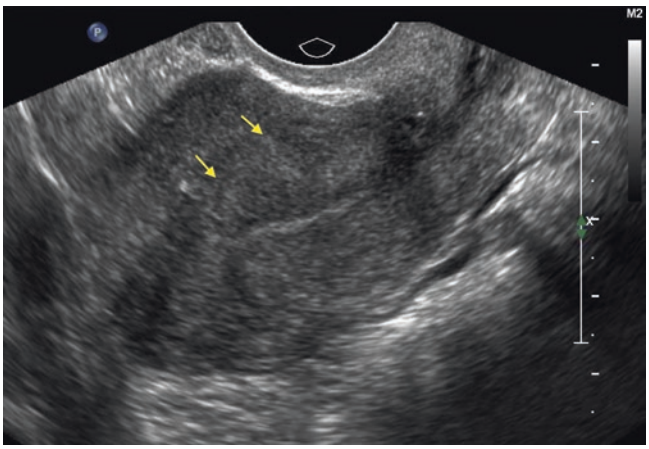

Fig. 7.24 Transvaginal sagittal image of the uterus shows myometrial hyperechoic striations more evident in the posterior wall (*arrows*)

Thickening of the Junctional Zone

A thickness of more than 12 mm is considered to be the most accepted criterion in the diagnosis of adenomyosis by MR, with an accuracy of 85% and specificity of 96%.

Uterine zonal anatomy was originally described by Hricak et al [18] in 1983, evidencing a signal hypointense band with the endometrium, which was called "junctional zone." It presents myocytes with a different morphology than other myometrial portions in its constitution, with a large nuclear area, and little extracellular matrix with a consequent small amount of water, reducing the signal on T2 weighted sequences. The concentric arrangement of myometrial fibers in the inner portion of the myometrium also adds to this (Fig. 7.10).

The junctional zone can vary according to age; it is thin in the pubarche patient, and more difficult to define in elderly patients who are post-menopausal, due to progressive loss of hydration of the outer myometrial layer, hence reducing its signal. It can also vary according to the menstrual cycle, reaching its peak during the menstrual period; some authors indicate performing MR in the ploriferative-secretorial final phase in order to increase sensitivity [18]. Its value, when regarded as normal, is less than 12 mm, with a median between 5 and 8 mm (Fig. 7.19).

Two other parameters are related to the extent of the junctional zone. The first is called *junctional zone differential*, described by Dueholm et al. [19] in 2001. It is calculated by the difference between the maximum and the minimum thickness of the anterior and posterior portions of the uterus. Its validity has yet to be proven, and it is not routinely used in practice. The other signal, known as *ratio of junctional zone thickness* and *miometrial thickness*, has already been rated by Bazot et al. [3], and its accuracy is not statistically better than the simple measurement of 12 mm in the true sagittal cut of sequences weighted in T2 [4, 14].

Additional Magnetic Resonance Imaging Parameters

Contrast Adenomyosis is most often a diffuse disease of the myometrium, it presents enhancement with inespecific patterns. Because of this, contrast use is unnecessary in most cases.

Diffusion Focal malignant lesions typically have low ADC values, and the benign ones tend to have low values. However, high levels of ADC may be found in hemorrhages and necrosis. They can be used as a complementary tool to differentiate sarcomas of degenerated myomas, because myomas with degeneration tend to have a higher ADC, and lower signal than sarcomas. ADC and diffusion parameters with statistical significance for adenomyomas have not yet been found.

Cine-MRI The dynamic images from Cine-MRI allow the differentiation between uterine contraction and focal adenomyosis in most of the cases. However, they are not widely used in clinical practice, because it consumed time and having been sucefully replaced by a another sagital T2 sequence, performed in the end of exam.

Differential Diagnosis

Focal Adenomyosis and Myoma

There are two types of focal adenomyosis: (a) when the disease affects a single uterine wall, or (b) when it has a pseudonodular feature, such as a rounded hypoechoic area, or inaccurate boundaries in relation to the adjacent myometrium, known as "adenomyoma" [20]. The adenomyoma is often confused with fibroids, and both can have the same clinical presentation. Fibroids can be surgically excised (myomectomies), while the definitive surgical treatment for adenomyomas is hysterectomy. This accurate differential diagnosis is very important, especially in patients who want to preserve fertility and will be subject to myomectomies or treatment with GnRH analogues [3].

Adenomyomas usually have ill-defined margins, while myomas are more circumscribed, with better defined edges [21, 22] (Figs. 7.25a–c, 7.26, and 7.27). In the colored Doppler study, myomas often have characteristic peripheral vasculature surrounding their margins, while adenomyomas present vascularization in their center [16] (Figs. 7.28a, b, and 7.29a, b). The presence of cystic gaps is also more frequent in adenomyomas and may eventually be present in myomas with hyaline degeneration [4]. The use of colored Doppler in these cases is essential for the differential diagnosis (Figs. 7.30a, b, and 7.31a, b). Special attention should be given in cases of concurrence between myomas and adenomyomas.

The adenomyoma, as well as the myoma, has low signal intensity on T2; however, the adenomyoma usually has small, hyperintense foci in T2, without large vessels identified on its periphery [23]. The cases of cystic adenomyoma correspond to excessive ectopic endometrial tissue, which produces focal hemorrhage. The lesion usually presents a cystic cavity greater than 1 cm, with signal content compatible with hemorrhagic material in its interior, surrounded by fibrous tissue with low signal intensity on T2 [24] (Fig. 7.32).

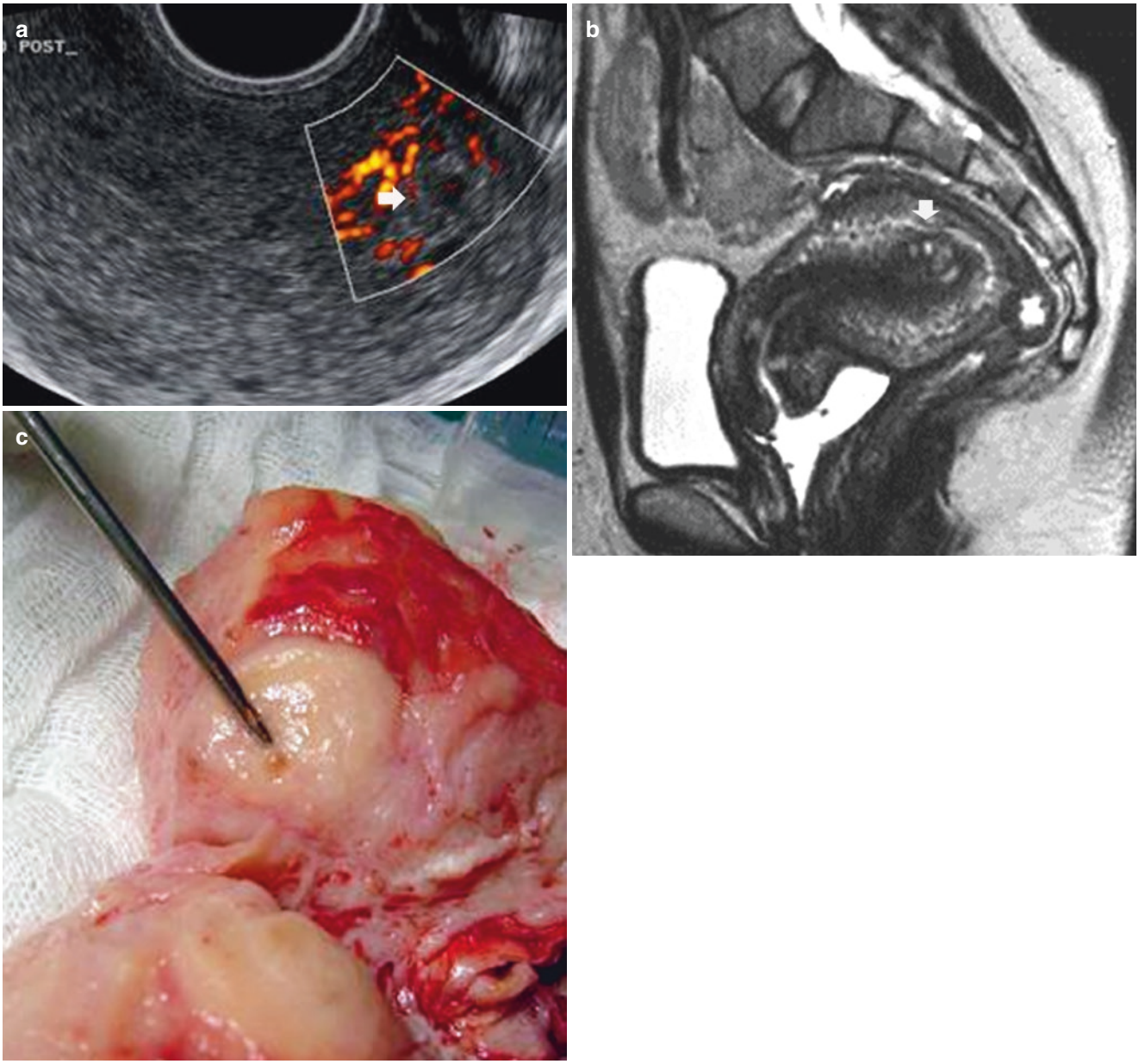

Fig. 7.25 (**a**) Transvaginal ultrasonography. In this image, a nodule can be seen (*arrow*), which is poorly defined in a discreetly heterogeneous myometrium, with no flow to the amplitude Doppler. (**b**) Sagittal, TSE, T2 weighting. The node identified in the US is heterogeneous and has a cystic component (*arrow*) compatible with cystic adenomyosis. (**c**) Surgical piece. Myometrial nodulation with cysts in its interior, compatible with adenomyosis

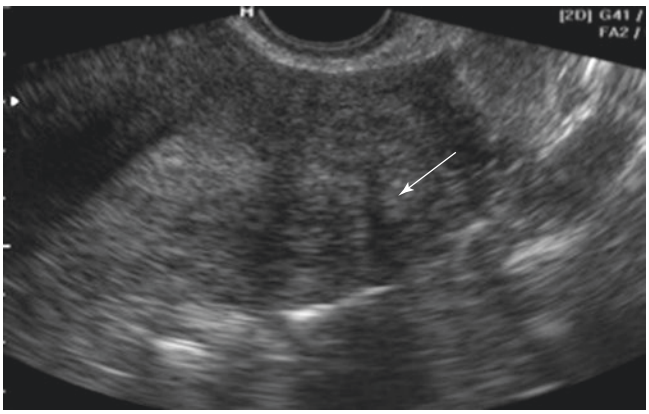

Fig. 7.26 Transvaginal transverse image of the fundus of the uterus shows an adenomyoma (*arrows*) on the left wall and hypoechoic, poorly defined nodule

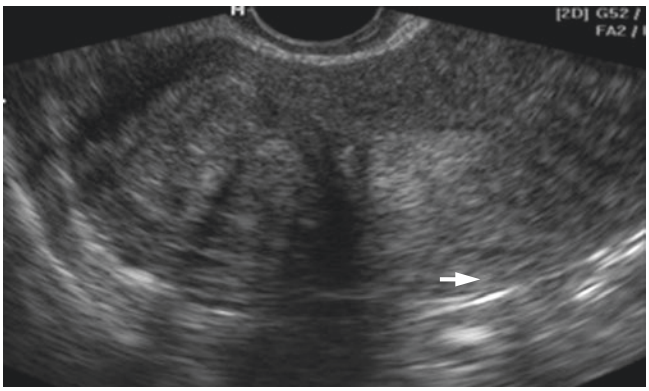

Fig. 7.27 Transvaginal oblique image of the uterus shows a myoma on the right wall and focal hypoechoic circumscribed nodule (*arrow*)

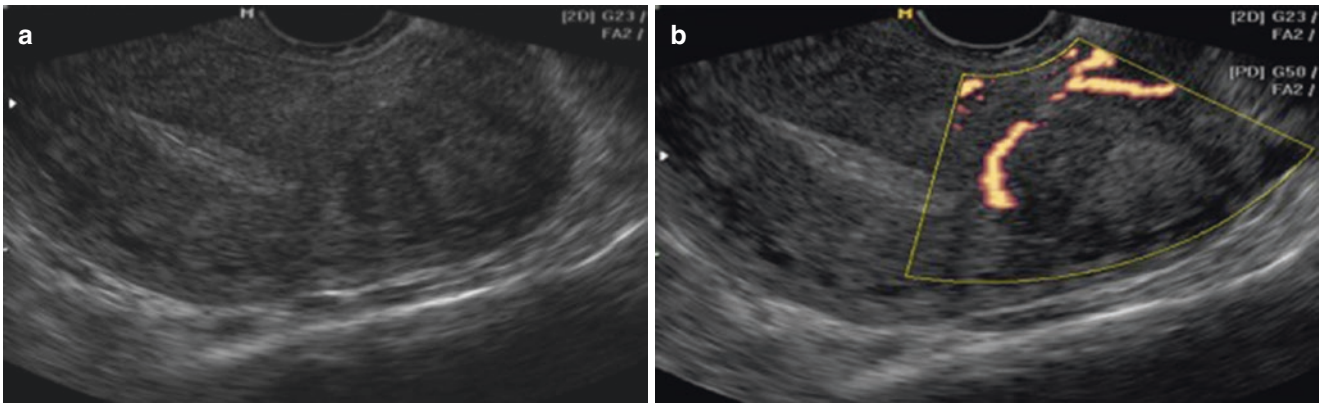

Fig. 7.28 Transvaginal oblique image of the uterus with a myoma on the fundus. (**a**) Grayscale shows focal hypoechoic circumscribed nodule. (**b**) Color Doppler sonogram shows vessels at the margin of the lesion

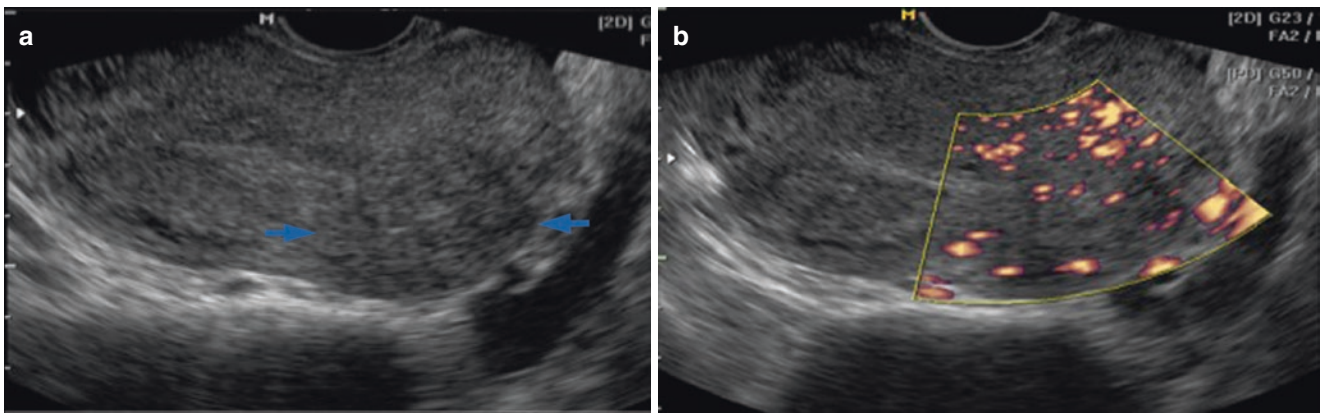

Fig. 7.29 Transvaginal oblique image of the uterus. (**a**) Grayscale shows adenomyoma on the fundus (*arrows*). (**b**) Color Doppler sonogram of the same image shows the presence of straight vessels traversing a hyper-trophic myometrium

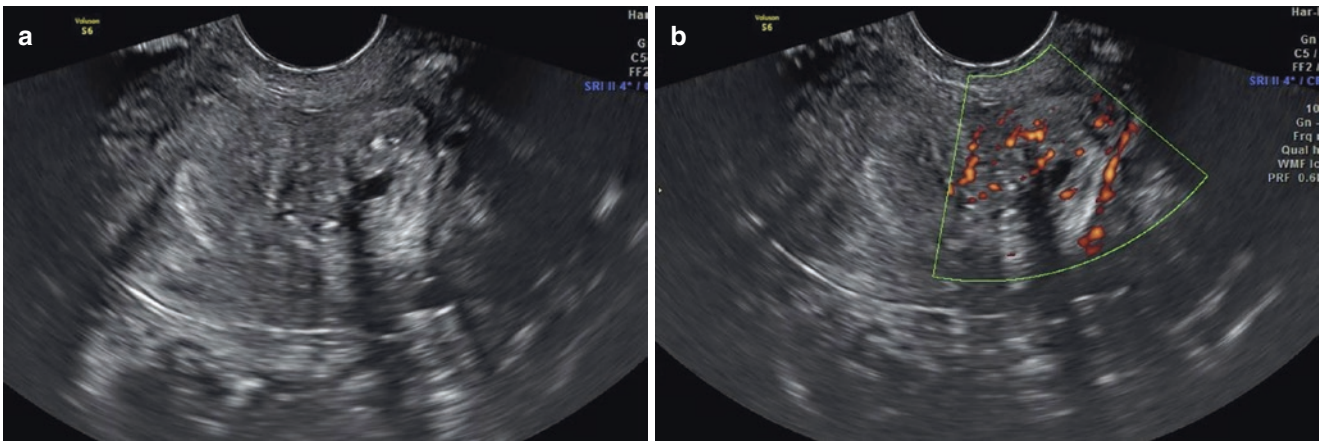

Fig. 7.30 Transvaginal oblique image of the uterus. (**a**) Grayscale shows adenomyoma on the dorsal left aspect of the uterus with central cystic area that can simulate a degenerated myoma. (**b**) Color Doppler sonogram of the same image shows the presence of straight vessels traversing a hyper-trophic myometrium

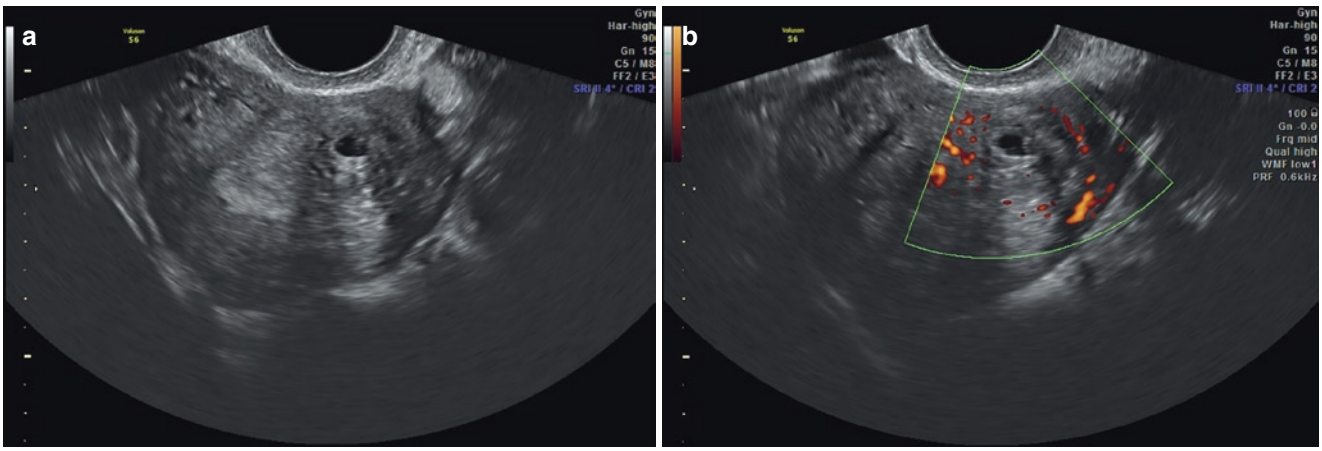

Fig. 7.31 Transvaginal transverse image of the uterus. (**a**) Grayscale shows a degenerated myoma as a well-circumscribed nodule with central cystic area. (**b**) Color Doppler sonogram of the same image shows the presence of straight vessels traversing a hyper-trophic myometrium

Fig. 7.32 Sagittal, TSE, T2 weighting. Note the *adenomyosis focus* in the posterior wall (*arrowheads*) and an exophytic subserosal myoma in the anterior wall (*arrows*)

Adenomyosis and Endometriosis

Patients with endometriosis tend to have more severe pelvic pain than those with adenomyosis. Endometriosis is implanted in the uterine serous, and its involvement is unconventional, usually associated with the obliteration of a recto-uterine recess and impairment of the front walls of the rectum or posterior vaginal fornix. A local involvement of external fibers of the myometrium and serous are more characteristic of endometriosis with myometrial invasion than of adenomyosis, in most cases (Figs. 7.33 and 7.34).

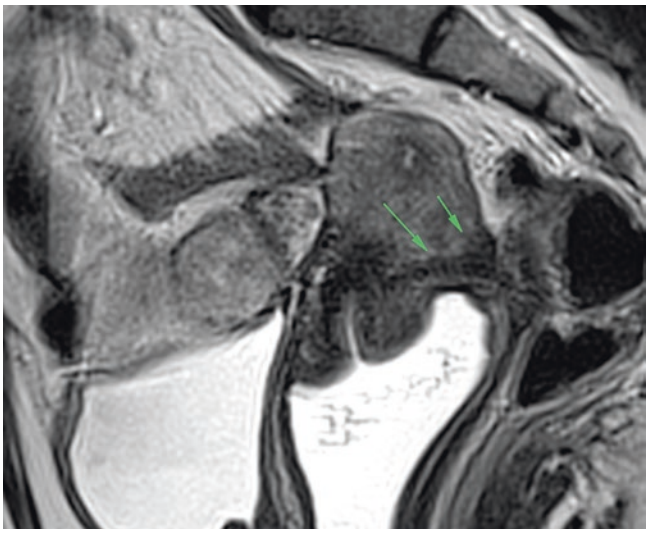

Fig. 7.33 Sagittal, TSE, T2 weighting. *Endometriosis*, when it affects the myometrium, starts by the serous, promoting adherence hypointense foci, and obliterating the posterior compartment (*arrows*). The focal involvement by adenomyosis may be a differential; however, its characteristics are different due to the process starting in the junctional zone, which in this case is preserved

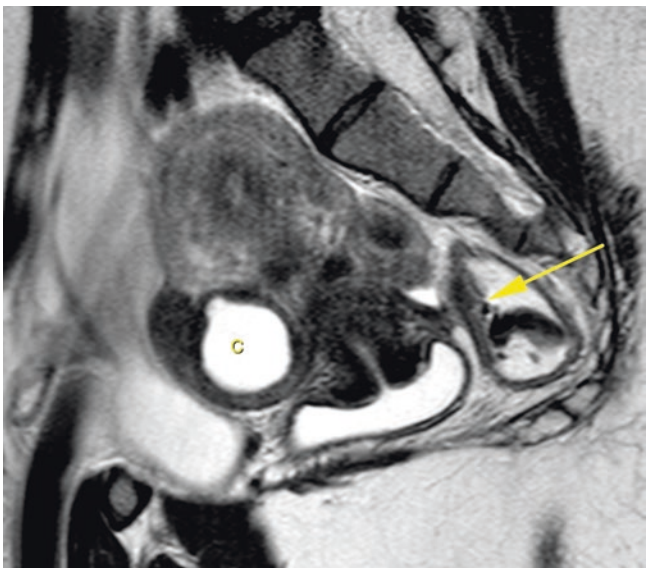

Fig. 7.34 Sagittal, TSE, T2 weighting. In this case there is a cyst (*C*) representing the *cystic adenomyosis* affecting the anterior body wall. Endometriosis adhesion bands in the rear compartment can also be noted (*arrow*)

References

1. Bird CC, McElin TW, Manalo-Estrella P. The elusive adenomyosis of the uterus-revisited. Am J Obstet Gynecol. 1972;112:583–93.
2. Siegler AM, Camilien L. Adenomyosis. J Reprod Med. 1994;39:841–53.
3. Bazot M, Cortez A, Emile D, Rouger J, Chopier J, Antonie J, Uzan S. Ultrasonography compared with magnetic resonance imaging for the diagnosis of adenomyosis: correlation with histopathology. Hum Reprod. 2001;16:2427–33.
4. Reinhold C, McCarthy S, Bret PM, et al. Diffuse adenomyosis: comparison of endovaginal US and MR imaging with histopathologic correlation. Radiology. 1996;199:151–8.
5. Azziz R. Adenomyosis: Current perspectives. Obstet Gynecol Clin N Am. 1989;16:221–35.
6. Panganamamula UR, Harmanli OH, Isik-Akbay EF, Grotegut CA, Dandolu V, Gaughan JP. Is prior uterine surgery a risk factor for adenomyosis? Obstet Gynecol. 2004;104:1034–8.
7. Lee NC, Dicker RC, Rubin GL, Ory HW. Confirmation of the preoperative diagnoses for hysterectomy. Am J Obstet Gynecol. 1984;150:283–7.
8. Kunz G, Beil D, Huppert P, Noe M, Kissler S, Leyendecker G. Adenomyosis in endometriosis prevalence and impact on fertility. Evidence from magnetic resonance imaging. HumReprod. 2005;20:2309–16.
9. Kunz G, Herbertz M, Beil D, Huppert P, Leyendecker G. Adenomyosis as a disorder of the early and late human reproductive period. Reprod BioMed Online. 2007;15:681–5.
10. Bazot M, Darai E, Hourani R, Thomassin I, Cortez A, Uzan S, Buy JN. Deep pelvic endometriosis: MR imaging for diagnosis and prediction of extension of disease. Radiology. 2004;232:379–89.
11. Brosens JJ, de Souza NM, Barker FG, Paraschos T, Winston RM. Endovaginal ultrasonography in the diagnosis of adenomyosis uteri: identifying the predictive characteristics. Br J Obstet Gynaecol. 1995;102:471–4.
12. Bazot M, Dara E, Rouger J, Detchev R, Cortez A, Uzan S. Limitations of transvaginal sonography for the diagnosis of adenomyosis, with histopathological correlation. Ultrasound Obstet Gynecol. 2002;20:603–11.
13. Keepek K, Tuncay YA, Goynumer G, Tutai E. Transvaginal sonography in the diagnosis of adenomyosis: which findings are most accurate? Ultrasound Obstet Gynecol. 2007;30(3):314–5.
14. Togashi K, Ozasa H, Konishi I, et al. Enlarged uterus: differentiation between adenomyosis and leiomyoma with MR imaging. Radiology. 1989;171:531–4.
15. Tamai K, Koyama T, Umeoka S, Saga T, Fujii S, Togashi K. Spectrum of MR features in adenomyosis. Best Pract Res Clin Obstet Gynaecol. 2006;20:583–602.
16. Atri M, Reinhold C, Mehio AR, Chapman WB, Bret PM. Adenomyosis: US features with histologic correlation in an in-vitro study. Radiology. 2000;215:783–90.
17. Chopra S, Lev-Toaff AS, Ors F, Bergin D. Adenomyosis: common and uncommon manifestations on sonography and resonance imaging. J Ultrasound Med. 2006;25(5):617–27.
18. Hricak H, Alpers C, Crooks LE, Sheldon PE. Magnetic resonance imaging of the female pelvis: initial experience. AJR. 1983;141:1119–28.
19. Dueholm M, Lundorf E, Hansen ES, Sorensen JS, Ledertoug S, Olesen F. Magnetic resonance imaging and transvaginal ultrasonography for the diagnosis of adenomyosis. Fertil Steril. 2001;76:588–94.
20. Reinhold C, Atri M, Mehio A, et al. Diffuse uterine adenomyosis: morphologic criteria and diagnostic accuracy of endovaginal sonography. Radiology. 1995;197:609–14.
21. Fedele L, Bianchi S, Dorta M, Arcaini L, Zanotti F, Carinelli S. Transvaginal sonography in the diagnosis of diffuse adenomyosis. Fertil Steril. 1992;58:94–7.

22. Botsis D, Kassanos D, Antoniou G, Pyrgiotis E, Karakitsos P, Kalogirou D. Adenomyoma and leiomyoma: differential diagnosis with transvaginal sonography. J Clin Ultrasound. 1998;26:21–5.
23. Batzer FR, Hansen L. Bizarre sonographic appearance of an adenomyoma and its presentation. J Ultrasound Med. 1996;15:599–602.
24. Fedele L, Bianchi S, Dorta M, Zanotti F, Brioschi D, Carinelli S. Transvaginal ultrasonography in the differential diagnosis of adenomyoma and leiomyoma. Am J Obstet Gynecol. 1992;167:603–6.

Müllerian Duct Anomalies

8

Lucas Rios Torres, Elisa Almeida Sathler Bretas, Priscila Silveira Salvatori, Renata Chehin, and Giuseppe D'Ippolito

Introduction

Among the various causes of infertility, uterine factors account for approximately 13% of cases [1], which are subdivided into cervical and corporal causes. Müllerian duct anomalies (MDAs), together with myomatosis, uterine adherence, endometrial polyps, adenomyosis, and other alterations of endometrial receptivity, belong to the latter group. In a large number of cases, the direct relationship between infertility and MDAs is not clear [1, 2]. These cases are associated more objectively with recurrent miscarriages, complications during pregnancy, and premature births [1, 3].

It is difficult to estimate the true prevalence of MDAs because many patients are asymptomatic [5]. Some of the literature estimates that they are present in up to 3% of the population, whereas others put the figure at up to 25%. The absence of uniform criteria for the diagnosis of MDAs contributes to the inconsistencies and variations found in different studies [6]. Of the various criteria already established for the classification of Müllerian anomalies [5, 7], the most widely used is that which has been recommended by the American Society for Reproductive Medicine, and whose advantages and disadvantages are discussed in this chapter.

In the propaedeutics of the evaluation of uterine causes of infertility, various imaging procedures have been used, especially when the tubal status is known [8]; these may be classified as optimal and sub-optimal [3, 9]. The examination is considered optimal when it is possible to diagnose and differentiate between the various types of MDAs, and this discrimination depends upon the ability to delineate the external (serous) and internal (endometrial) uterine fundal contours [6]. In this chapter we concentrate on two of these imaging techniques – three-dimensional ultrasound (3-D US), and magnetic resonance imaging (MRI), whose results have been described in various studies in the literature [4, 8, 10, 11].

The diagnosis and proper categorization of MDAs is necessary for better management of resources and correct orientation of patient treatment [1]. The aim of this chapter is the didactic compilation of the diagnostic criteria for the MDAs together with illustrations, complemented by the theoretical aspect in legends of figures of the clinical cases. In bringing the image and concept together, the goal is to make this chapter a source for quick consultation, with accessible information that may enable greater precision in diagnoses.

L.R. Torres (✉) • E.A.S. Bretas • P.S. Salvatori
Abdominal Imaging, Department of Diagnostic Imaging,
Escola Paulista de Medicina – Universidade Federal de São Paulo (EPM-Unifesp), São Paulo, SP, Brazil
e-mail: lucasriostorres@gmail.com

R. Chehin
Ultrassonographer, Hospital Beneficencia Portuguesa de São Paulo, São Paulo, SP, Brazil

G. D'Ippolito
Department of Diagnostic Imaging,
Escola Paulista de Medicina – Universidade Federal de São Paulo (EPM-Unifesp), São Paulo, SP, Brazil

L.R.M.F. de Souza et al. (eds.), *Atlas of Imaging in Infertility*, DOI 10.1007/978-3-319-13893-0_8

Embryology: A Brief Review

Interrelationship Between the Ductal Systems

The anatomical integrity of the uterus depends on the correct development, fusion, and reabsorbtion of the walls juxtaposed to the Müllerian ducts, resulting in the unity of the uterus-cervix-vagina triad. All these stages are supported and induced by the Wolffian ducts, which have two other functions: formation of the vaginal plateau, and the ureteric bud. When the inducing function of these ducts is interrupted, alterations such as renal agenisis, vaginal atresia, and uterine fusion defects may occur. The proximity and interrelation between the two ductal systems explains the concomitance of abnormalities found (see Fig. 8.1). In practical terms, this should be a forewarning of more obvious uterine malformations, and concomitant genital and urinary alterations should be sought, which may be responsible for the dominant clinical condition and whose detection will indicate the most adequate treatment [5].

If there is any disorder in the Wolffian duct, there will be impairment in the kidney formation, and the "floating" of the Müllerian duct, inducing a loss of anatomical uterine integrity – simultaneous genitourinary alterations.

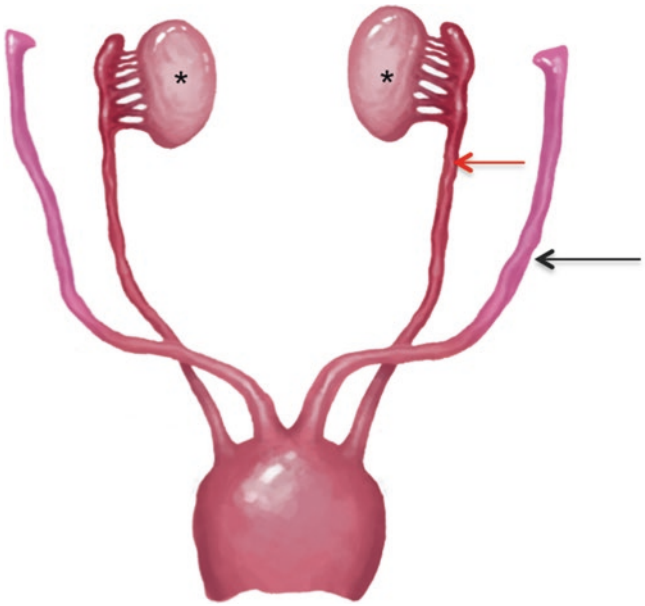

Fig. 8.1 Schematic drawing of the Muller and Wolf Ducts

Types of Malformations

The classifications recomended by the American Society for Reproductive Medicine are divided into seven categories and focus on the evaluation of the resulting uterine anatomy based on three types of alteration: absence of development and/or hypoplasia of the Mullerian ducts; incomplete fusion of the Mullerian ducts; or partial reabsorbtion of the interjacent myometrium when they fuse [12, 13].

The widespread acceptance of this form of classification is due to its simplicity, especially for the identification of the findings and the good correlation between anatomical alterations and the obstetric prognosis of patients [5]. However, some limitations are worth pointing out; these include the impracticality in cases of more complex malformations [3–6]; the fact that they are based on repercussions of fertility [5]; obstructive conditions resulting from aplasia and/or vaginal hypoplasia with normal uterus that are not represented; the fact that they do not provide objective aid to differentiate some subtypes of MDAs (e.g., differentiation between a subseptate uterus and arcuate uterus) [6]; and the fact that there is no determination of which diagnostic methods should be used in the radiological propedeutics [9].

Types of MDAs

- Hypoplasia/agenisis, with Rokitansky syndrome the main disorder in this category
- Unicornuate uterus
- Didelphic uterus
- Bicornuate uterus
- Septate uterus
- Arcuate uterus
- Alterations resulting from diethylstilbestrol (DES) use

Morphology and Uterine Morphometry

There are useful morphological and morphometrical criteria in the differentiation among diverse sub-types, and also for the definition of normal uterus, as described below.

Anatomical Reference: Interostial Line

The interostial line is that formed when the extremities of the intramural regions of the uterine tubes join. The necessity to obtain images on a true coronal plane of the uterus for the adequate positioning of this line used in the measurements must be emphasized.

Measurement of the Fundal Indentation

This indentation is the distance between the interostial line and the apex of the serous uterine fundus. This measurement defines whether there is any defect in uterine fusion, which is useful in differentiating the septate uterus and bicornuate uterus.

Measurement of Depth of Impression in the Fundal Myometrium in the Uterine Cavity

This line defines the degree of deformity upon the endometrial cavity. It is used in the differentiation between the septate uterus and arcuate uterus (respecting the limits of normal fundal myoendometrial distance).

Normal Uterus

- Normal uterine anatomy (Fig. 8.2)
- Morphometrical criteria
- Interostial line: joins both internal ostia of the uterine tubes
- Yellow arrow: distance between interostial line and fundal serous. This distance must be greater than or equal to 0.5 cm
- Red arrow: distance between interostial line and myoendometrial interface. This distance should be up to 1.0 cm

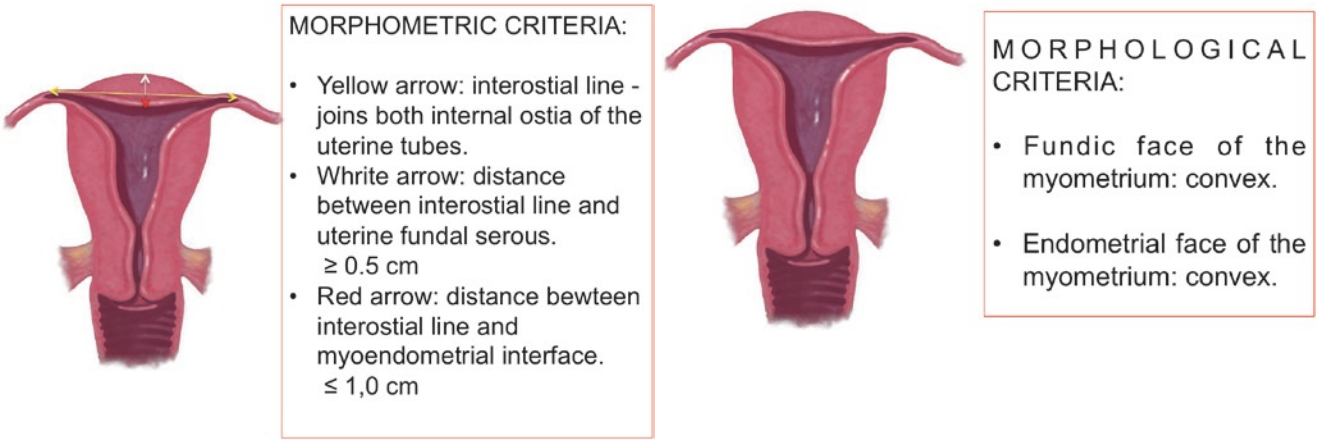

Fig. 8.2 Morphology and morphometry of normal uterus. The *yellow arrows* show the positioning of the interostial line. The *white arrow* shows the measurement of the distance between the interostial line and the fundal uterine serous. This distance should be from the center of the interostial line to the fundal uterine serous. From this measurement, fusion and reabsorption disorders are distinguished. The endometrial margin of the uterine fundus usually has a convex, rectilinear or even concave aspect. The degree of depth should be measured from the center of the interostial line, and should not be greater than 1.0 cm. (Figure courtesy: Athos Correia Sampaio, Federal University of Bahia)

Arcuate Uterus

- Morphometrical criteria (Fig. 8.3)
- Interostial line: joins both ostia of the uterine tubes
- White arrow: distance between the interostial line and the fundal serous. This distance must be greater than or equal to 0.5 cm
- Differentiates fusion and reabsorbtion disorders
- Red arrow: distance between interostial line and the myo-endometrial interface
- The distance must be greater than or equal to 1.0 in and smaller than 1.5 cm

Fig. 8.3 The main difference between the normal uterus and the arcuate uterus is the degree of impression of the fundal myometrium on the endometrial cavity. (Figure courtesy: Athos Correia Sampaio, Federal University of Bahia)

Septate Uterus

- Morphometrical criteria (Fig. 8.4)
- Interostial line: joins both internal ostia of the uterine tubes
- White arrow: distance between interostial line and fundal serous. This distance must be greater than or equal to 0.5 cm
- Differentiates between fusion and reabsorbtion disorders
- Red arrow: distance between interostial line and myoendometrial interface. This distance must be greater than 1.5 cm

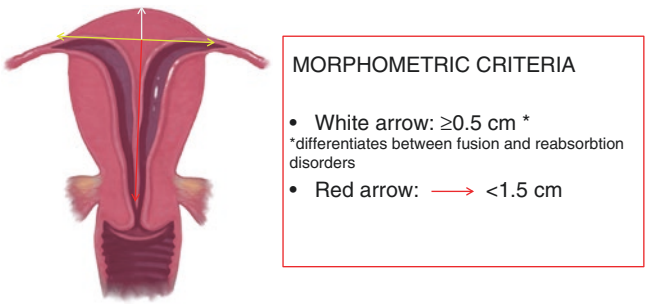

Fig. 8.4 The length of the septum is variable. When it extends to the external ostia of the colon, it is considered complete septate. (Figure courtesy: Athos Correia Sampaio, Federal University of Bahia)

Bicornuate Uterus

- Morphological criteria (Fig. 8.5)
- Fork aspect
- Morphometrical criteria
- Interostial line: joins both ostia of the uterine tubes
- White arrow: distance between interostial line and fundal serous. This distance should be less than 0.5 cm
- Differentiates between fusion and reabsorbtion disorders
- Biconuate and didelphic uterus: fusion disorders
- Septate and arcuate uterus: absorbtion disorders

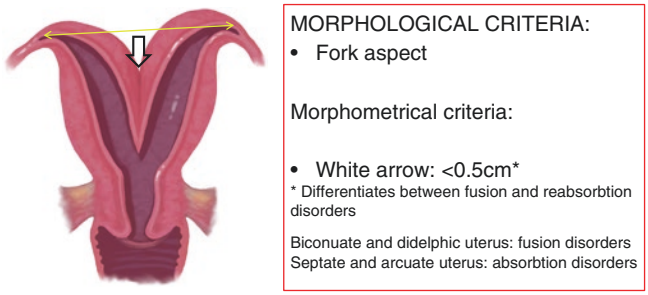

Fig. 8.5 The main morphometrical criterion is the distance from the interostial line to the apex of the fundal serous. When it is less than 0.5 cm, it is considered to have a fusion defect. The presence of a corporal junction between the two hemi-uteri, with or without myometrical reabsorpion between them, differentiates the bicornuate uterus from the didelphic one. There may be as much duplication as septation of the colon and/or the body of the uterus. (Figure courtesy: Athos Correia Sampaio, Federal University of Bahia)

Didelphic Uterus

- Morphological criteria (Fig. 8.6)
- There is no fusion between the two hemi-uteri
- Variations in appearance and clinical condition resulting from duplication/patency of the vagina

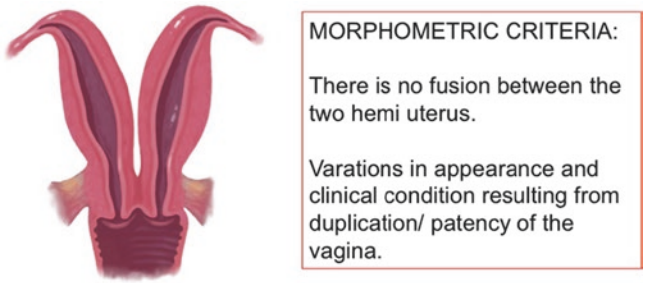

Fig. 8.6 In this type of MDA, there is no corporal fusion between the two primordial uteri. A greater difficulty in interpretation may arise in cases where there is junction or fusion of the cervix, when it may resemble a bicornuate uterus. This often occurs with vaginal septum or duplication, which can trigger dysmenorrhea during the menstrual period. (Figure courtesy: Athos Correia Sampaio, Federal University of Bahia)

Unicornuate Uterus

- Morphological criteria (Fig. 8.7)
- Agenisis of one of the hemi-uteri
- Incomplete fusion of the hypoplasic horn:
  - Without functioning endometrium
  - With functioning but non-communicating endometrium
  - With functioning and communicating endometrium

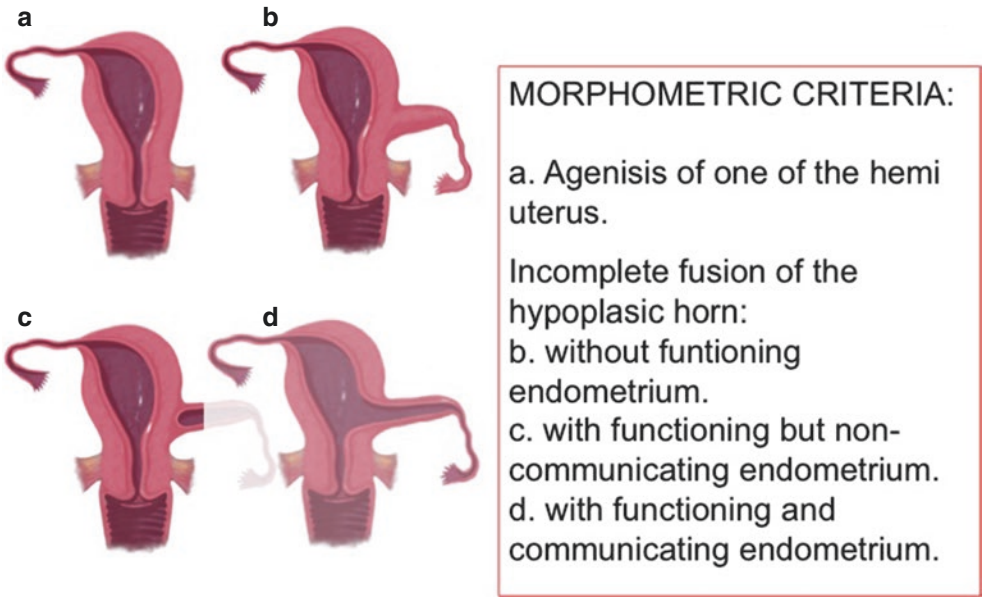

Fig. 8.7 Unicornuate uterus. (Figure courtesy: Athos Correia Sampaio, Federal University of Bahia)

Mayer-Rokitanski Syndrome

- Morphological criteria (Fig. 8.8)
- Agenisis or hypoplasia of both Müllerian ducts
- Agenisis or hypoplasia of the superior two-thirds of the vagina
- Ovaries with preserved dimensions and functionality, ensuring female sexual features

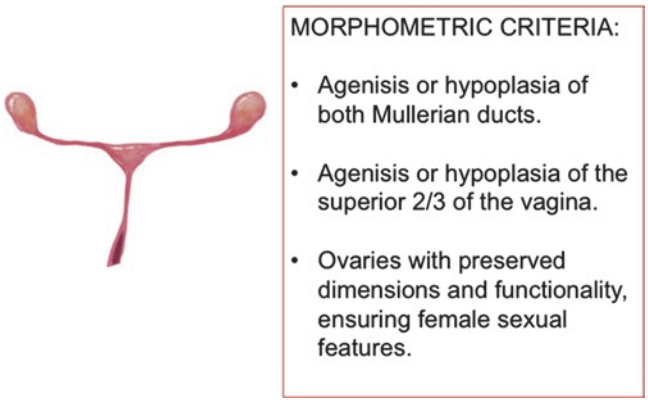

Fig. 8.8 Mayer-Rokitanski syndrome. (Figure courtesy: Athos Correia Sampaio, Federal University of Bahia)

Ultrasound and MR Images of Uterine Anatomy

3-D Ultrasound

The images obtained from ultrasound are produced by echoes formed by the interaction between the beams emitted by the transducers and the organs being studied. The greater the number of echoes produced, the whiter or clearer the structure appears in the images. Taking the quantity of echoes produced by the myometrium as a base, the echogenicity of all other uterine structures can be divided in the following way (Figs. 8.9, 8.10, and 8.11):

- Hyperechogenic produces a higher number of echoes than the myometrium
- Isoechogenic produces the same echo as the myometrium
- Hypoechogenic produces a lower number of echoes than the myometrium
- Anechoic does not produce echoes, and allows sound waves to pass through

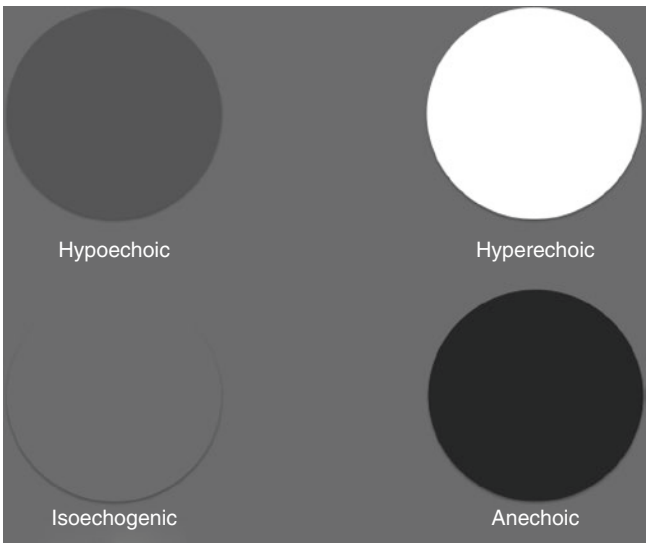

Fig. 8.9 Hypoechogenic: produces a lower number of echoes than the myometrium

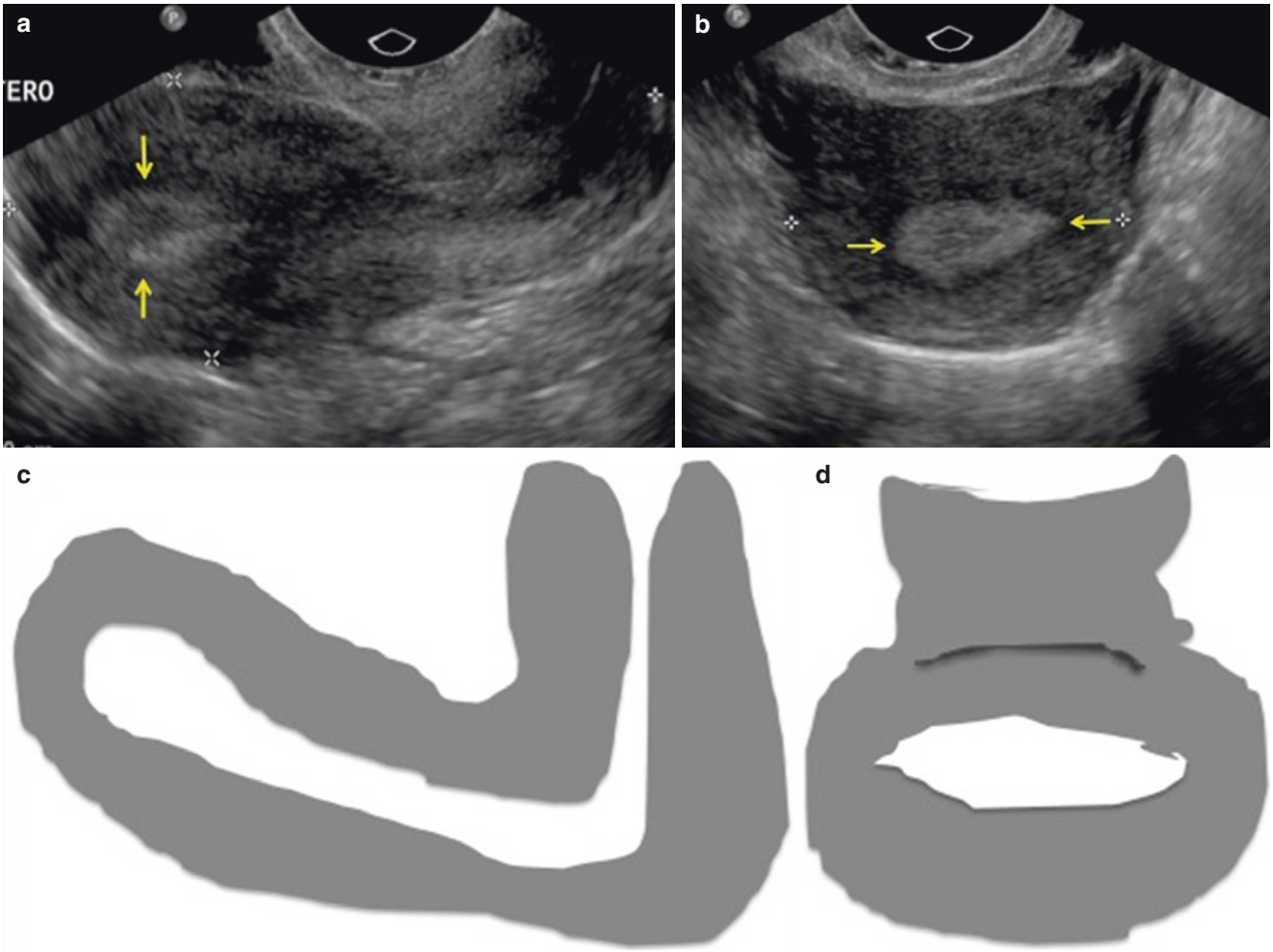

Fig. 8.10 (**a**) Image of the uterus in the sagittal plane (or "lateral view") represented in schematic form in image **c**). (**b**) Image of the uterus in the coronal plane (or "anterior view") represented in schematic form in image (**d**). The *yellow arrows* show thick and hyperechogenic endometrium (secretory phase)

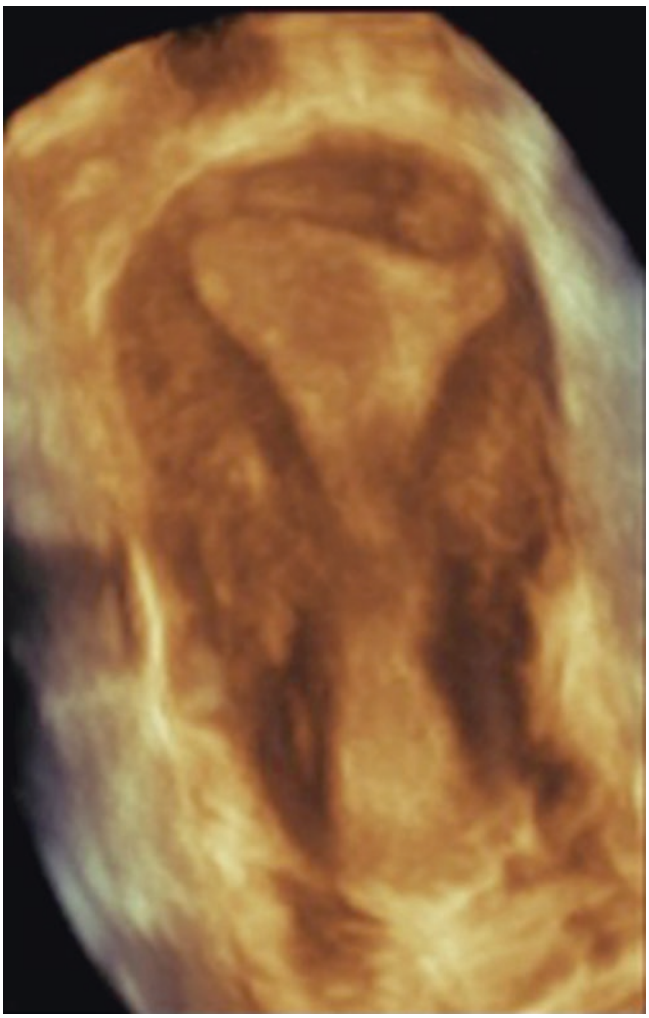

Fig. 8.11 Three-dimensional reconstruction of the uterus from Fig. 8.7. Notice how both the external and internal fundal contours are well defined. The echogenic endometrium facilitates the visualization of the cavity contours, and thus makes the secretory phase the best time in which to carry out the examination

Ultrasound in the Assessment of MDAs

- Carried out in the later stages of the menstrual cycle (endometrium more echogenic)
- Duration 15–30 min
- 3-D >2-D
- Does not use ionizing radiation
- Limitations: assessment of rudimentary and non-communicating uterine horns

Magnetic Resonance

MR images are obtained from signals emitted by hydrogen protons after stimulation by way of radiofrequency pulses. Two types of images can be acquired: T1 weighted images and T2 weighted images. The latter are more widely used in uterine malformations, and are characterized mainly by the high-signal intensity emitted by structures containing liquid. Regarding the myometrium, the structures can thereby be classified in relation to its signal (Figs. 8.12, 8.13, and 8.14):

- Hypointense signal
- Hyperintense signal
- Isointense signal

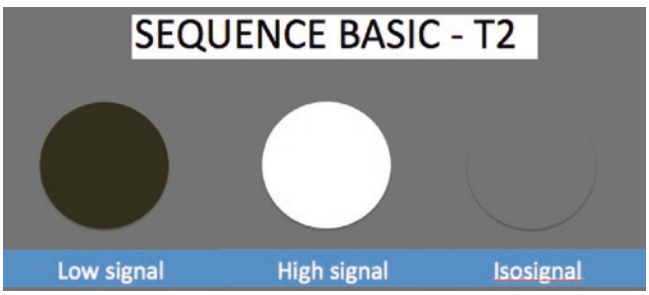

Fig. 8.12 Various signal intensities in MRI. When the uterus is taken as a reference, the structures can have a hyperintense, hypointense, or isointense signal

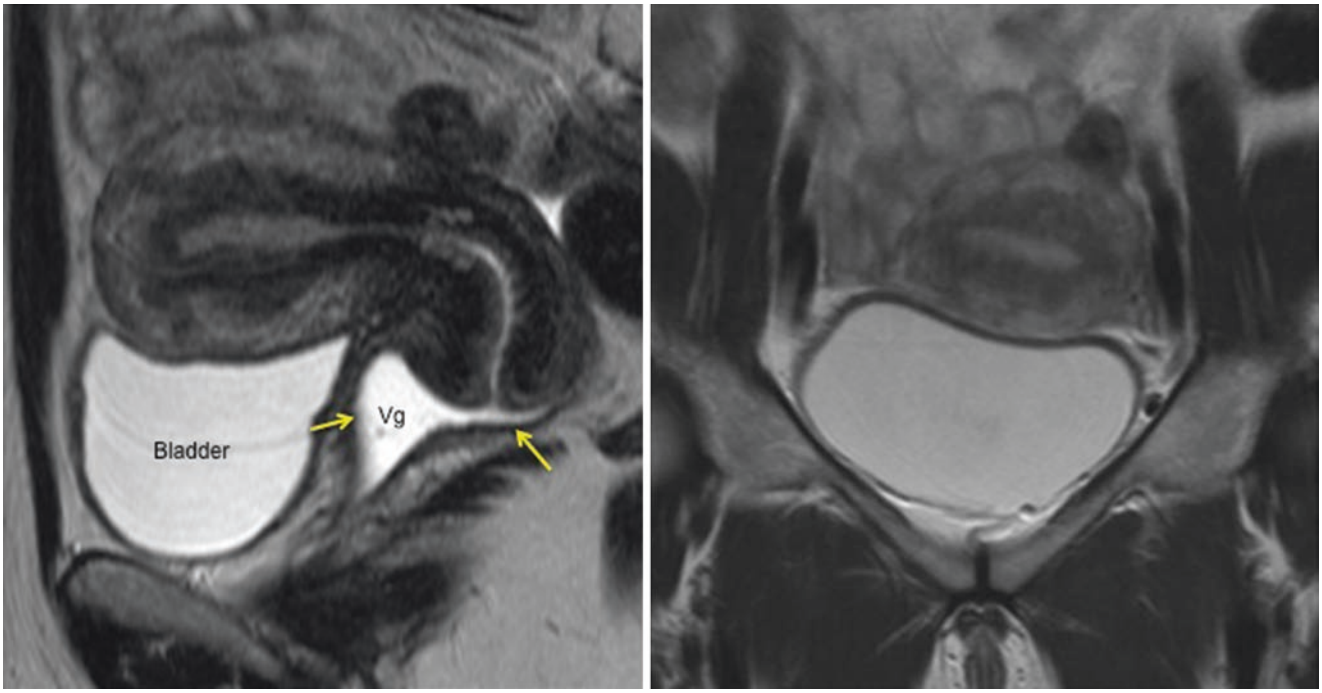

Fig. 8.13 T2 weighted images in the coronal and sagittal planes. The myometrium has an intermediate signal intensity on T2 weighted images whereas the endometrium (end) has a high signal intensity. Gel was routinely used for vaginal distention (*vg – yellow arrows*)

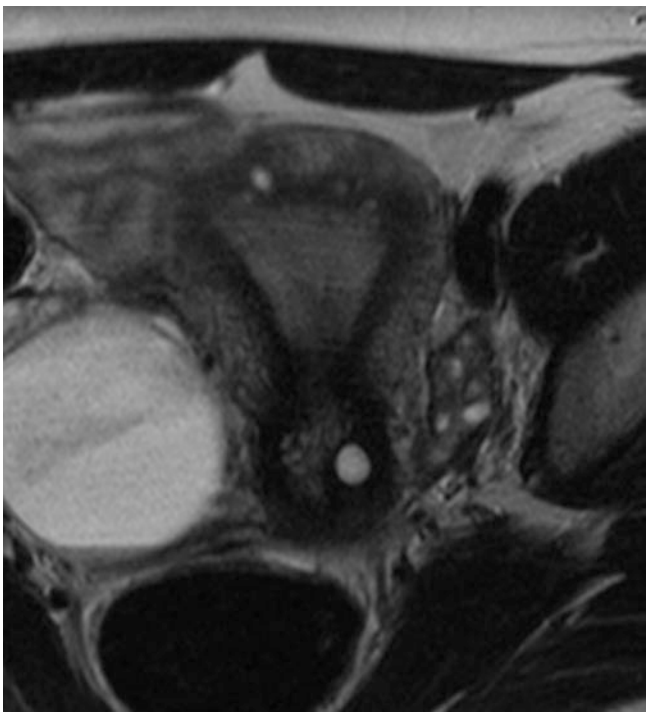

Fig. 8.14 True coronal plane image of the uterus on T2 weighted. As with 3-D US, the contour of the fundal and endometrial serous are well defined

MRI in MDA Assessment

- Any phase of the menstrual cycle
- Duration 30 min
- EV contrast: not obligatory
- Vaginal gel and antispasmodics: improve quality of exam
- Does not use ionizing radiation
- Limitations:
  - Claustrophobic patients
  - Uncooperative patients
  - Pacemakers
  - First trimester of pregnancy (Fig. 8.15)

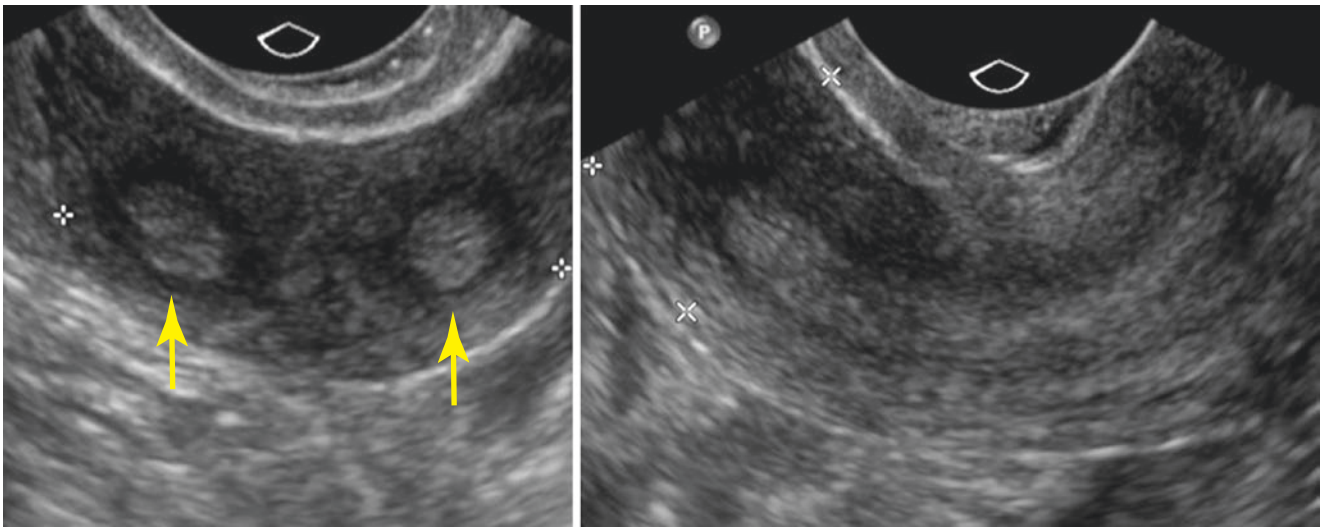

Fig. 8.15 2-D coronal and axial ultrasound images of a patient with a history of two miscarriages. In the coronal plane, a bifid of endometrial echo was detected (yellow arrows). In the sagittal plane, no abnormality was identified. This is an example of a sub-optimal exam, where a uterine malformation is diagnosed but is not characterized. Up to this point it is still not clear whether we are dealing with a septate, bicornuate, or didelphic uterus

Clinical Cases

To review and fix the knowledge presented in the text, Fig. 8.12–8.40 represent illustrated clinical cases.

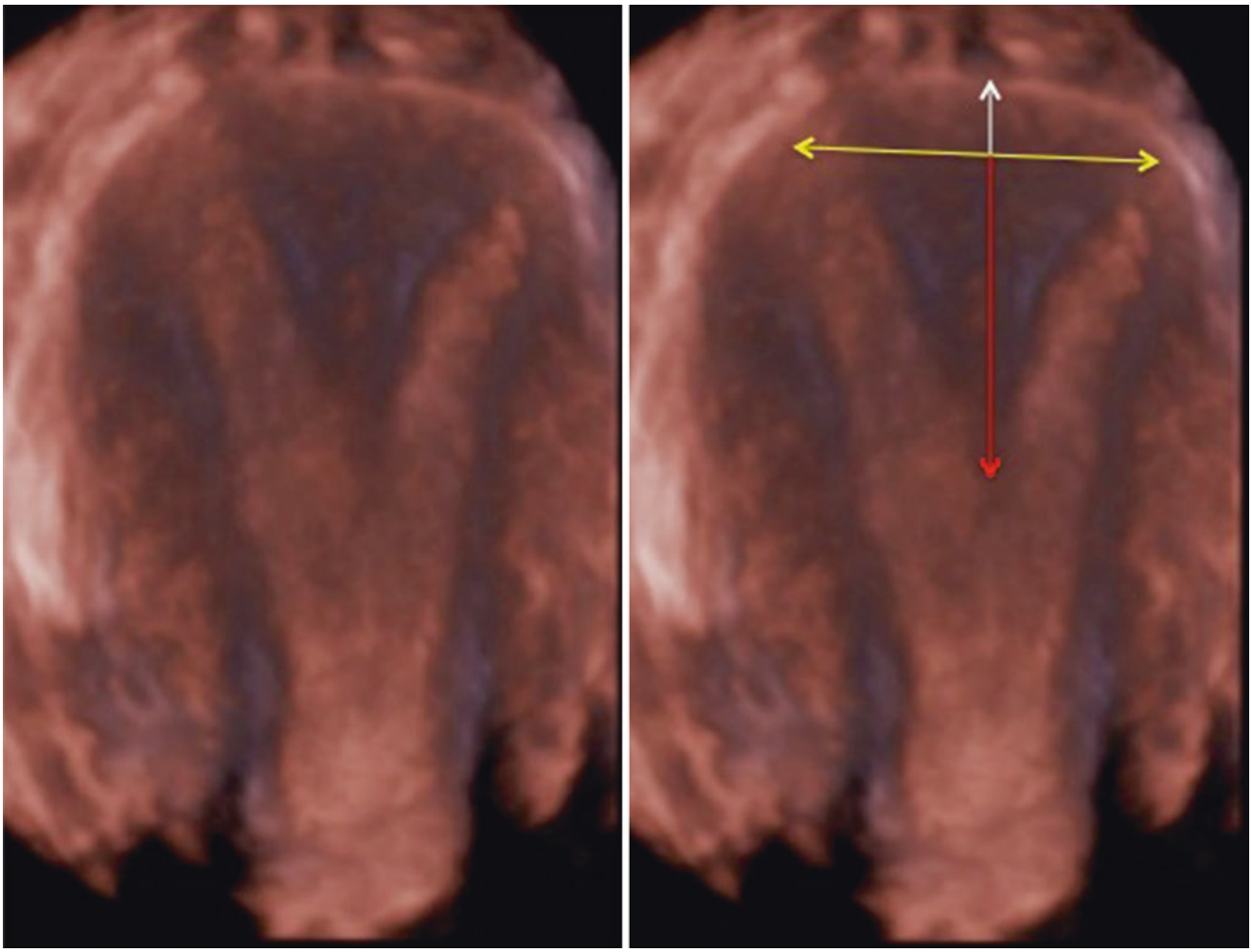

Fig. 8.16 3-D US reconstruction. There is a clear symmetrical division of the endometrial cavity by a wide-based partial septum. Repeating the method used in the schematic graphics, we see the depth of myometrial impression to the interior of the endometrial cavity. In the cases where septoplasty is recommended, it is useful to provide the longitudinal extension of the septum and the thickness of the fundal myometrium that remains after the removal of the septum. When the thickness is less than 0.5 cm, there is a greater chance of uterine rupture during gestation [14] (Courtesy of Dr. Renata Cechin, Portuguese Charity Hospital of São Paulo)

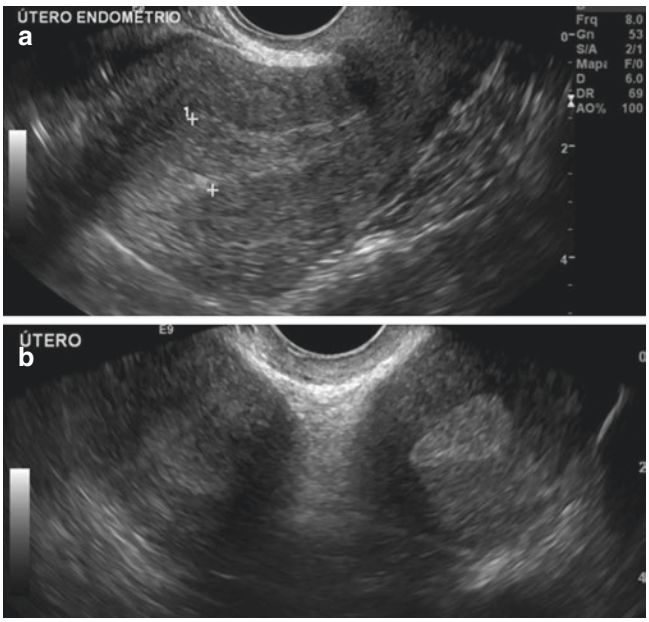

Fig. 8.17 A case similar to the previous, where no abnormality was identified in the sagittal plane (**a**). In the coronal slice of the uterus (**b**), a bifid of endometrial echo and a certain degree of divergence are noted. It was not possible however, to distinguish between a bicornuate, didelphic and septate uterus

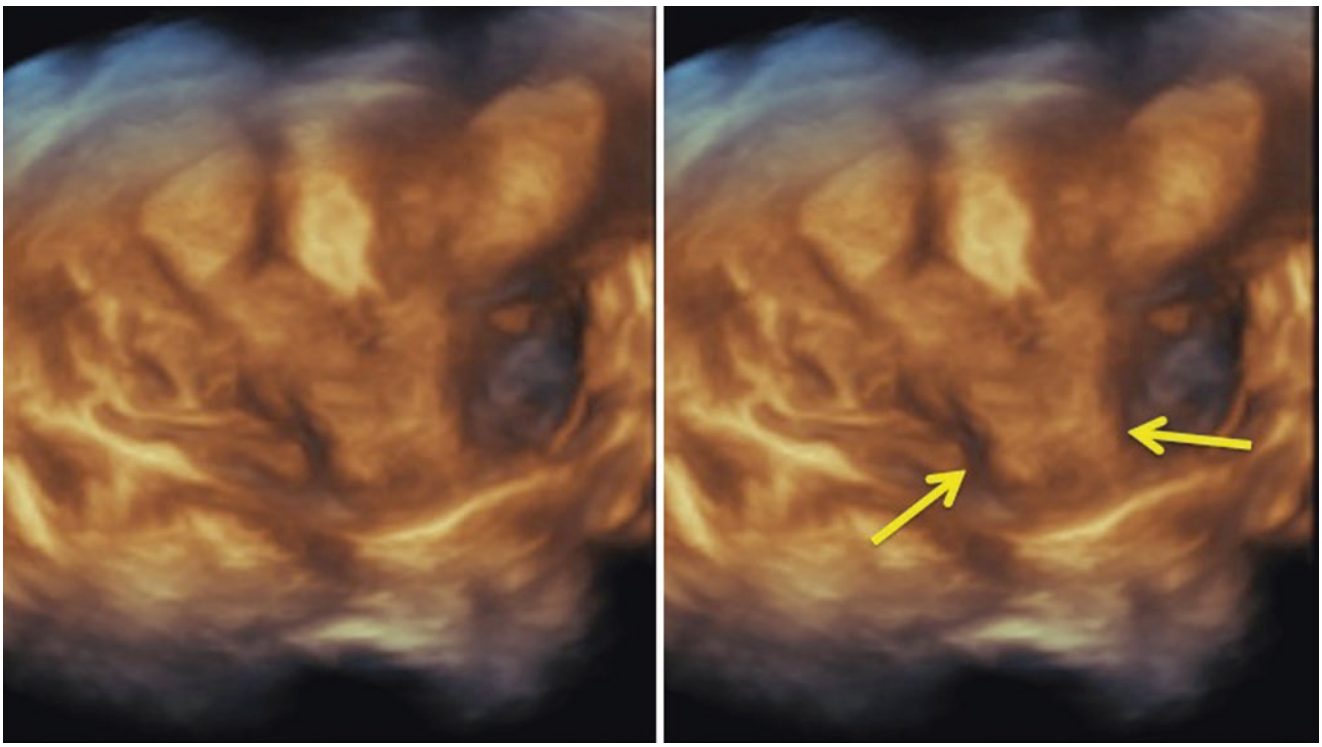

Fig. 8.18 3-D reconstruction showing fusion of the lateral walls of the cervix (*yellow arrows*), without fusion of the body, and with cornual divergence. The uterus was classified as bicollis bicornuate uterus

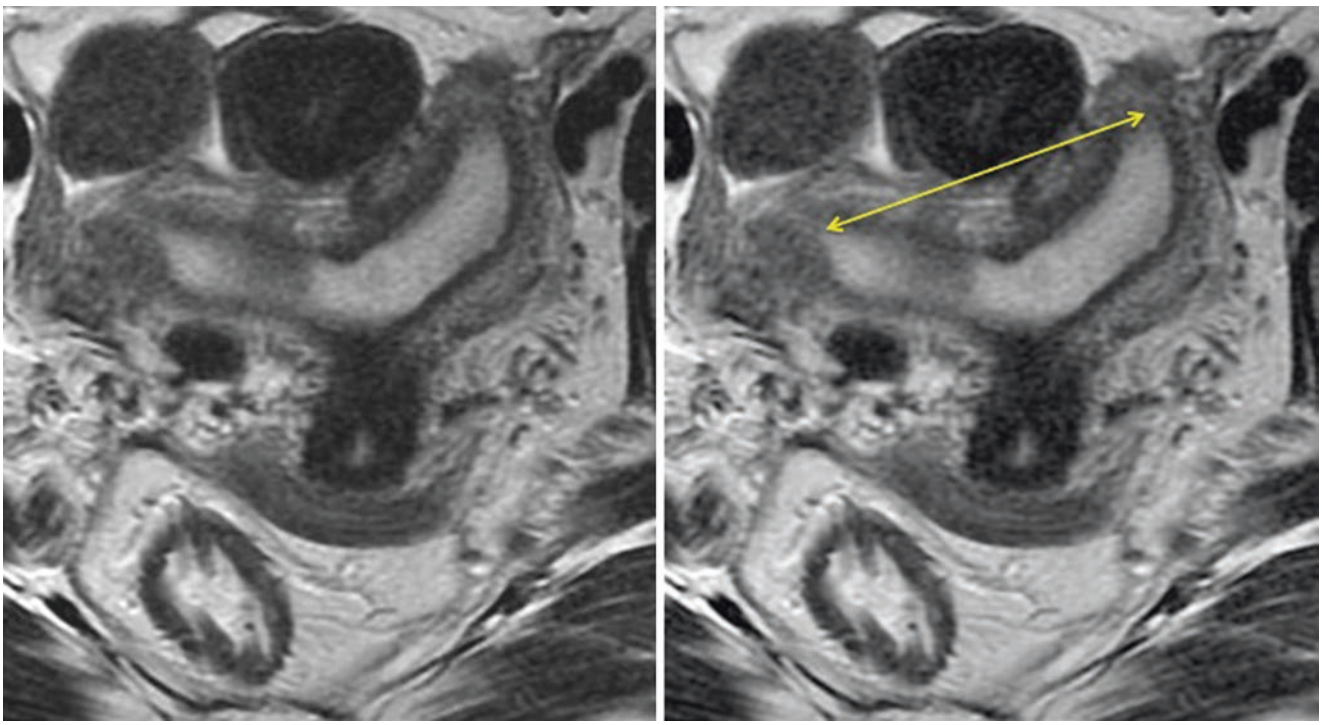

Fig. 8.19 Example of a unicollis bicornuate uterus. Notice how there is fusion of the cervix but not of the fundal portion, where the horns diverge. The fundal summit is located below the interostial line (*yellow arrow*), characterizing the existence of a fusion disorder.

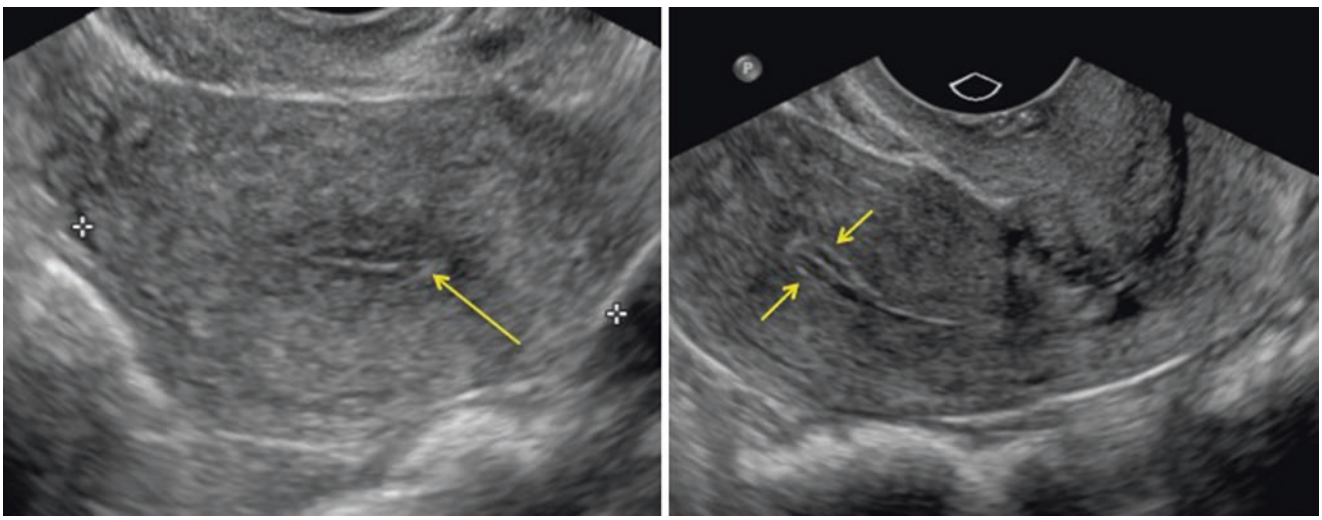

Fig. 8.20 Patient underwent routine exam. Unlike the examples shown in Figs. 8.12 and 8.14, there is no bifid of endometrial echo; in this patient it has a trilaminal aspect (*yellow arrows*) (Courtesy of Dr. Renata Cechin, Portuguese Charity Hospital of São Paulo)

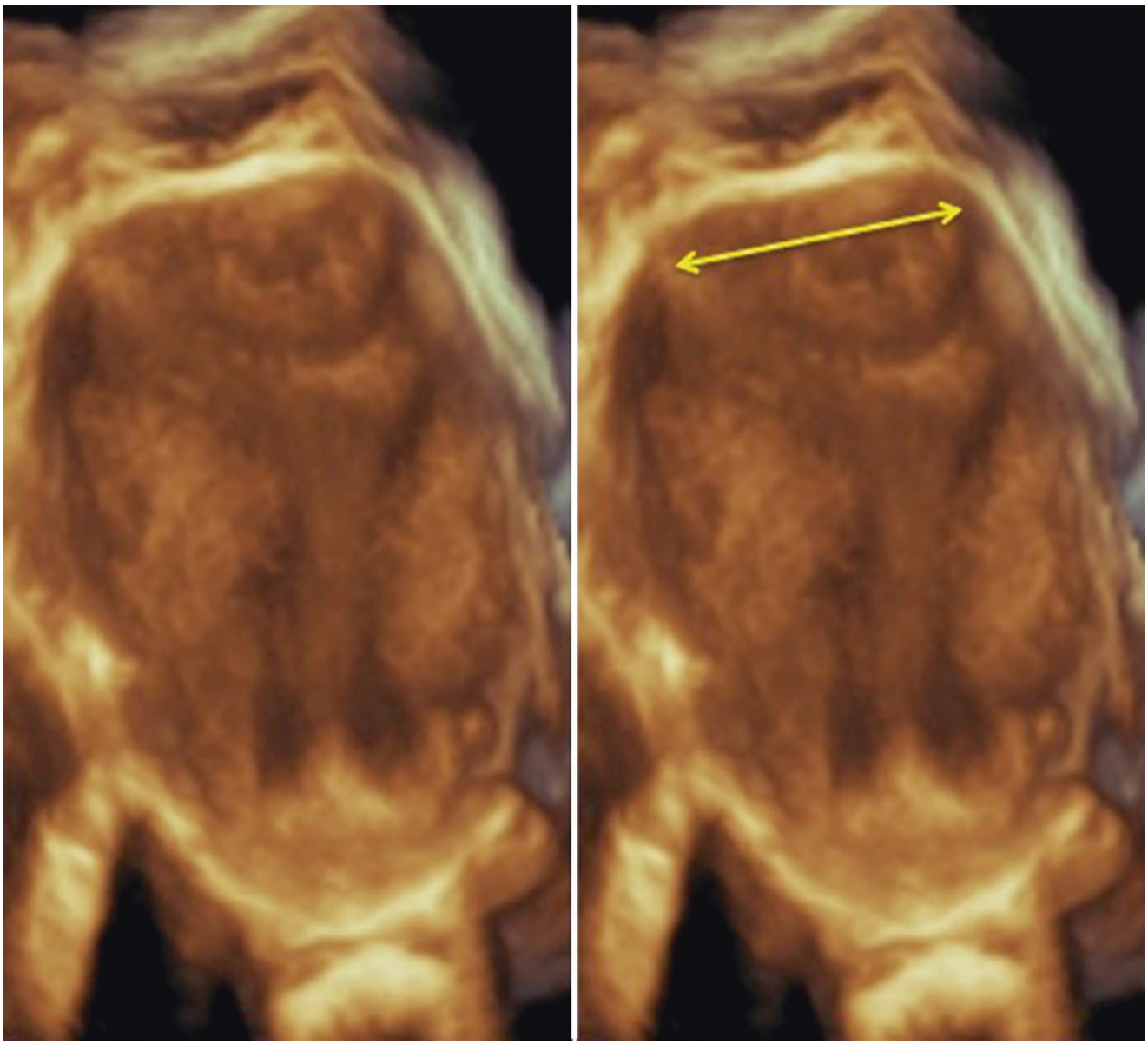

Fig. 8.21 3-D US of the same patient as in the previous figure. The uterus presents an arcuate aspect, a type of benign malformation with regards to the patient's reproductive life [6] (yellow arrows: interostial line)

Fig. 8.22 Hysterosalpingography in the assessment of the uterine tubes of a patient with repeated miscarriages. From this image alone, it is not possible to acertain whether the uterus is didelphic, bicornuate, or septate

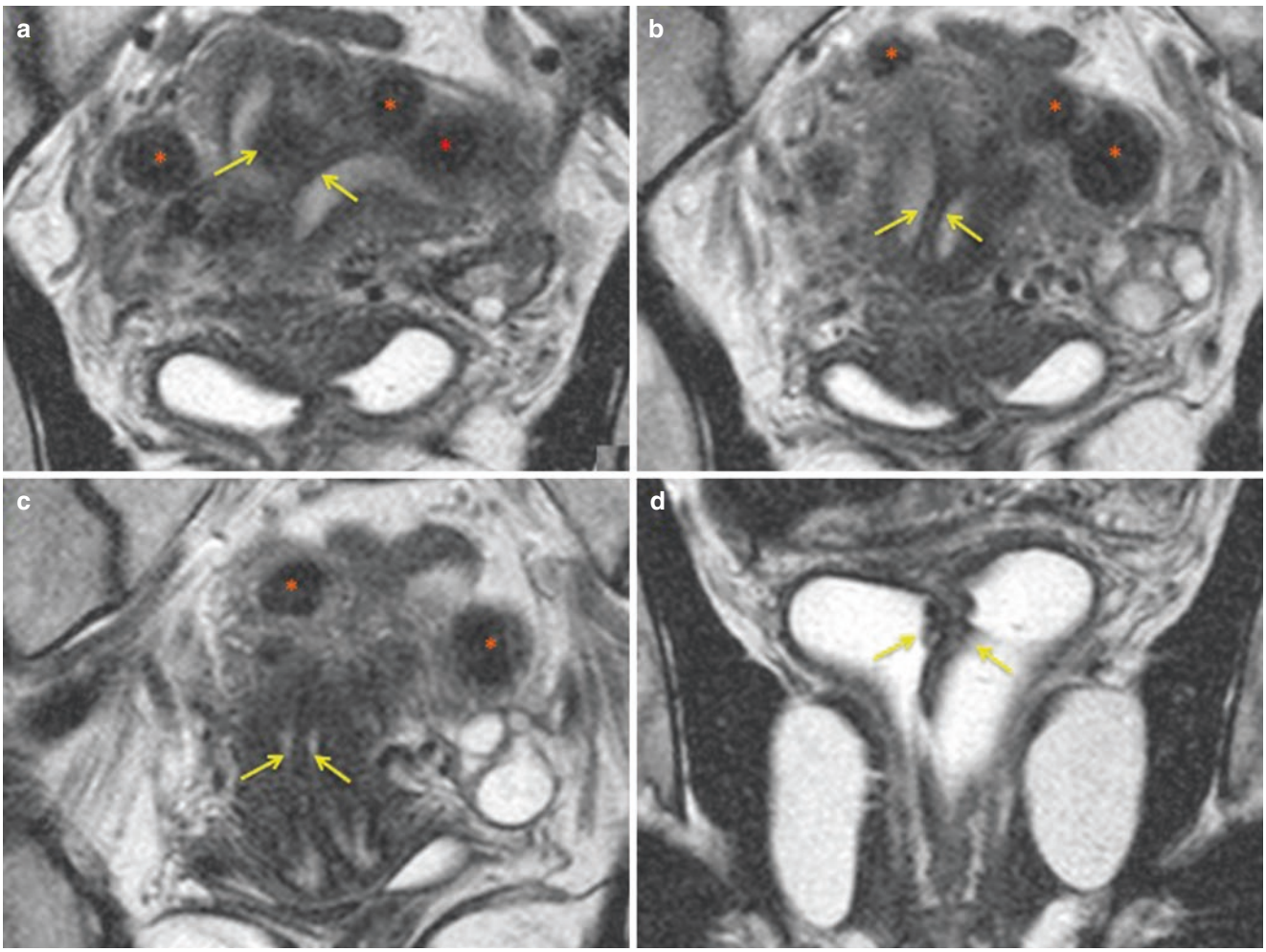

Fig. 8.23 MRI of the same patient. Images (**a**-**c**) are successive slices of the uterus, where the *yellow arrows* show a wide-based septation (**a**), extending to the endometrial cavity (**b**) of the endocervix (**c**), and reaching the superior third of the vagina (**d**). This is a septate uterus, with the superior portion of the septum (**a**) presenting muscular component with isointense signal in relation to the myometrium, and the remaining portions showing a fibrous tissue of low- signal intensity on T2 weighted images. The vaginal septum is found in up to 23% of septate uteri [4]. The asterisks indicate diverse leiomyomas dispersed throughout the myometrium

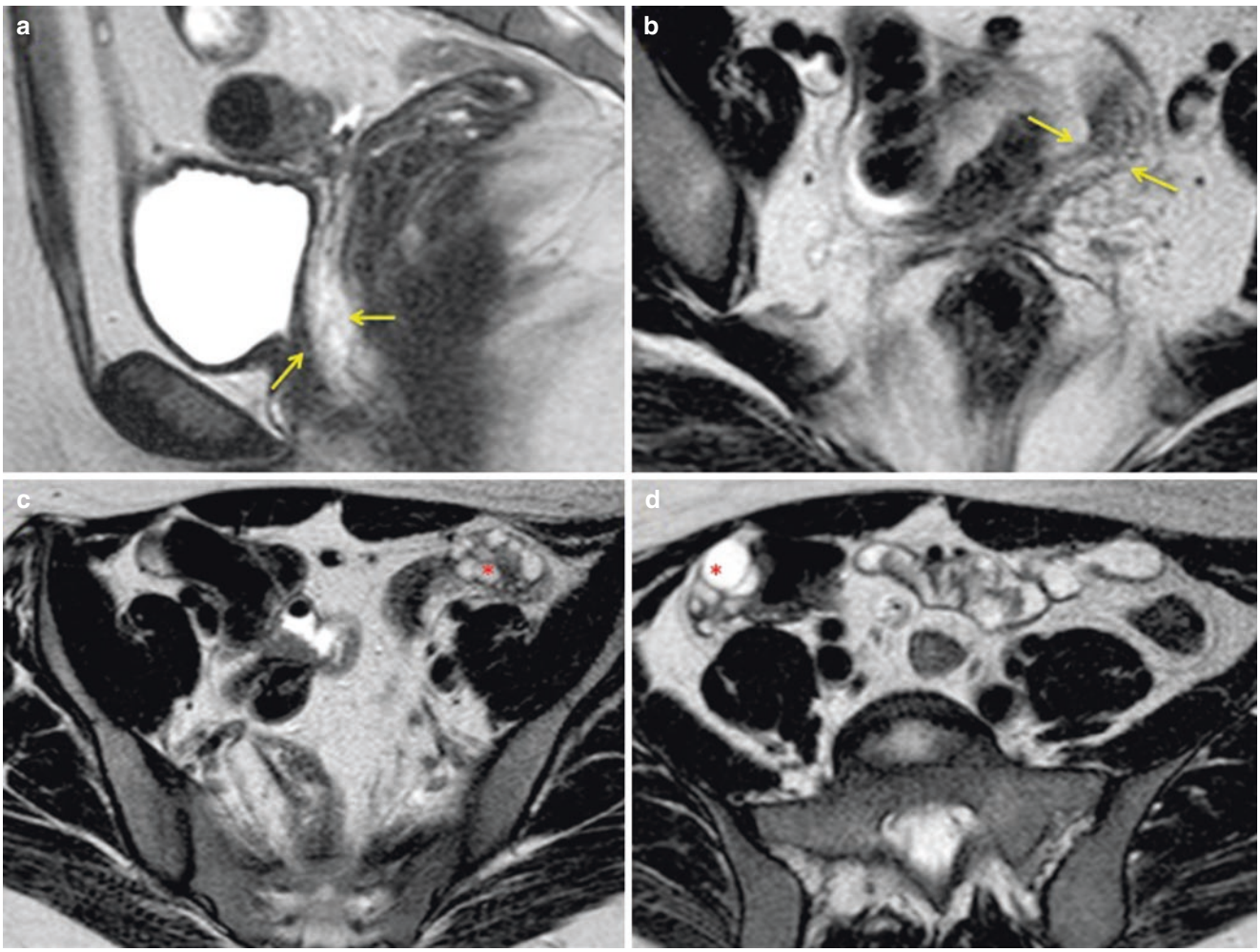

Fig. 8.24 A 19-year-old patient presenting primary amenorrhea and short vagina. The *yellow arrows* in (**a**) show that on the midline of the pelvic region there is adipose tissue in the topography of the uterus and the superior third of the vagina. In (**b**) the *yellow arrow* shows a uterine bud with its base directed toward the midline. The *asterisks* in (**c**,**d**) show the ovaries. This is a case of Mayer-Rokitansky-Kuster-Hauser syndrome

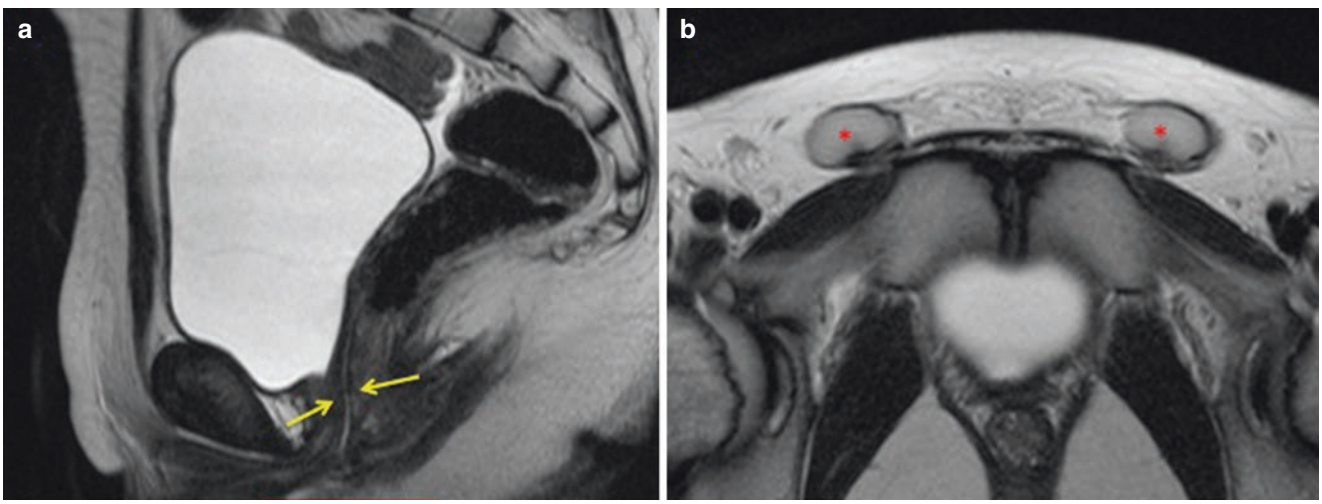

Fig. 8.25 A similar case, of a patient presenting primary amenorrhea and short vagina. This patient also presents a filiform tissue with a similar signal to the fat occupying the topography of the vagina and uterus (*yellow arrows* in **a**). In the inguinal region, the presence of two testicles can be characterized. This is called Morris syndrome. Although it is not included in Müllerian duct anomalies, it is the main differential diagnosis for SMRKH

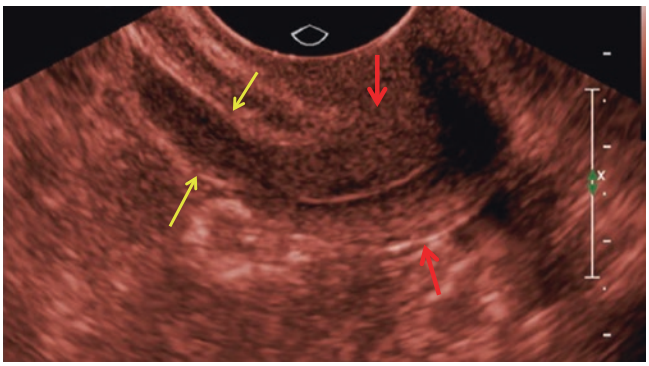

Fig. 8.26 A 40-year-old nulligravida patient. Sagittal transvaginal ultrasound image. The *yellow arrows* demarcate the uterus, and the *red arrows* the colon. There is dimensional disproportion of both, being that the colon is larger than the uterus, forming a hypoplastic uterus

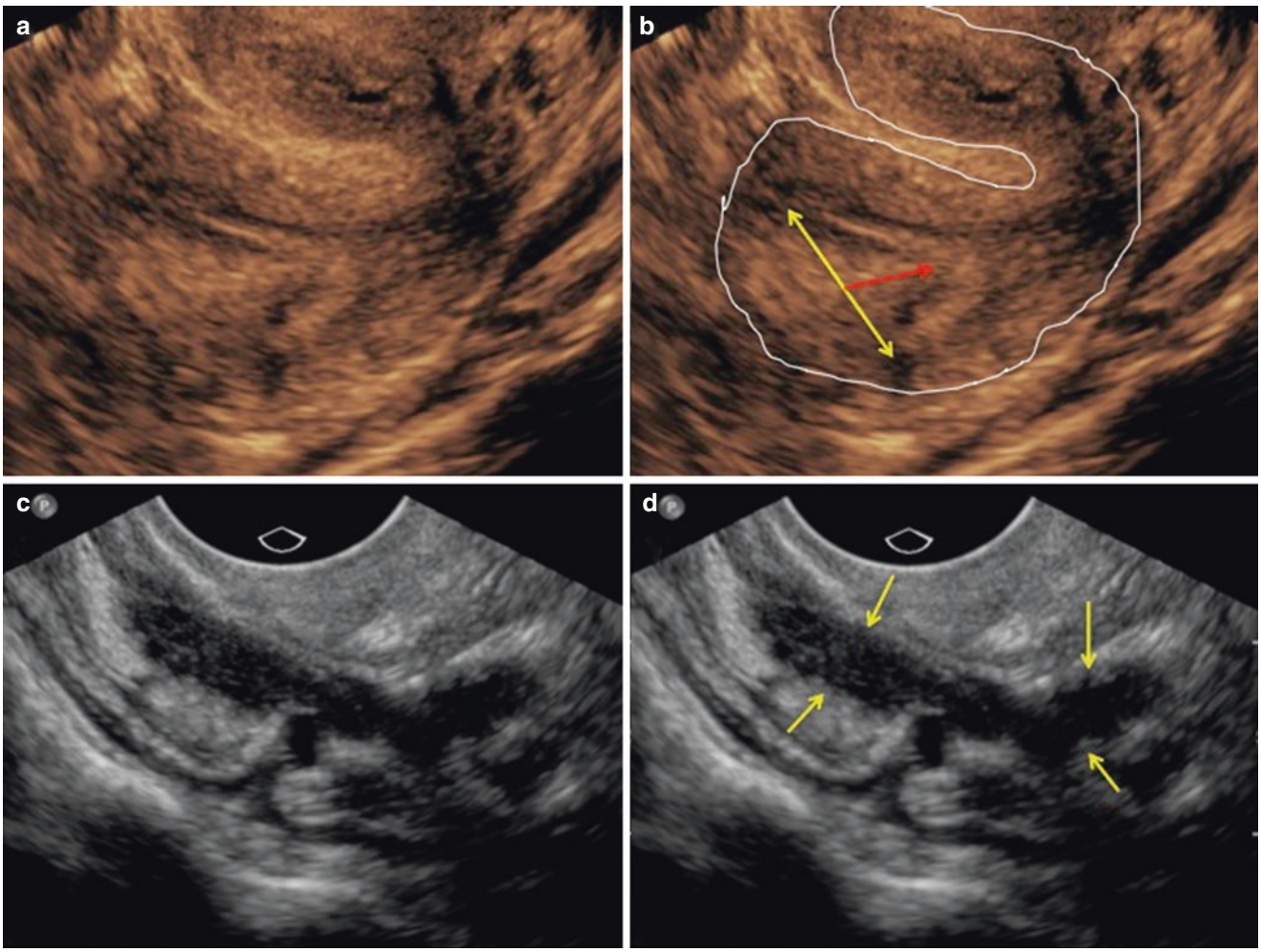

Fig. 8.27 (**a**) coronal image of the uterus. (**b**) the *yellow arrow* demonstrates the interostial line; the *red arrow* demonstrates the depth of the impression of the myometrium, configuring a septate uterus. (**c**) Image of a segment of a loop in the sagittal plane. (**d**) *yellow arrows* demonstrate asymmetric parietal thickening related to endometriosis. Septate uterus with extensive focus of the endometriosis affecting the sigmoid colon. A wide and partial septum can be seen emerging from the internal fundal uterine margin. There is an association between MDAs and endometrioses, especially in cases where there is an obstruction of the outflow

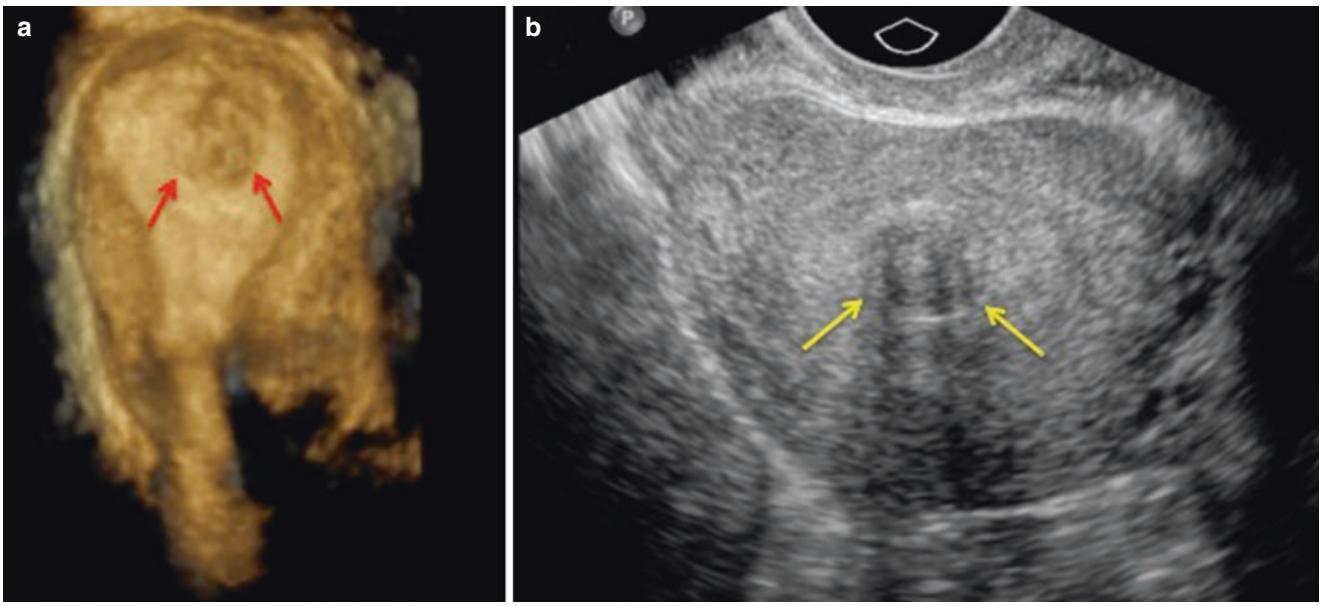

Fig. 8.28 The presence of leiomyomas can make the interpretation of exams difficult, representing one of the pitfalls, as in this case. In image (**a**), the *red arrows* show an impression on the fundal myometrium, suggesting a septate uterus. The *yellow arrows* in image (**b**) show that this is a case of submucous leiomyoma totally projected into the endometrial cavity

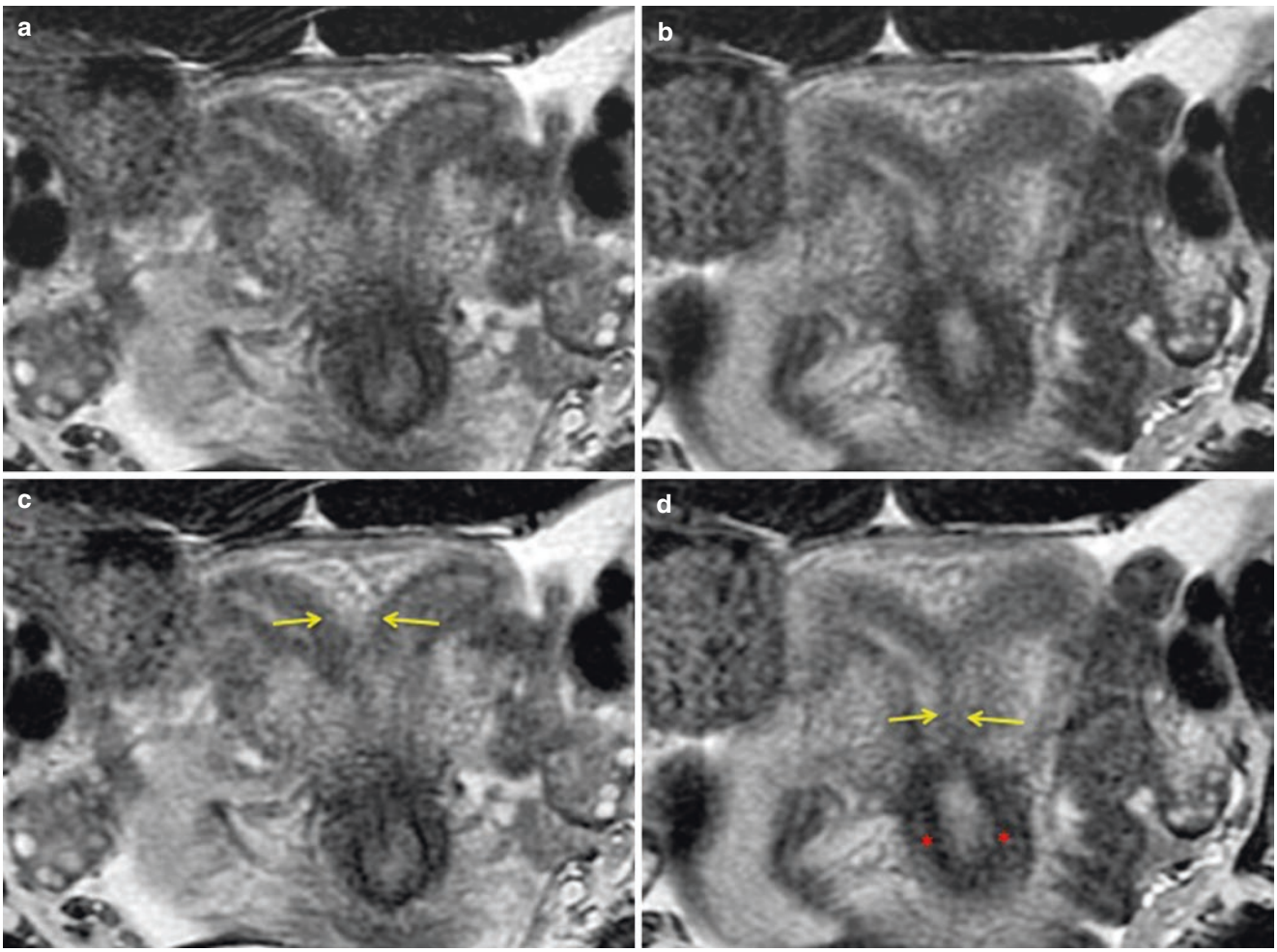

Fig. 8.29 Successive coronal sections of the uterus (**a, b**). The *arrows* in (**c**) show a muscular component of the septum. The *yellow arrows* in (**d**) show its more fibrous component, which has a filiform aspect and low-intensity signal on T2, extending to the internal ostia of the uterine colon (*red asterisks*)

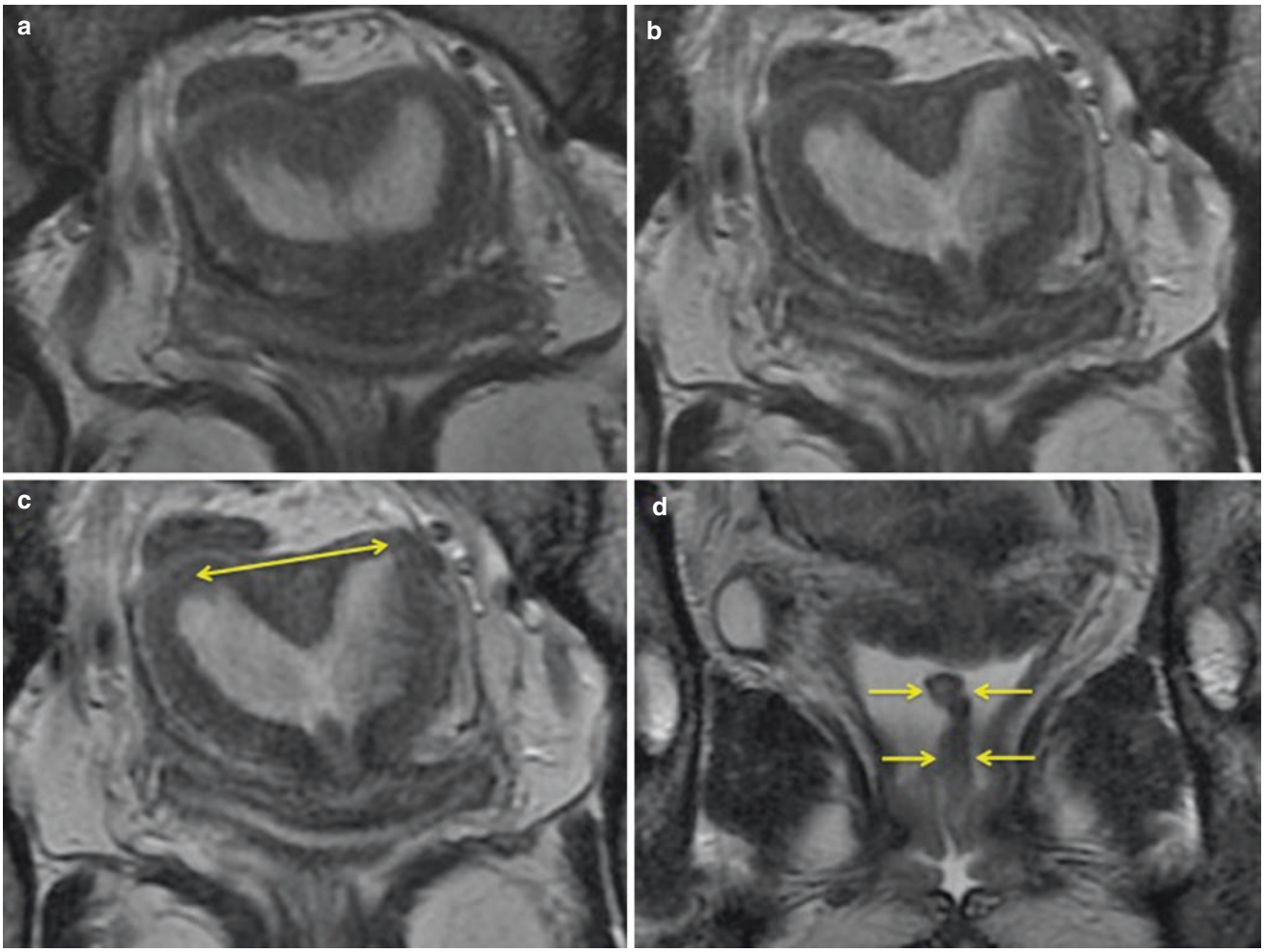

Fig. 8.30 (**a**, **b**) two successive images of the uterus in the true coronal plane. In (**c**), the *yellow arrow* demarcates the interostial line, an aspect which according to the morphometrical criteria represents a bicornuate uterus. (**d**) the *yellow arrows* indicate the vaginal septum

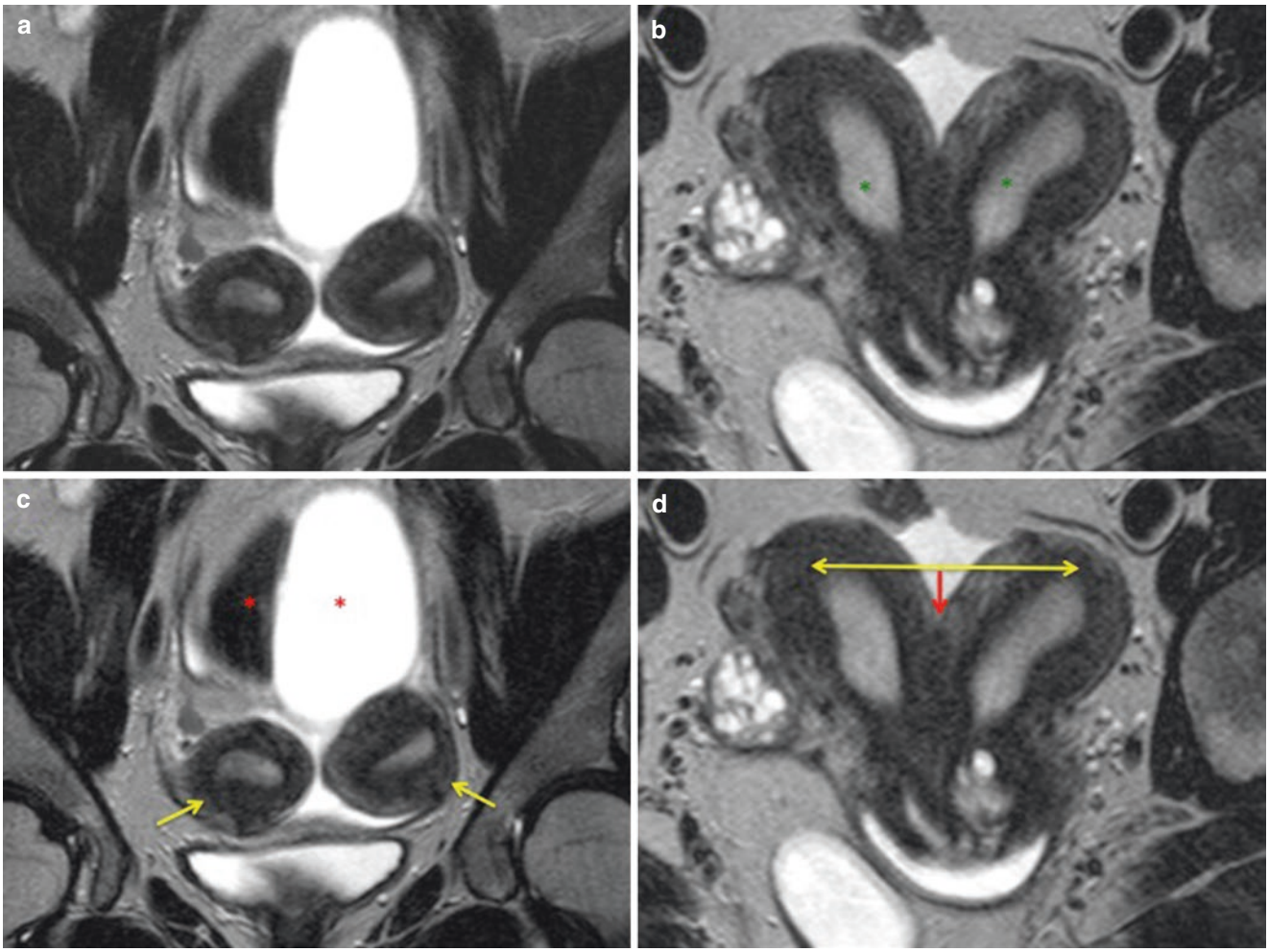

Fig. 8.31 (**a**) T2 weighted image in the coronal plane; (**b**) Axial plane image revealing a fundal indentation. The *green asterisks* of figure b show a high signal intensity on T2 weighted images of the endometrium (secretory phase) the *yellow arrows* in (**c**) show a bifid of the endometrial cavities. *Red asterisks* demonstrate part of the sigmoid colon and pelvic cyst. (**d**) Positioning of the interostial line (*yellow arrow*), There is a fissure in the uterine fundus (*red arrow*), whose myometrium merges near the cervix. This is a bicollis bicornuate uterus

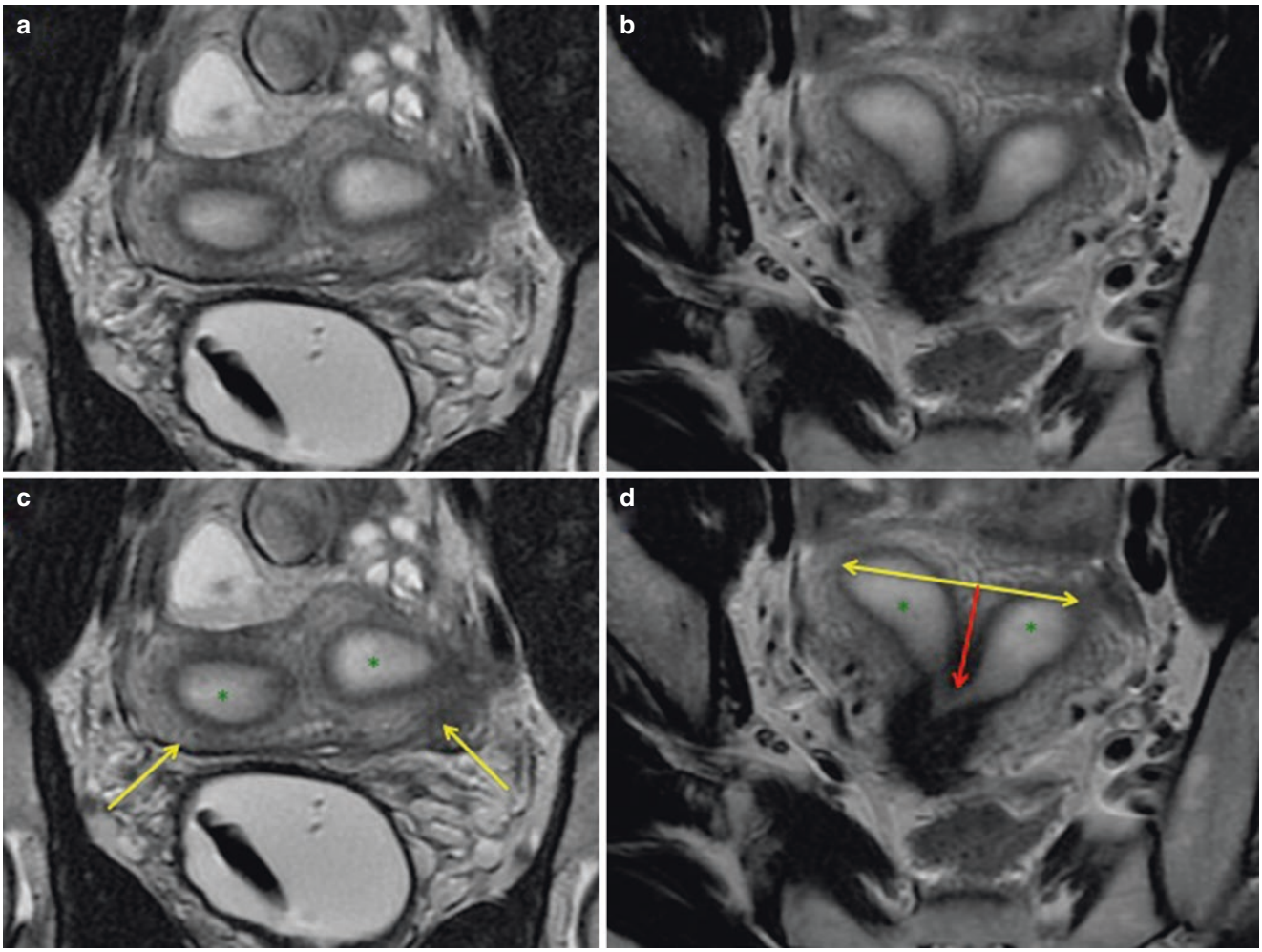

Fig. 8.32 (**a**) Coronal image showing the presence of two uterine cavities with tissue of a signal intensity similar to that of the myometrium interposing between the cavities (*yellow arrows* in **c**). (**b**) Unlike the previous exam, as can be seen, the fundal summit is rectilinear and located above the interostial line (shown in **d**). This is a partial septate uterus, with only a single colon. The septum in this case is composed of muscular tissue, as with most uteri with partial septation [4]

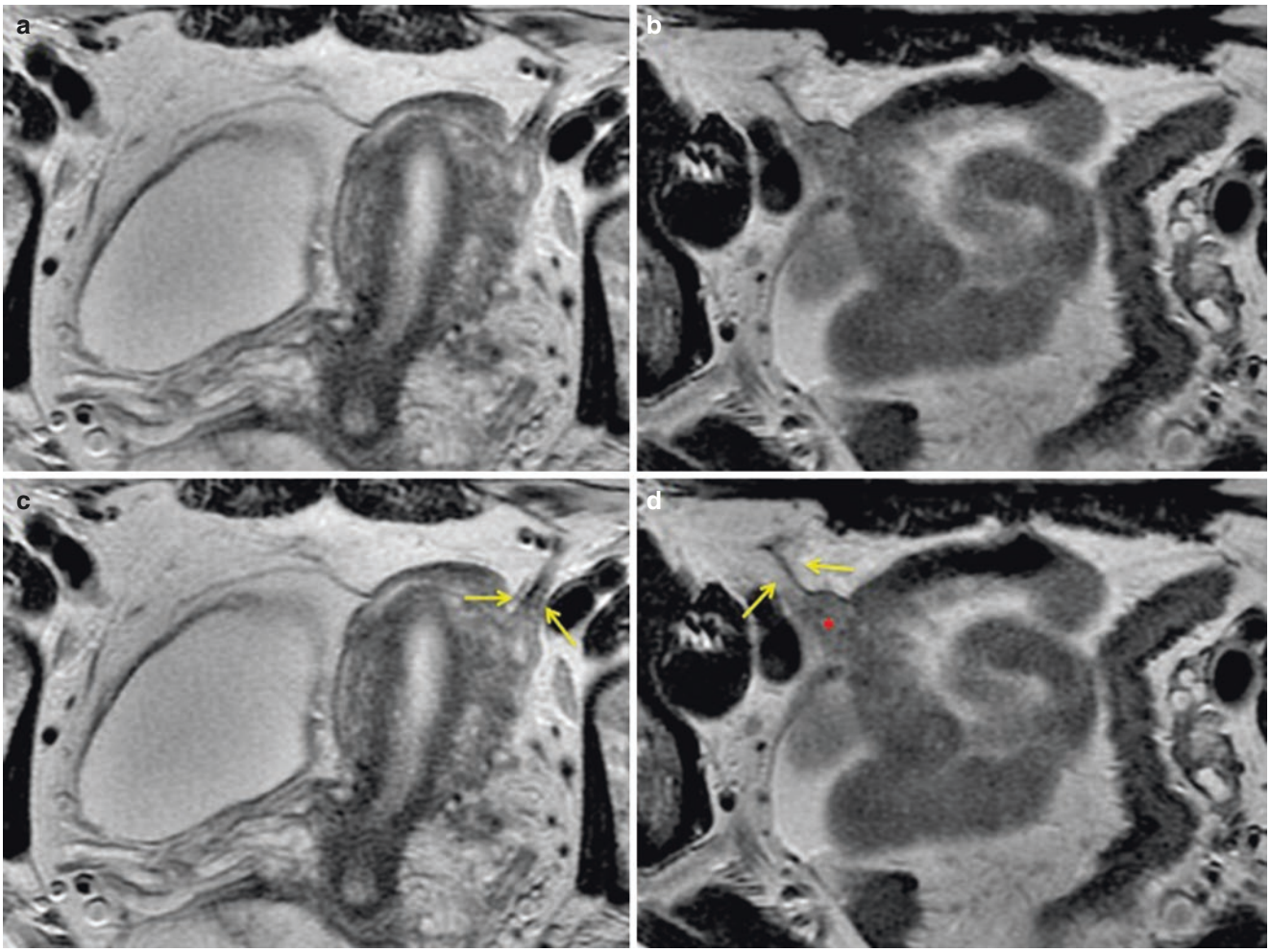

Fig. 8.33 T2 weighted axial images. The uterus has a fusiform and elongated aspect, without the triangular piriformis configuration, forming a unicornuate uterus. In these cases we aim to identify the round ligaments (*yellow arrows* in images **c**, **d**). When there is complete aplasia of one of the uterine horns, these ligaments emerge directly from the ovary (*asterisks* in image **d**). In our case, an intermediate signal intensity can be seen adjacent to the round ligament of the right side. This is a non-communicating rudimentary horn with a non-viable endometrium [15]

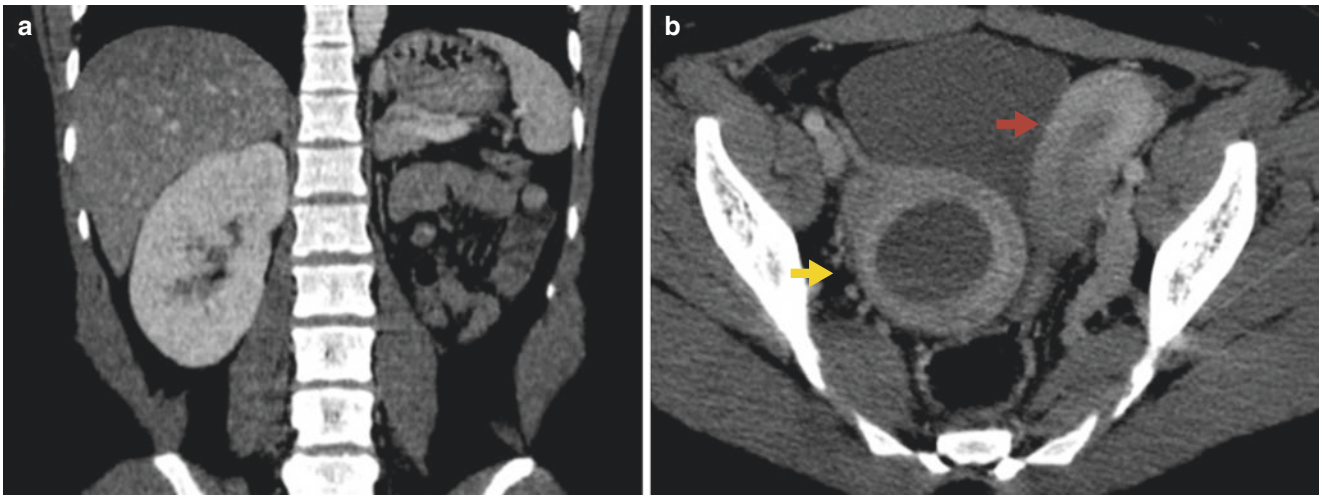

Fig. 8.34 Tomography is not used in the assessment of uterine malformations due to the ionizing radiation and because it is a sub-optimal examination since it cannot determine whether there are concommitant vaginal and cervical alterations. Occasionally, however, some types of MDAs can present conditions with acute abdominal pain, as in this case. (**a**) Shows agenisis of the left kidney. In the pelvic region, an elliptic fusiform uterine horn was identified on the left side (*red arrow* in **b**). On the right side, there is an oval-shaped image with a hypodense center (*yellow arrow* in **b**). The final diagnosis was a unicornuate uterus, with a non-communicating cavitated right horn and a non-viable endometrium. This painful condition is a result of distention of the non-communicating horn, whose influx of endometrial content may occur in the interior of the uterine cavity, causing endometriosis. It is one of the few cases in which surgery is indicated in MDAs. At the time of diagnosis, it was not possible to differentiate between the unicornuate and didelphic uterus (and their diverse variations), and there were no concommitant vaginal alterations. Vaginal septa are present in 25% of bicornuate uteri and in 75% of septate uteri [4]

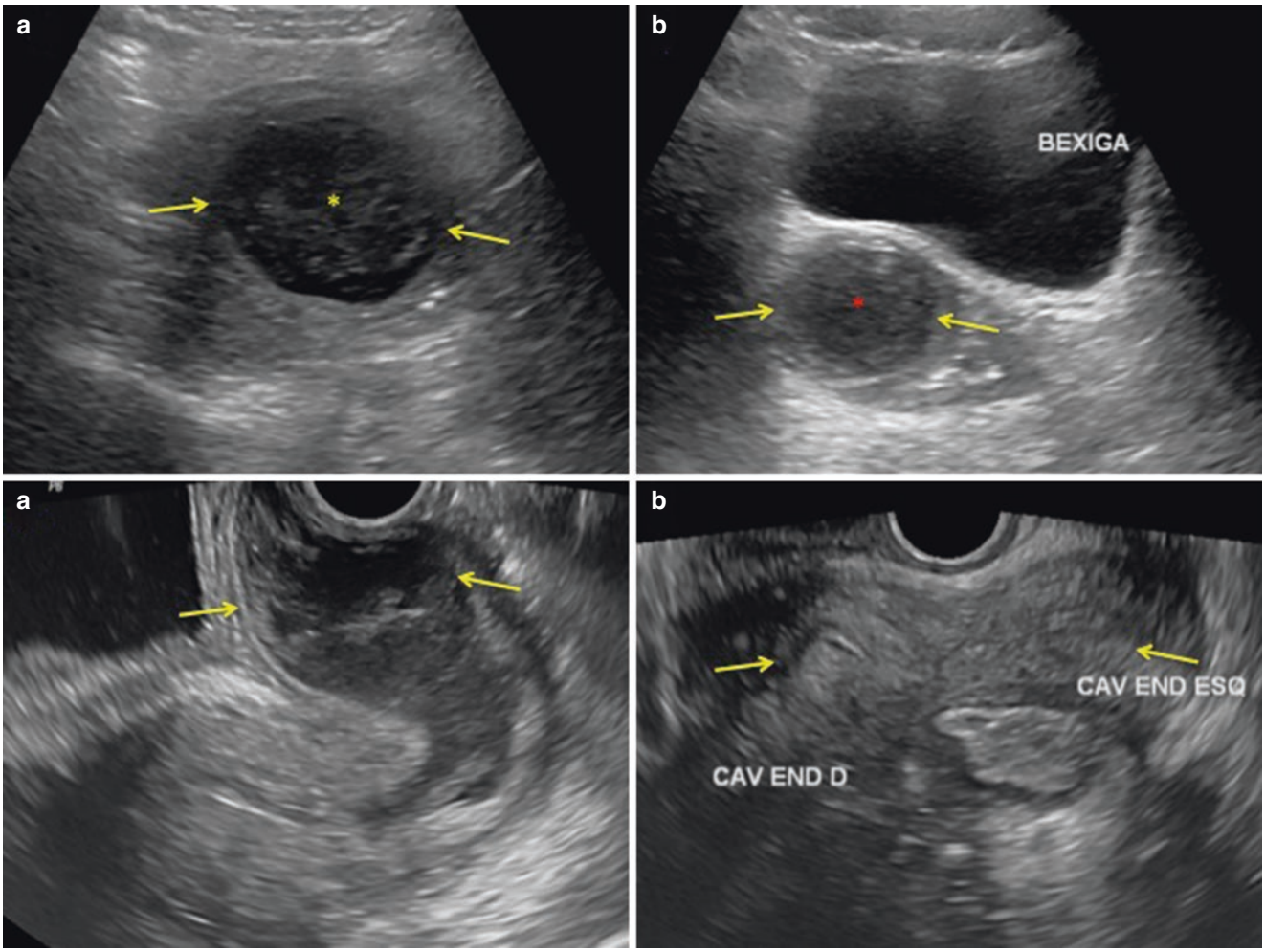

Fig. 8.35 A 25-year-old patient with fever, abdominal pain and signs of peritonitis. Presented to the emergency room where suprapubic and trans-vaginal ultrasound exams were carried out initially. (**a**) Axial image of a circumscribed hypoechogenic lesion of the mesogastric region (*yellow arrows*); the intralesional content is thick (*red asterisk*). (**b**) Suprapubic ultrasound revealing oval-shaped hypoechogenic lesion located in the retropubic region (*yellow arrows*). *Red asterisk*: thick intralesional content. (**c**) Transvaginal ultrasound images: a thick and echogenic content similar to that shown in the *asterisks* of figures a and b filling part of the vaginal cavity (*yellow arrows*). (**d**) Bifid and divergence of the endometrial cavity (*yellow arrows*). The patient underwent a total abdominal computed tomography (CT)

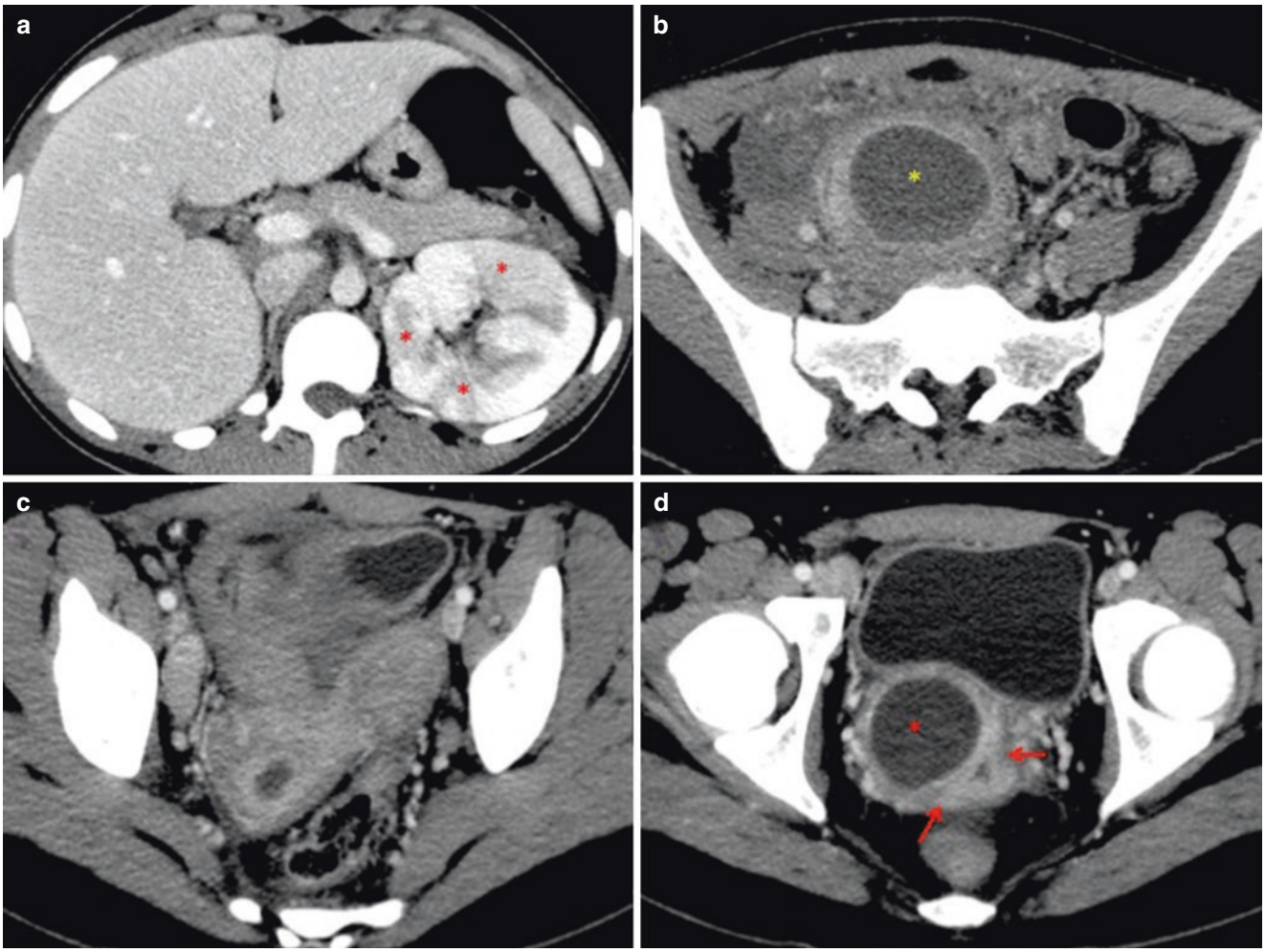

Fig. 8.36 Axial CT images of the complete abdomen with intravenous contrast. (**a**) Agenisis of the right kidney, with the left presenting vicarious aspects and signs of pyelonephritis, characterized by the sparse hypodense cuneiform areas in the parenchyma (*red asterisks*). (**b**) The *yellow asterisk* corresponds to image (**a**) of Fig. 32 (mesogastric lesion). (**c**) Clear bifid and divergence between the uterine horns (*yellow arrows*). (**d**) Distention of the vaginal cavity (*red asterisk*, corresponding with images (**b**) and (**c**) of Fig. 8.32). The *red arrows* show one of the compressed vaginal canals. The final diagnosis was Herlyn-Werner-Wunderlich syndrome, which is characterized by the triad of a didelphic uterus, obstructed hemivagina, and unilateral renal agenisis

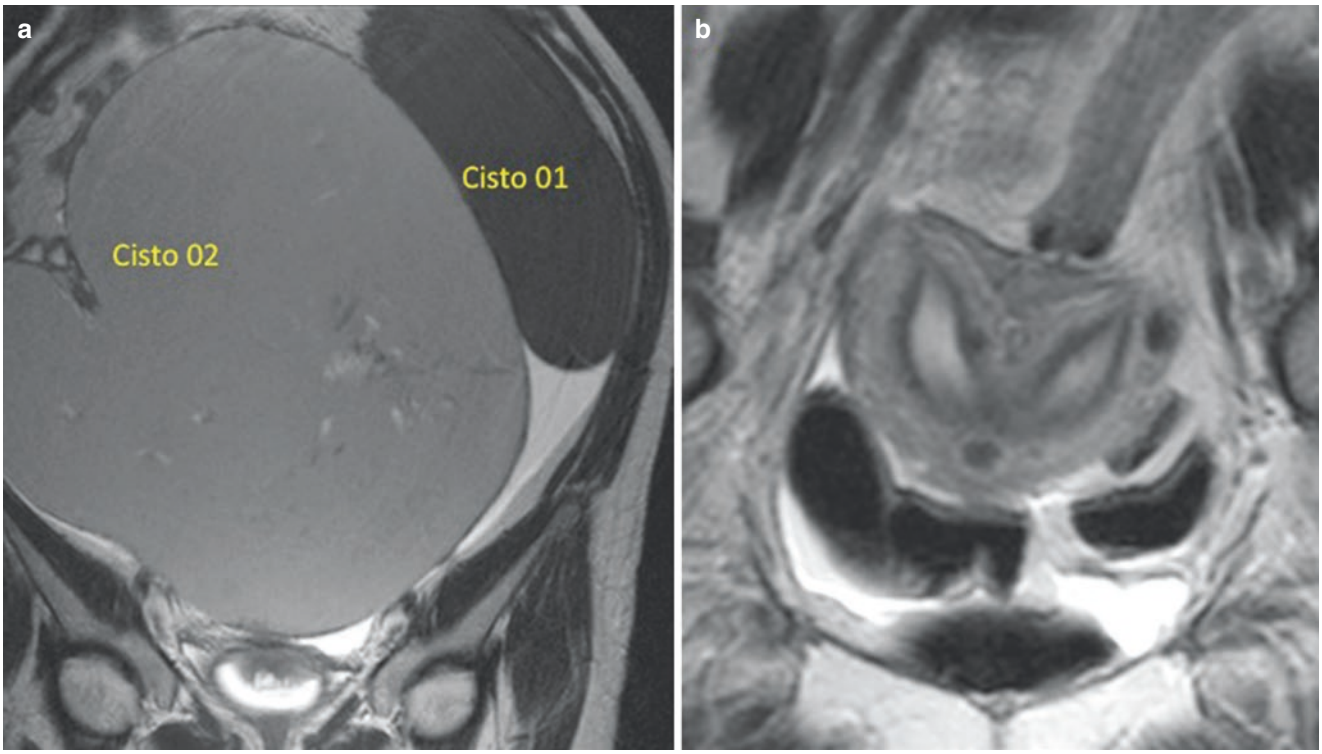

Fig. 8.37 T2 weighted coronal image of a 52-year-old patient presenting with increased abdominal volume. (**a**) Two volumous cystic formations, one with a low-intermediate signal intensity and the other with low-signal intensity on T2 weighted image. (**b**) Septate uterus, discovered by chance. The cystic formations were removed and diagnosed as two volumous endometriomas

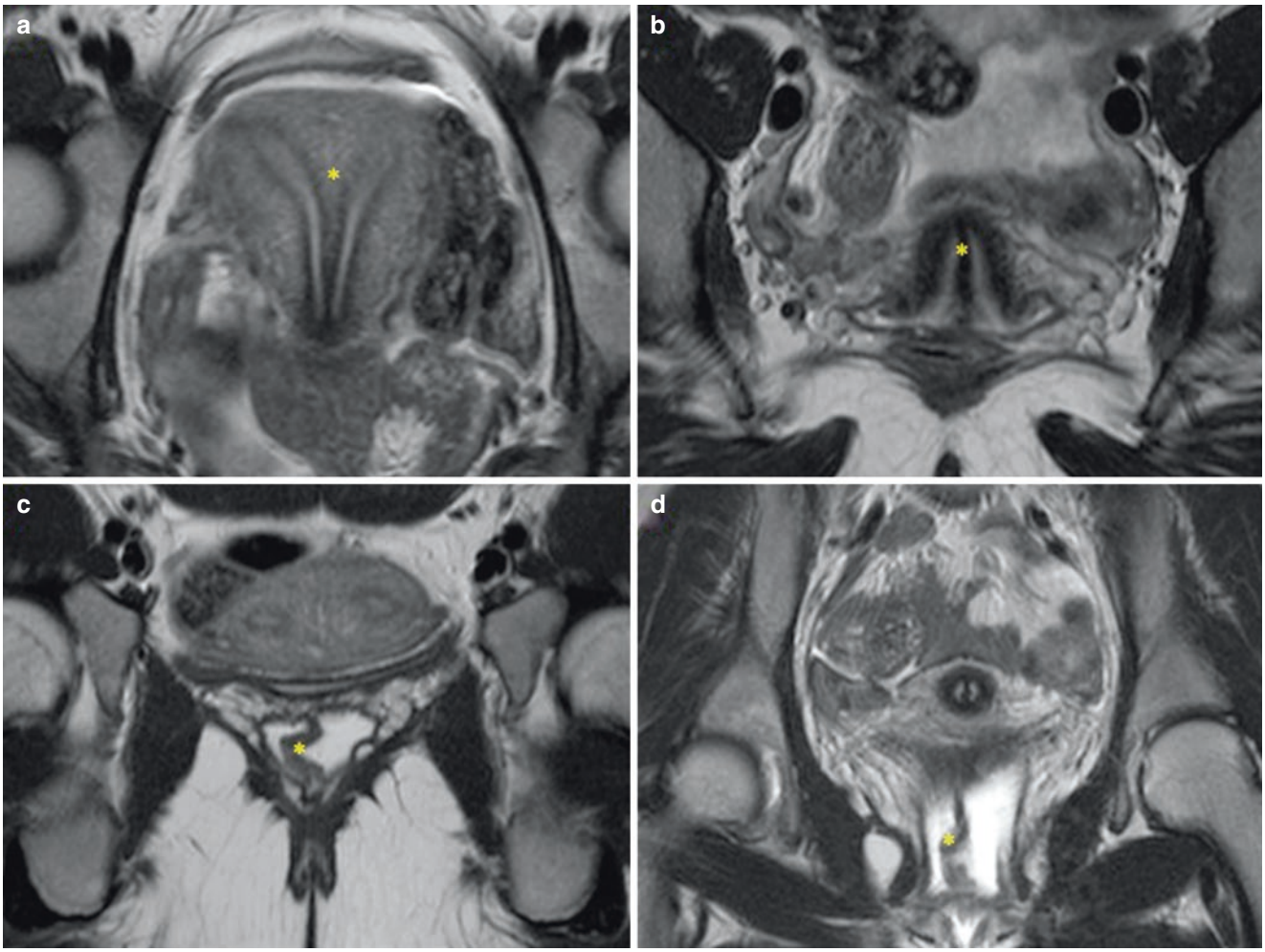

Fig. 8.38 The asterisks in images (**a**–**d**) show the extension of the septum until the inferior third of the vagina, forming a complete septate uterus

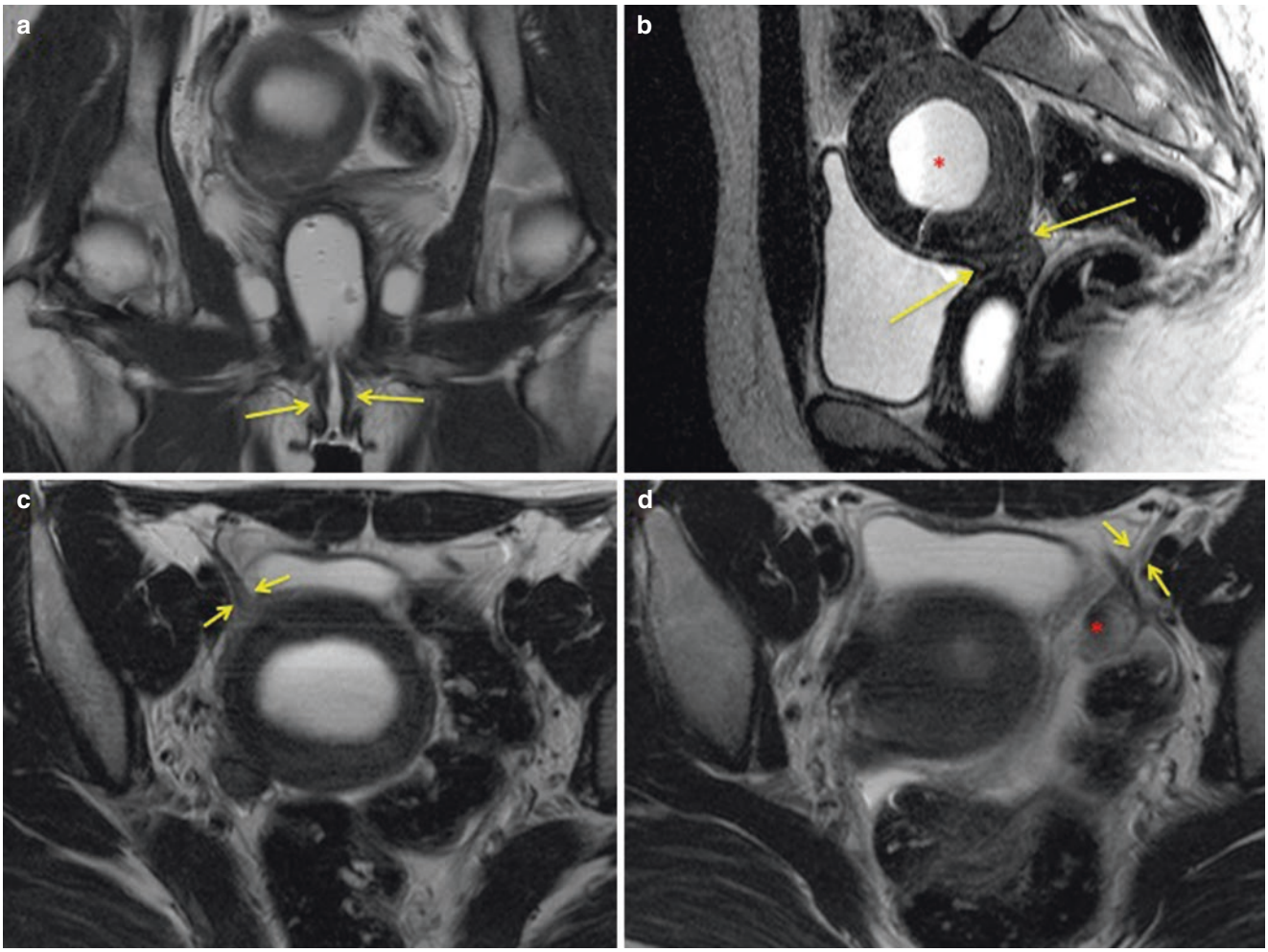

Fig. 8.39 This case shows one of the variants of MRKH syndrome. (**a**) The *yellow arrows* point to the inferior third of the vagina, which can be identified in its entire extension. (**b**) Vagina in blind fundus, without the uterine body. The uterus has a rudimentary aspect, with its cavity distended by liquid/hematic content (red asterisk). (**c**,**d**) The *yellow arrows* point to the round ligament. The red asterisk is located in the remaining contralateral uterus. Surgery revealed a hypoplastic uterus, with agenisis of the colon and foci of superficial endometriosis on the external serous (not identified in exam). Diverse combinations can be found in MRKH syndrome: normal uterus with vaginal agenisis, rudimentary uterus with normal vagina, and agenisis of the body and colon with normal vagina, among others [16]

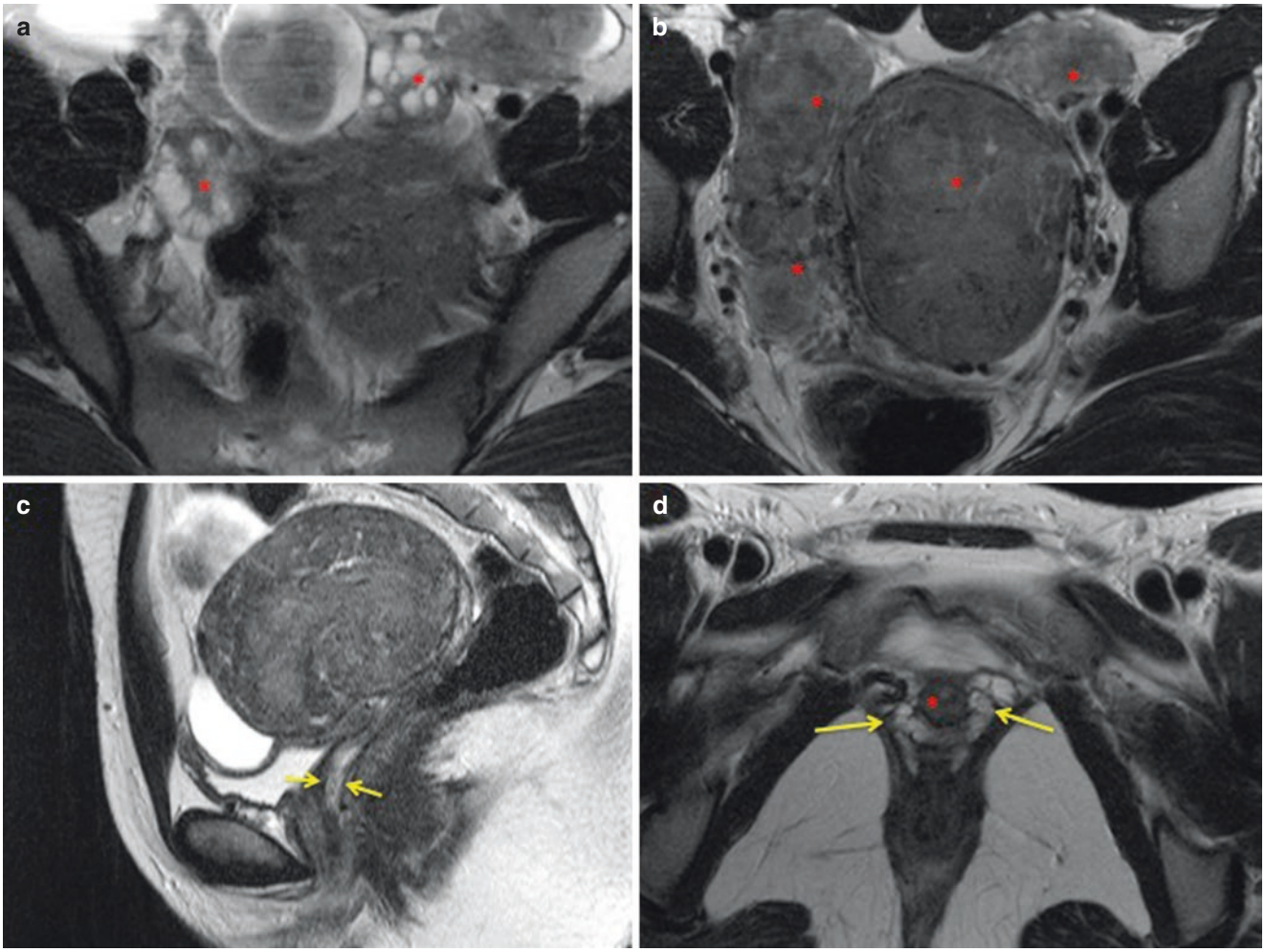

Fig. 8.40 A difficult case for classification of AFRS, identified in T2 weighted images. (**a**) *Asterisks* demarcate the two ovaries, which present a multicystic aspect. (**b**) The *red asterisks* are located in solid nodules with signal intensity similar to that of leiomyomas, which occupy the greater part of the pelvic cavity. (**c**) Sagittal image showing agenisis of the superior and middle third of the vagina, and absence of the urethra (*red asterisk*) where the vagina is not identified. The patient presents with amenorrhea and short vagina, with longitudinal diameter 4.0 cm (**d**) Left ovary (*red asterisk*) and round ligament (*yellow arrow*)

References

1. Tognotti E. Causa uterina. In: Tognotti E, editor. Infertilidade: da prática clinica a laboratorial. Primeira edição ed. São Paulo: Editora Manole; 2014. p. 111–42.
2. Pabuccu R, Gomel V. Reproductive outcome after hysteroscopic metroplasty in women with septate uterus and otherwise unexplained infertility. Fertil Steril. 2004;81(6):1675–8.
3. Chan YY, Jayaprakasan K, Zamora J, Thornton JG, Raine-Fenning N, Coomarasamy A. The prevalence of congenital uterine anomalies in unselected and high-risk populations: a systematic review. Hum Reprod Update. 2011;17(6):761–71.
4. Troiano RN, McCarthy SM. Mullerian duct anomalies: imaging and clinical issues. Radiology. 2004;233(1):19–34.
5. Acien P, Acien MI. The history of female genital tract malformation classifications and proposal of an updated system. Hum Reprod Update. 2011;17(5):693–705.
6. Mucowski SJ, Herndon CN, Rosen MP. The arcuate uterine anomaly: a critical appraisal of its diagnostic and clinical relevance. Obstet Gynecol Surv. 2010;65(7):449–54.
7. Di Spiezio SA, Campo R, Gordts S, Spinelli M, Cosimato C, Tanos V, et al. The comprehensiveness of the ESHRE/ESGE classification of female genital tract congenital anomalies: a systematic review of cases not classified by the AFS system. Hum Reprod. 2015;30(5):1046–58.
8. Moini A, Mohammadi S, Hosseini R, Eslami B, Ahmadi F. Accuracy of 3-dimensional sonography for diagnosis and classification of congenital uterine anomalies. J Ultrasound Med. 2013;32(6):923–7.
9. Saravelos SH, Cocksedge KA, Li TC. Prevalence and diagnosis of congenital uterine anomalies in women with reproductive failure: a critical appraisal. Hum Reprod Update. 2008;14(5):415–29.
10. Salim R, Regan L, Woelfer B, Backos M, Jurkovic D. A comparative study of the morphology of congenital uterine anomalies in women with and without a history of recurrent first trimester miscarriage. Hum Reprod. 2003;18(1):162–6.
11. Bermejo C, Martinez Ten P, Cantarero R, Diaz D, Perez Pedregosa J, Barron E, et al. Three-dimensional ultrasound in the diagnosis of Mullerian duct anomalies and concordance with magnetic resonance imaging. Ultrasound Obstet Gynecol. 2010;35(5):593–601.
12. Piccinini PS, Doski J. Herlyn-Werner-Wunderlich syndrome: a case report. Rev Bras Ginecol Obstet. 2015;37(4):192–6.
13. Yoo RE, Cho JY, Kim SY, Kim SH. A systematic approach to the magnetic resonance imaging-based differential diagnosis of congenital Mullerian duct anomalies and their mimics. Abdom Imaging. 2015;40(1):192–206.
14. Homer HA, Li TC, Cooke ID. The septate uterus: a review of management and reproductive outcome. Fertil Steril. 2000;73(1):1–14.
15. Buy JN. Congenital abnormalities of the Mullerian ducts. In: Buy JN, editor. Gynecological imaging. Berlin/Heidelberg: Springer; 2013. p. 513–31.
16. Bailão LA. As Anomalias Uterinas Congênitas. In: Bailão LA, editor. Diagnóstico Ultrassonográfico em Ginecologia. Rio de Janeiro: Livraria e Editora REVINTER Ltda; 2013. p. 221–313.

Part II

Imaging of Male Infertility

Obstructive Disorders

9

Dáfne Daniela Dias Melquiades
and Leonardo Kayat Bittencourt

Obstructive Diseases
1. Congenital bilateral agenesis of vas deferens
2. Obstruction of ejaculatory ducts
3. Prostate cysts

Obstructive Diseases
1. Abnormal development of vas deferens and seminal vesicles
2. Inflammatory changes in seminal tract
3. Prostatic cysts

Introduction

The knowledge of embryology and the anatomy of the genitourinary system is essential for understanding the anomalies and diseases of the male reproductive system. The main causes of male infertility can be classified as congenital, acquired, infectious, or hormonal. The evaluation of male infertility is based on history, physical examination, and laboratory tests, with imaging an essential tool for diagnosing obstructive conditions.

Ultrasonography (US), computed tomography (CT), and magnetic resonance imaging (MRI) can provide high-resolution images of the genitourinary system, thereby enabling a more accurate diagnosis and hence proper treatment.

D.D.D. Melquiades (✉)
Department of Radiology, CDPI Clinics (DASA),
Rio de Janeiro, RJ, Brazil
e-mail: dafnedani@yahoo.com.br

L.K. Bittencourt
Department of Radiology, CDPI Clinics (DASA) and Fluminense
Federal University (UFF), Rio de Janeiro, RJ, Brazil

L.R.M.F. de Souza et al. (eds.), *Atlas of Imaging in Infertility*, DOI 10.1007/978-3-319-13893-0_9

Male Reproduction

The conditions required for male fertility involve a reproductive system formed by functional ectopic testes and normal seminal passageways with no obstructions (epididymis, vas deferens [VD], and urethra) alongside normal accessory glands (prostate, seminal vesicles [SVs], and bulbourethral glands).

- The testes are responsible for the synthesis of steroid hormones, the production of mature sperm, and the development and maintenance of secondary sexual characteristics and libido.
- The maturation, transport, concentration, and storage of sperm occur in the epididymis – a system of ductules that emerges posteriorly from the testis.
- The VD is responsible for storing and transporting sperm toward the urethra; moreover, it reabsorbs sperm that has not yet been expelled.
- The SVs are glands responsible for secreting a thick, alkaline liquid that blends with the sperm when passing through the ejaculatory ducts and the urethra.
- The prostate secretes part of the semen that is expelled through the urethra. Bulbourethral glands are responsible for secreting the first part of the ejaculate and serve to lubricate the reproductive tract (Fig. 9.1 Anatomy).

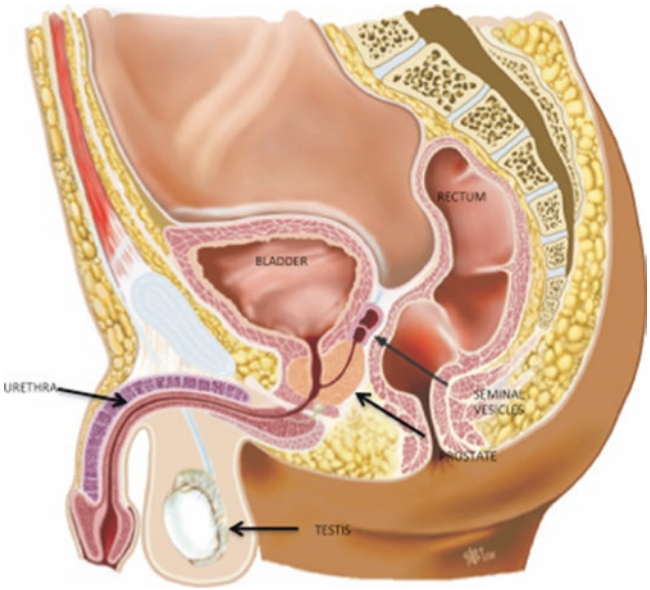

Fig. 9.1 Normal anatomy (Courtesy of Joao Paulo Kawaoka Matushita Junior, AC Camargo-Cancer Center)

Embryology and Anatomy of the Genitourinary Tract

In the 5th week of gestation, the ureteric bud (metanephric duct) becomes a branch of the Wolffian duct, next to its entry in the cloaca, which joins the metanephric blastema and becomes the primitive kidney at about the 6th week of gestation. Between the 6th and 7th weeks, the embryonic kidneys ascend, while the ureter acquires a separate opening to the bladder and migrates cranially [1].

In the 9th week of pregnancy, the kidneys are already as present as they are in adulthood. This relative upswing is basically due to the growth of the embryo's body caudally toward the kidneys, which take their retroperitoneal position (Fig. 9.2 Normal development of kidney).

In the 5th week of pregnancy, the early stages of gonadal development occurs alongside the differentiation of Leydig cells, leading to the apoptotic degeneration of paramesonephric ducts (Müllerian ducts) and the maintenance of Wolffian ducts in males. The two Müllerian ducts develop and run caudally, meeting and fusing in the midline with the growth of the urogenital sinus, eventually forming the prostatic utricle [1].

At 8 weeks of gestation, the proximal portion of each mesonephric duct becomes twisted, forming the epididymis. The remainder forms both the vas deferens and ejaculatory ducts.

The Wolffian ducts influence the development of the prostatic ducts that emerge from three areas of the epithelium and adjacent mesenchyme, in the portion of the urogenital sinus to be the floor of the prostatic urethra. Each of these groups is the source of each of the three zones of the prostate.

From the 12th week of pregnancy onward, seminal vesicles emerge as lateral outgrowths of the caudal end of each mesonephric duct. The seminal vesicles are located obliquely above the prostate, between the bottom of the bladder and the rectum; they drain into the ejaculatory ducts, which, in turn, drain into the prostatic urethra [2].

The ejaculatory ducts are tubular, bilateral structures that begin at the junction of the vas deferens and seminal vesicles and pass through the prostate into the prostatic urethra in the so-called *verumontanum* region [1].

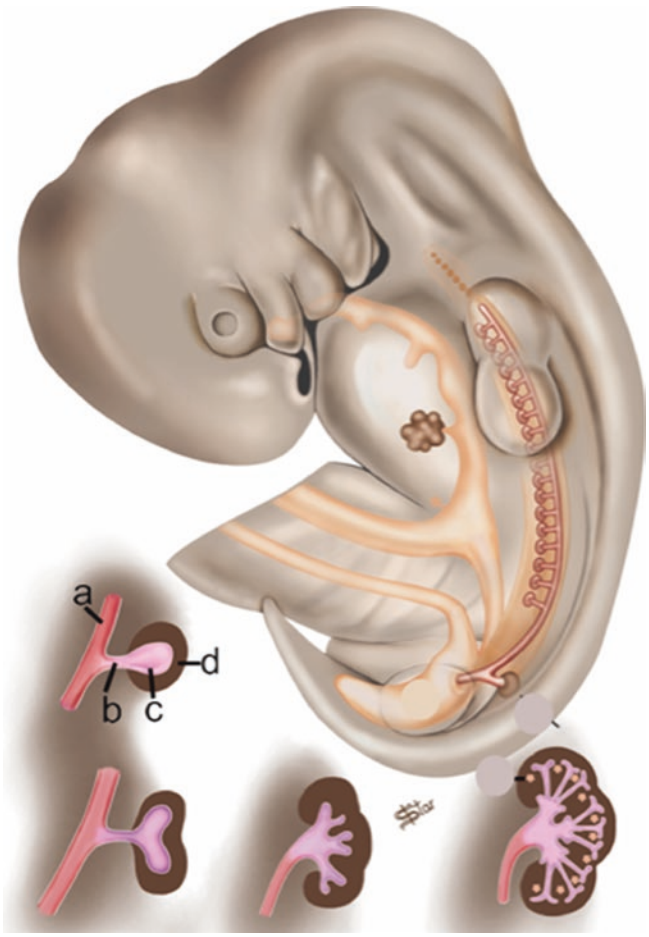

Fig. 9.2 Normal development of urogenital organs. (*a*) Mesonephic duct. (*b*) Ureteric. (*c*) Bud ureteric. (*d*) Metanephricblastema (Courtesy of Joao Paulo Kawaoka Matushita Junior, AC Camargo-Cancer Center)

Imaging Methods

The understanding of normal imaging findings on suprapubic or endorectal US, CT, and MRI is essential for understanding the obstructive causes of male infertility.

Ultrasonography (US)

US is easily accessible and is usually the first imaging study used to evaluate the genitourinary system. It is an innocuous method, with no ionizing radiation, and it enables dynamic images. However, US is one of the most operator-dependent imaging techniques. SVs are seen as symmetrical structures, with regular contours, homogeneous and hypoechoic in echotexture.

The vas deferens is seen as a slightly dilated tubular structure (ampulla) which can be seen medially to SVs. In oblique images, SVs and the terminal portion of the vas deferens can be seen together to form the ejaculatory duct [3].

The prostate gland at the base level shows more homogeneous echotexture and increased echogenicity than that of the seminal vesicles. At the midline level of the prostatic base, we often observe a hypoechoic, regular, and homogeneous area. At the glandular apex level there is the so-called "peripheral zone," which shows homogeneous echotexture [3] (Fig. 9.3).

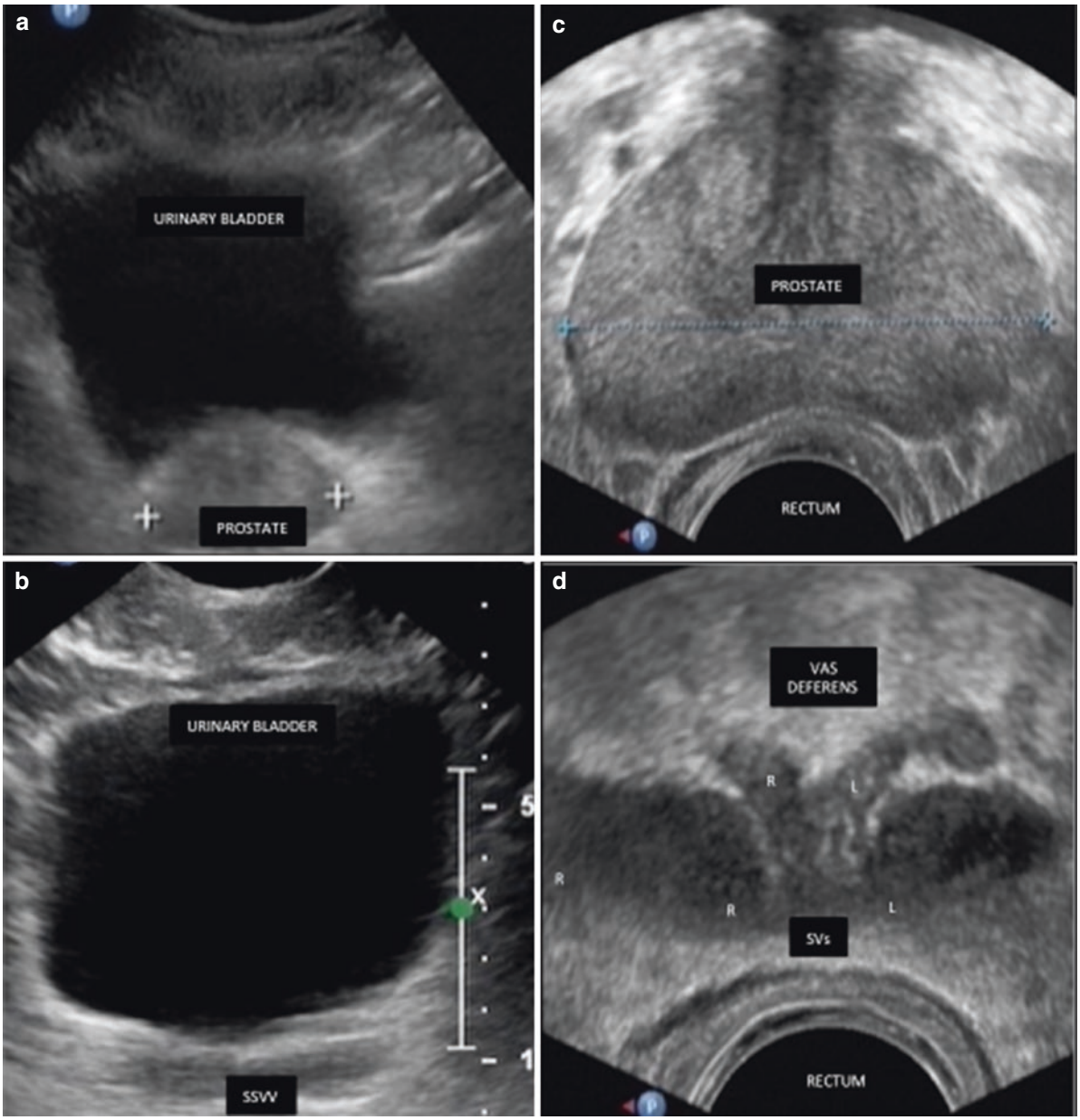

Fig. 9.3 Anatomy of the prostate, seminal vesicles, and vas deferens. (**a**,**b**) Abdominal US. (**c**,**d**) Transrectal US. Seminal vesicles (SVs) are two homogeneous, hypoechoic ovals that extend laterally upward from the bladder. Prostate is an elliptical, chestnut-shaped gland with smooth margins and a homogeneous internal echo pattern. The distal portion of the vas deferens is seen as a slightly dilated tubular structure (ampulla) medial to the SVs

Computed Tomography (CT)

A CT scan (X-ray CT) is another imaging method that can aid in diagnosis, especially of genitourinary system abnormalities. The disadvantage of CT is, nevertheless, its ionizing radiation as well as the lack of contrast in neighboring structures.

SVs are tubular, elongated, hypodense structures in a "bowtie" format, with some thin septa that can be identified after intravenous contrast [4].The prostate is presented as a hypodense image with homogeneous contrast uptake (Fig. 9.4).

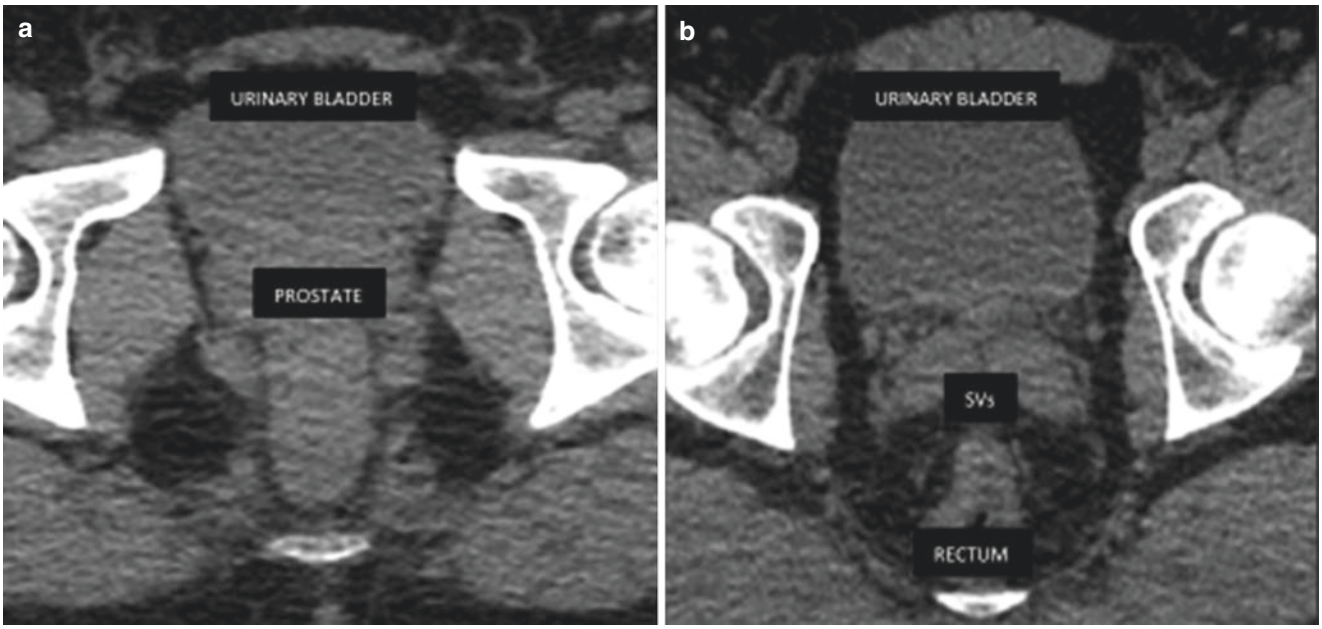

Fig. 9.4 Anatomy of the prostate, seminal vesicles and vas deferens. (**a,b**) Axial CT image. CT noninvasive modality, identifying calcifications, soft tissue masses or cystic lesions, but radiation involved

Magnetic Resonance Imaging (MRI)

Currently, MRI has emerged as a method with excellent accuracy for the diagnosis of both acquired and congenital lesions. MRI can assess the ejaculatory duct bilaterally, from the junction of VD and SVs to the *verumontanum*.

SVs are seen as structures containing fluid, elongated with thin septa and low-signal intensity on T1 weighted images and high-signal intensity on T2-weighted images [4]. The intra-abdominal VD portions are seen as bilateral symmetric tubular structures with low-signal intensity on both T1- and T2-weighted images.

The prostate on T2-weighted images shows homogeneous high signal intensities in the shape of a "crescent moon" or horn on the axial plane. The prostatic capsule defines the contour of the gland and is seen as a thin hypointense line. The central, transitional, and periurethral zones are not clearly distinguished from each other by MRI; as a result, they are jointly assessed and receive the generic name of "internal gland" [5]. The normal internal gland shows intermediate signal intensity on T2 and is often interspersed with hyperintense limited foci, related to hyperplastic nodules of benign prostatic hyperplasia (BPH) in greater or smaller volume. This, in turn, is delimited by the peripheral zone structure called "surgical prostatic capsule," which presents as a hypointense thin layer on T2, with a well-limited aspect [2, 5, 6] (Fig. 9.5).

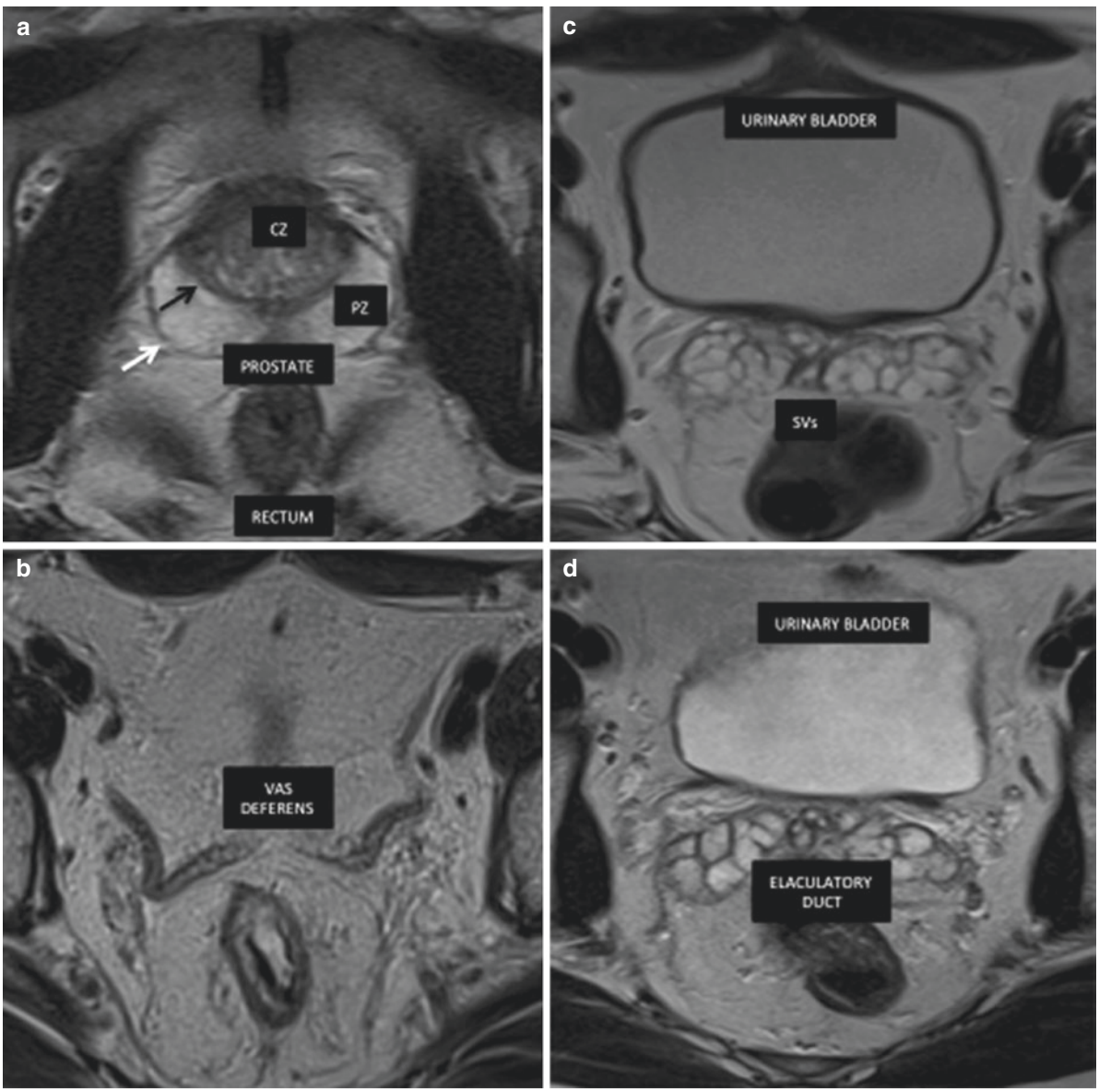

Fig. 9.5 Anatomy of the prostate, seminal vesicles and vas deferens. MRI modality of choice due to its soft tissue contrast and multi-planar capabilities and no ionizing radiation. (**a**) Axial T2-weighted MR image shows peripheral zone (*PZ*) of the prostate with homogeneous hyperintensity, and the central zone (*CZ*) with hypointensity of the prostate capsule (*white arrow*) and the surgical capsule (*black arrow*). (**b**) The vas deferens is seen as a tubular structure medial to the seminal and displays low T2 signal intensity. (**c**) Axial T2-weighted MR image shows the normal hyperintensity lobulated pattern of the seminal vesicles. (**d**) Axial T2-weighted MR image shows the anatomy of the ejaculatory duct (ED)

Development Anomalies of Vas Deferens and Seminal Vesicles

VD and SVs are urogenital subsidiary bodies, as described above. The development of these organs is related to the urinary system.

During embryogenesis, SVs or VD anomalies may be associated with renal and/or ureteral anomalies. Due to their anatomical location, SVs and VD may be involved in diseases of adjacent organs, such as the prostate and rectum [5].

SVs are responsible for most of the ejaculate; thus, agenesis or hypoplasia may lead to changes in both the volume and the quality of semen, which is, in some patients, a cause of infertility. VD tubes act as passage tubes for sperm into the ejaculatory ducts. They are also responsible for maintaining the properties of the sperm on their way to the urethra. Therefore, agenesis may, in some cases, cause changes in seminal parameters, generating infertility.

Congenital Abnormalities

Congenital Changes: Seminal Vesicles

Clinical Manifestation

In general, changes in SVs are found incidentally during imaging; in some cases, however, patients may present hematospermia, recurrent infections, and infertility.

Unilateral Agenesis of the SVs

Unilateral agenesis of the SVs occurs when there is a change in embryogenesis before the 7th week of pregnancy, when the ureteric bud originates from the mesonephric duct. It is usually associated with ipsilateral renal agenesis (79% of cases) or other renal anomalies (12% of cases), or even with normal kidney (9%) [1, 7–9] (Figs. 9.6 and 9.7).

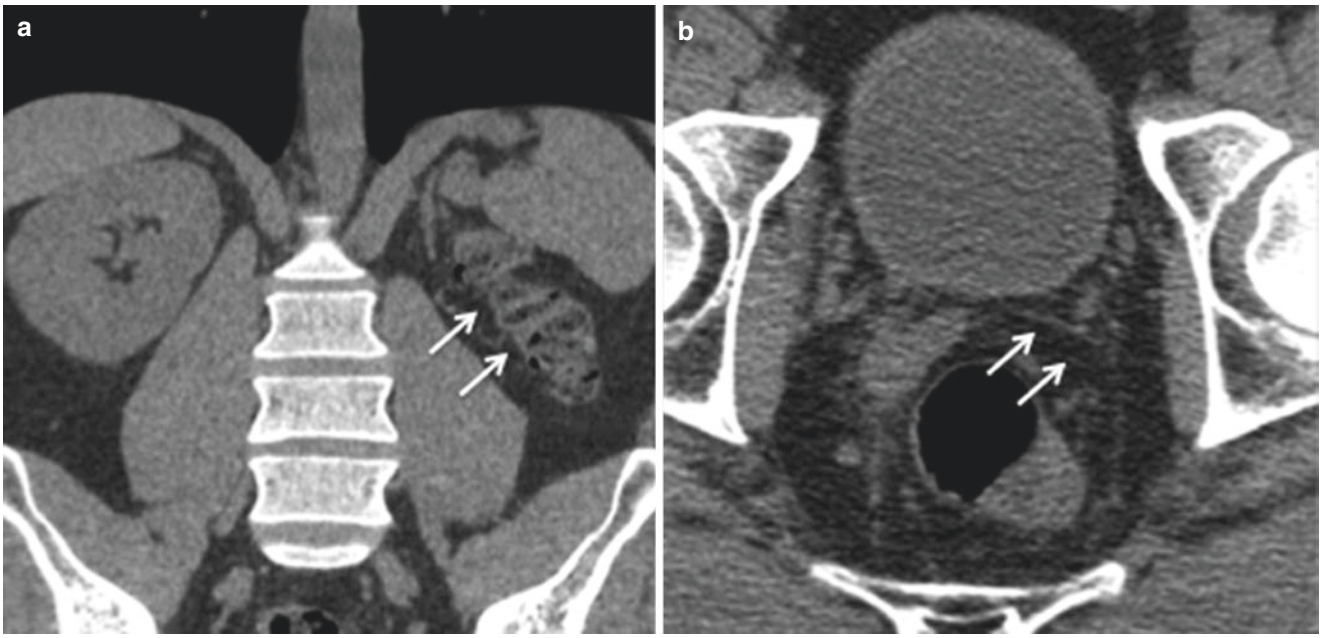

Fig. 9.6 Agenesis of the SV and of the kidney in a 32-year-old man with infertility. CT image in the coronal (**a**) and axial (**b**) shows left renal agenesis (*arrow*) and ipsilateral absence of the SV (*arrows*)

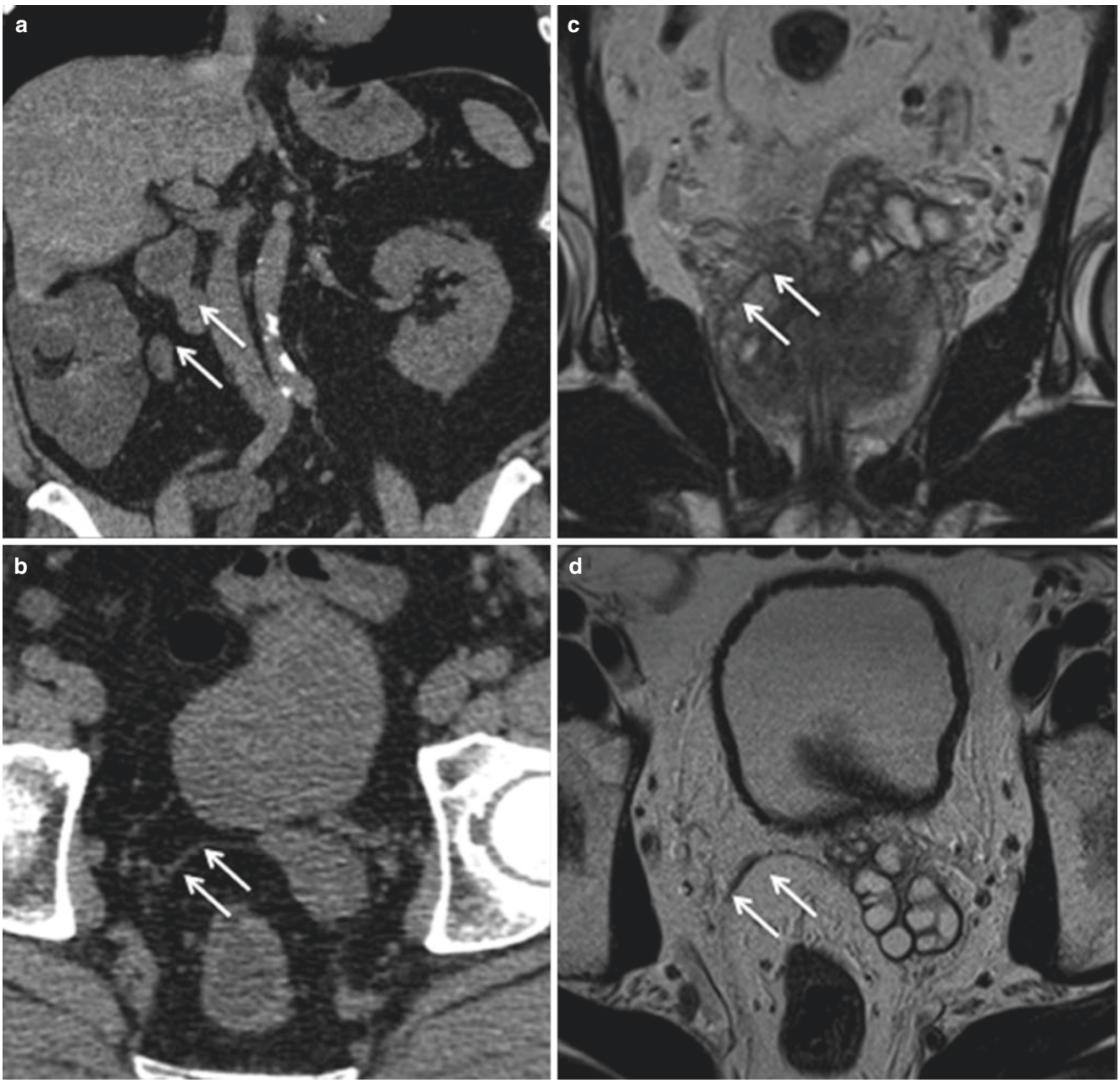

Fig. 9.7 Agenesis of the SV and of the kidney in a 30-year-old man with infertility. CT image shows right renal agenesis (**a**) and absence of the SV (**b**) ipsilateral (*arrows*). Coronal (**c**) and axial (**d**) T2-weighted MR image shows again

Bilateral Agenesis of the SVs

Bilateral agenesis of the SVs is associated with gene mutations in the cystic fibrosis transmembrane conductance regulator (CFTR), causing luminal blockage by thick secretions. It is usually associated with bilateral agenesis of the VD and normal kidneys [1, 7–9] (Fig. 9.8).

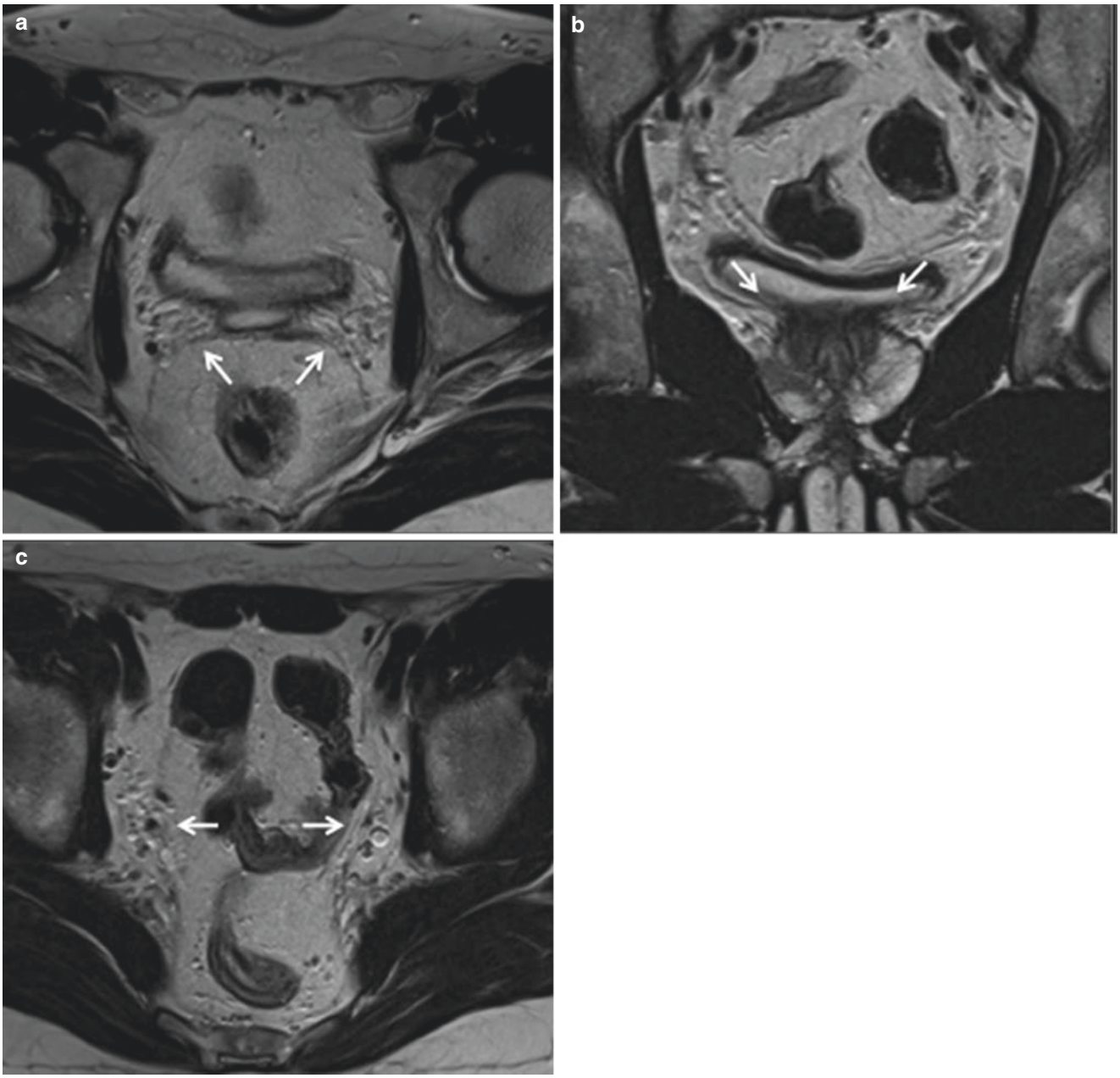

Fig. 9.8 Agenesis of the SV and ED in a 26-year-old man with infertility. Axial (**a**) and coronal (**b**) T2-weighted MR image shows bilateral absence of the SV (*arrows*). Axial (**c**) T2-weighted MR image shows bilateral absence of the ED (*arrows*)

Hypoplasia of the SVs

Hypoplasia of the SVs refers to small congenital glands detected as imaging findings with smaller and thin septa. It may be associated with hypogonadism, cryptorchidism, and other congenital abnormalities of the genitourinary system, or be an isolated finding [1, 7–9] (Fig. 9.9)

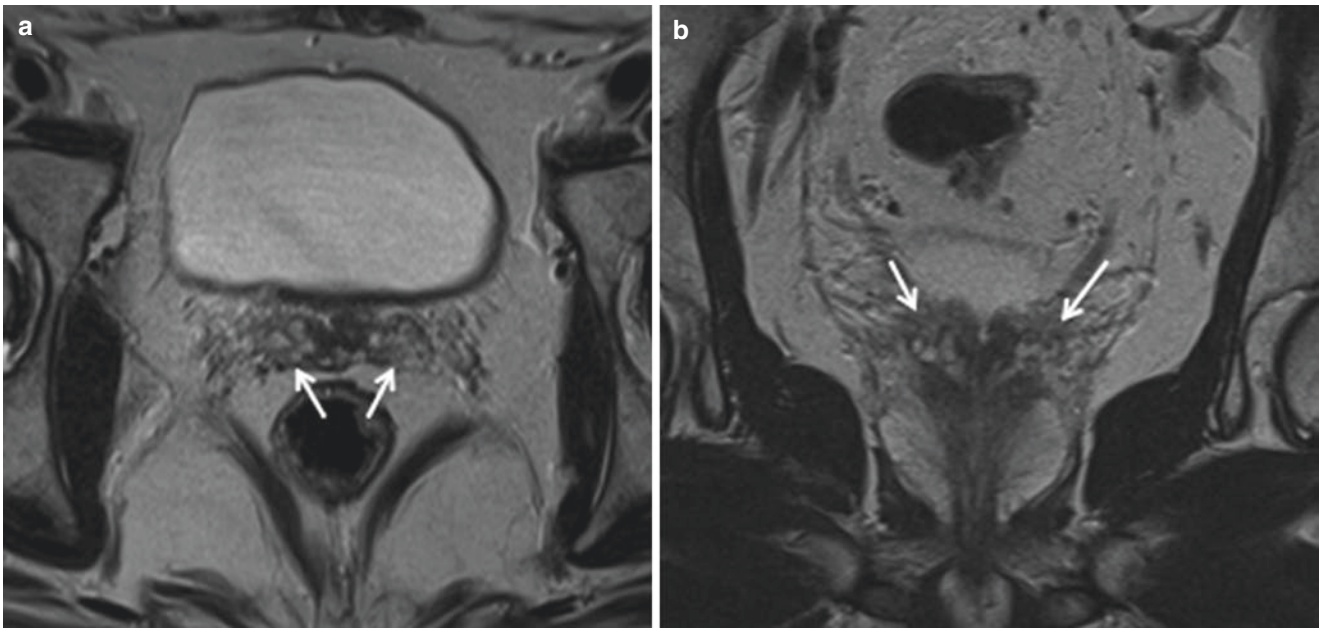

Fig. 9.9 Bilateral SV hypoplasia in a 31-year-old man with infertility. Axial (**a**) and coronal, (**b**) T2-weighted MR image shows a bilateral small SV (*arrows*)

Congenital Cysts in the SVs

A congenital cyst in the SVs is usually an incidental or isolated finding. In a few cases, it is associated with ipsilateral renal agenesis, ectasia of the seminal vesicle (SV), or anomalous insertion of the ureter, known as Zinner syndrome [1, 10, 11] (Figs. 9.10 and 9.11).

The ectopic ureteral insertion in the SVs, vas deferens, ejaculatory ducts, or even in the prostatic urethra, may occur in some patients. Another finding is the association of cysts in the SVs with autosomal-dominant polycystic kidney disease (ADPKD) [1 7, 11].

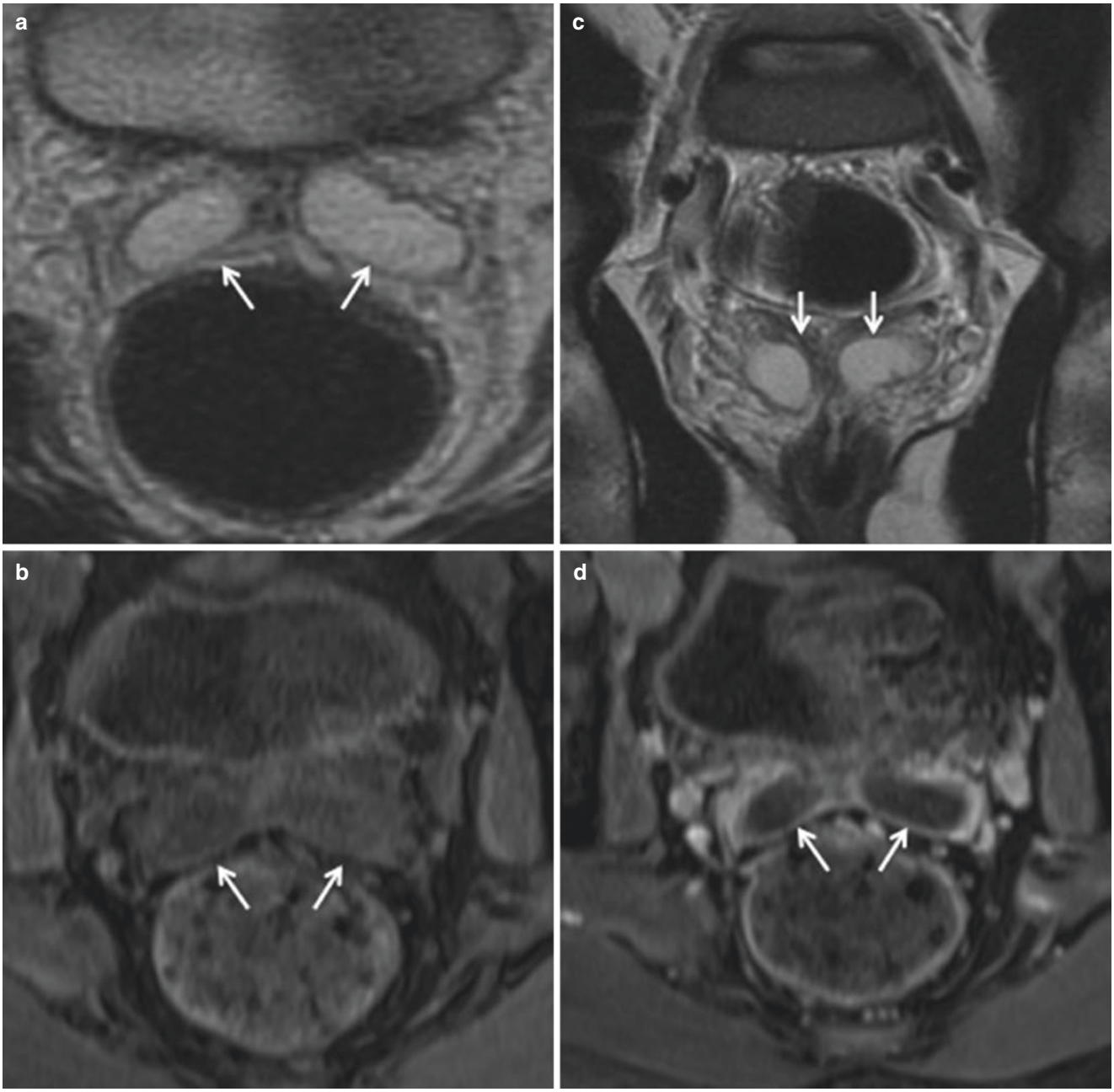

Fig. 9.10 Bilateral SV cysts in a 30-year-old man with infertility. Axial (**a**) and coronal (**c**) T2-weighted MR image shows bilateral SV cysts (*arrows*). Axial (**b**) T1-weighted MR image obtained with fat saturation shows again (*arrows*). Axial (**d**) gadolinium-enhanced T1 weighted MR image shows cysts periphery enhancement (*arrows*)

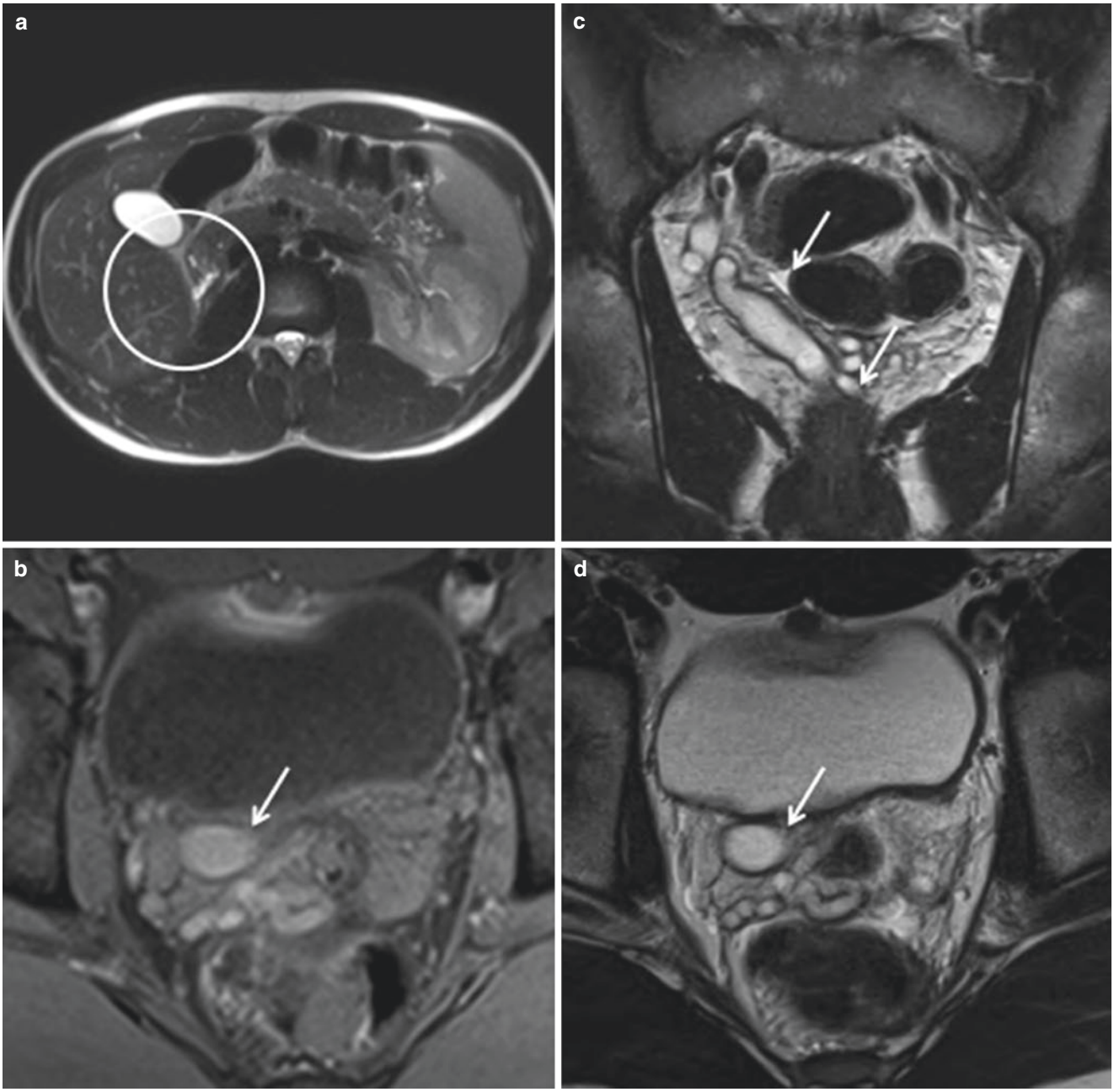

Fig. 9.11 Zinner syndrome in 30-year-old man with infertility and hematospermia. Axial (**a**) T2-weighted MR image shows right renal agenesis (*circle*). Axial (**b**) T1 weighted MR image fat saturation. Note the high signal intensity within the dilated ducts, probably due to high proteinaceous/hemorrhagic content as a result of stasis (*arrows*). Coronal (**c**) T2-weighted MR image shows cystic dilatation of the seminal vesicle on the right side and right-sided ectopic ureter opening into the vas deferens inferiorly (*arrows*). Axial (**d**) T2-weighted MR image shows dilated duct that is seen indenting the posterior wall of the urinary bladder (*arrow*)

Congenital Abnormalities

Vas Deferens Clinical Manifestations

Generally, anomalies of the vas deferens are incidentally found during imaging. However, in a few cases, patients may complain of pelvic pain and/or hematospermia and infertility. In other patients, there may be an association with cystic fibrosis, which is considered the lightest genetic expression of the disease.

Unilateral agenesis of the VD is rare, but can occur in association with hypoplasia or agenesis of the Wolffian duct derivatives as well as the epididymis and SVs [1].

Contralateral or ipsilateral agenesis of the SVs was found in 86% and 20% of patients with unilateral agenesis of the VD, respectively. Renal agenesis was found in 11% of patients with bilateral agenesis of the VD and 26% of patients with unilateral agenesis of the VD [12] (Fig. 9.12).

Bilateral agenesis of the VD, according to Schlegel et al. [1, 7], is present in 45% of patients with bilateral agenesis of the VD. Agenesis of the SVs and bilateral VD are often associated with cystic fibrosis in about 99% of male patients [1, 7].

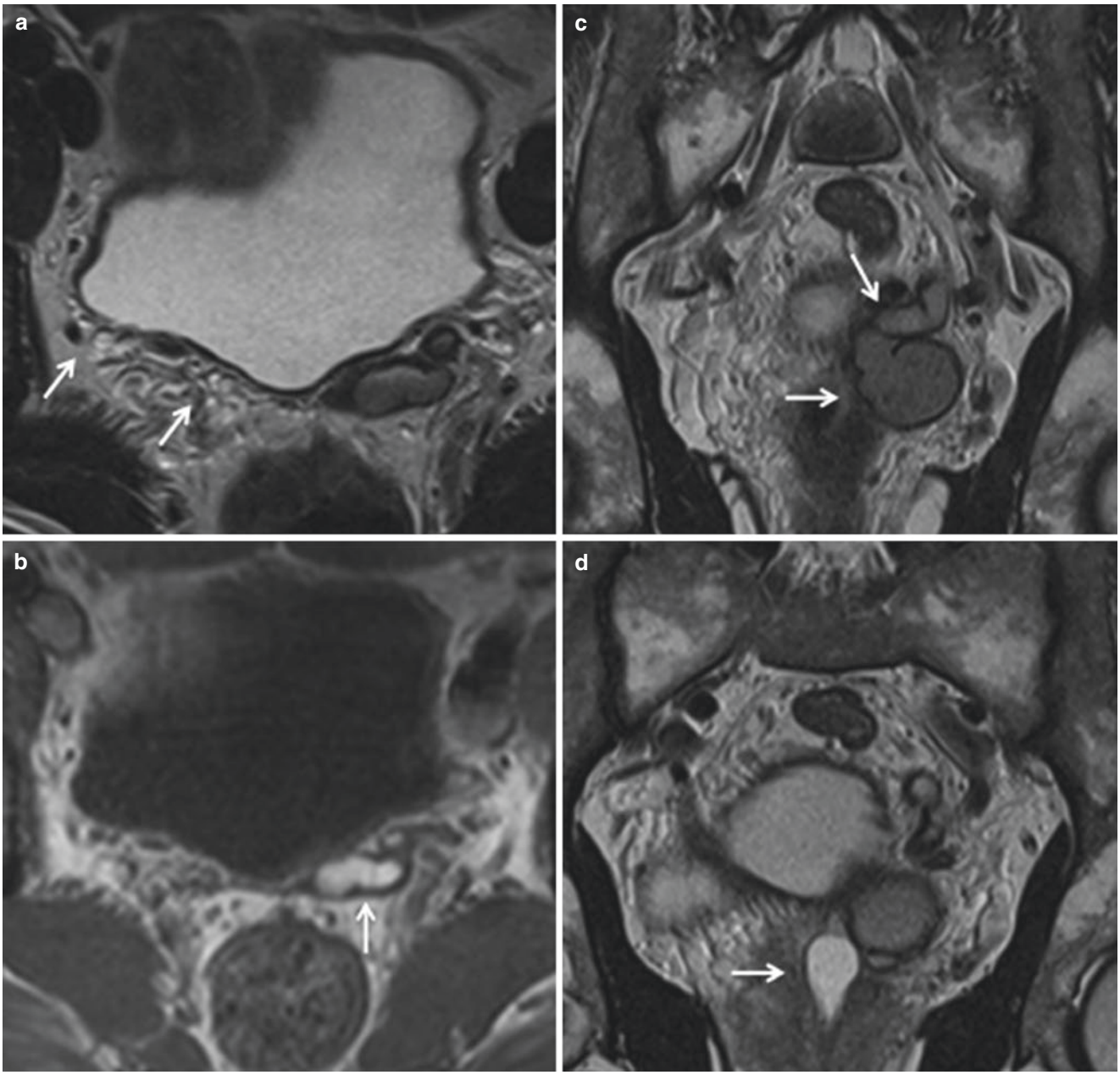

Fig. 9.12 Agenesis of the SV and vas deferens (VD) in a 35-year-old man with infertility and hematospermia. Axial (**a**) T2-weighted MR image shows right absence of the SV and VD (*arrows*). Axial (**b**) T1-weighted MR image shows high signal intensity within the left vas deferens, probably due to high proteinaceous/hemorrhagic fluid content as a result of stasis (*arrow*). Coronal (**c**) T2-weighted MR image shows dilated left VD and ED (*arrows*). Coronal (**d**) T2-weighted MR image. Note midline utricular duct cyst (*arrows*)

Inflammatory Changes in the Seminal Tract

Acute inflammation of the prostate, the SVs, and the seminal tract sometimes develop into a chronic form. It is the most common urogenital disease in men, usually associated with urinary tract infections.

Some factors contributing to this situation are the decrease in the immune potential of the population, resulting from unfavorable environmental situations, tobacco and alcohol abuse among men, and an increase in sexually transmitted diseases [2]. Under normal conditions, the VD presents a defense mechanism (oblique path, peristalsis, and ciliary movements) to prevent the progression of bacteria to the gonads. Seminal tract inflammations may cause changes in semen, and in some cases there is an increase in leukocytes, which may be associated with infertility.

Clinical Manifestations

In most of the cases, patients are asymptomatic, but may show some systemic symptoms such as fever, chills, hematospermia, recurrent urinary tract infections, or pelvic pain, as well as some pain upon ejaculation. Digital rectal examination (DRE) shows no changes in most cases. Laboratory tests and serum hormone levels can also help direct the diagnosis [2, 13]. Imaging tests help locate the primary site of infection, thus enabling the appropriate treatment.

Prostatitis

Prostatitis occur because of changes that result in increased pressure during urination that generate vesicoureteral reflux into the prostate gland, whether as a result of anatomical or neurophysiological disorders. They are divided according to the time of evolution and can be acute or chronic (with symptoms persisting for 3 months or more). They are divided into categories I to IV; asymptomatic inflammatory prostatitis is the last category and it can be detected in patients with infertility due to evidence of seminal inflammation (Fig. 9.13).

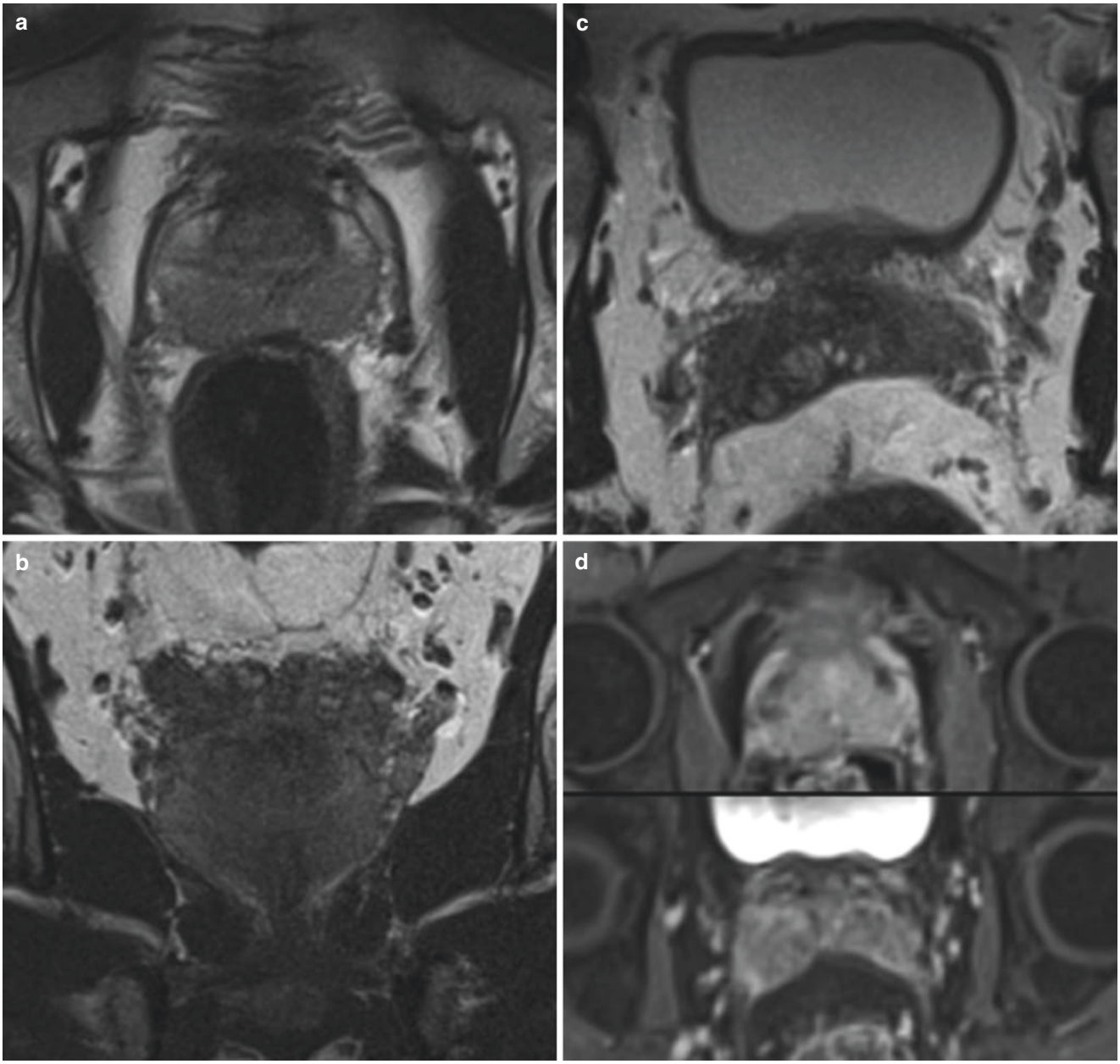

Fig. 9.13 Prostatitis in a 30-year-old man with prostate-specific antigen level of 5.0. Axial (**a**,**c**), coronal (**b**) T2-weighted MR image shows diffuse low-signal intensity in entire peripheral zone and SV due to prostatitis. Axial (**d**) gadolinium-enhanced T1 weighted MR image shows diffuse enhancement

Orchitis

Orchitis is characterized by inflammation of the testes. The main cause is the association with the mumps virus (*Paramyxoviridae*), but it may derive from an initial epididymitis (orchiepididymitis). It can be acute or chronic, and symptoms can persist for 6 weeks. It can also be viral, disseminating via blood – or bacterial, resulting from epididymal infection reaching the testicles [14].

In younger patients, orchitis may lead to acute scrotum and testicular torsion and hence cause infertility. In patients with mumps, which has an affinity for germinal epithelium, evolution can determine testicular atrophy and infertility (Fig. 9.14).

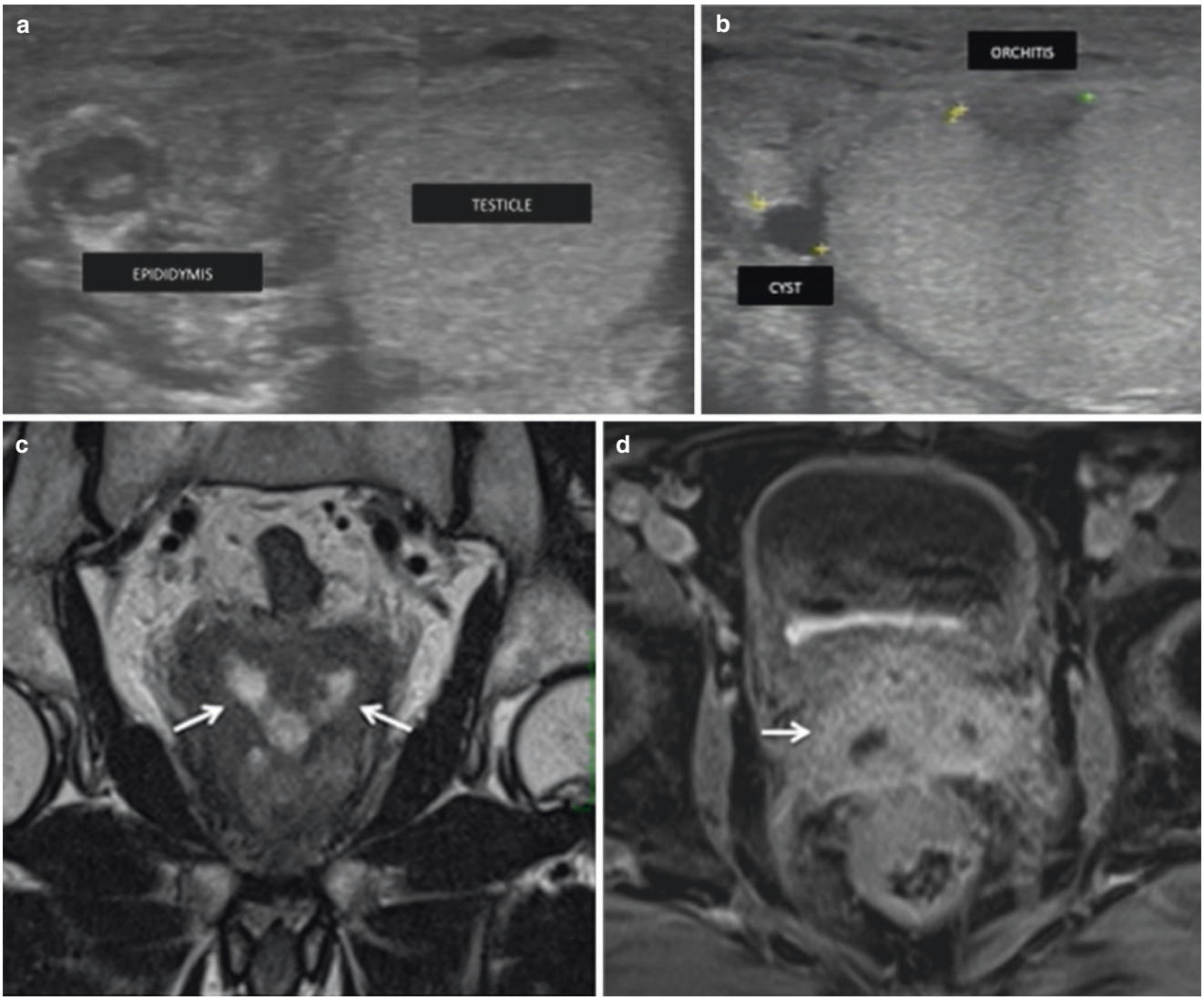

Fig. 9.14 Epididymo-orchitis and prostate abscess in a 29-year-old man with hematospermia and lower urinary tract infection. US image (**a**) the epididymis is enlarged, echogenicity is decreased, and its echotexture is heterogeneous. US image (**b**) testicular focal involvement, hypoechoic area and cyst in body of the epididymis. Coronal (**b**) T2-weighted MR image shows the prostate currently more irregular and enlarged (*arrows*). Axial (**c**) contrast-enhanced fat-suppressed T1 weight MR image shows frank pockets of fluid collection confirming the inflammatory nature of the process. (**d**) Similar changes are also noted in the seminal vesicles (*arrow*)

Epididymitis

Epididymitis is an inflammation of the epididymis. The infection originates in the bladder, urethra, or prostate, and bacteria travel via VD to the epididymis [14]. It can be acute or chronic (when symptoms persist for more than 6 weeks). In most cases, the infection may progress and reach the testis, causing orchiepididymitis. Its complications may cause abscess formation, testicular atrophy and infarction, and even, in more severe cases, infertility (Fig. 9.15).

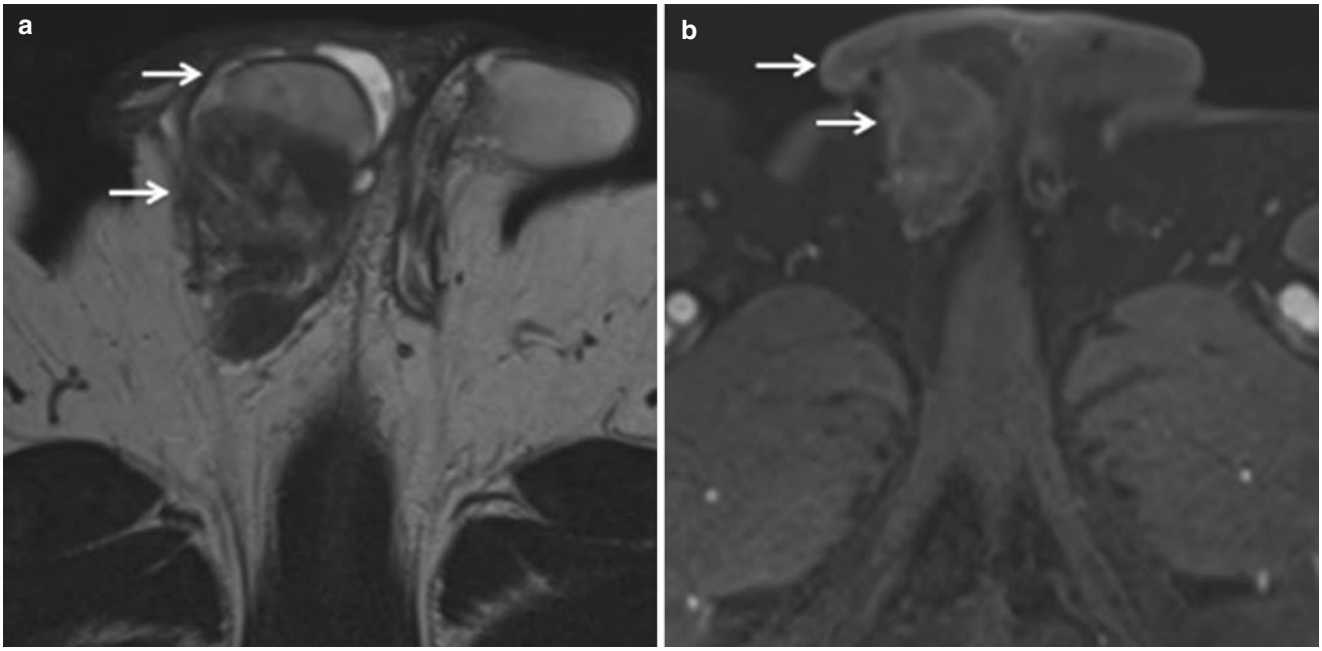

Fig. 9.15 Epididymitis-orchitis in a 28-year-old man with acute right scrotal pain. Axial (**a**) T2-weighted MR image shows heterogeneous increased signal intensity of the right testis compared with the left (*arrows*). Axial (**b**) contrast-enhanced fat-suppressed T1 weight MR image depicts diffuse increased enhancement of the right testis, epididymis, and overlying subcutaneous tissues (*arrows*)

Seminal Vesiculitis

Inflammatory processes in SVs are usually secondary to bacterial prostatitis, and in some cases, recurrence of urinary tract infections, which can develop into abscesses [1]. It can also be acute or chronic. When chronic, it can lead to atrophy of the affected SV and, as a result, to infertility (Figs. 9.16 and 9.17).

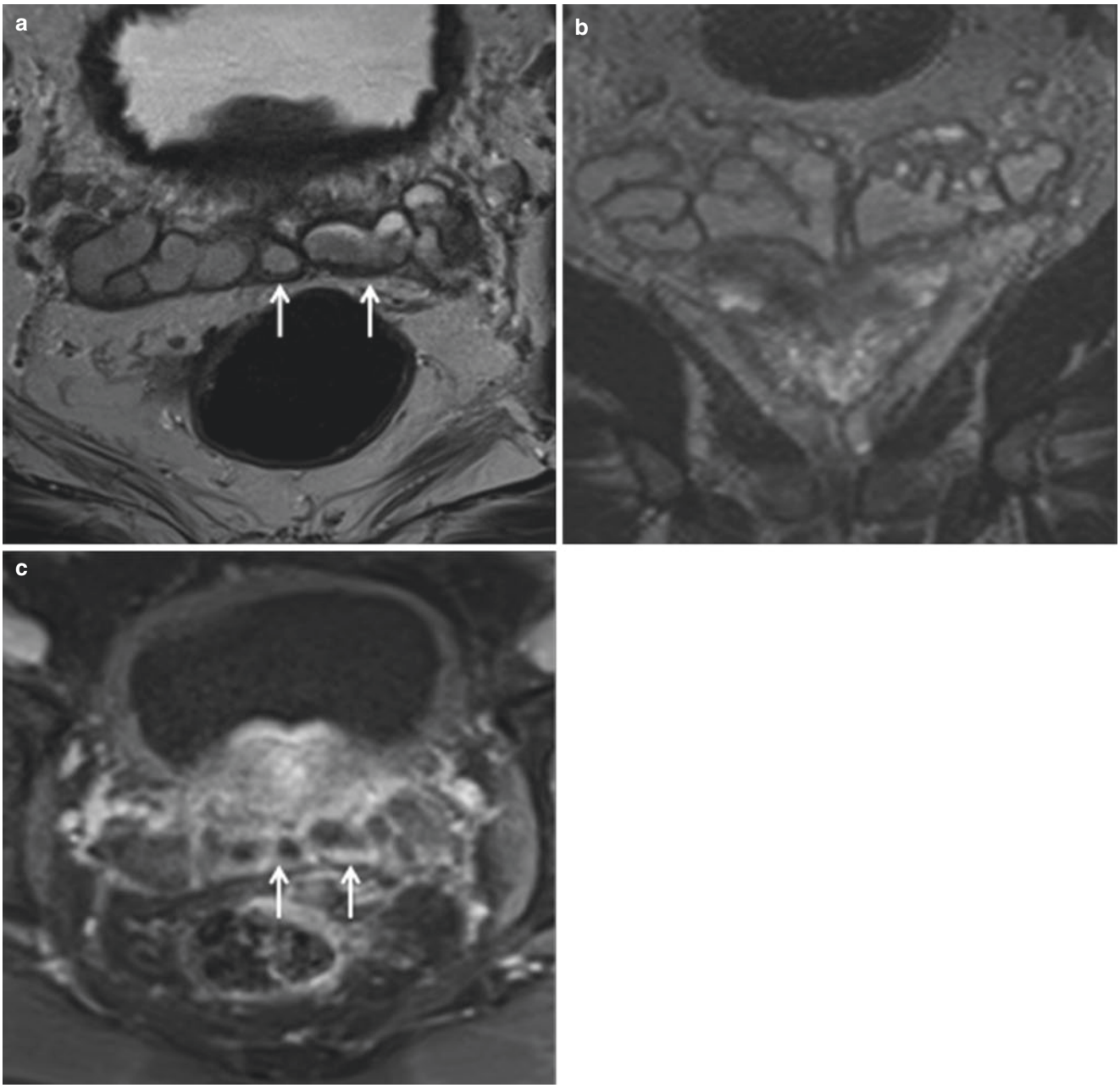

Fig. 9.16 Seminal vesiculitis in a 34-year-old man with hematospermia. Axial (**a**), coronal (**b**) T2-weighted MR image and axial, (**c**) contrast-enhanced fat-suppressed T1 weight MR image show diffuse wall thickening of the SVs (*arrows*)

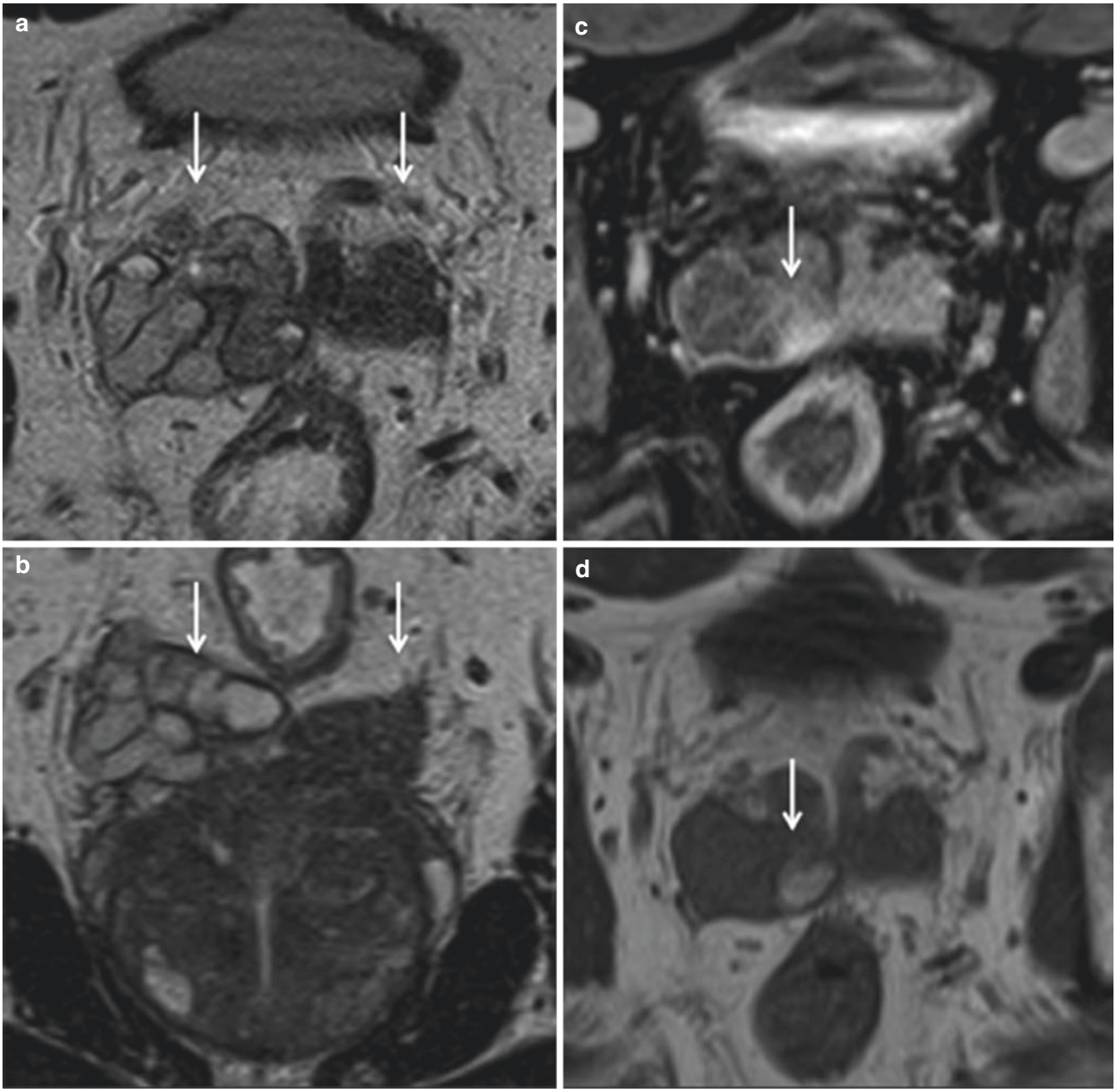

Fig. 9.17 Seminal vesiculitis in a 30-year-old man with hematospermia. Axial (**a**), coronal (**b**) T2-weighted MR image and axial (**c**) contrast-enhanced fat-suppressed T1 weight MR image through the SV shows asymmetric dilation of the right SV, with focal areas of wall thickening (*arrows*). Axial (**d**) T1-weighted MR image high T1 signal throughout the right SV, consistent with hemorrhage (*arrow*)

Obstruction of Ejaculatory Ducts

The obstruction of the ejaculatory ducts may be of congenital etiology, among which we highlight atresia of the ejaculatory ducts and midline cysts. In some cases, such as postsurgical changes, it can be acquired, or from seminal vesicles whose changes originate from calculi, infectious, or inflammatory processes [1, 7]. These diseases may cause alterations in seminal parameters and a complete obstruction can cause azoospermia, and hence infertility (Figs. 9.18, 9.19, and 9.20).

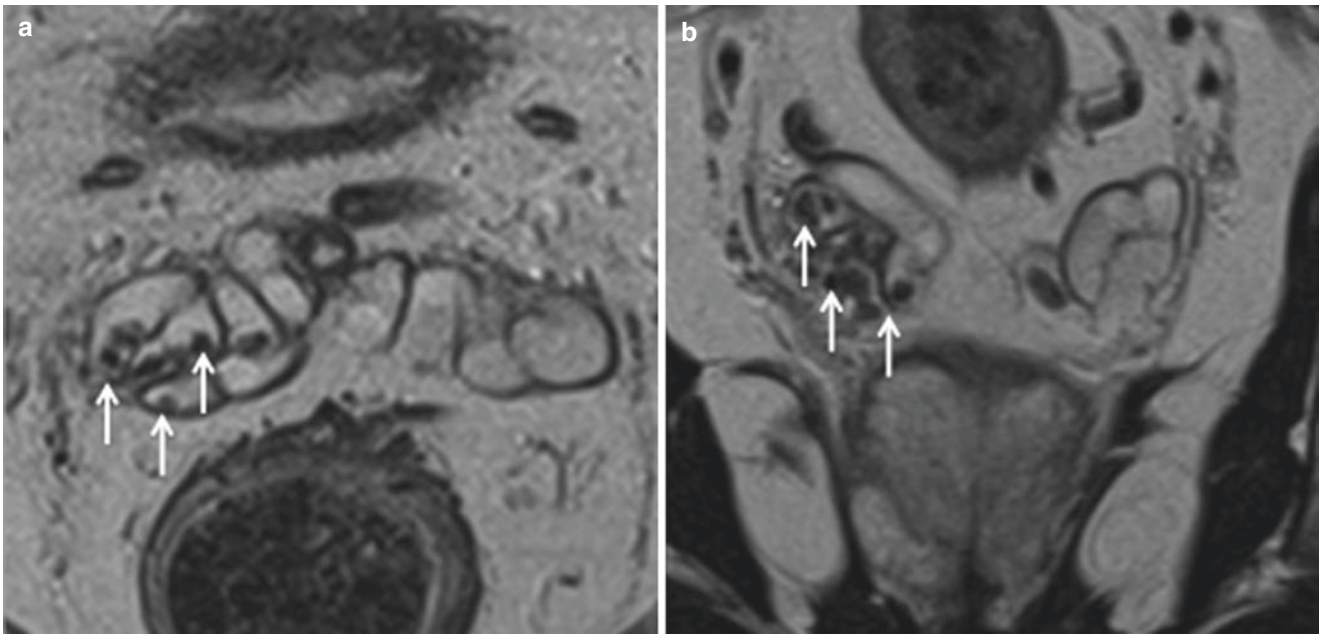

Fig. 9.18 Calculi in a 30-year-old man with hematospermia. Axial (**a**) and coronal (**b**) T2-weighted MR image shows calculi in the right SV (*arrows*)

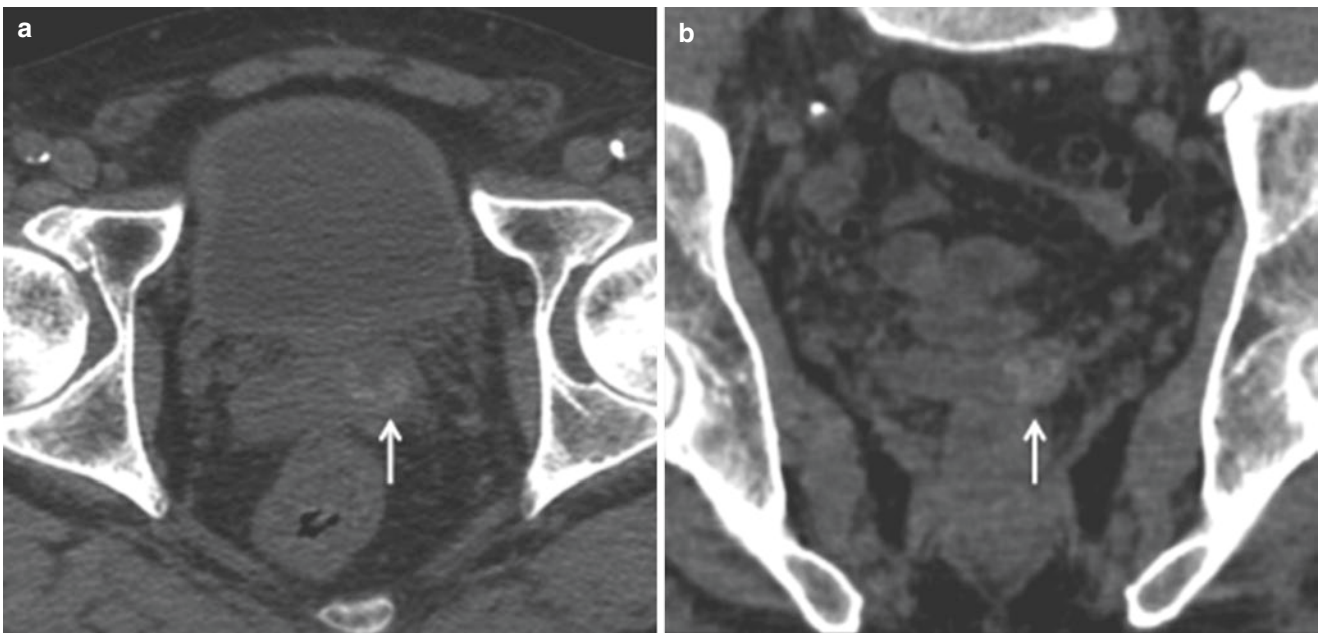

Fig. 9.19 Calculi in a 31-year-old man with hematospermia. Axial (**a**) and coronal (**b**) CT sections show calculi in the left SV (*arrows*). Axial (**c**) and coronal (**d**) T2-weighted MR image shows again (*arrows*)

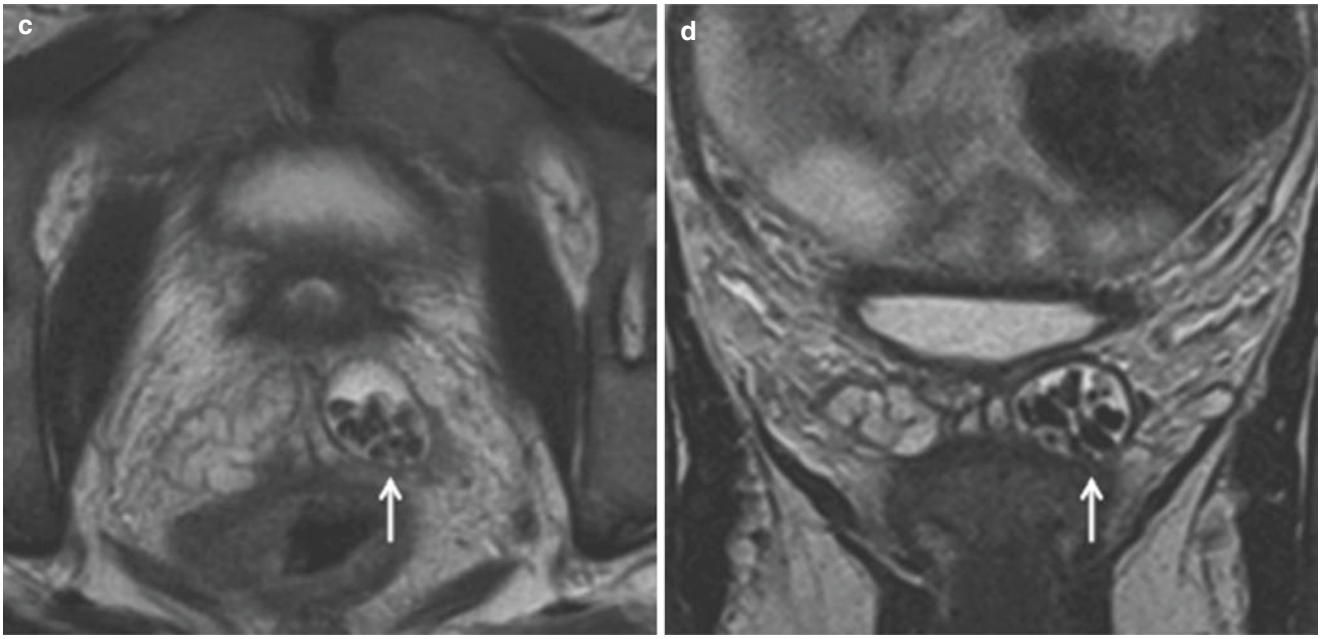

Fig. 9.19 (continued)

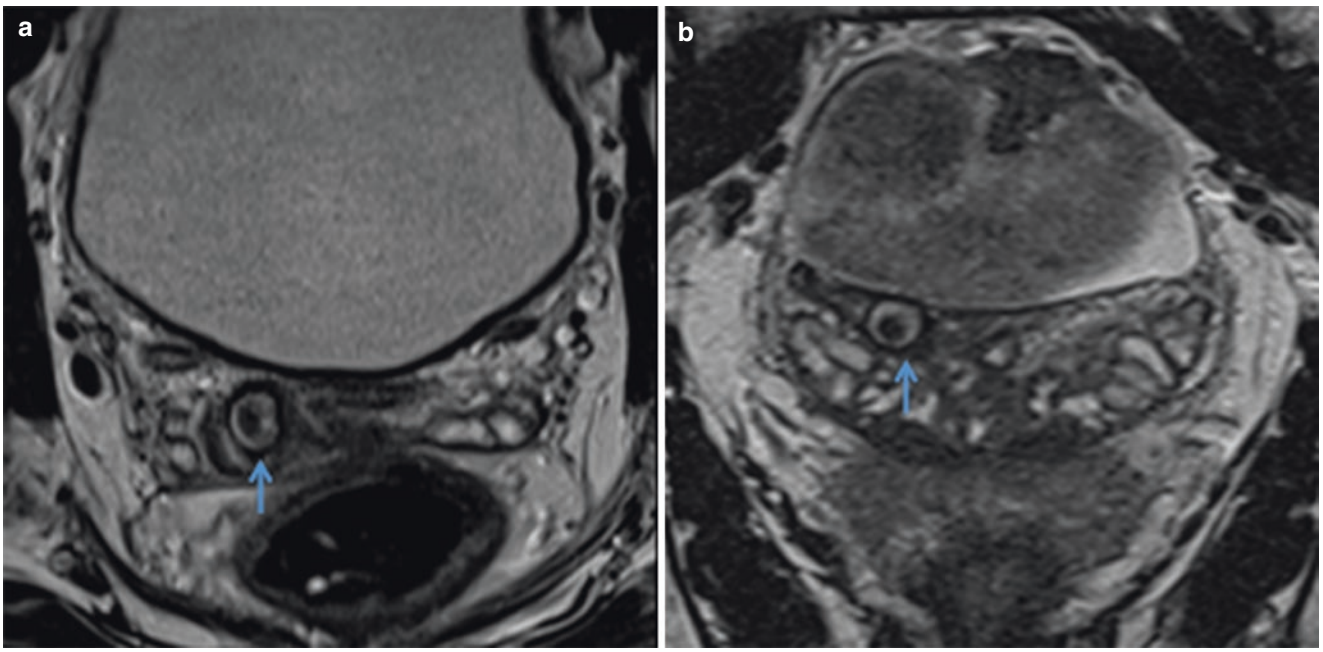

Fig. 9.20 Calculi in a 29-year-old man with hematospermia. Axial (**a**) and coronal (**b**) T2-weighted MR image shows calculi in the right ED (*arrows*)

Prostatic Cysts

Cysts of the lower male genitourinary tract are uncommon, often of questionable origin, and usually benign [15]. The cysts are divided into two main groups: extraprostatic and intraprostatic. Some diseases may mimic these types of cysts: ureterocele, transurethral resection of the prostate, and bladder diverticulum [16].

Clinical Manifestations

In some patients, prostatic cysts are asymptomatic. Symptomatic patients may complain of recurrent urinary tract infections, pelvic pain, urinary incontinence, epididymitis, prostatitis, and hematospermia. In some patients, prostatic cysts may be related to infertility due to the obstruction of the seminal tract.

Classification of Prostatic Cysts

Prostatic cysts are generally classified as median, paramedian, or lateral cysts, or even as intraprostatic periprostatic cysts [17].

Intraprostatic Cysts

Intraprostatic cysts are median cysts, such as prostatic utricle cysts and Müllerian duct cysts, which are located in the midline behind the upper half of the prostatic urethra.

Prostatic Utricle Cysts

Prostatic utricle cysts are of endodermal origin, being confined to the prostate due to partial regression of the Müllerian duct during embryonic development. There is a communication with the posterior urethra and the ejaculatory duct. They are commonly found in males under the age of 20 and occur in approximately 1–5% of the general population.

They are associated with abnormalities of the genitourinary system, among which we highlight hypospadias, intersex disorders, cryptorchidism, and ipsilateral renal agenesis [18] (Figs. 9.21, 9.22, and 9.23)

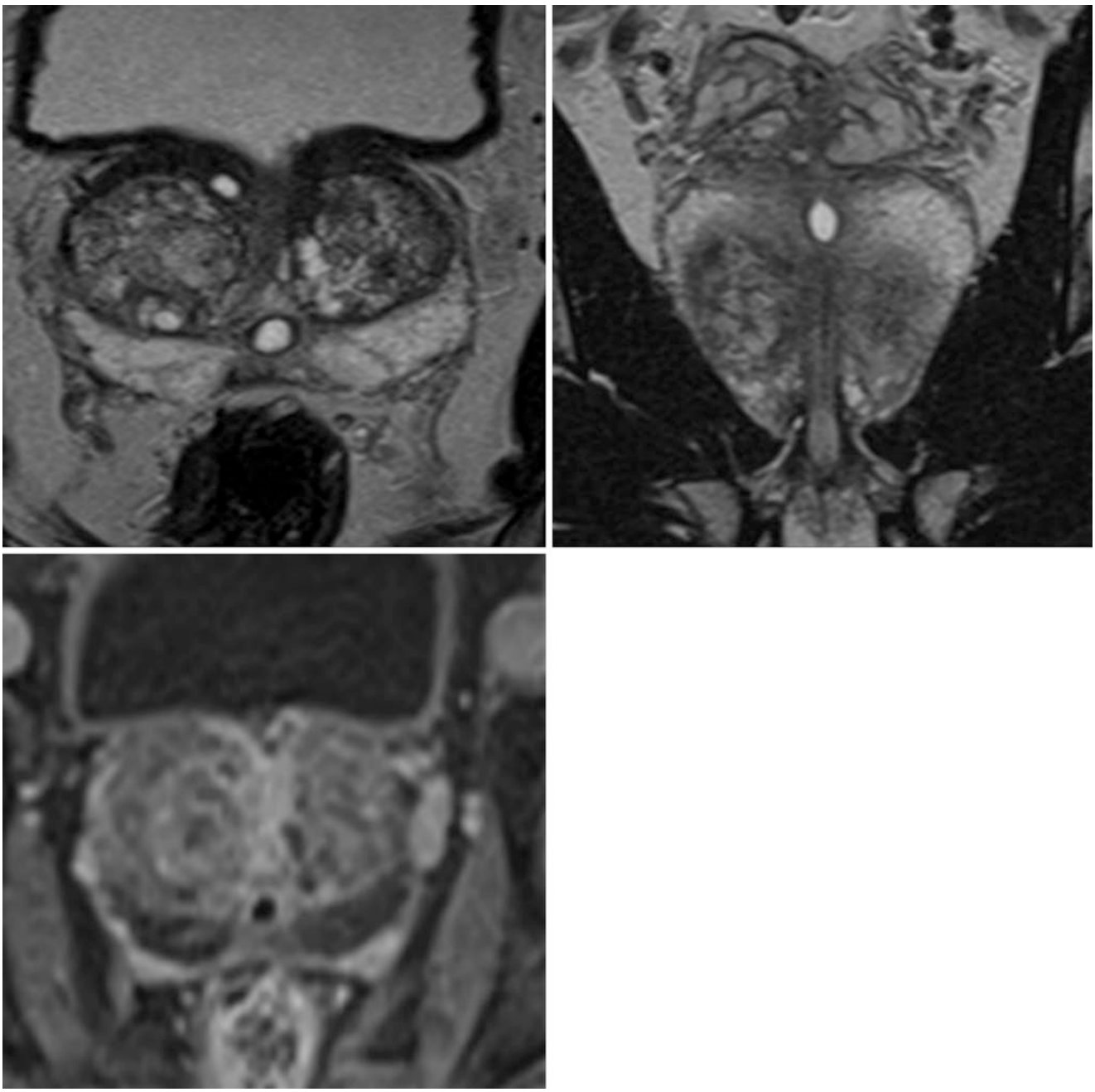

Fig. 9.21 Prostatic utricle cyst in a 30-year-old man. Axial (**a**), coronal (**b**) T2-weighted MR images and axial (**c**) contrast-enhanced fat-suppressed T1-weight MR image show a midline high-signal-intensity prostatic utricle cyst

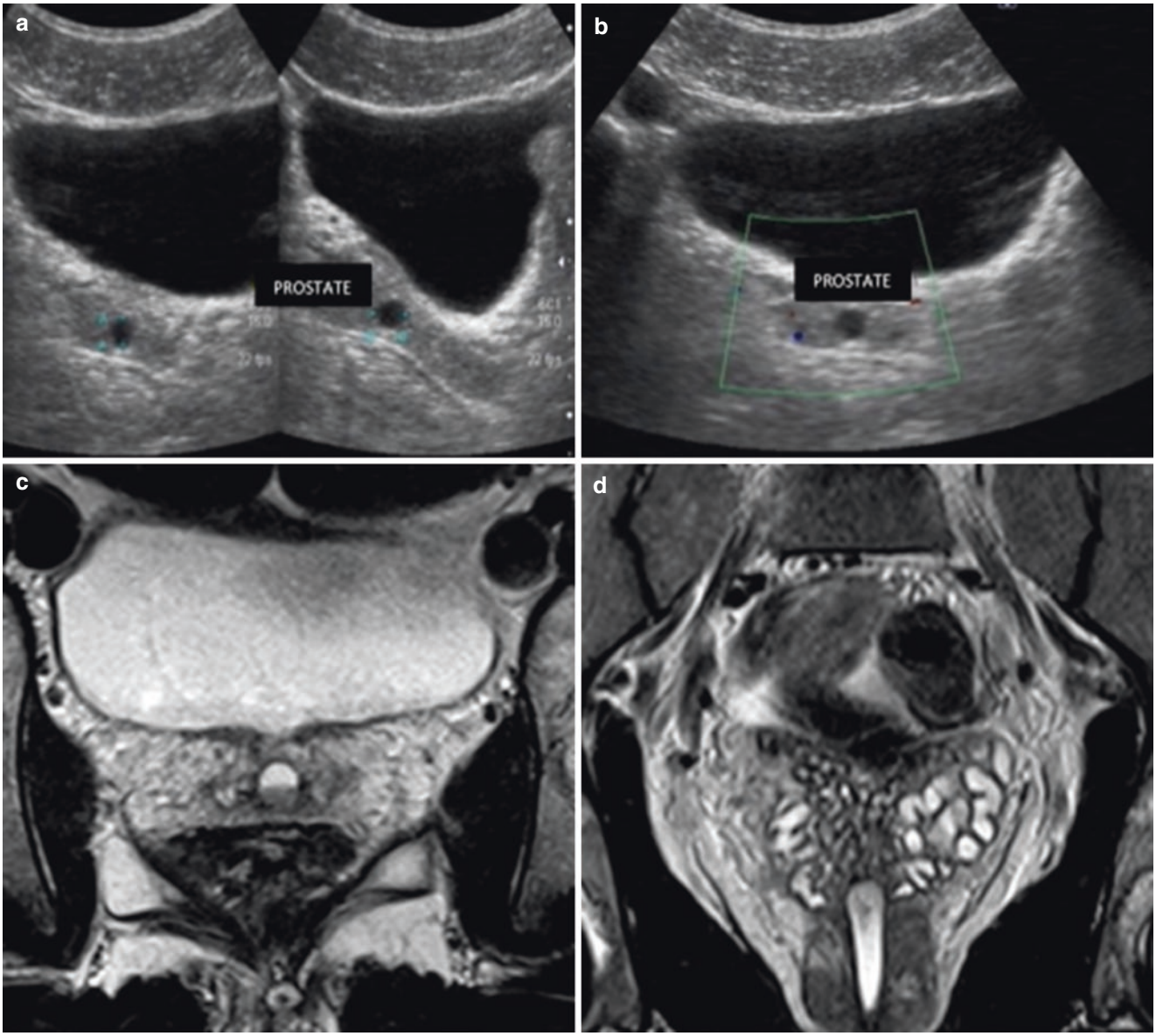

Fig. 9.22 Prostatic utricle cyst in a 30-year-old man with hematospermia. Transabdominal US (**a**,**b**) shows a small midline prostatic utricle cyst anechoic at US. Axial (**c**) and coronal (**d**) T2-weighted MR images show up again, but as a high-signal-intensity prostatic cyst indicative of hemorrhagic content

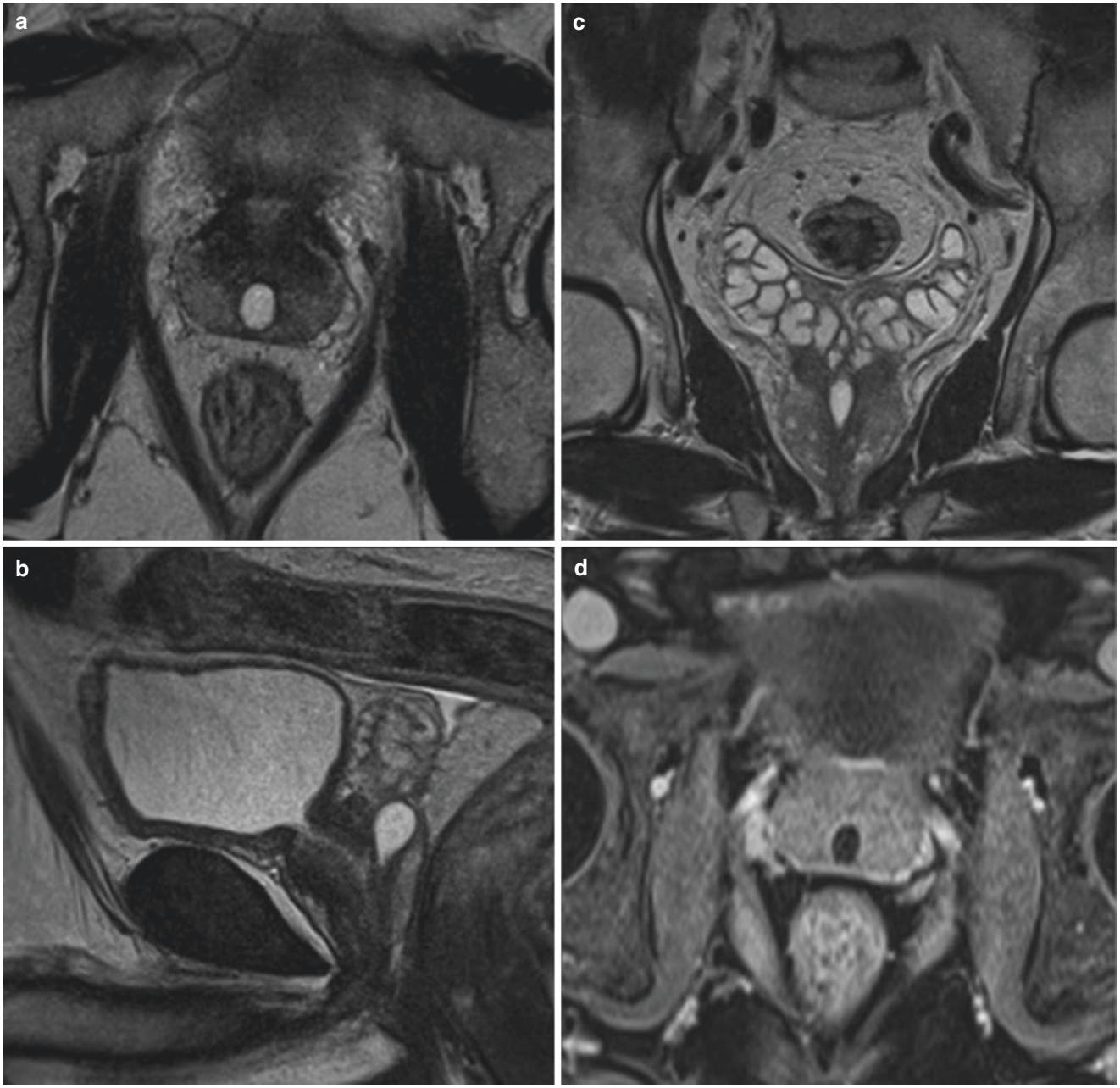

Fig. 9.23 Prostatic utricle cyst in a 33-year-old man. Axial (**a**), sagittal (**b**), coronal (**c**) T2-weighted MR images and axial (**d**) contrast-enhanced fat-suppressed T1-weight MR image show a midline high-signal intensity prostatic utricle cyst

Müllerian Duct Cysts

Müllerian duct cysts are of mesodermal origin and develop from a focal fault and saccular focal dilatation of the mesonephric ducts. Peak incidence occurs between age 20 and 40 [17]. They are teardrop-shaped structures that extend above the prostate, and they do not communicate with the posterior urethra or ejaculatory ducts [19] (Fig. 9.24).

Paramedian cysts (cysts of the ejaculatory ducts).

Paramedian cysts are situated laterally, near the midline, and posterior.

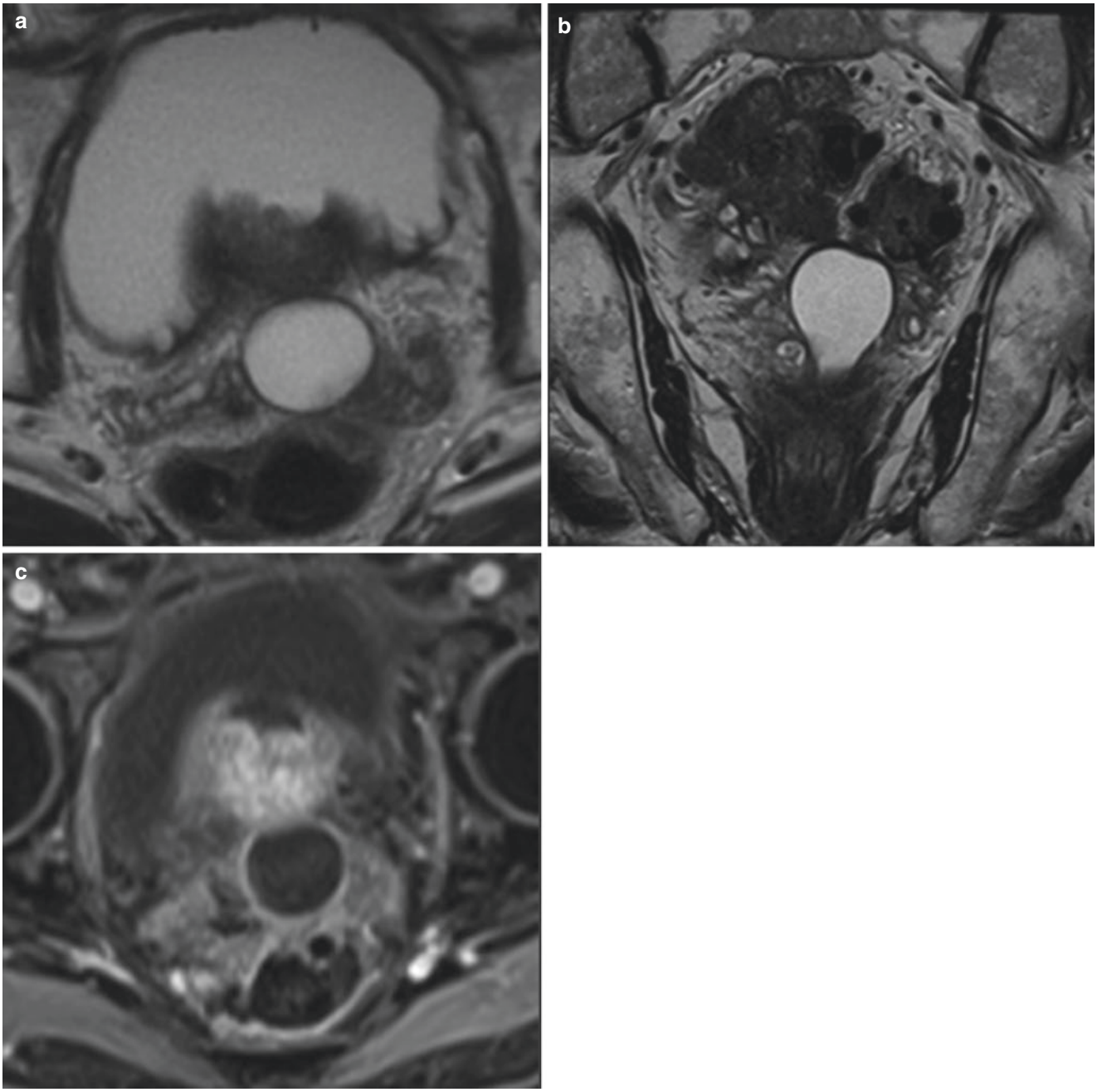

Fig. 9.24 Prostatic Müllerian duct cyst in a 32-year-old man with lower urinary tract symptoms. Axial (**a**), coronal (**b**) T2-weighted MR images, and axial (**c**) contrast-enhanced fat-suppressed T1-weight MR image show a midline high-signal intensity prostatic cyst extending above the base of the prostate to the seminal vesicles

Ejaculatory Duct Cysts

Ejaculatory duct cysts are caused by congenital or acquired obstruction of the ejaculatory duct. Cyst aspiration may contain calculi and, in some cases, pus or blood [2, 17] (Fig. 9.25).

Lateral Cysts (Cystic Degeneration of Benign Prostatic Hyperplasia).

Lateral cysts are located far from the midline and may involve any prostatic zone [5, 17] (Fig.9.26).

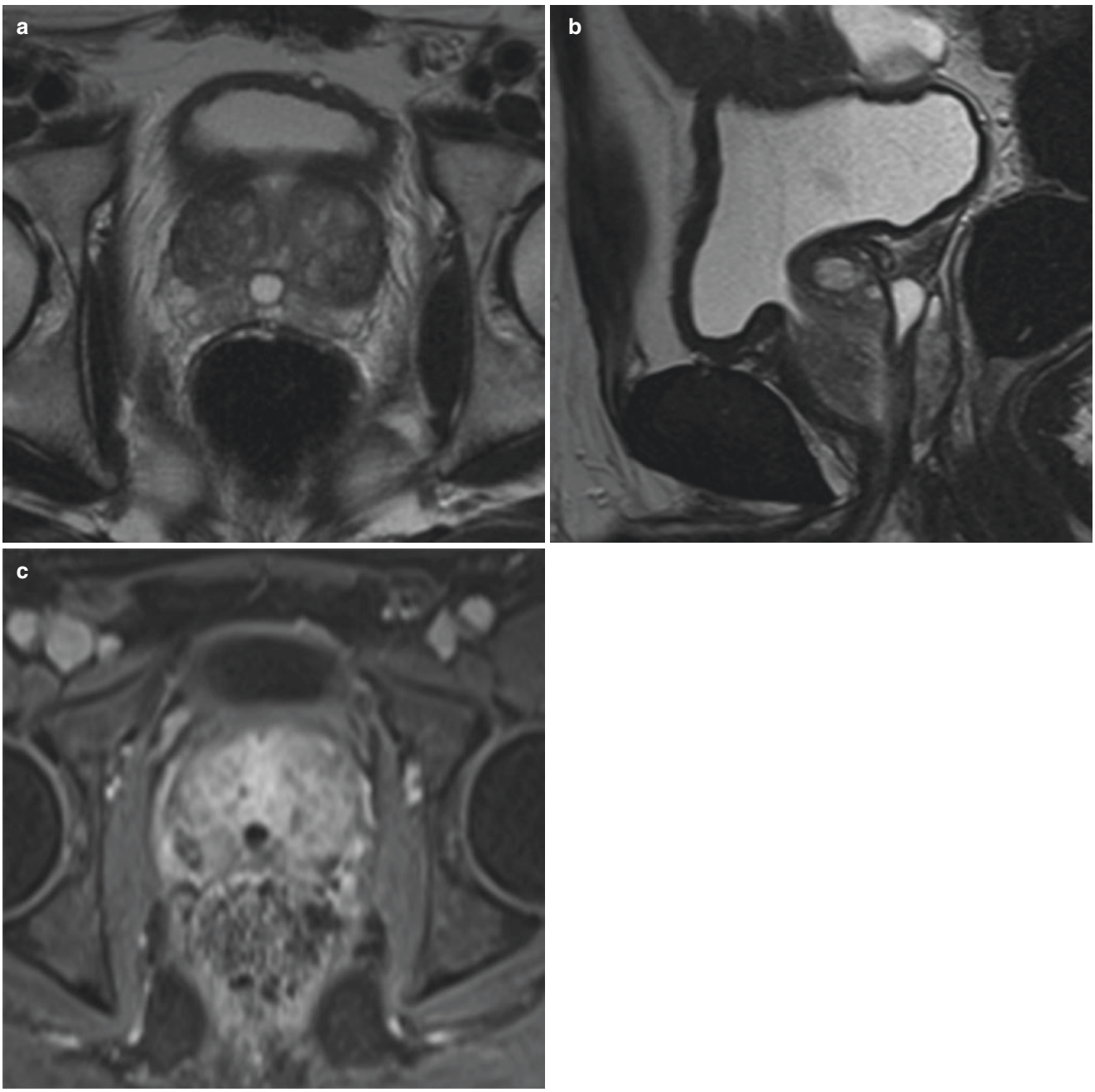

Fig. 9.25 Ejaculatory duct cyst in a 30-year-old man with oligospermia. Axial (**a**), sagital (**b**) T2-weighted MR images, and axial (**c**) contrast-enhanced fat-suppressed T1-weighted MR image show a midline high-signal-intensity oval lesion just lateral to the midline along the course of the right ejaculatory duct just posterior to the bladder neck, a finding that is a consistent with cyst

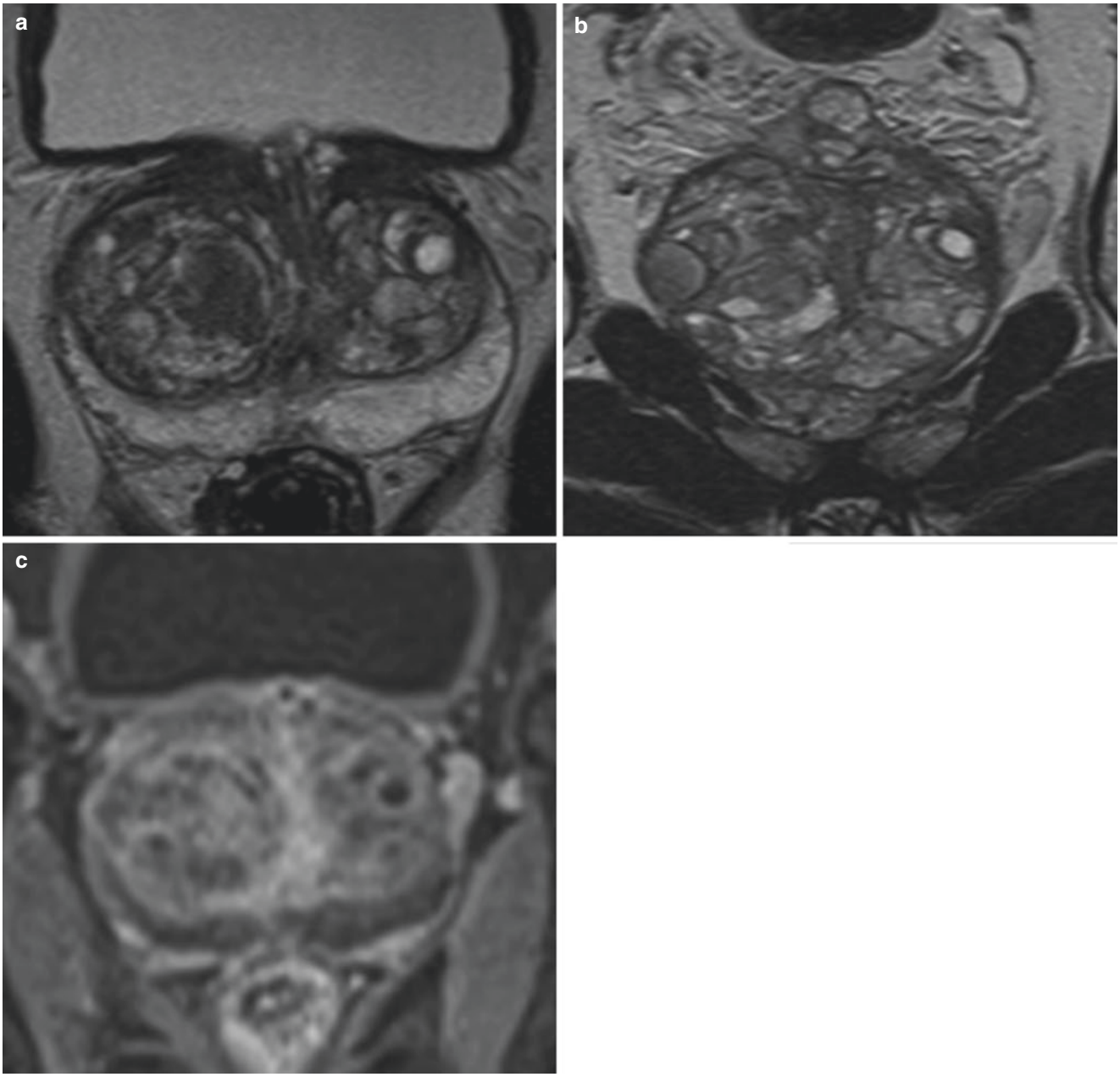

Fig. 9.26 BPH in a 32-year-old man with lower urinary tract symptoms. Axial (**a**), coronal (**b**) T2-weighted MR images and axial (**c**) contrast-enhanced fat-suppressed T1-weight MR image show enlarged transitional zone with heterogeneous signal intensity, compatible with BPH

Conclusion

Conjugal infertility can be defined as the inability of a couple to become pregnant after 1 year of trying (that is, having frequent sexual intercourse without contraceptive methods and well distributed throughout the menstrual cycle). Male and female factors must be addressed together.

Ejaculation consists of sperm and secretions originale in the testis, epidymis, vas deferens, ejaculatory duct, seminal vesicles, prostate, prostatic urethra, penile urethra, and membranous urethra. Pathological changes at any point along the anatomical pathway can lead to infertility.

References

1. Kim B, Kawashima A, Ryu J-A, Takahashi N, Hartman RP, King BF. Imaging of the seminal vesicle and vas deferens. RadioGraphics. 2009;29(4):1105–21.
2. Parsons RB, Fisher AM, Bar-Chama N, Mitty HA. MR imaging in male infertility. RadioGraphics. 1997;17(3):627–37.
3. Trigaux JP, Van Beers B, Delchambre F. Male genital tract malformations associated with ipsilateral renal agenesis: sonographic findings. J Clin Ultrasound JCU. 1991;19(1):3–10.
4. Arora SS, Breiman RS, Webb EM, Westphalen AC, Yeh BM, Coakley FV. CT and MRI of congenital anomalies of the seminal vesicles. Am J Roentgenol. 2007;189(1):130–5.
5. Bittencourt LK, Hausmann D, Sabaneeff N, Gasparetto EL, Barentsz JO. Multiparametric magnetic resonance imaging of the prostate: current concepts. Radiol Bras. 2014;47(5):292–300.
6. Kayat Bittencourt L, Litjens G, Hulsbergen-van de Kaa CA, Turkbey B, Gasparetto EL, Barentsz JO. Prostate cancer: the European Society of Urogenital Radiology prostate imaging reporting and data system criteria for predicting extraprostatic extension by using 3-T multiparametric MR imaging. Radiology. 2015. doi:10.1148/radiol.15141412.
7. Schlegel PN, Shin D, Goldstein M. Urogenital anomalies in men with congenital absence of the vas deferens. J Urol. 1996;155(5):1644–8.
8. Jones J, Dahms SE, Fichtner J, Hohenfellner M, Thüroff JW. An unusual case of ureteral ectopia in the seminal vesicle: diagnosis and surgical management. Urol Int. 1999;62(2):130–2.
9. King BF, Hattery RR, Lieber MM, Williamson B, Hartman GW, Berquist TH. Seminal vesicle imaging. Radiogr Rev Publ Radiol Soc N Am Inc [Internet]. 1989 [cited 2015 Nov 19];9(4). Available from: http://mayoclinic.pure.elsevier.com/en/publications/seminal-vesicle-imaging(117cbfd6-69fd-448d-8053-392ef8e50708).html
10. King BF, Hattery RR, Lieber MM, Berquist TH, Williamson B, Hartman GW. Congenital cystic disease of the seminal vesicle. Radiology. 1991;178(1):207–11.
11. Steers WD, Corriere JNJ. Case profile: seminal vesicle cyst. Urology. 1986;27(2):177–8.
12. Donohue RE, Fauver H. Unilateral absence of the vas deferens: a useful clinical sign. JAMA. 1989;261(8):1180–2.
13. Lee CH, Akin-Olugbade O, Kirschenbaum A. Overview of prostate anatomy, histology, and pathology. Endocrinol Metab Clin North Am. 2011;40(3):565–75, viii–ix.
14. Krieger JN, Nyberg L, Nickel JC. NIH consensus definition and classification of prostatitis. JAMA. 1999;282(3):236–7.
15. McNeal JE. Regional morphology and pathology of the prostate. Am J Clin Pathol. 1968;49(3):347–57.
16. McDermott VG, Meakem TJ, Stolpen AH, Schnall MD. Prostatic and periprostatic cysts: findings on MR imaging. AJR Am J Roentgenol. 1995;164(1):123–7.
17. Shebel HM, Farg HM, Kolokythas O, El-Diasty T. Cysts of the lower male genitourinary tract: embryologic and anatomic considerations and differential diagnosis. Radiogr Rev Publ Radiol Soc N Am Inc. 2013;33(4):1125–43.
18. Avolio Luigi, MD. Genital anomalies: overview, anomalies in males, anomalies in females. 2015; [cited 2015 Nov 20]; Available from: http://emedicine.medscape.com/article/1016681-overview
19. Jaidane M, Hidoussi A, Slama A, Hmida W, Sorba NB, Mosbah F. An acute urinary retention in an old man caused by a giant müllerian duct cyst: a case report. Cases J. 2009;2(1):203.
20. Kaushik R, Attri AK, Kaur L, Nada R. Leiomyoma of the vas deferens. J Postgrad Med. 2001;47(2):133.

Non-obstructive Diseases of the Testes

10

Osmar Cassio Saito

Clinical and Laboratory Findings: An Overview

Many factors can be related to male infertility, such as an inherited disorder, hormonal imbalance, varicocele around the testicle, or a condition that blocks the passage of sperm. Most men with infertility do not notice symptoms other than the inability to conceive a child, but signs and symptoms associated with male infertility include reduced sexual desire, chromosomal or hormonal abnormality, the absence of ejaculation or small volumes of fluid ejaculated, and even erectile dysfunction [1–3].

Main causes of male infertility:

Sperm production abnormalities	Chromosomal or genetic causes Undescended testes Infection Testicle torsion Varicocele Radiation damage Other unknown causes
Blockage of sperm ejaculate	Infection Prostatic disease Absence of vas deferens Vasectomy
Abnormal erections and ejaculate	Retrograde or premature ejaculation Absence of ejaculation Erectile dysfunction Spinal cord injury Absence of intercourse Prostatic surgery with damaged nerves Specific medicines
Hormonal diseases	Pituitary neoplasm Congenital lack of leuteinizing hormone/follicle-stimulating hormone Androgenic steroid abuse
Sperm antibodies	Vasectomy Infection of epididymis Unknown causes

O.C. Saito
Department of Radiology, Clinicas Hospital – University of São Paulo, São Paulo, SP, Brazil
e-mail: ocsaito@gmail.com

Semen Analysis

A laboratory analysis of semen determines the number of sperm and discovers abnormalities in the (morphology) and (motility) of the spermatozoids. The lab analysis of semen can also detect signs or problems such as infections.

Spermatozoids counts can fluctuate significantly, so in most cases, several semen analysis tests are done over a period of 1 year. The low number of spermatozoids occurs when the count is fewer than 15 million sperm per milliliter of semen or a total sperm count of less than 39 million per ejaculate [2, 3].

Hormone Testing

Testosterone is an androgenic hormone that is responsible for the development of the external male genitalia and secondary sexual characteristics. Most of this important hormone is secreted by the testicular Leydig cells and a minor part of this hormone is secreted by the adrenal cortex. Normal adult testosterone values range from 250 to 1100 ng/dL, with levels dropping slowly after age 30 [1, 2].

Post-ejaculation Urinalysis

The presence of spermatozoids in urine can indicate that sperm is going backward into the bladder instead of out of the penis during ejaculation; this is called retrograde ejaculation [1].

Genetic Tests

Whenever the spermatozoids concentration is extremely low, the cause of infertility can be genetic, and a specific blood test can reveal subtle changes in the Y chromosome. Signs of a genetic abnormality can be related to various congenital or inherited syndromes [1, 3].

L.R.M.F. de Souza et al. (eds.), *Atlas of Imaging in Infertility*, DOI 10.1007/978-3-319-13893-0_10

Testicular Biopsy

This procedure involves removing samples from the testicle with a needle. Whenever the results of testicular biopsy show that sperm production is normal, the infertility is likely caused by a blockage or another problem with sperm delivery; however, this sort of examination is not often used to diagnose the cause of infertility [1, 3].

Scrotal Ultrasound

This examination uses high-frequency sound waves to produce anatomical images. A scrotal ultrasound can help detect scrotal abnormalities such as varicocele, hypogonadism, posttorsion, epididymal cysts, absent epididymis, and tumors.

Nonobstructive Diseases of the Testes

Varicocele

Varicocele is caused by a dilatation of the pampiniform venous plexus and the internal spermatic vein. Clinically, varicoceles present a palpable, soft scrotal mass. Sometimes they are associated with moderate pain. Varicocele usually decreases testicular function; it occurs in approximately 15–20% of all males and in 40% of infertile males. Ultrasound examination is an excellent means of evaluating the pampiniform venous plexus, and with color Doppler it is possible to detect venous reflux during a Valsalva maneuver even in subclinical varicoceles [4–6].

Ultrasound B-mode shows tortuous, tubular, anechoic structures adjacent to the superior part of the testis and then correspond to dilated veins of the pampiniform plexus with calibers more than 2–3 mm during the Valsalva maneuver in the orthostatic position. Color Doppler ultrasound shows reflux into the pampiniform venous plexus and in the spermatic vein that increases during the Valsalva maneuver and can also be classified [4–7] (Figs. 10.1, 10.2, 10.3, and 10.4).

Color Doppler Ultrasound Varicocele Grading

Grade	Features
1	No dilated scrotal veins Reflux in the spermatic cord veins (inguinal channel) during Valsalva
2	Small dilated veins at upper pole of testis Reflux only under Valsalva in the upright position
3	No enlarged veins in the supine position Enlarged veins in the upright position Reflux only under Valsalva
4	Enlarged veins even in the supine position Reflux only under Valsalva
5	Dilated veins Reflux without Valsalva maneuver

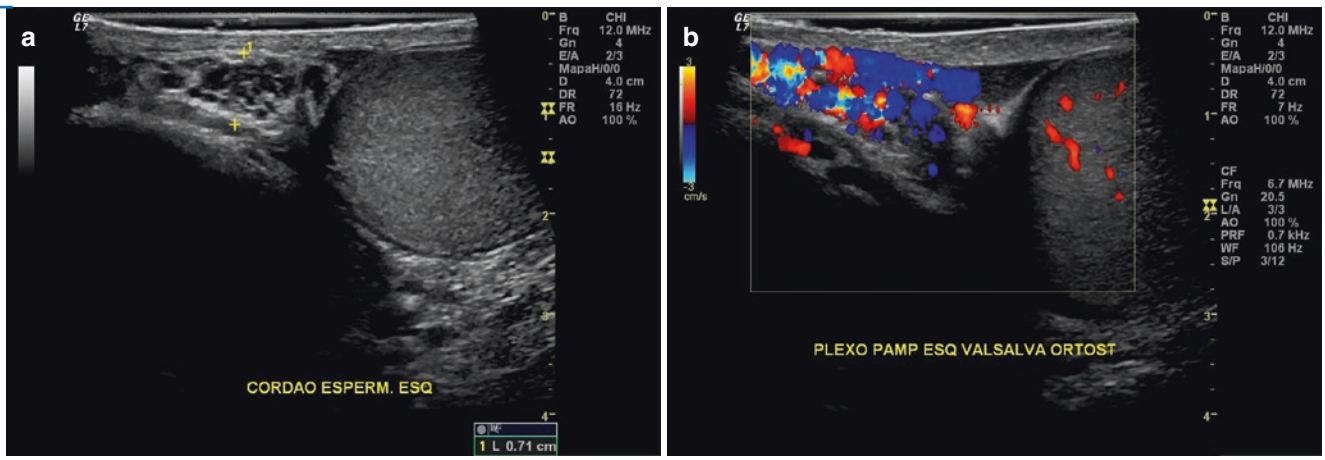

Fig. 10.1 Varicocele Grade 1. (**a**) No dilated intrascrotal veins. (**b**) Presence of reflux in the spermatic cord veins only during Valsalva maneuver

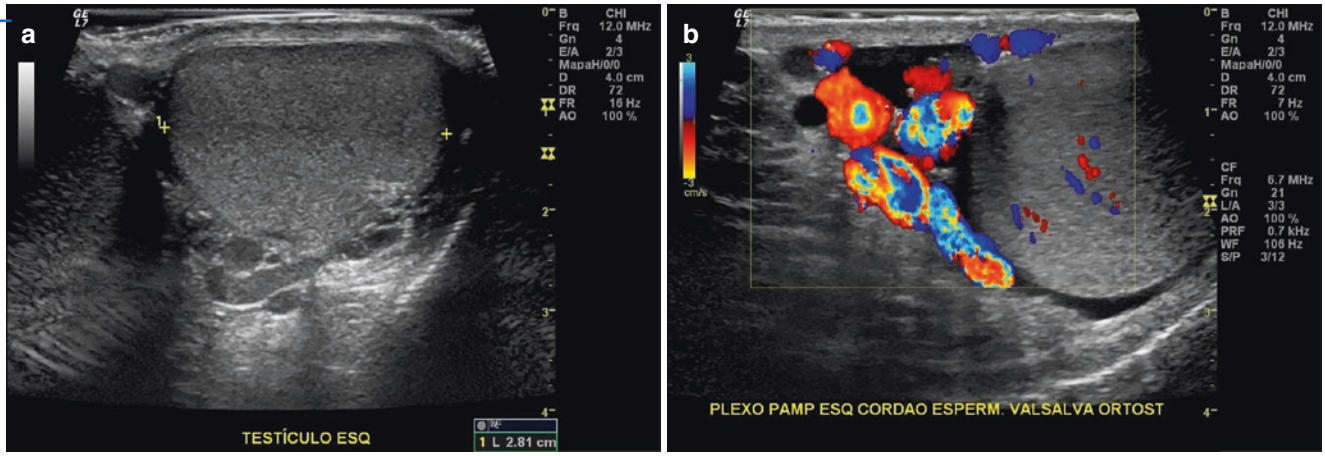

Fig. 10.2 Varicocele Grade 2. (**a**) B-mode shows dilated veins in the upper pole of the testicle. (**b**) Color Doppler shows reflux in the pampinform vein during Valsalva

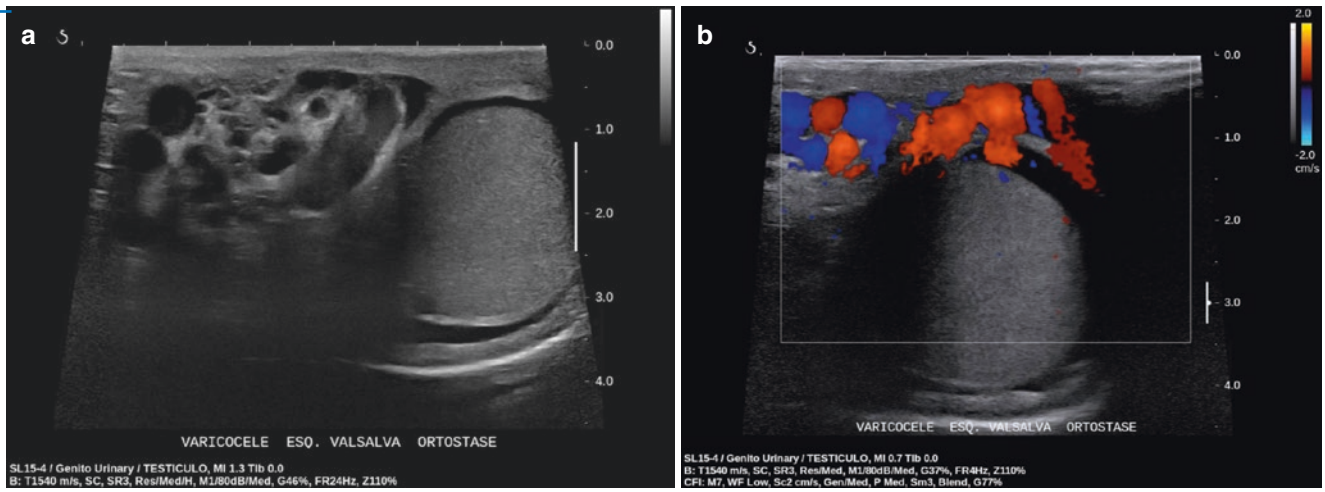

Fig. 10.3 Varicocele Grade 3. (**a**) B mode ultrasound shows enlarged veins in the upper pole and in front of the testicle only in standing position. (**b**) Color Doppler shows reflux in the pampinform vein during Valsalva

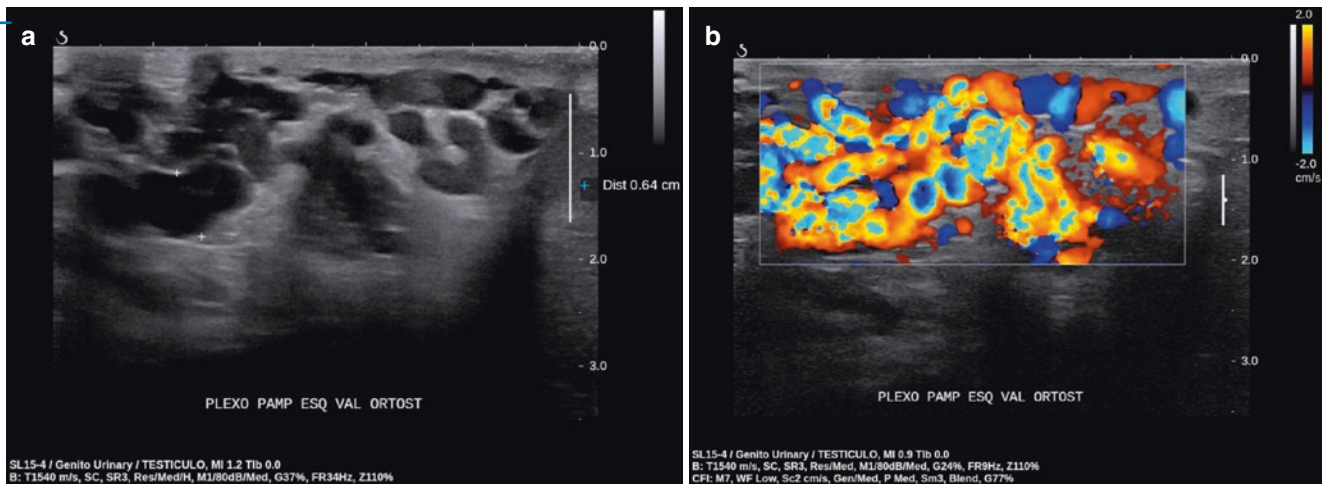

Fig. 10.4 Varicocele Grade 4. (**a**) B mode ultrasound shows enlarged veins in the upper pole and in front of the testicle even in the supine position. (**b**) Color Doppler shows reflux in the pampinform vein during Valsalva

Cryptorchidism

Cryptorchidism is the absence of one or both testes in the scrotum. This is a common birth defect of the male genitalia [4]. About 30% of premature infant boys are born with at least one undescended testis. When the testis is absent from the normal scrotal position, it can be found along the retroperitoneal path of descent from below the kidney, to the inguinal ring or in the inguinal channel. However, when testis is found outside that path, it is called *ectopic*, usually outside the inguinal channel, located under the skin of the thigh, in the perineum or in the femoral channel. Usually those testes are undeveloped (*hypoplastic*) or severely abnormal (*dysgenetic*).

Usually, undescended testes are associated with reduced fertility, increased risk of testicular seminomas, and psychological problems in adulthood. Besides that, undescended testes are more susceptible to torsion and to inguinal hernias [7–9] (Fig. 10.5).

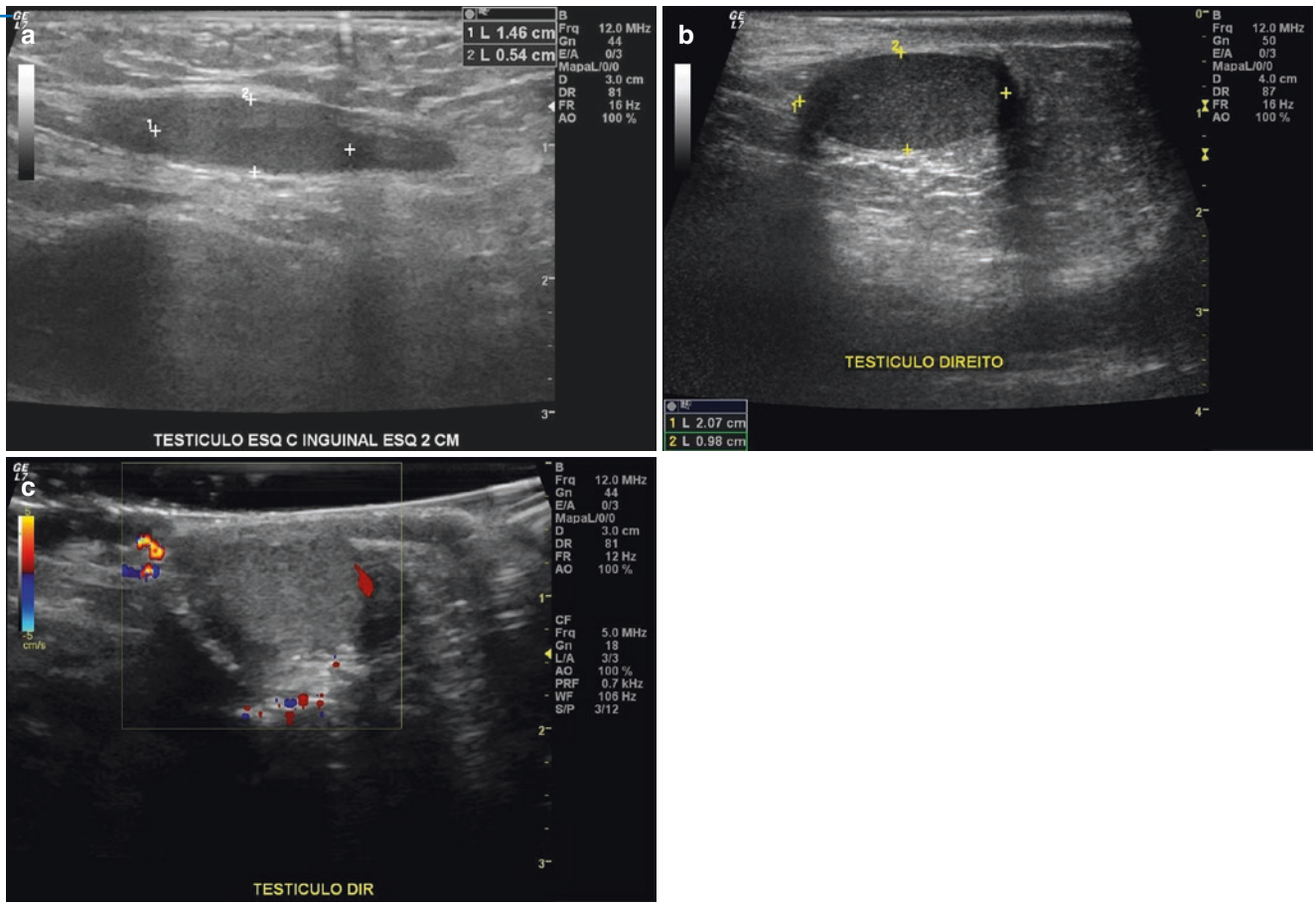

Fig. 10.5 Cryptorchidism. (**a**) B mode ultrasound shows reduced testicle in the inguinal channel. (**b**) B mode ultrasound shows testicle in the inguinal channel. (**c**) Color Doppler ultrasound shows hypovascular testicle in the inguinal channel

Hypogonadism

Hypogonadism is a condition in which the body does not produce enough of the testosterone hormone. Clinically low testosterone levels lead to the absence of secondary sex characteristics, infertility, muscle wasting, and many other abnormalities. Testicular, hypothalamic, or pituitary abnormalities can cause low testosterone levels. Ultrasound examinations show small homogeneous testicles and epididymis [4, 7, 9] (Fig. 10.6).

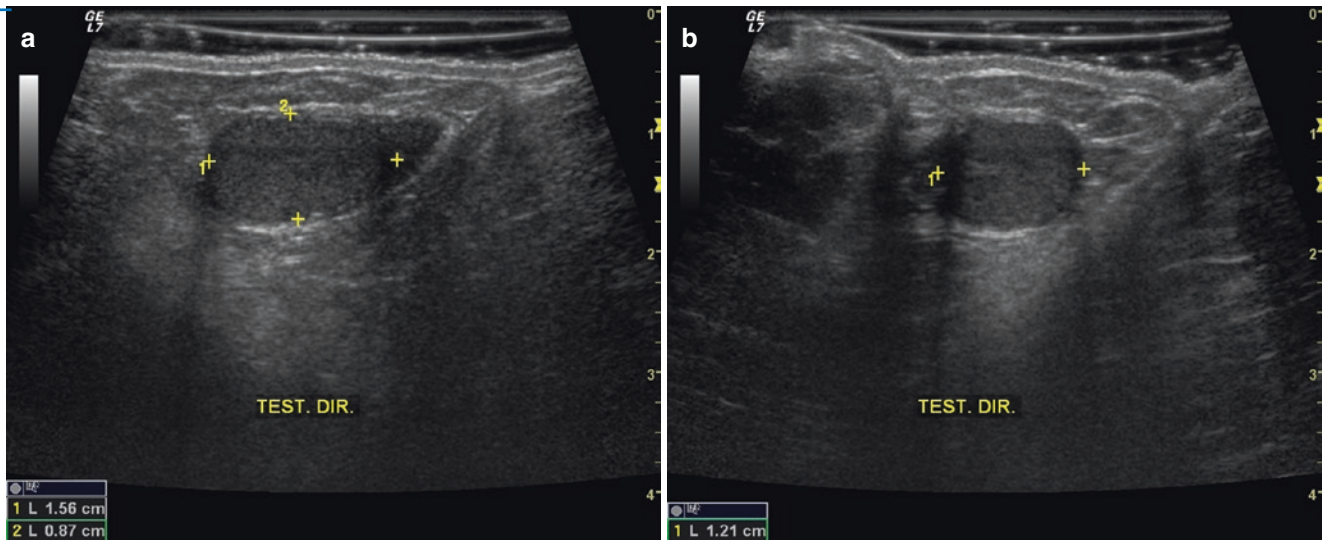

Fig. 10.6 Adult hypogonadism. (**a**,**b**) B mode longitudinal and transverse scan shows a small, homogeneous testicle

Obstructive Disorders

Congenital Bilateral Absence of the Vas Deferens

Congenital absence of the vas deferens occurs when the tube that carries spermatozoids from the testes (the vas deferens) fails to develop properly. Usually the testes develop and their function is normal, but sperm cannot be transported through the vas deferens. Men with this condition are infertile. This condition has not been reported to affect sexual performance. Clinically, these patients present with azoospermia, and ultrasound findings include the total absence or lack of part of the vas deferens, ectasia of rete testis (anechoic tubular structures in mediastinum testes), tubular ectasia of the epididymis (multiple cystic lesions in the head), and increase in testicular volume (>13 cc) [1, 10] (Fig. 10.7).

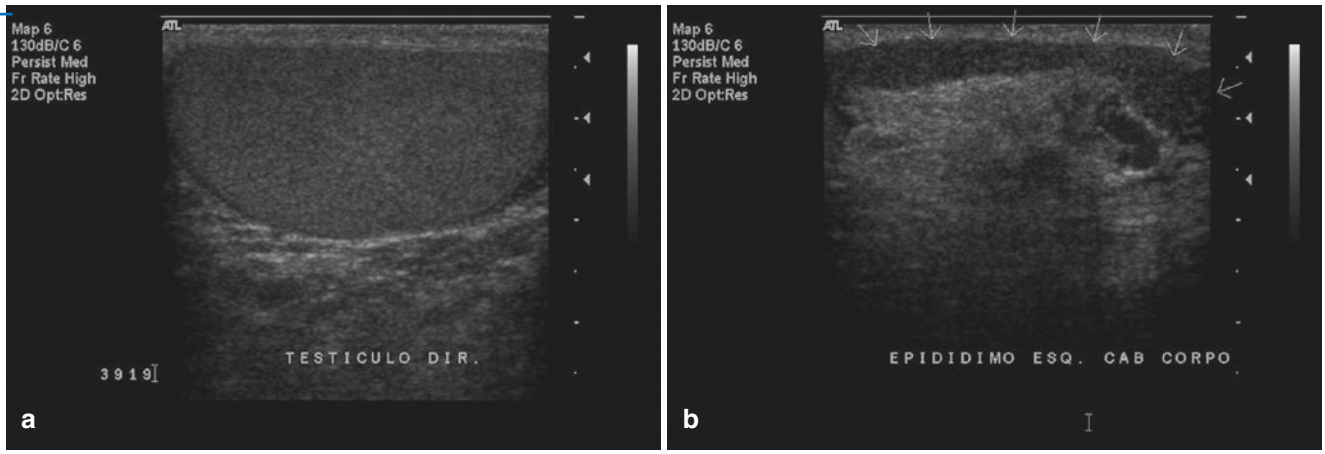

Fig. 10.7 Patient with azospermia due to vas deferens agenesia. (**a**) Increased homogeneous testicle volume. (**b**) Enlarged epidydimis and no vas deferens was seen

Epididymal Cysts

Epididymal cysts and spermatocele are a very common finding, and when large they can block the upper epididymis or efferent ductules. They are of lymphatic origin. The cysts contain serous fluid, lymphocytes, spermatozoa, and sometimes debris. They can manifest as a palpable mass. Up to one-third of patients can be asymptomatic. The cysts can also be solitary.

Ultrasound cyst content is anechoic, with no internal echoes and with posterior acoustic enhancement. While larger cysts may contain septations and can displace the testis, this is an important sign for differentiating cysts from hydrocele, as the former does not envelopes the testis [4, 9, 11] (Fig. 10.8).

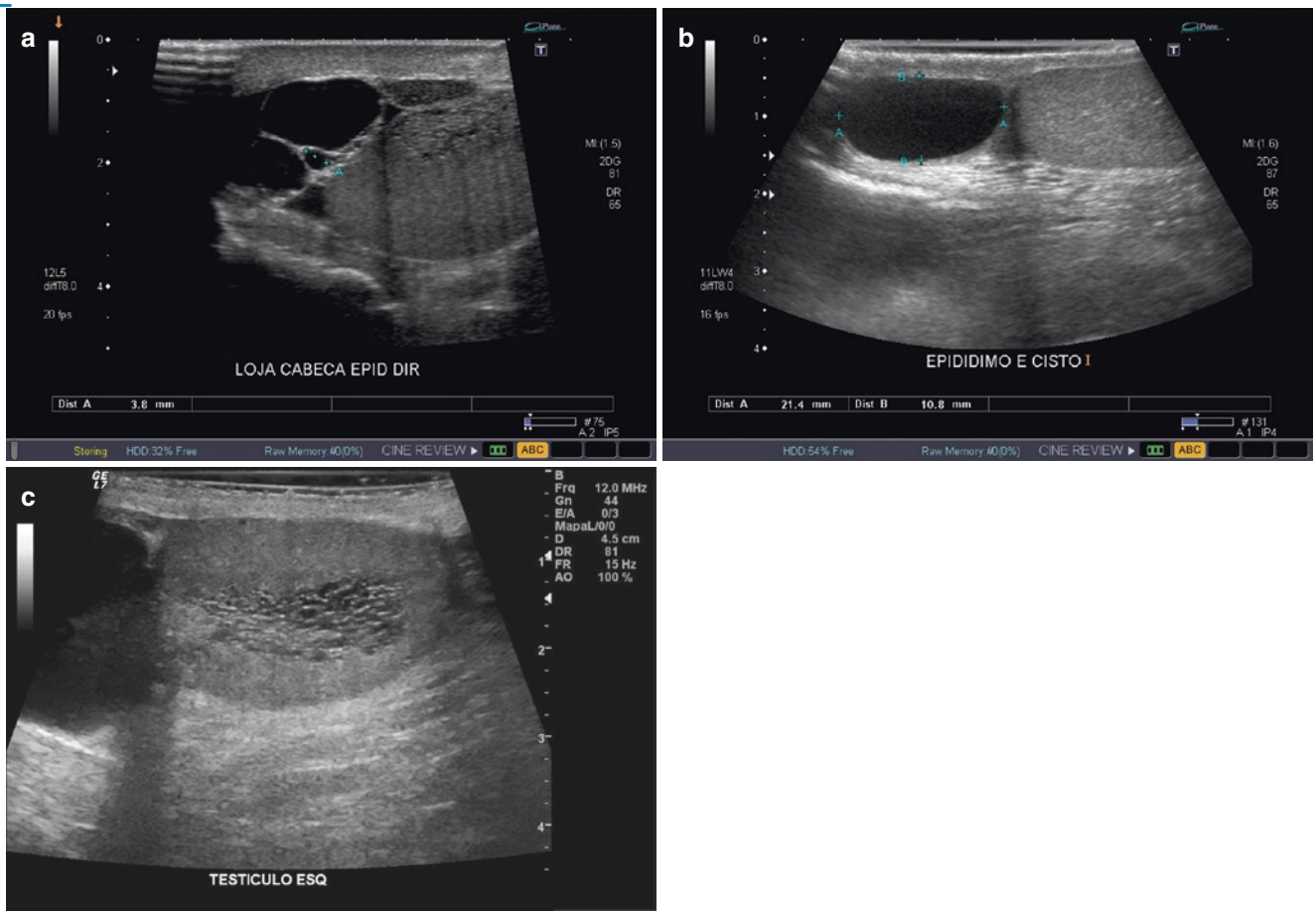

Fig. 10.8 Cyst in the epididymis head. (**a**) B mode ultrasound shows septated cyst in the epididymis head. (**b**) B-mode ultrasound shows simple cyst in the epididymis head. (**c**) B mode ultrasound shows dilated rete testis

Ejaculatory Duct Obstruction

Ejaculatory duct obstruction is a congenital or acquired condition that is caused by the obstruction of one or both ejaculatory ducts. Usually both ejaculatory ducts are completely obstructed. Basically, affected men are infertile due to aspermia or azospermia. They suffer from a very low volume of semen that lacks the gel-like fluid of the seminal vesicles – or they will suffer from no semen at all.

This obstruction is frequently caused by cysts located on the ejaculatory ducts. Transrectal sonography plays a critical role in the identification of ejaculatory duct obstruction. On ultrasound, normal ejaculatory ducts are seen on transverse scans as small hypoechoic structures within the central region of the prostate. In the sagittal scan, they appear as linear structures coursing from seminal vesicles into the urethra. In many patients with duct obstruction, the ejaculatory ducts are not visible, but the presence of cysts located posterior to prostatic urethra, with or without dilatation of the seminal vesicle can suggest this diagnosis. The differential diagnosis for prostatic cysts includes utricle cysts, Müllerian cysts, prostatic retention cysts, seminal vesicle cysts, and ejaculatory duct cysts [1, 4, 10] (Fig. 10.9).

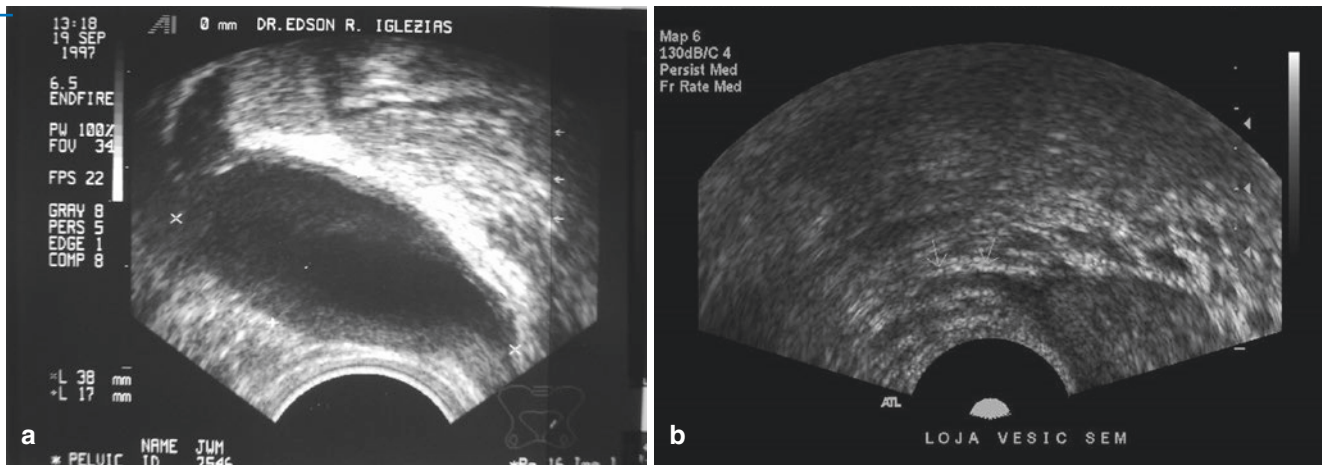

Fig. 10.9 Ejaculatory duct obstruction. (**a**) Transrectal sagittal scan shows a cyst in the seminal vesicle. (**b**) Sagittal scan shows no vesicle in the anatomic site (*arrows*)

References

1. Phillipson GTM, Petrucco OM, et al. Congenital bilateral absence of the vas deferens, cystic fibrosis mutation analysis and intracytoplasmatic sperm injection. Hum Reprod. 2000;15(2):431–5.
2. Nallella KP, Sharma RK, et al. Significance of sperm characteristics in the evaluation of male fertility. Fertil Steril. 2006;85(3):629–34.
3. Yatsenko AN, Georgiadis AP, et al. Mutations, meiotic arrest and azoospermia in infertile men. N Engl J Med. 2015;372:2097–107.
4. Horstman W. Scrotal imaging. Urol Clin North Am. 1997;24(3):653–71.
5. Beddy P, Geoghegan RF, et al. Testicular varicoceles. Clin Radiol. 2005;60:1248–55.
6. Pauroso S, Di Leo N. Varicocele: ultrasonographic assessment in daily clinical practice. JUltrasound. 2011;14:199–204.
7. Aso C, Enriques G, et al. Gray scale and color Doppler sonography of scrotal disorders in children: an update. Radiographics. 2005;25:1197–214.
8. Woodward PF, Soahey R, et al. Tumors and tumorslike lesions of the testis: radiologic–pathologic correlation. Radiographics. 2002;22:189–216.
9. Saito OC. Ultrassonografia do escroto. In: Saito OC, editor. Ultrassonografia de Pequenas Partes. 2nd ed. Revinter Rio de Janeiro Brazil; 2013.p. 173–227.
10. Moon MH, Kim SH, et al. Scrotal US for evaluation of infertile men with azoospermia. Radiology. 2006;239(1):168–73.
11. Ammar T, Sidhu PS, et al. Male infertility: the role of imaging in diagnosis and management. Br J Radiol. 2012;85:559–68.

Part III

Others Diseases

The Sella Turcica

11

Paulo Eduardo de Aguiar Kuriki

Anatomy Imaging

The sella turcica is a cavity located in the superior surface of the sphenoid bone. The pituitary gland is located inside the sella turcica and comprises three lobes: anterior, intermediate, and posterior. In humans, the intermediate lobe is a thin, indistinct layer; as a result, it is often considered part of the anterior lobe. The suprasellar cistern is located above it, and the cavernous sinuses are paired laterally to the sella turcica. At the top of the suprasellar cistern is the optic chiasm. The pituitary stalk makes the connection between the hypothalamus and the posterior lobe [1]. A normal sella turcica anatomy is shown below (Fig. 11.1).

The dimensions of the pituitary gland may vary according to age and gender, averaging 3–8 mm in height, 12 mm in width, and 8 mm anteroposterior. It may increase in size as a result of physiological hormones, mainly in girls and pregnant women. At female puberty, it may measure 10 mm in height; for boys, the normal height of a pituitary gland can be up to 8 mm. During pregnancy, the pituitary gland can show a more significant growth, measuring up to 12 mm, with the maximum height reached immediately postpartum [2].

The pituitary gland vascularization is provided mainly from the hypophyseal portal venous system. Branches from the internal carotid artery and the superior and inferior hypophyseal arteries also exist. Because of this mixed combination of arterial and venous supply, differential rates of enhancement of the pituitary gland can be seen during dynamic scans after bolus administration of an intravenous contrast agent (Fig. 11.2).

Magnetic resonance imaging (MRI) is an excellent method for studying the sella turcica [3]. The anterior and posterior lobes of the pituitary gland can be distinguished. Whereas the anterior lobe appears with signal intensities similar to normal white matter in all sequences, the posterior lobe shows hyperintensity on T1, making it very easy to be identified even on non-contrast examinations. After the administration of intravenous (IV) contrast, both anterior and posterior lobes exhibit intense enhancement (Fig. 11.3).

The exception to this signal pattern is seen in newborns, where the anterior lobe exhibits higher signal intensity on T1 images [4] (Fig. 11.4). This signal intensity usually lasts until age 2 months and begins decreasing until the anterior lobe shows hypointensity, just like in adults, sometime between the 4th and 6th months.

P.E. de Aguiar Kuriki
Departamento de Diagnóstico por Imagem, Universidade Federal de São Paulo, São Paulo, SP, Brazil
e-mail: paulokuriki@gmail.com

L.R.M.F. de Souza et al. (eds.), *Atlas of Imaging in Infertility*, DOI 10.1007/978-3-319-13893-0_11

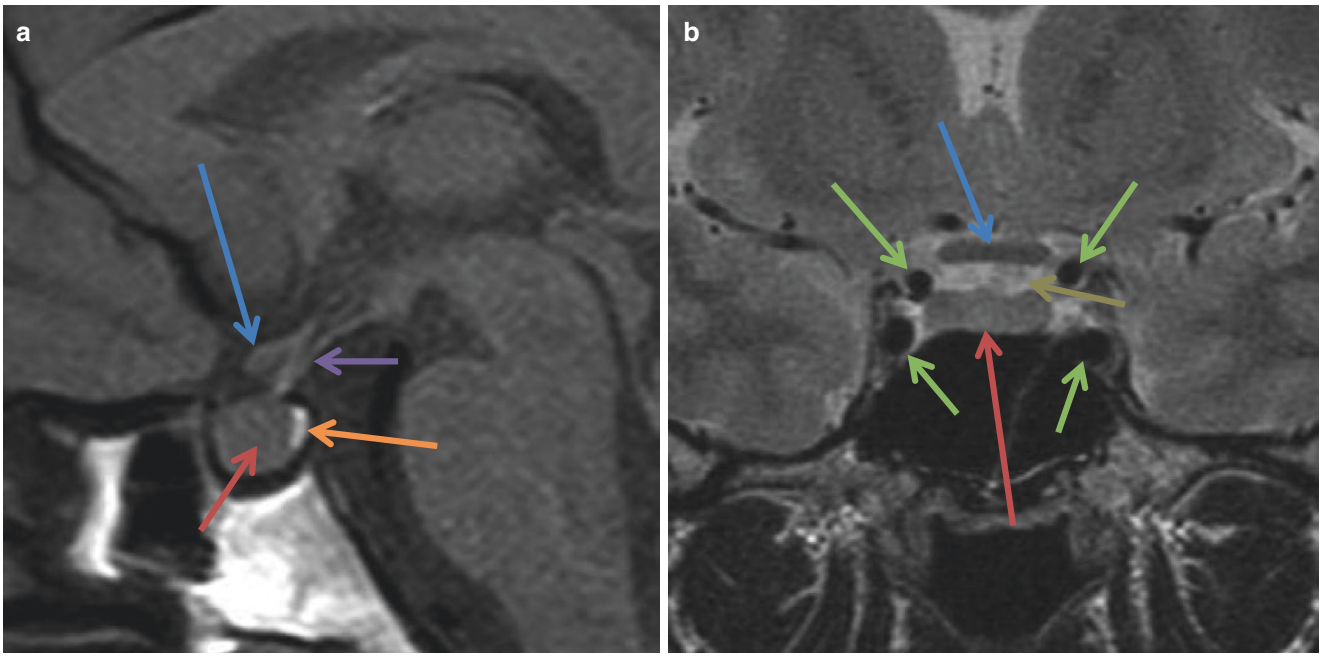

Fig. 11.1 Normal anatomy is shown above. (**a**) Sagittal T1. (**b**) Coronal T2. Legend: *Red arrow*: pituitary anterior lobe (adenohypophysis), *Orange*: pituitary posterior lobe (neurohypophysis), *Blue*: optic chiasm, *Purple*: pituitary stalk, *Brown*: suprasellar cistern, *Green*: internal carotid arteries running inside the cavernous sinuses

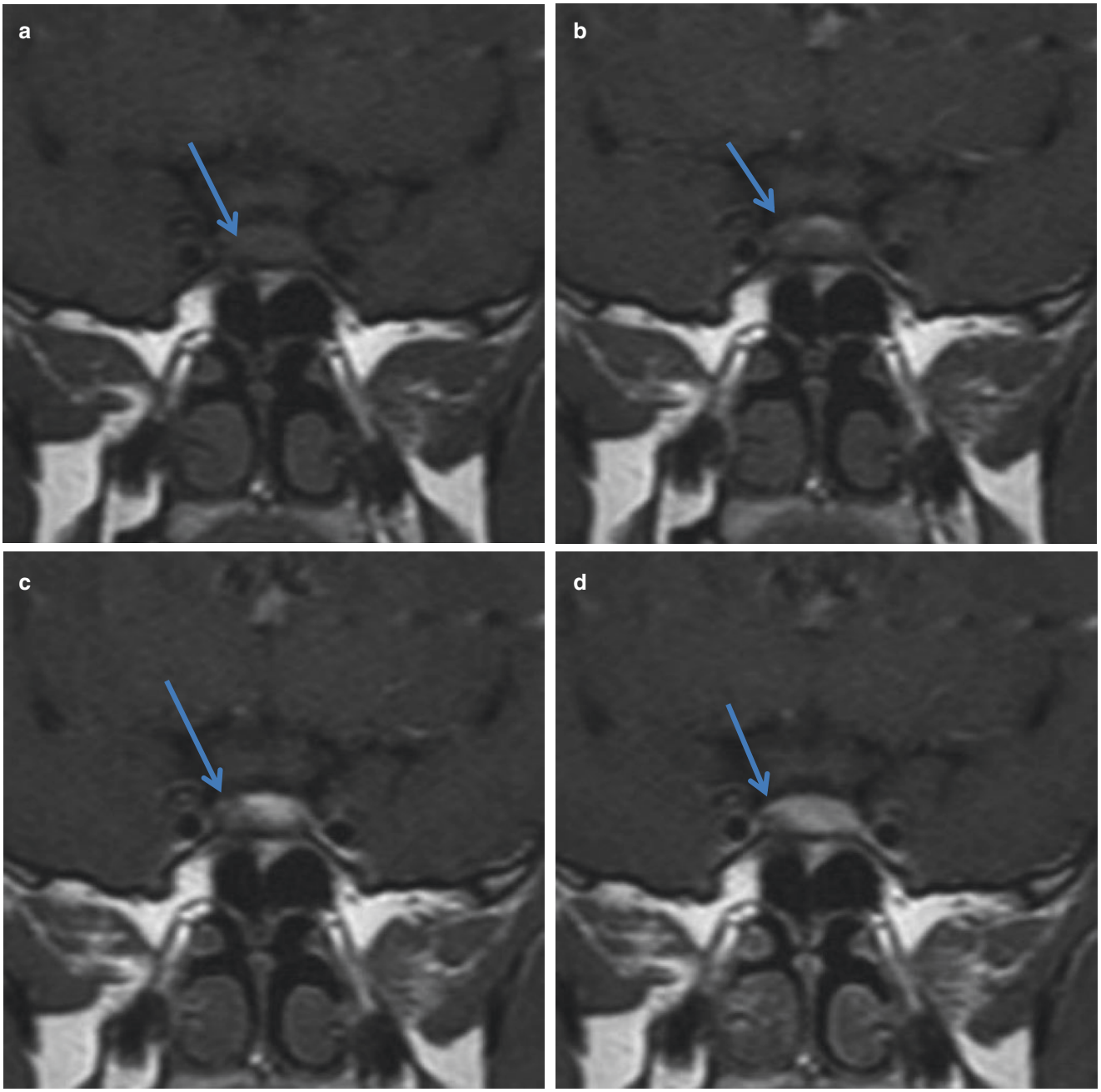

Fig. 11.2 Microadenoma. T1-weighted coronal images obtained dynamically after the bolus injection of intravenous gadolinium (**a–d**); the time interval between each sequence is 20 s. It is possible to see the gradual enhancement of the gland starting from its top part until it is fully complete. Note a small area of hypoperfusion at the right *blue arrow*, corresponding to a nodule, that is better seen at the last sequence.

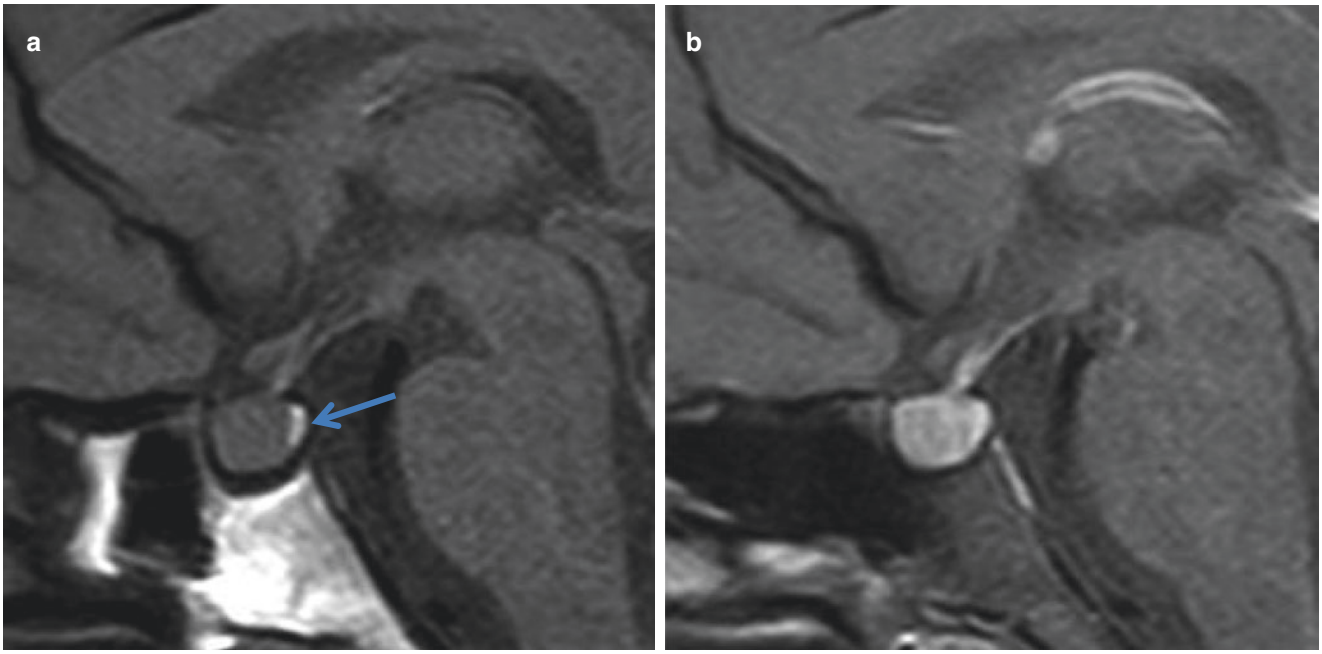

Fig. 11.3 Normal neurohyposhisis anatomy. T1-weighted sagittal images pre- and post-contrast. The *arrow* points to the spontaneous bright neurohypophysis, located at the sella turcica posteriorly. After the injection of IV gadolinium, the entire gland exhibits an intense enhancement

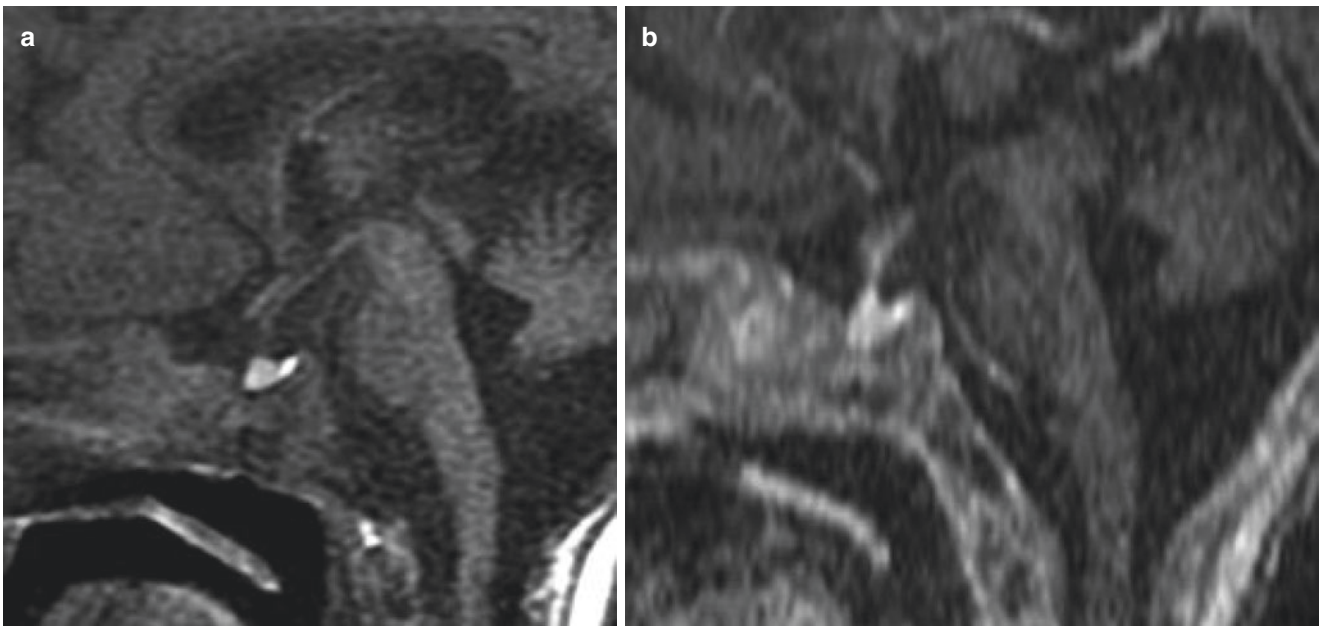

Fig. 11.4 Normal anatomy of newborns. (**a**) T1 Sagittal pre-contrast. Anterior lobe showing hyperintensity on sagittal T1-weighted image. (**b**) T1 sagittal post-contrast injection. Normal enhancement of the anterior lobe as well as the pituitary stalk

Imaging Techniques

The best modality used for evaluating the sella turcica is the MRI. It generates images with high resolution, enabling a proper identification of the sella turcica and the pituitary gland and its parts, thus allowing the visualization of lesions [5].

Images are usually performed in two planes, coronal and sagittal. The coronal plane is great for identifying the sella turcica, pituitary gland, cavernous sinus, internal carotid arteries, and the suprasellar cistern. Because of the typical T1 hyperintensity, the sagittal plane is good for confirming the location of the posterior lobe of the pituitary gland inside the sella turcica. Some pituitary microadenomas can show hyperintensity in T2 images, so a coronal T2 image is commonly included in all protocols.

The paramagnetic contrast-enhanced images can increase the sensitivity for detecting small microadenomas. As adenomas exhibit different contrast-enhancement rates, dynamic images should be taken immediately after the injection of the contrast medium [6]. The adenomas usually show less enhancement than a normal gland around it during the first seconds. As the image contrast begins to dissipate, the visual difference between the adenoma and the rest of the normal gland can disappear. As this time can vary with different adenomas, this is the reason that dynamic enhanced images obtained after the injection of the contrast medium can increase the sensitivity for detecting microadenomas (Fig. 11.5).

Many services suggest scanning T1-weighted images in coronal and sagittal planes. If no lesion is detected, the IV contrast is injected and coronal dynamic T1-weighted images are immediately obtained. After the dynamic images, conventional T1-weighted spin-echo images are scanned. A T2-weighted coronal sequence can be performed to evaluate lesions at the suprasellar cistern, optic chiasm extrinsic compressions, or hypothalamic lesion.

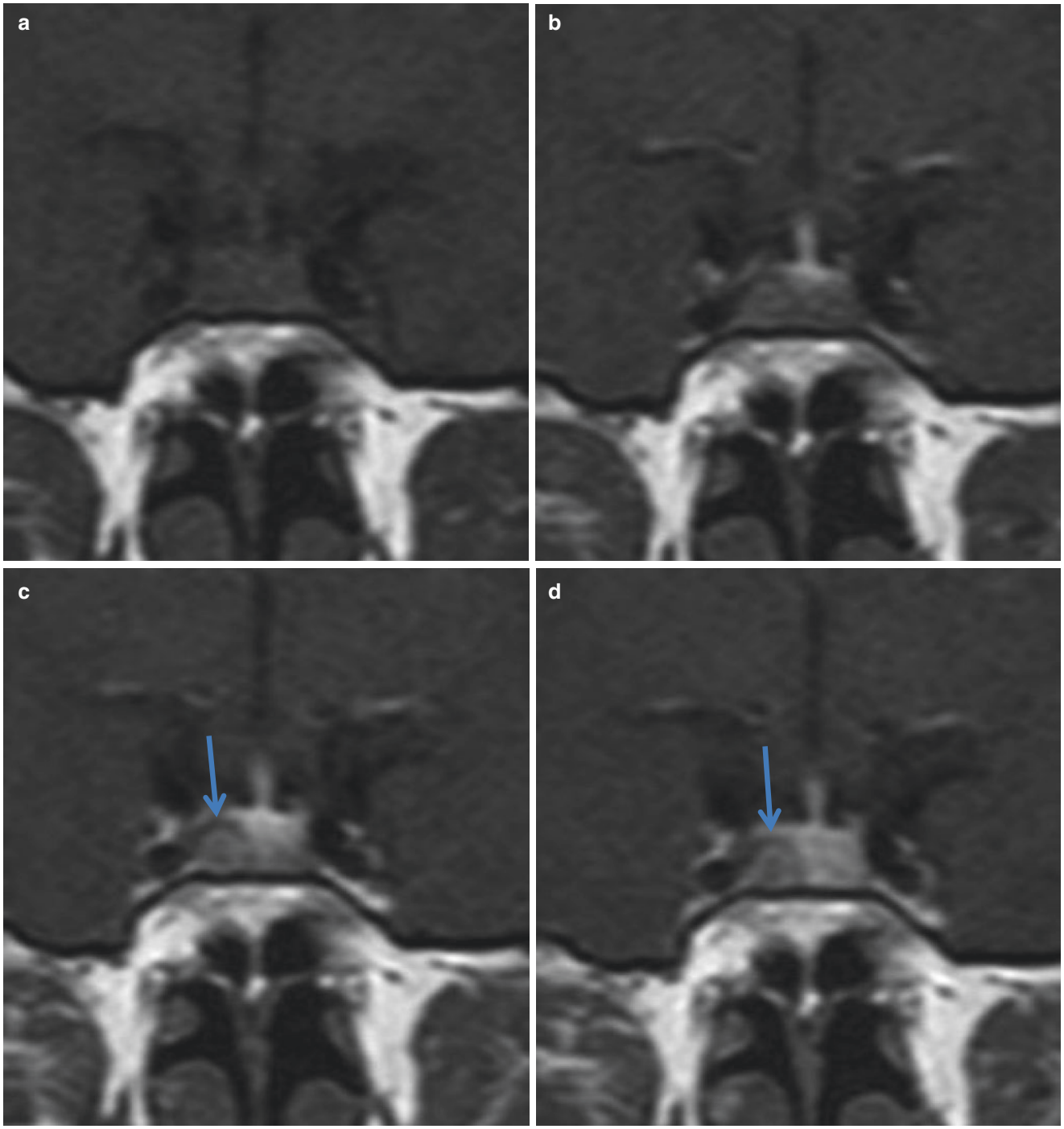

Fig. 11.5 Post-contrast dynamic acquisition. (**a**–**d**) Coronal T1 weighted images acquired dynamically after the injection of IV contrast. The same microadenoma from this figure (*blue arrow*) shows less enhancement than the rest of the pituitary gland

Congenital Abnormalities

Pituitary Gland Hypoplasia

Short stature and growth hormone failure are common indications for sella turcica evaluation. Many patients also have anterior pituitary hormone deficiencies [7]. MRI can show some of these findings: small sella turcica, small anterior pituitary gland lobe, absence of T1-weighted hyperintensity related to the neurohypophysis, absent or hypoplastic distal pituitary stalk, and atopic neurohypophysis located close to the proximal pituitary stalk (Fig. 11.6). Other midline malformations such as Chiari I malformation, optic nerve hypoplasia, and medial deviation of the carotid arteries can be present.

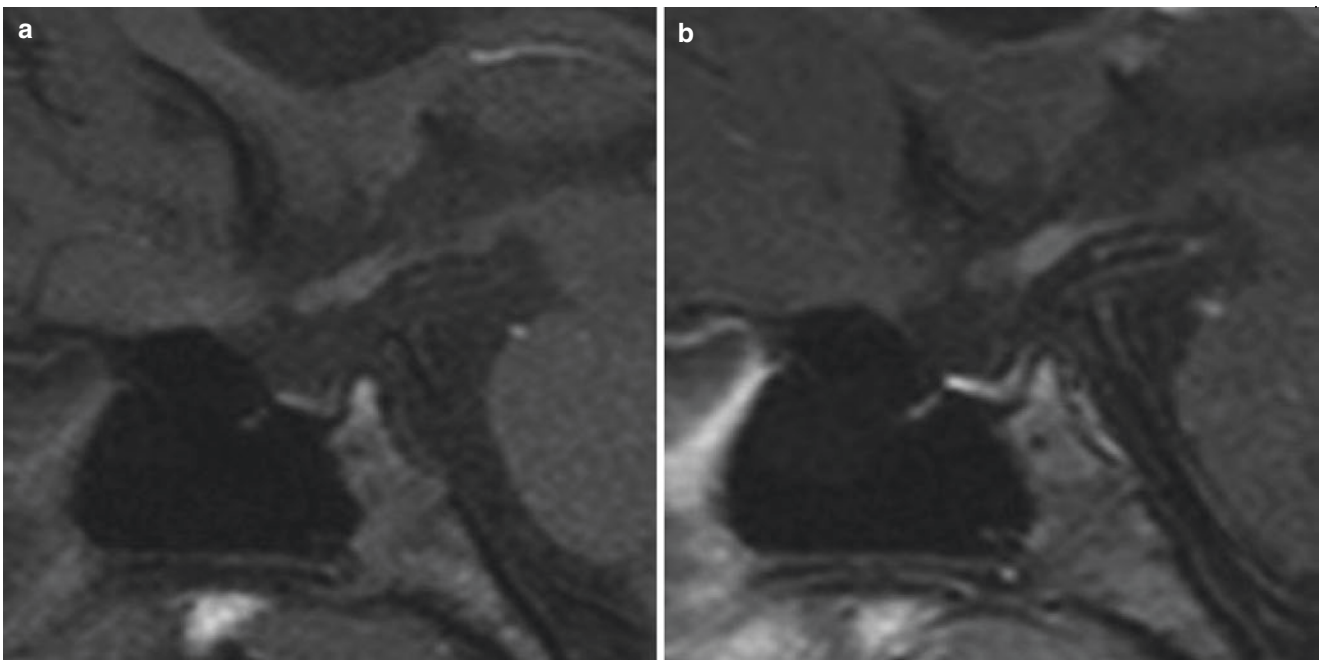

Fig. 11.6 Pituitary gland hypoplasia. (**a**) Sagittal T1-weighted image pre-gadolinum and (**b**) post-gadolinium injection shows a small sella turcica, with a small pituitary gland and the absence of the characteristic T1 bright spot related to the neurohypophysis

"Empty Sella Turcica"

The term "empty sella turcica" refers to a pituitary gland that is present but flattened, with the sella turcica filled with CSF (Fig. 11.7). In some cases, the sella can become enlarged due to CSF pulsation. This finding is usually incidental, and has little or no clinical significance [8]. When symptoms are present, patients can exhibit visual field loss, CSF rhinorrhea or endocrine dysfunction. Other non-specific complaints such as headache, memory loss, or dizziness can be seen. In some cases, the above-mentioned findings can be related to idiopathic intracranial hypertension (IIH), also known as benign intracranial hypertension or pseudotumor cerebri.

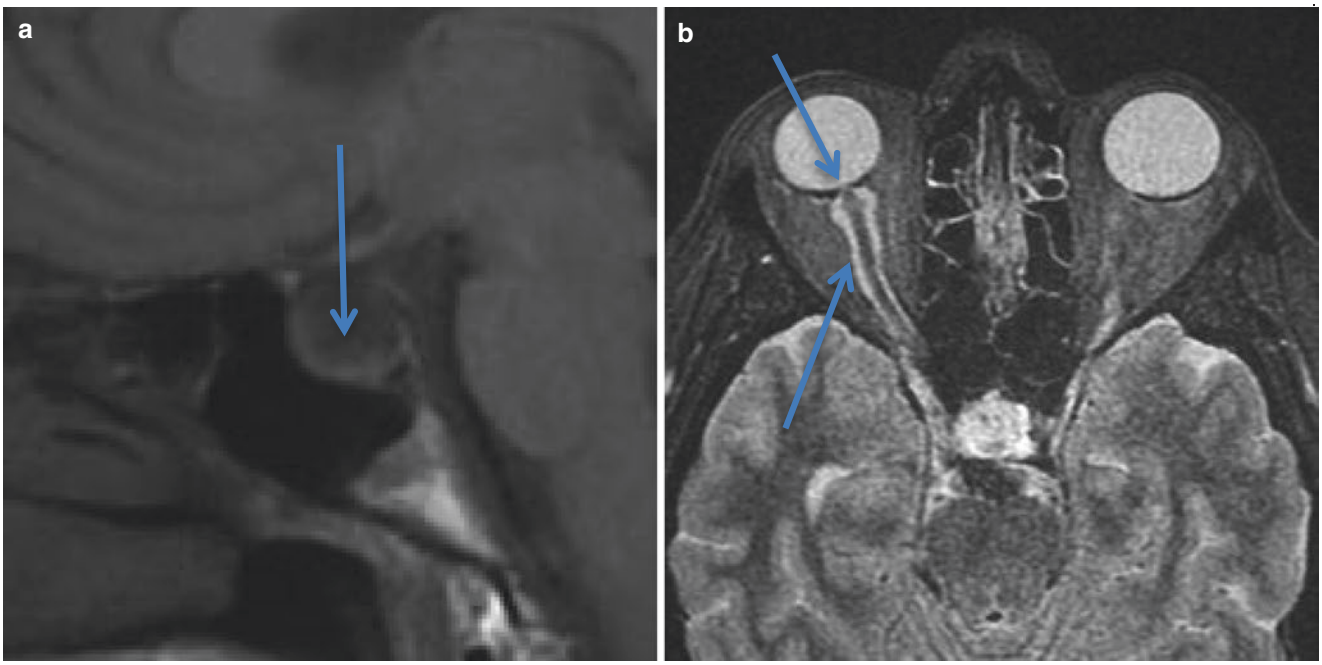

Fig. 11.7 Empty sella turcica. (**a**) Sagittal T1-weighted image showing an enlarged sella turcica filled with cerebralspinal fluid (**CSF**). The pituitary gland is flattened (*arrow*) against the floor. (**b**) A female patient with idiopathic intracranial hypertension. Besides the empty sella, the MRI shows a prominent subarachnoid space around the optic nerves (*posterior arrow*) and flattening of the posterior sclera (*anterior arrow*), characterizing papilloedema

Tumors

Pituitary Microadenoma

The pituitary microadenomas represent 10–15% of all intracranial neoplasms and are the most common sella turcica tumor. Almost all pituitary tumors are benign adenomas. A nodule measuring up to 10 mm is called a microadenoma, and when it is larger than 10 mm, it is considered a macroadenoma [9]. Adenomas can still be classified as functional or nonfunctional, depending on the presence or absence of hormonal activity. Approximately 25% of all adenomas will be nonfunctioning tumors, and 75% will present clinical symptoms, depending on the kind of hormone secreted. Usually, functional adenomas are discovered early because of the signs and symptoms of hypersecretion hormone. Some large tumors can also be discovered when they cause dysfunction due to normal pituitary gland or chiasm compression.

Among functional tumors, 50% will be prolactinomas, which secrete prolactin, leading to galactorrhea, amenorrhea, infertility, loss of libido, and impotence. These symptoms can be more discrete in men and postmenopausal women. After prolactinomas, adenomas that produce growth hormone and ACTH are the next most prevalent functional tumors.

While functional tumors can be detected early, nonfunctional tumors can be discovered when compressing or invading adjacent structures. They can lead to visual disturbance when compressing the optic chiasm, and headache due to the third ventricle and hydrocephalus or cranial nerve palsy and the cavernous sinus is invaded.

On MRI, the pituitary adenoma can show as a subtle hypointensity lesion on T1-weighted images compared to a normal gland signal. When old blood is present, the nodule can appear hyperintense on T1. On T2 images, one-third to one-half of microadenomas will be hyperintense (Fig. 11.8). Most are isointense to normal gland. Other image findings can be seen in microadenomas: unilateral contour deformities and contralateral deviation of the pituitary stalk.

In case small isointense adenomas cannot be detected on non-enhanced images, the dynamic T1-weighted images can be obtained just after the bolus injection of IV contrast. Because of the different rate of enhancement between a normal gland and an adenoma, the latter will remain as a hypointense lesion surrounded by a normal enhancing gland (Figs. 11.9 and 11.10).

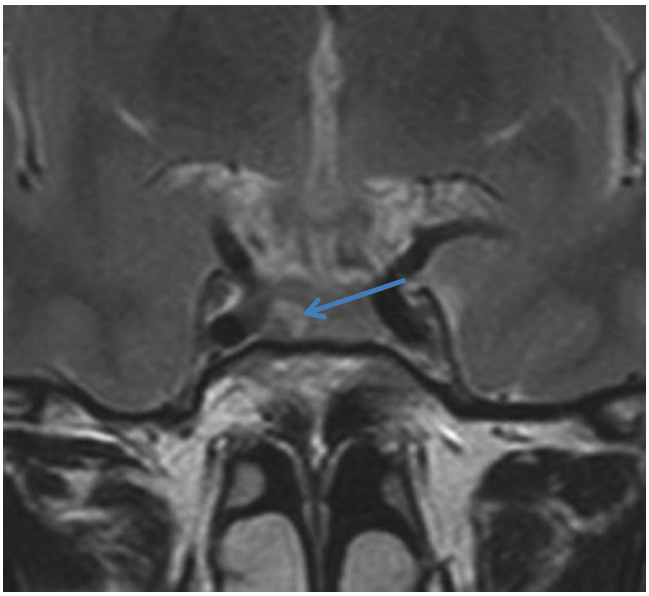

Fig. 11.8 Microadenoma detected on non-enhanced images. (**a**) Coronal T2-weighted image showing a hyperintense microadenoma (*arrow*) at the right portion of the sella turcica.

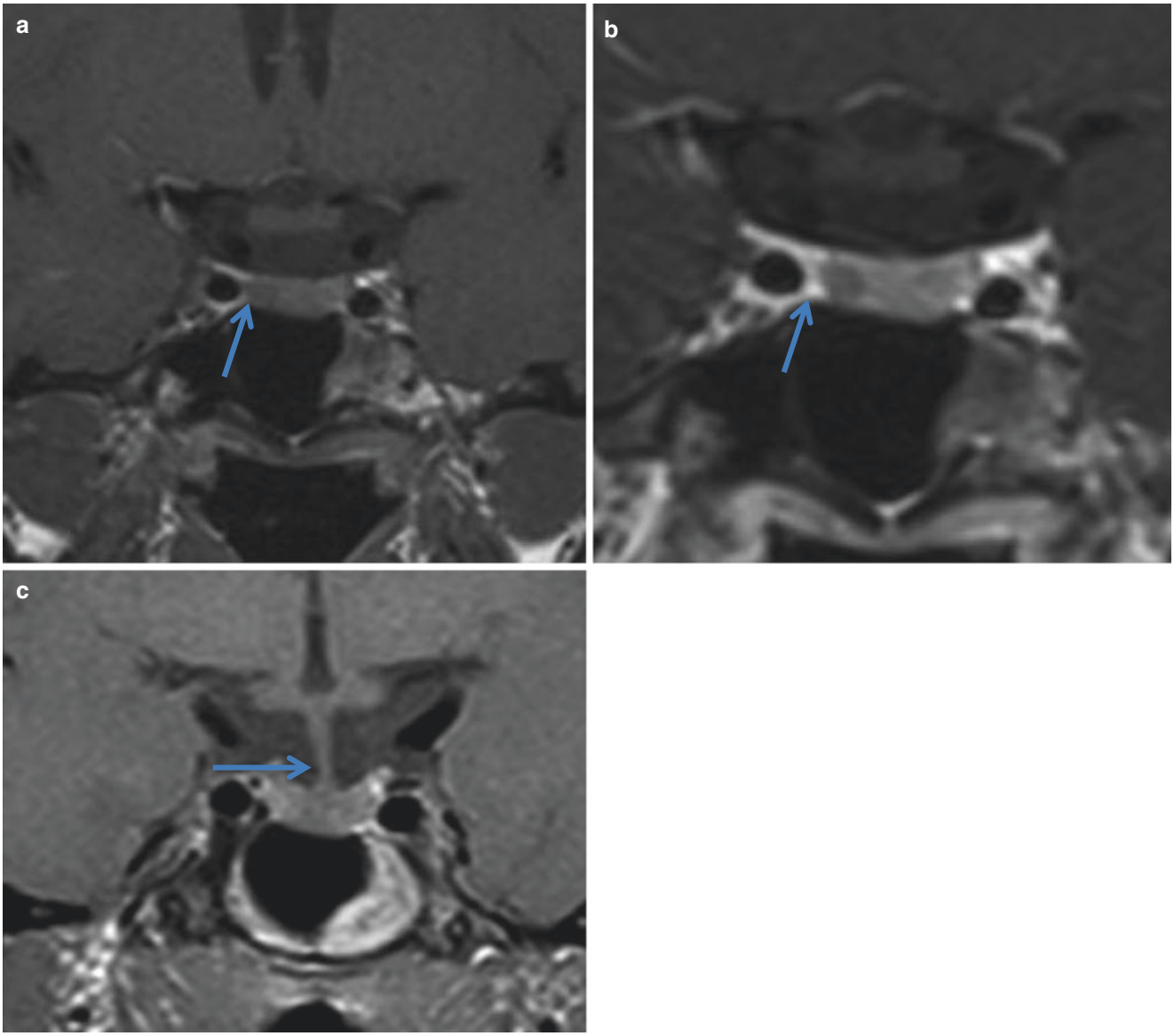

Fig. 11.9 Microadenoma. (**a**) Coronal T1 – a subtle hypointense nodule (*arrow*) is seen on the right side of the pituitary gland. (**b**) After the contrast injection, this small nodule takes less contrast than a normal gland, making the diagnosis very easy. (**c**) Coronal T1 located more posteriorly. It is possible to see a subtle pituitary stalk deviation to the left (*arrow*) caused by the right nodule described above

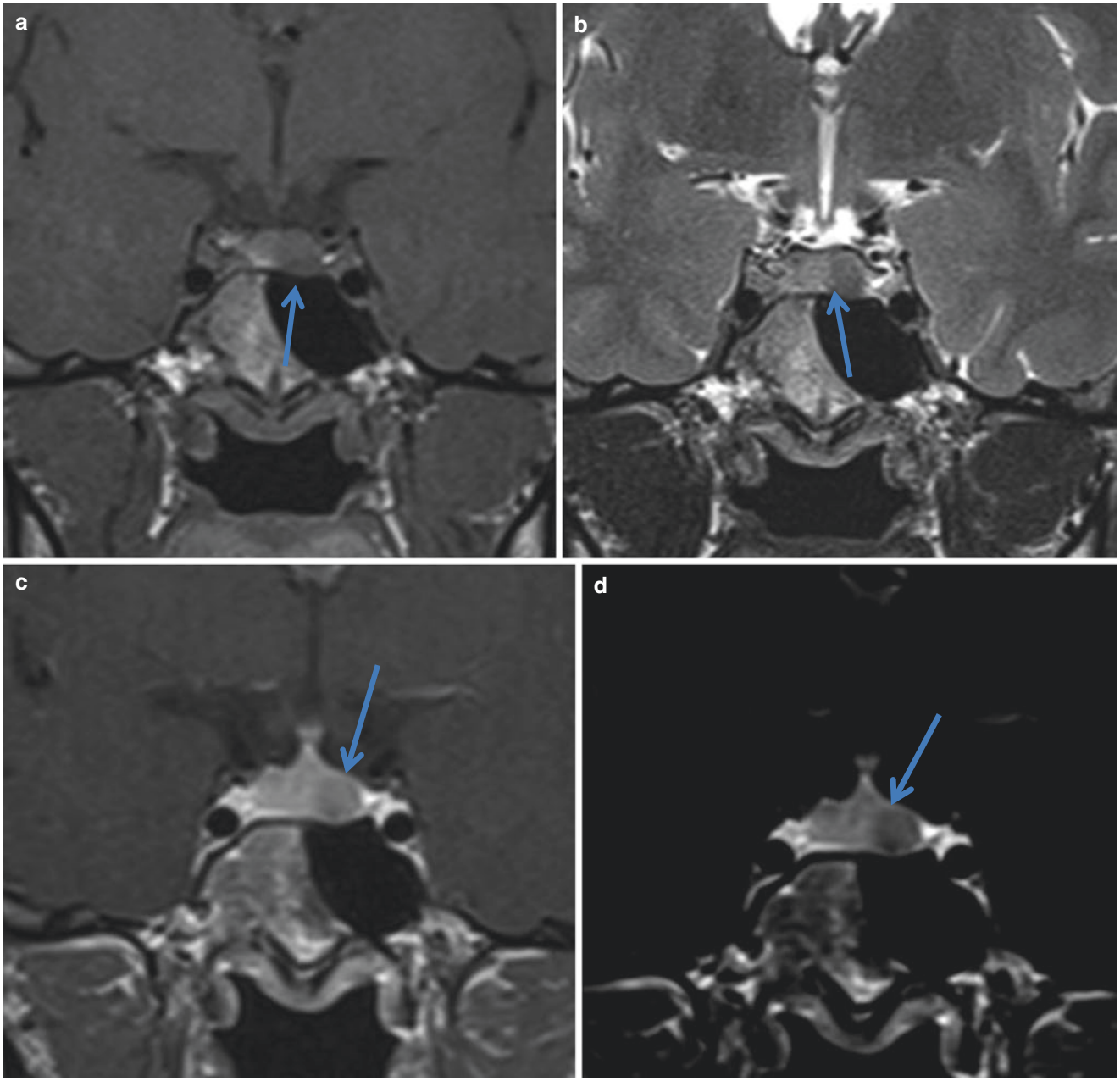

Fig. 11.10 Microadenoma. (**a**) Coronal T1 non-enhanced. It is possible to identify a small remodeling of the pituitary fossa at the left. (**b**) Coronal T2. The nodule is subtly hypointense in comparison to the normal gland signal at the right. (**c**) Coronal T1 post-gadolinium injection. We can see the nodule exhibiting less enhancement than the rest of the gland. (**d**) The same sequence as in (**c**), but after being windowed to allow a better contrast between the nodule and the rest of the normal gland

Pituitary Macroadenoma

Pituitary macroadenomas are usually non-functioning tumors. For this reason, they can reach a significant volume before becoming clinically detectable, due to the compression of surrounding structures [10]. In many cases, the tumor can occupy the entire sella turcica, so a normal gland cannot be visualized due to compression from the macroadenoma. Another common feature is the size enlargement of the sella turcica promoted by the slow growth of the tumor.

The macroadenoma can extend to the suprasellar cistern, compressing the optic nerves, chiasm, and tracts. When the tumor extends to the suprasellar cistern, passing through the sellar diaphragm, the classic snowman configuration can take place (Fig. 11.11).

Laterally, the invasion of the cavernous sinuses can be seen. This invasion can be suggested when two-thirds or more of the internal carotid artery is surrounded by the tumor or when the tumor is seen between the lateral wall of the cavernous sinus and the artery [11] (Fig.11.12).

Adenomas can be treated clinically or surgically. Along with prolactine level reduction, in some cases it is possible to see important tumor shrinkage (Fig. 11.13).

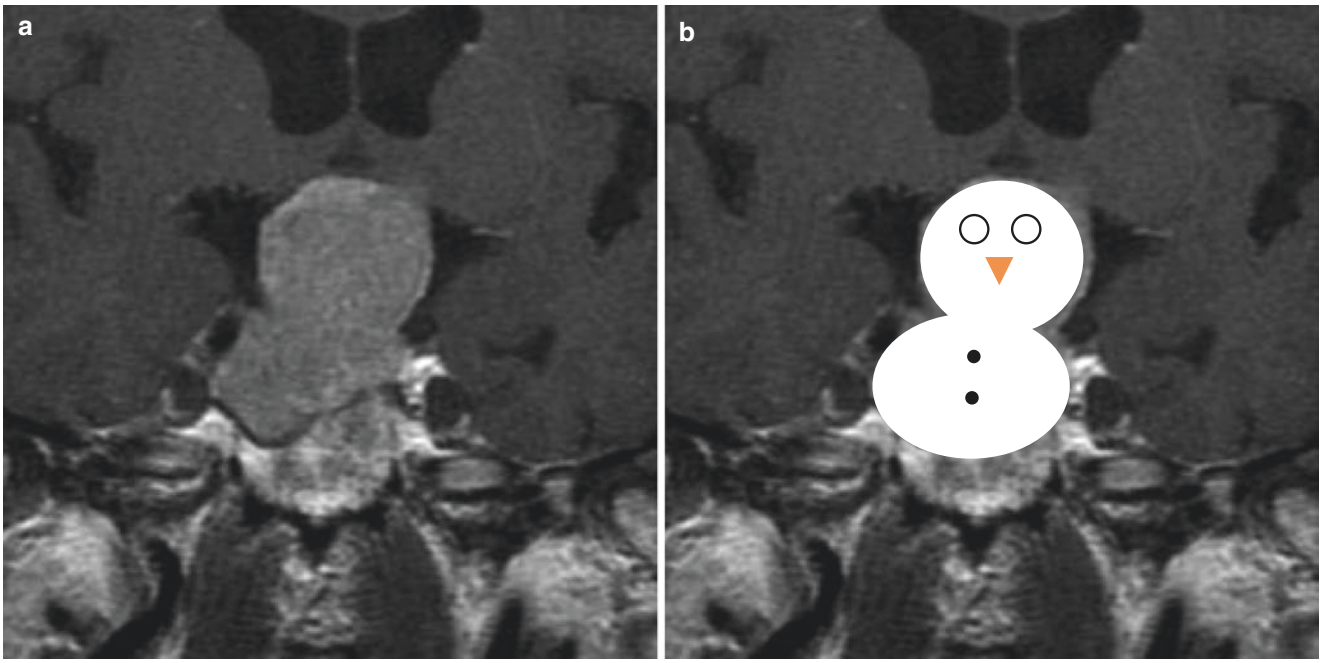

Fig. 11.11 Macroadenoma. T1 post-contrast injection showing a macroadenoma occupying the sella turcica and the suprasellar cistern. A typical characteristic is the "neck" separating the intrasellar and suprasellar components of the tumor, giving the classic aspect of snowman appearance

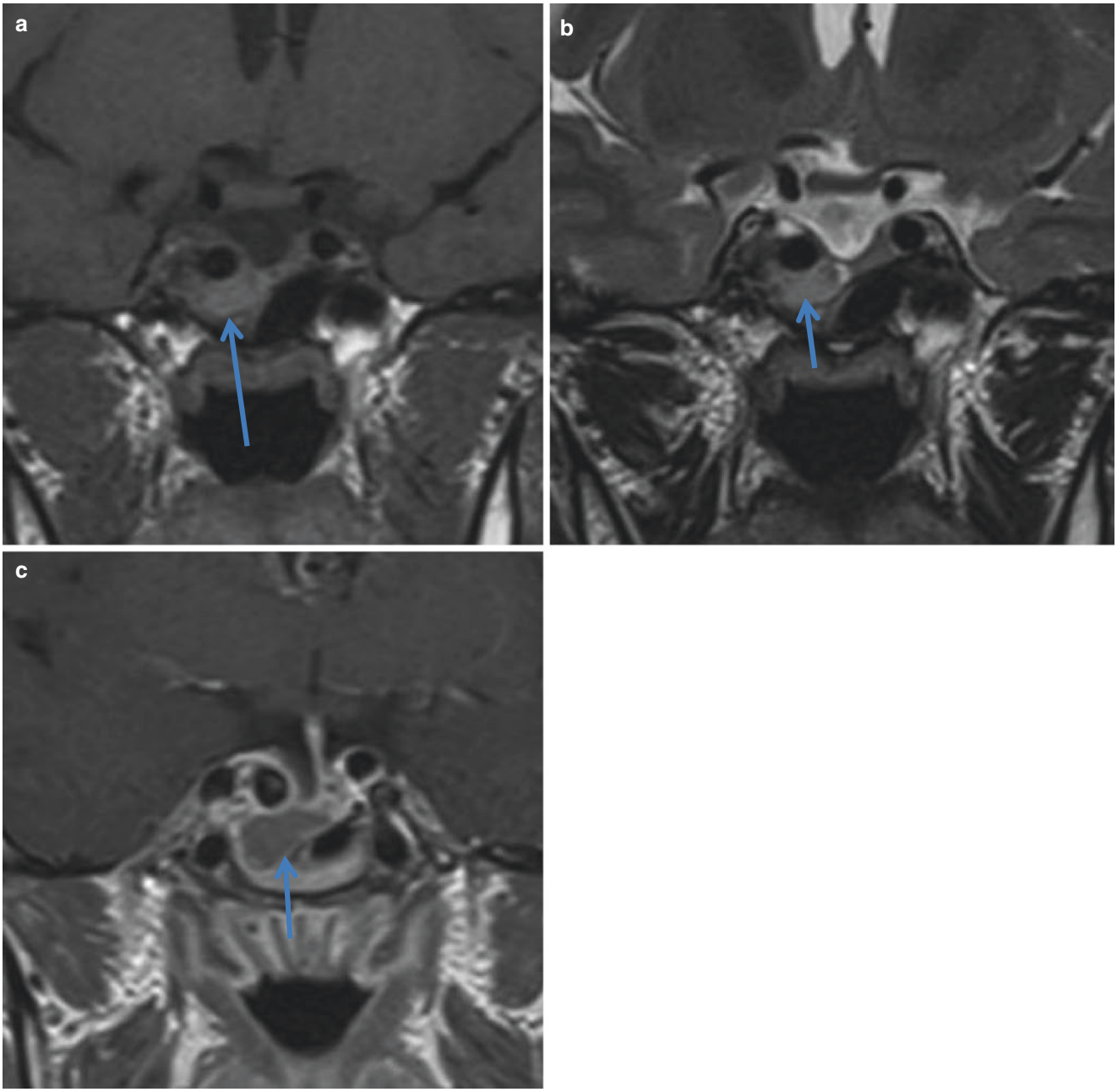

Fig. 11.12 Macroadenoma. (**a**) Coronal T1 demonstrates deformity of the right sellar floor. (**b**) Coronal T2 delineates a nodule located on the right side of the sella turcica involving part of the internal carotid artery. (**c**) Coronal T1 contrast enhanced. The image is located two slices posteriorly and the nodule can be better depicted, including the extension to the cavernous sinus, laterally to the internal carotid artery. The pituitary stalk is also dislocated to the left

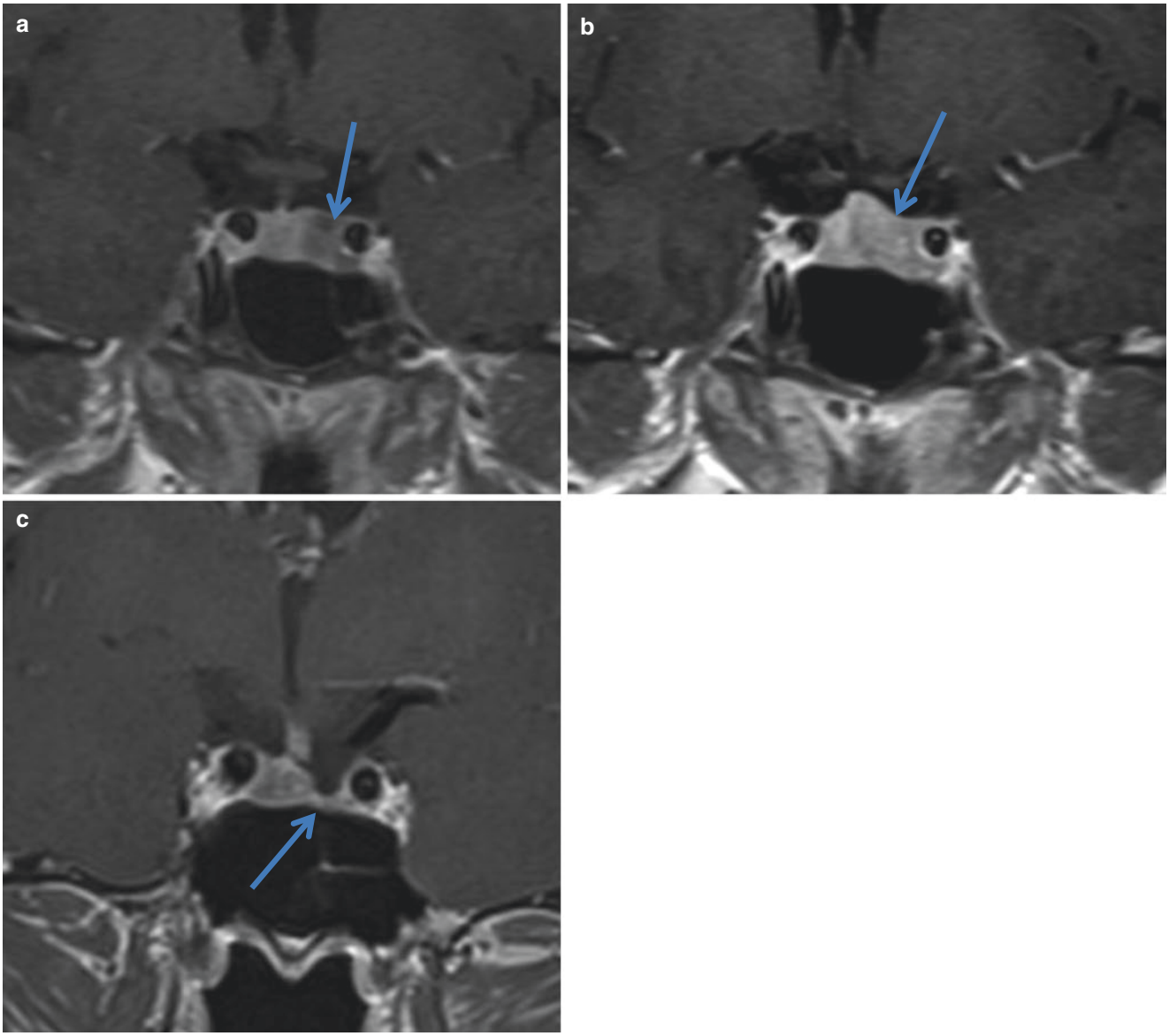

Fig. 11.13 Macroadenoma follow-up. Coronal T1 post gadolinum images. (**a**) Nodule located at the left is encasing at about half of the internal carotid perimeter. It is not possible to confirm cavernous sinus invasion. (**b**) After 1 year, the nodule enlarged, encasing two-thirds of the internal carotid artery. This is very suggestive of cavernous sinus invasion. (**c**) One year after treatment using cabergoline, the nodule cannot be identified anymore

Craniopharyngiomas

Craniopharyngiomas are nonfunctional tumors that can occur in the area of the sella turcica, suprasellar cistern, or in the third ventricle, being more common in the suprasellar cistern [12]. They have a bimodal age distribution, more than half in childhood and adolescence, with a peak of incidence among 5- to 10-year-olds. The second peak occurs around the sixth decade.

The most common form of craniopharyngioma is the adamantinomatous. Patients usually present this tumor during the first two decades of life. The more frequent location is the suprasellar cistern. Adamantinomatous craniopharyngioma commonly presents itself as a solid-cystic tumor, with calcifications. As CT is a very good method for evaluating calcifications, it can improve the radiologist's confidence when a craniopharyngioma is suspected (Fig. 11.14).

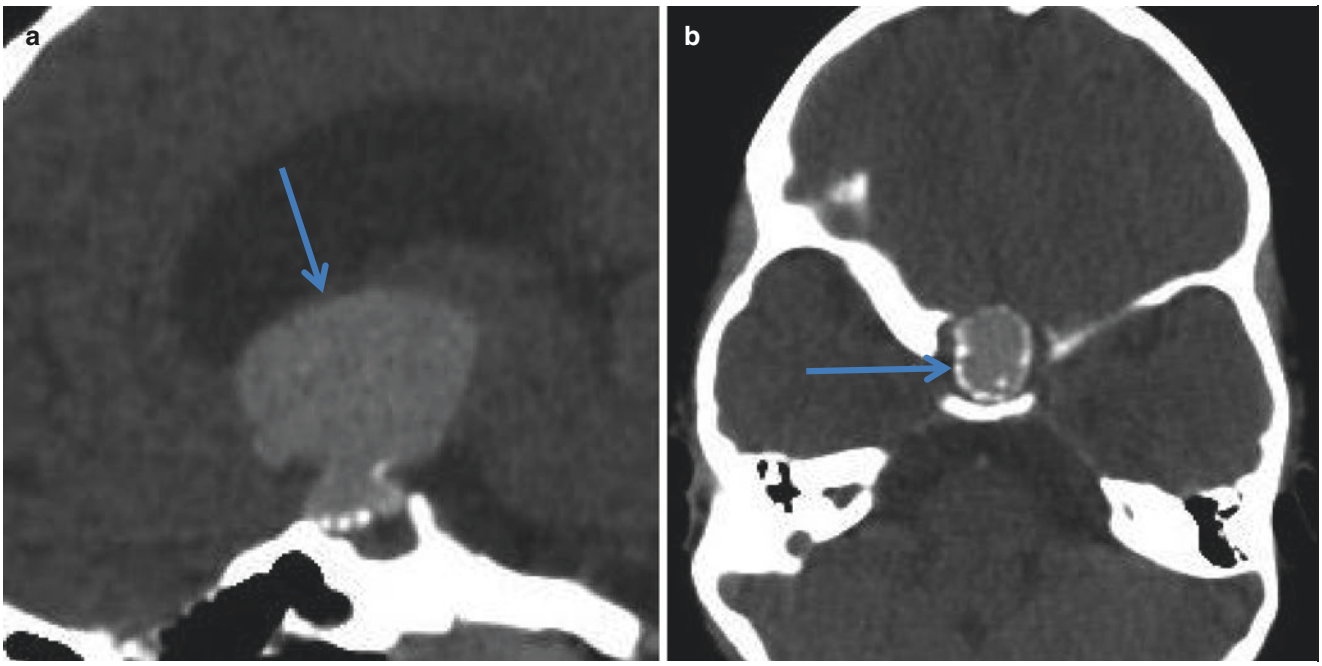

Fig. 11.14 Craniopharyngioma. A 7-year-old boy presenting with headache and visual loss. (**a**, **b**) Post-contrast CT sagittal and coronal reformation. Suprasellar mass compressing the third ventricle, causing hydrocephalus. There are calcifications at the lesion margins (*arrow*), suggesting the diagnosis of craniopharyngioma

Rathke Cleft Cyst

Rathke cleft cyst is a common incidental finding. Most are small and asymptomatic, and 90% are located in the center of the gland [13]. They can be symptomatic once they become large enough, causing compression over adjacent structures or bleeding [14]. The MRI can be hyperintense in T1- and T2-weighted images when the cyst contains mucoid fluid, making the craniopharyngioma as a differential diagnosis [10]. If it shows serous content, the signal will match the CSF (Fig. 11.15).

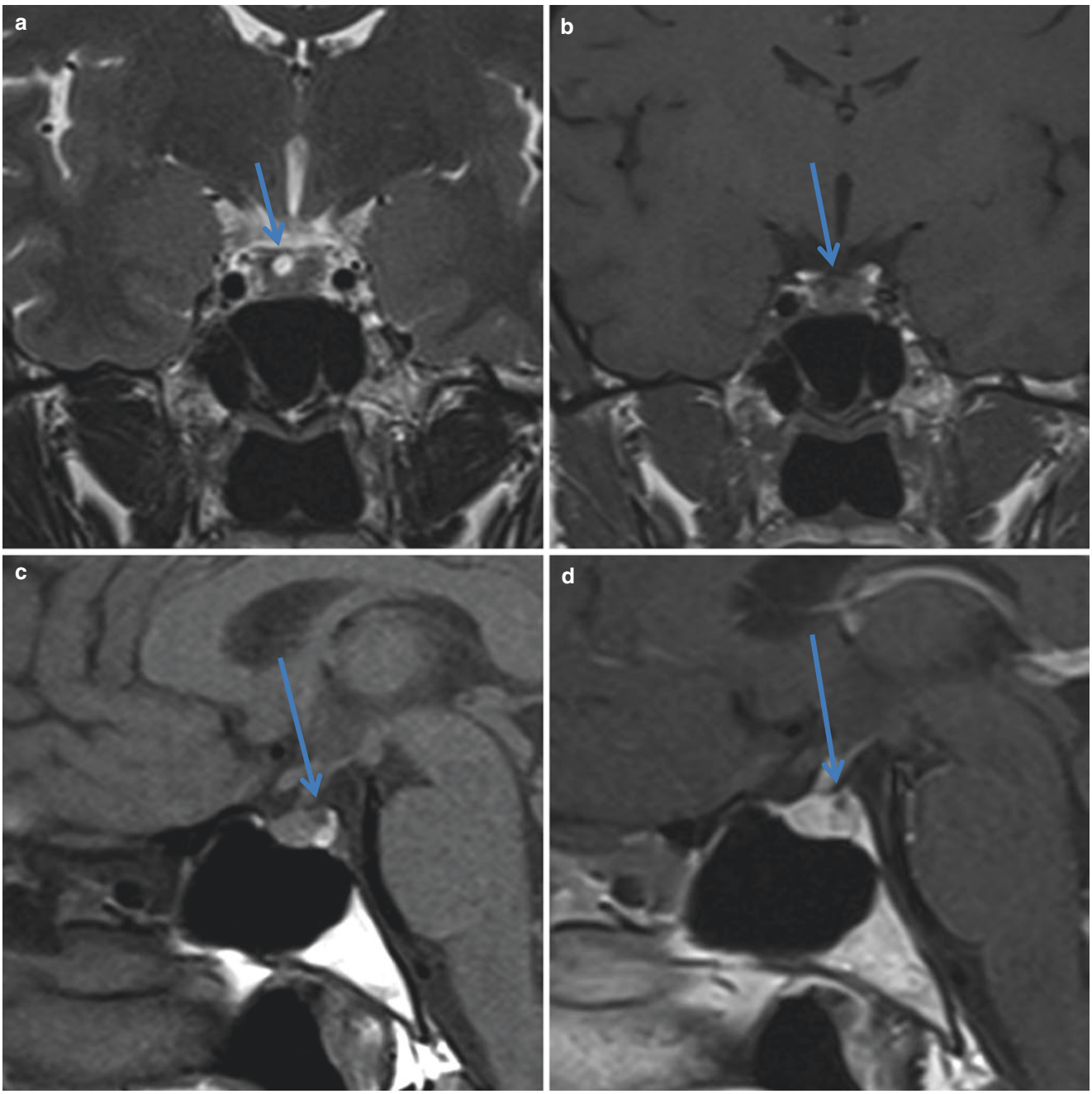

Fig. 11.15 Rathke cleft cyst. (**a**) Coronal T2 image showing a cystic hyperintense lesion. (**b**) Coronal T1 image, the cystic lesion exhibits hypointense signal. (**c**, **d**) Sagittal T1 pre- and post- contrast enhanced. This cystic lesion is located posteriorly, between the anterior and posterior lobe and does not enhance

Meningioma

Meningiomas are usually slow-growing tumors that can determine extrinsic compression over optic nerves, chiasm and tract, leading to a differential diagnosis of macroadenomas [15]. Approximately 10% of meningiomas can occur in the parasellar region. A clear separation between the meningioma and the pituitary gland can indicate that the tumor did not originate from it (Fig. 11.16).

Frequently, meningiomas promote hyperostosis and calcifications, and intensify intensely, often showing a thick dural increase (the classic "dural tail sign").

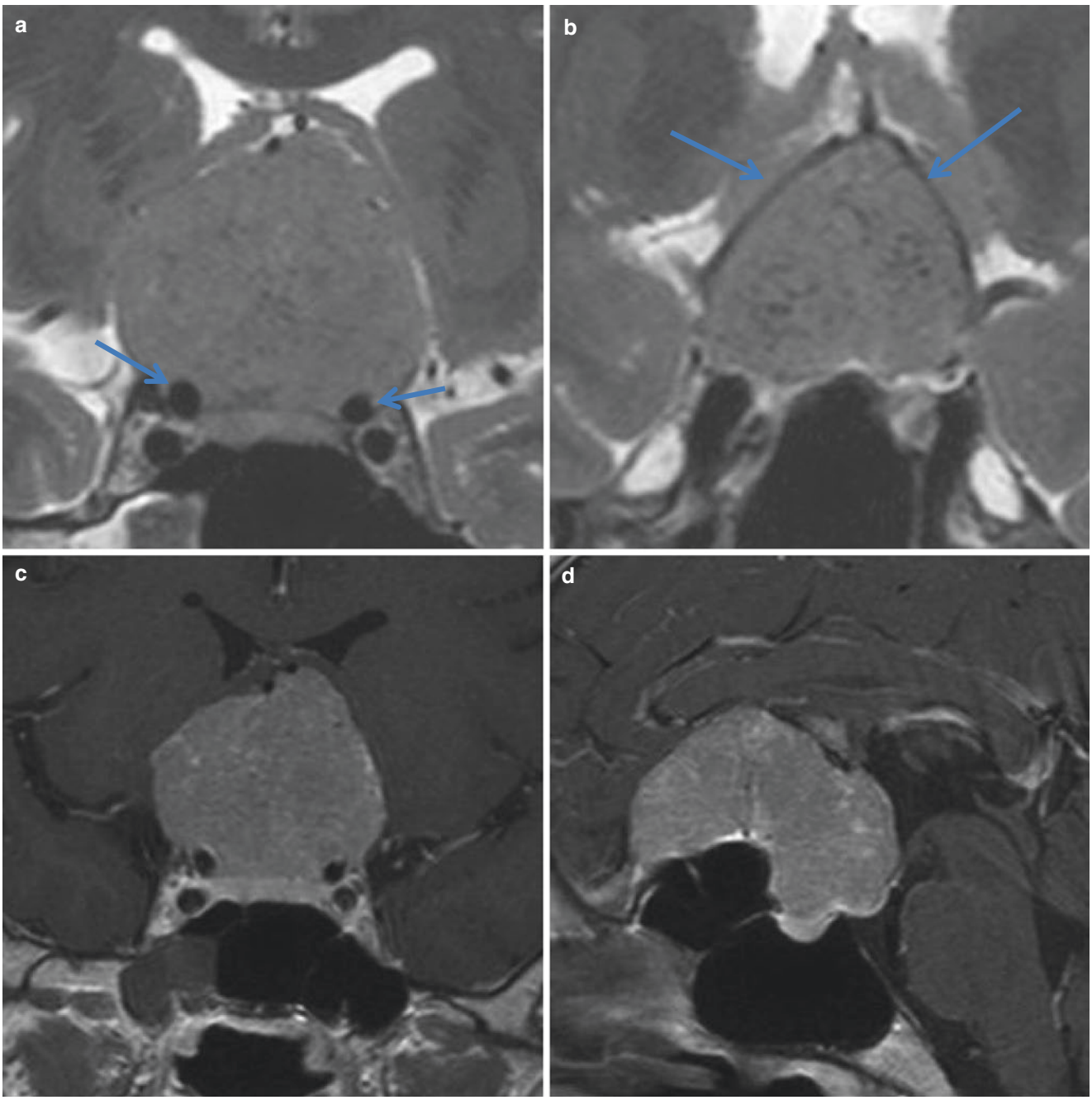

Fig. 11.16 Meningioma. (**a**, **b**) Coronal T2 images showing a mass occupying the sella turcica and the suprasellar cistern. It involves the supraclinoid segment of internal carotid arteries without invading the cavernous sinuses (*arrows*) (**a**) and displaces upward both anterior cerebral arteries (*arrows*) (**b**). (**c**) Coronal T1 weighted image shows the different intensity of enhancement between the mass and the normal pituitary gland inside the sella turcica. (**d**) Sagittal T1 post contrast IV injection; the mass extends anteriorly to the planum sphenoidale, promoting sphenoidal sinus hyperpneumatisation and characterizing the pneumosinus dilatans that are commonly found in meningiomas

Vascular Lesions

Aneurysms

Saccular aneurysms arising from internal carotid arteries can simulate sellar tumors [16]. As endoscopic endonasal transsphenoidal surgery can be disastrous, it is important to differentiate between the two entities. MRI can demonstrate a lack of signal on spin-echo images due to rapid bloodflow, called "signal void." The thrombus can show a hypersignal on T1-weighted images. Partially thrombosed aneurysms can show signal void areas representing patent lumens than can increase after administering IV contrast materials (Fig. 11.17).

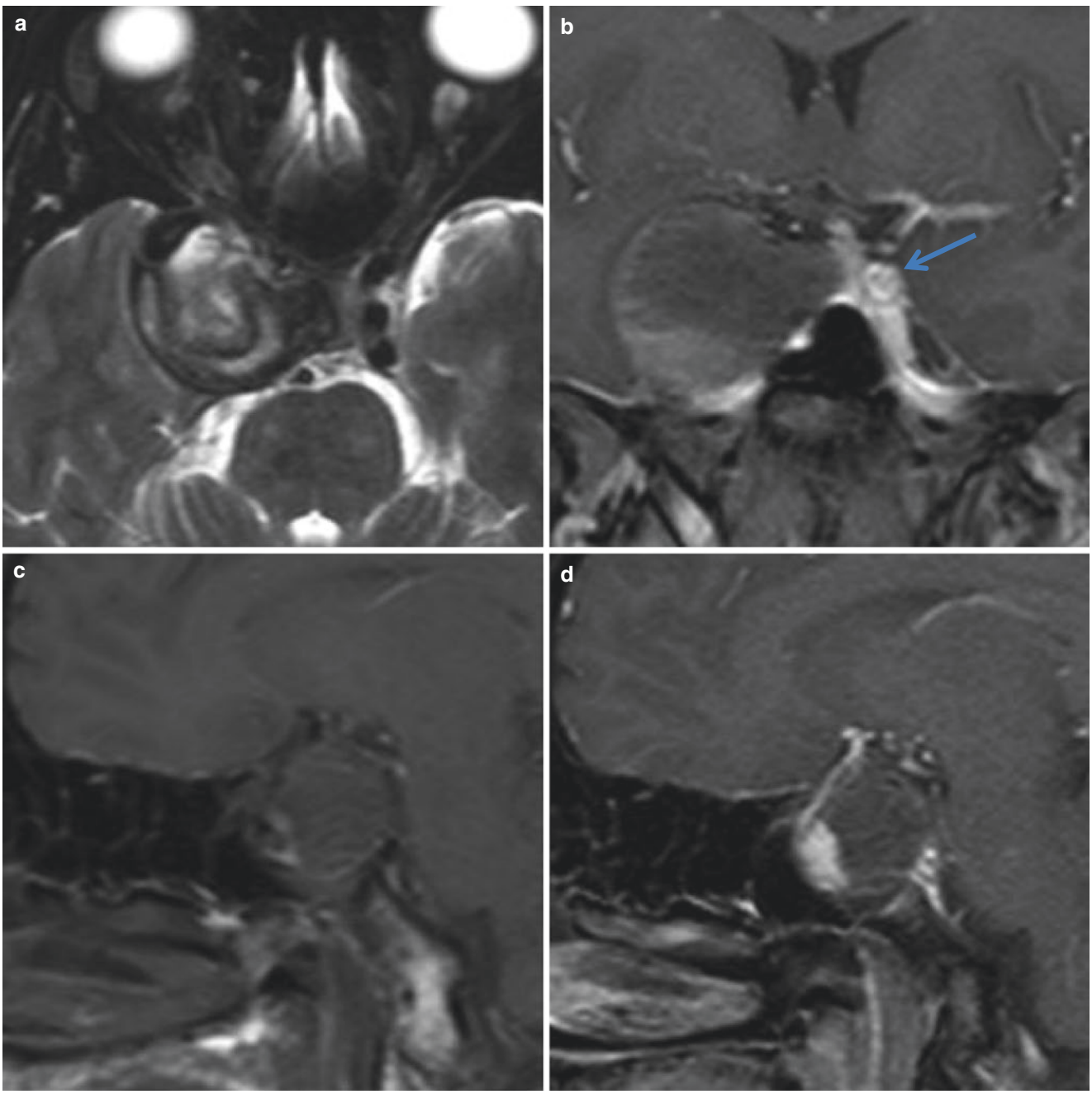

Fig. 11.17 Aneurysm. (**a**) Coronal T2, a heterogeneous mass occupying the right part of the sella turcica, extending to the cavernous sinus and cranial middle fossa. (**b**) Coronal T1 post-contrast. The left internal carotid artery (*arrow*) is identifiable, whereas the right one is not. (**c**, **d**) Sagittal T1 pre- and post-contrast IV injection shows that the mass has some parts with spontaneous hypersignal and partial enhancement. This particular example is a partially thrombosed parasellar aneurysm

Apoplexy and Sheehan's Syndrome

As adenomas grow, they can lead to necrosis or hemorrhage characterizing an acute degeneration. When this happens, it is called apoplexy [17]. Many adenomas can exhibit apoplexy, although only 25% will be symptomatic. In most cases, it will be seen as an enlarged sella turcica. The signal can vary depending on the time of the hemorrhage, representing the normal breakdown or hemoglobin products (Fig. 11.18).

During pregnancy, there is a normal pituitary gland enlargement due to prolactin cell hyperplasia. Postpartum complications, such as hemorrhage and shock, can lead to postpartum pituitary necrosis, also known as Sheehan's syndrome [18]. The MRI findings can be very similar, except for the absence of sella turcica remodeling (Fig. 11.19).

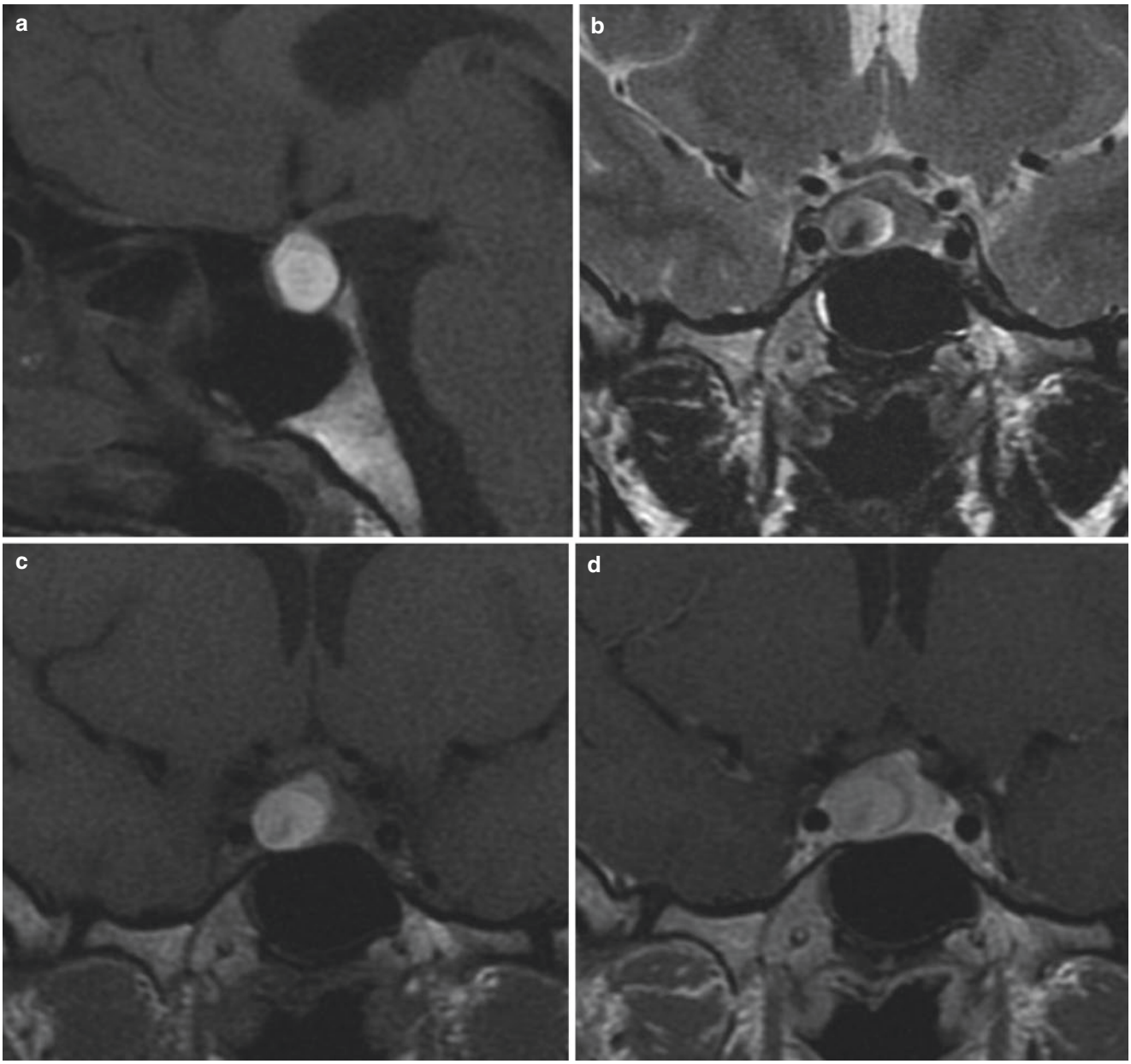

Fig. 11.18 Late sub-acute hemorrhage. (**a**, **c**) Sagittal and coronal T1 pre-contrast. Hyperintense nodule occupying central and right portion of the gland, compatible with methemoglobin. (**b**) T2 coronal. Heterogeneous signal corresponding to intracellular methemoglobin (hypointense) and extracellular methemoglobin (hyperintense) components. (**d**) T1 Coronal post-gadolinium. The rest of the gland exhibits normal enhancement

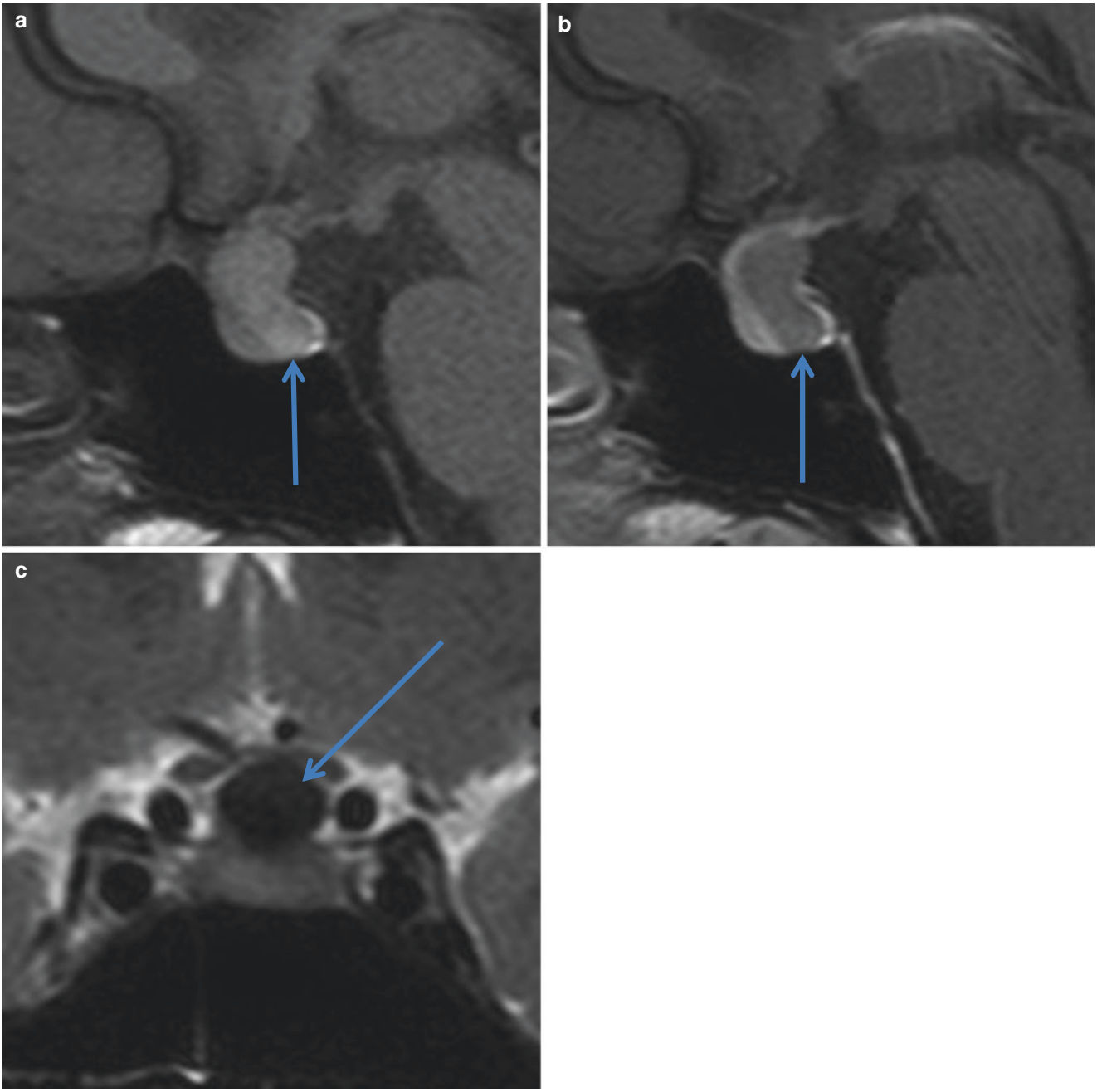

Fig. 11.19 Sheehan's syndrome. Acute hemorrhage. (**a**) Sagittal T1 pre-contrast. There is a subtle hyperintense hemorrhagic collection occupying the pituitary gland and extending to the suprasellar cistern, with liquid-liquid level. (**b**) Sagittal T1 after IV gadolinium injection. Only the the normal anterior lobe shows enhancement. (**c**) T2 coronal. The hemorrhagic collection presents as hypointense in T2-weighted images, corresponding to intracellular deoxyhemoglobin

References

1. Yousem DM, Grossman RI. Neuroradiology: the requisites. 3rd ed. Philadelphia: Mosby/Elsevier; 2010. xvii, 619 p.
2. Tsunoda A, Okuda O, Sato K. MR height of the pituitary gland as a function of age and sex: especially physiological hypertrophy in adolescence and in climacterium. AJNR Am J Neuroradiol. 1997;18(3):551–4.
3. Buchfelder M, Nistor R, Fahlbusch R, Huk WJ. The accuracy of CT and MR evaluation of the sella turcica for detection of adrenocorticotropic hormone-secreting adenomas in Cushing disease. AJNR Am J Neuroradiol. 1993;14(5):1183–90.
4. Dietrich RB, Lis LE, Greensite FS, Pitt D. Normal MR appearance of the pituitary gland in the first 2 years of life. AJNR Am J Neuroradiol. 1995;16(7):1413–9.
5. Buchfelder M, Schlaffer S. Imaging of pituitary pathology. Handb Clin Neurol. 2014;124:151–66.
6. Chaudhary V, Bano S. Imaging of the pituitary: Recent advances. Indian J Endocrinol Metab. 2011;15(Suppl 3):S216–23.
7. Murray RA, Maheshwari HG, Russell EJ, Baumann G. Pituitary hypoplasia in patients with a mutation in the growth hormone-releasing hormone receptor gene. AJNR Am J Neuroradiol. 2000;21(4):685–9.
8. Saindane AM, Lim PP, Aiken A, Chen Z, Hudgins PA. Factors determining the clinical significance of an "empty" sella turcica. AJR Am J Roentgenol. 2013;200(5):1125–31.
9. Sonksen P, Sonksen C. Pituitary incidentaloma. Clin Endocrinol. 2008;69(2):180.
10. Kitajima M, Hirai T, Katsuragawa S, Okuda T, Fukuoka H, Sasao A, et al. Differentiation of common large sellar-suprasellar masses effect of artificial neural network on radiologists' diagnosis performance. Acad Radiol. 2009;16(3):313–20.
11. Cottier JP, Destrieux C, Brunereau L, Bertrand P, Moreau L, Jan M, et al. Cavernous sinus invasion by pituitary adenoma: MR imaging. Radiology. 2000;215(2):463–9.
12. Eldevik OP, Blaivas M, Gabrielsen TO, Hald JK, Chandler WF. Craniopharyngioma: radiologic and histologic findings and recurrence. AJNR Am J Neuroradiol. 1996;17(8):1427–39.
13. Park M, Lee SK, Choi J, Kim SH, Kim SH, Shin NY, et al. Differentiation between cystic pituitary adenomas and Rathke cleft cysts: a diagnostic model using MRI. AJNR Am J Neuroradiol. 2015;36(10):1866–73.
14. Bonneville JF. Hemorrhagic pituitary adenoma versus Rathke cleft cyst: a frequent dilemma. AJNR Am J Neuroradiol. 2016;37(3):E27–8.
15. Rao VJ, James RA, Mitra D. Imaging characteristics of common suprasellar lesions with emphasis on MRI findings. Clin Radiol. 2008;63(8):939–47.
16. Weir B. Pituitary tumors and aneurysms: case report and review of the literature. Neurosurgery. 1992;30(4):585–91.
17. Semple PL, Jane JA, Lopes MB, Laws ER. Pituitary apoplexy: correlation between magnetic resonance imaging and histopathological results. J Neurosurg. 2008;108(5):909–15.
18. Kaplun J, Fratila C, Ferenczi A, Yang WC, Lantos G, Fleckman AM, et al. Sequential pituitary MR imaging in Sheehan syndrome: report of 2 cases. AJNR Am J Neuroradiol. 2008;29(5):941–3.

Adrenal Gland Diseases

12

Jorge Elias Jr., Paula Condé Lamparelli Elias,
Sara Reis Teixeira, and Valdair Francisco Muglia

Adrenal gland diseases determine a wide range of effects, depending on the type and extent of hormonal changes, the age at onset, the amount of time without treatment, and, obviously, gender. For example, in females with congenital adrenal hyperplasia (CAH), excessive androgen exposure in utero leads to virilization of the external genitalia and urogenital malformations [1]. In men, this condition may lead to the development of testicular adrenal rest tumors (TART), with an estimated prevalence of 21%, and it is suggested that gonadal dysfunction may be already present before puberty [1].

Considering that most of the circulating testosterone in women normally derives from adrenal precursors, disorders that increase adrenal dehydroepiandrosterone sulfate cause hyperandrogenemia, which can impair fertility [2]. This has a minor impact on circulating testosterone in men. Another example of adrenal hormonal excess, hypercortisolism, may affect women's fertility and, to a lesser extent, men's fertility when there is sufficient suppression of gonadotropin production [2].

Congenital and acquired adrenal diseases that may lead to infertility are presented in Table 12.1.

Congenital Adrenal Hyperplasia

Congenital adrenal hyperplasia is a group of autosomal recessive disorders resulting from the deficiency of one of the five enzymes required for the synthesis of cortisol in the adrenal cortex [3, 4]. Up to 95% of cases are related to impaired steroidogenesis caused by 21-hydroxylase deficiency (21OH-CAH) [1, 5]. With the advent of cortisone therapy in the 1960s and screening of newborns in the 1990s, most children with 21OH-CAH now reach adulthood [3]. In adults with CAH, infertility is one of many significant possible health problems alongside obesity, short stature, neoplasia, and bone loss, leading to a reduced quality of life [3].

Clinical manifestations of CAH depend mainly on the phenotype that is ultimately related to variations in concurrent adrenal hormonal deficiencies [4]. Classic 21-hydroxylase deficiency can have a concurrent defect in aldosterone biosynthesis (salt-wasting type), and a form with apparently normal aldosterone biosynthesis (simple virilizing type) [4]. A mild, non-classic form of CAH may occur and tends to be asymptomatic or associated with signs of postnatal androgen excess [4]. Girls with classic 21OH-CAH are exposed to high systemic levels of adrenal androgens and will develop ambiguous genitalia, but these complex sexual differentiation problems are not within the scope of this chapter, nor is congenital hypoandrogenism that causes sexual infantilism.

J. Elias Jr. (✉) • S.R. Teixeira • V.F. Muglia
Radiology Division of Internal Medicine Department, Ribeirão Preto Medical School of University of São Paulo, Ribeirão Preto, SP, Brazil
e-mail: jejunior@fmrp.usp.br

P.C.L. Elias
Endocrinology and Metabology Division of Internal Medicine Department, Ribeirão Preto Medical School of University of São Paulo, São Paulo, SP, Brazil

L.R.M.F. de Souza et al. (eds.), *Atlas of Imaging in Infertility*, DOI 10.1007/978-3-319-13893-0_12

Table 12.1 Adrenal glands diseases and infertility

	Congenital			Acquired		
		Mechanism	Clinical and imaging findings		Mechanism	Clinical and imaging findings
Hyperandrogenism	21OH-CAH	Gonadal axis blockade	Genital ambiguity (classical forms) TART	Adrenal tumor	Sexual virilization	Adrenal mass. Hormonal laboratory findings are diagnostic.
Hypercortisolism	–	–	–	Cushing's syndrome, functioning adrenocortical tumors	Gonadal axis blockade	Functioning adrenal adenoma or carcinoma. Relatively high accuracy of CT and MRI.
				AIMAH	Gonadal axis blockade	Presents as incidental radiological finding of macronodular adrenal hyperplasia or with subclinical or overt CS, occasionally with secretion of mineralocorticoids or sex steroids. Imaging finding of macronodular adrenal hyperplasia
				Carney complex	Gonadal axis blockade	Myxomas of the heart and skin, hyperpigmentation of the skin (lentiginosis), and PPNAD
				ACTH-dependent	Gonadal axis blockade	Abnormal production of ACTH due, in 80% of cases, to ACTH oversecretion by a pituitary adenoma (Cushing's disease) and in 20% of cases to ectopic ACTH secretion
Hypoandrogenism	17αOH-CAH	Adrenal and gonadal enzymatic deficiency	Sexual infantilism	Addison's disease	Chronic degenerative disease/ neoplasias/granulomatous adrenal infection	Bilateral adrenal infarction, bilateral adrenal tumors, fungal adrenal bilateral involvement
				Adrenoleukodystrophy	Inability to catabolize VLCFAs	Testicular disease due to accumulation of VLCFA

21OH-CAH 21 hydroxylase deficiency – congenital adrenal hyperplasia, *17αOH-CAH* 17α hydroxylase deficiency – congenital adrenal hyperplasia, *AIMAH* ACTH-independent macronodular adrenal hyperplasia, *TART* testicular adrenal rest tumors, *PPNAD* primary pigmented nodular adrenocortical disease, *VLCFA* very long-chain fatty acids, *CS* Cushing's syndrome

Imaging Findings of Adrenals in CAH

As the "hyperplasia" term stands, a common imaging finding in CAH is a diffuse enlargement of both adrenal glands, while preserving their typical shape and heterogeneous post-contrast enhancement on CT and MRI (Figs. 12.1, 12.2, and 12.3) [1, 6–14]. Interestingly, adrenal size is positively correlated with plasma concentration of dehydroepiandrosterone sulphate [15]. However, it is very important to note that an imaging finding of normal adrenal glands does not exclude the possibility of CAH [16–18]. Also, imaging appearance in CAH may have no difference from ACTH-dependent Cushing's syndrome (Figs. 12.4 and 12.5), in which fertility is often impaired due to hypercortisolism (Table 12.1).

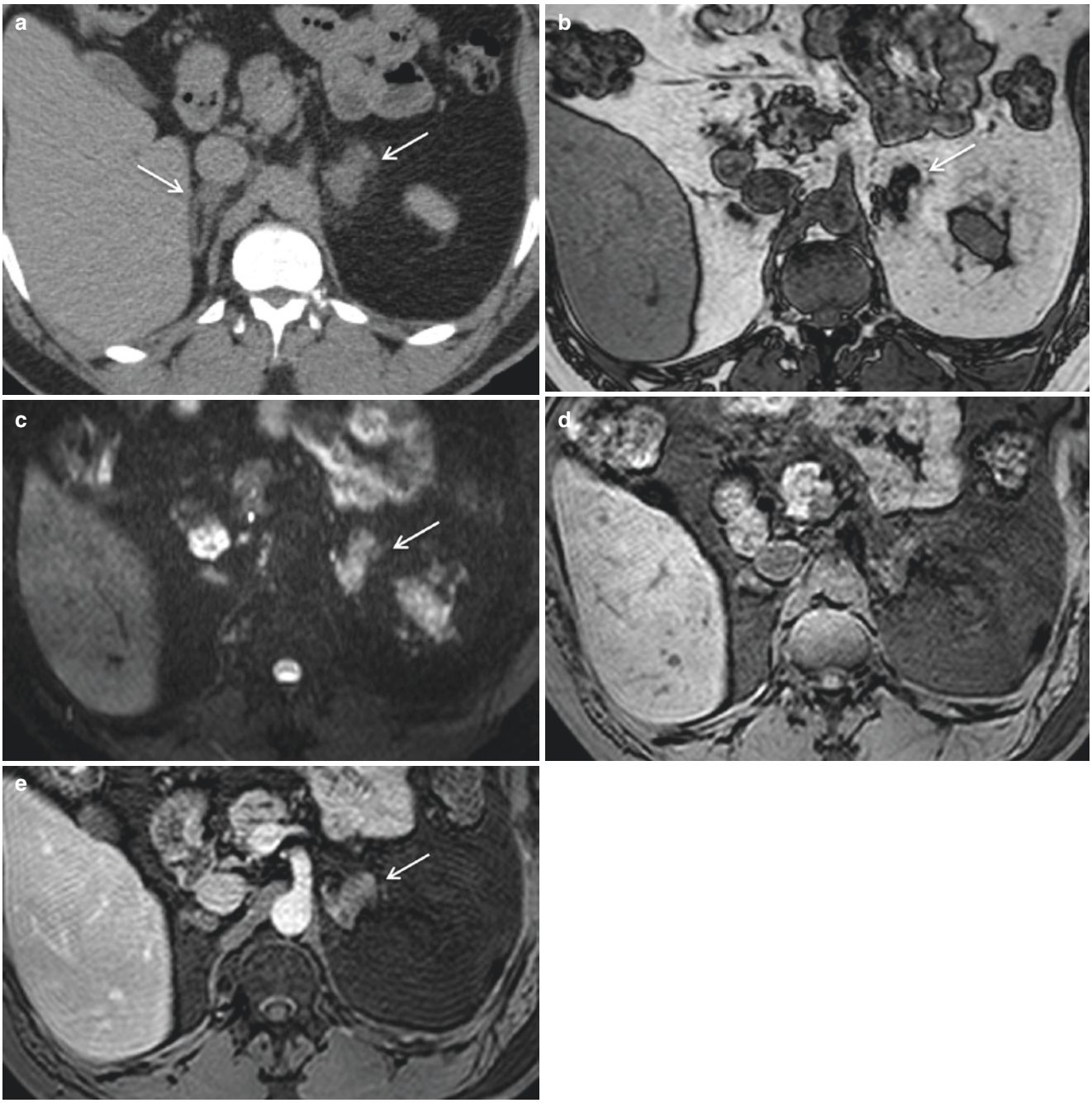

Fig. 12.1 Adrenal hyperplasia. Diffuse enlargement of both adrenal glands, most evident on left adrenal (*white arrows*), on CT (**a**), and MRI (**b**-**e**)

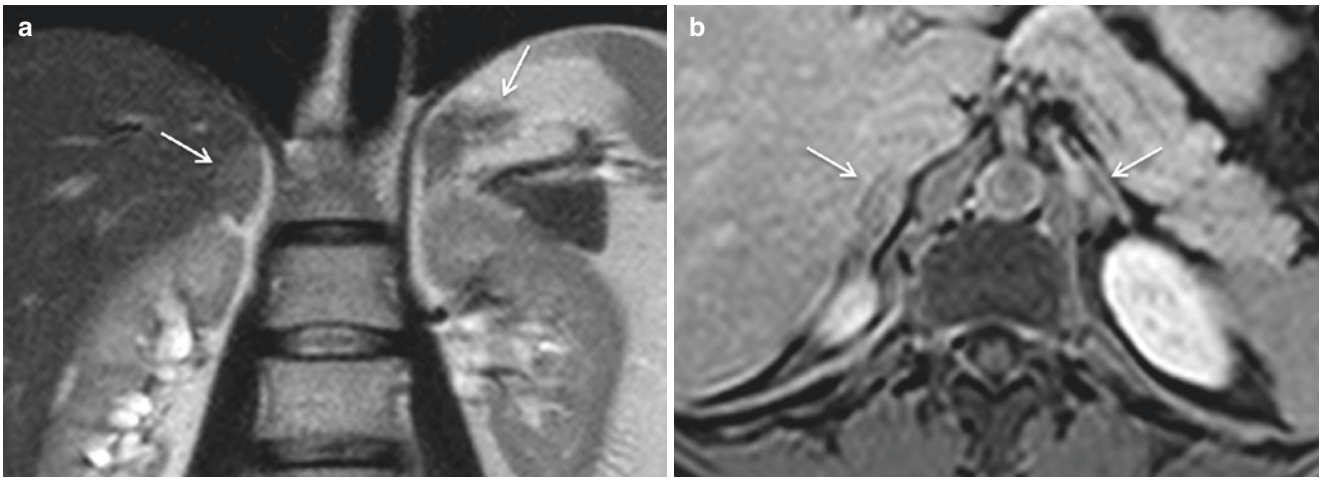

Fig. 12.2 Adrenal hyperplasia. Diffuse enlargement of both adrenal glands on coronal T2-weighted MRI (**a**) and axial T1-weighted post-gadolinium (**b**) images (*white arrows*)

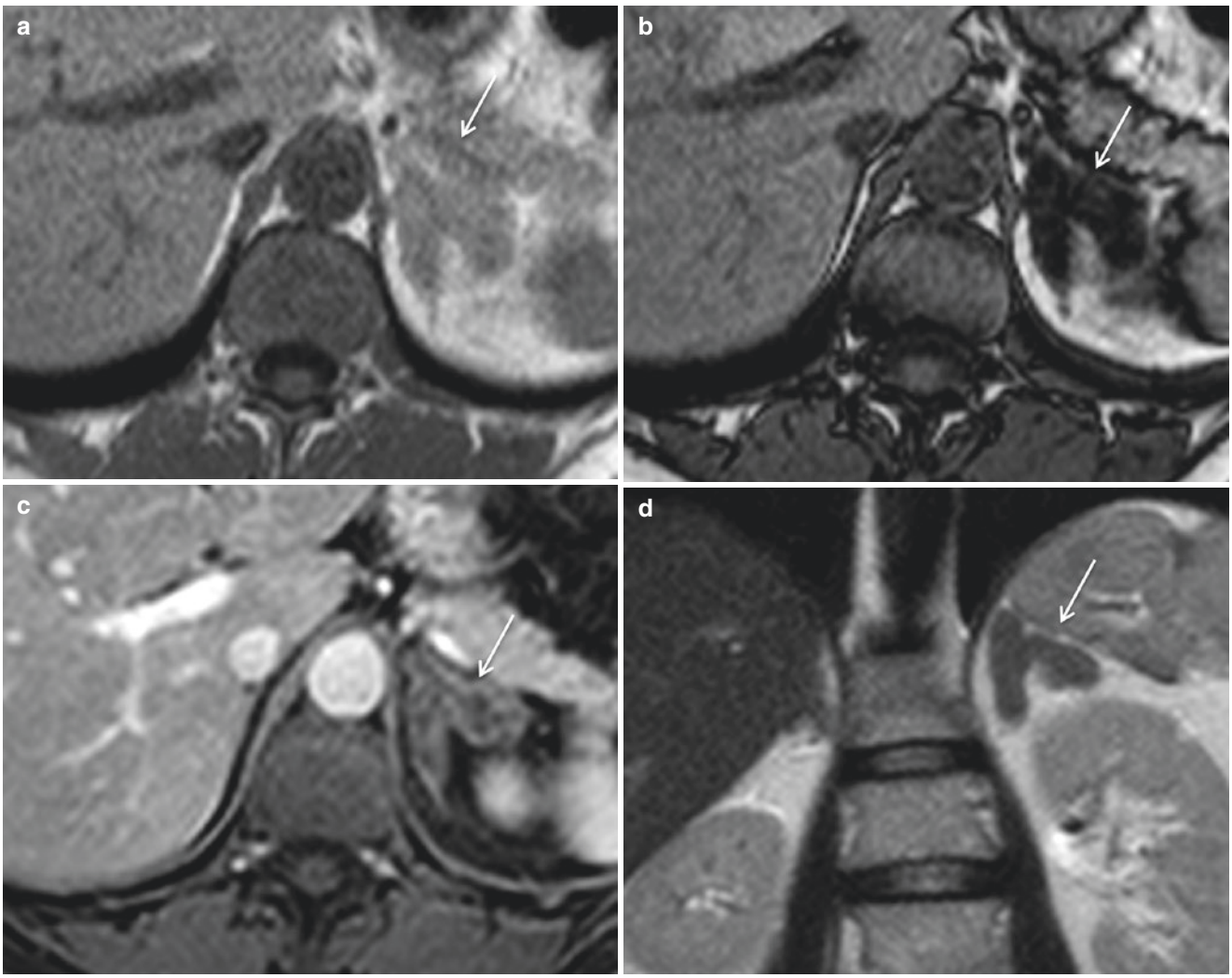

Fig. 12.3 Adrenal hyperplasia. Accentuated diffuse enlargement of left adrenal gland showed on in-phase (**a**) and out-of-phase (**b**) axial T1-weighted, as well as on post-gadolinium axial T1-weighted (**c**) and coronal T2-weighted (**d**) images (*white arrows*)

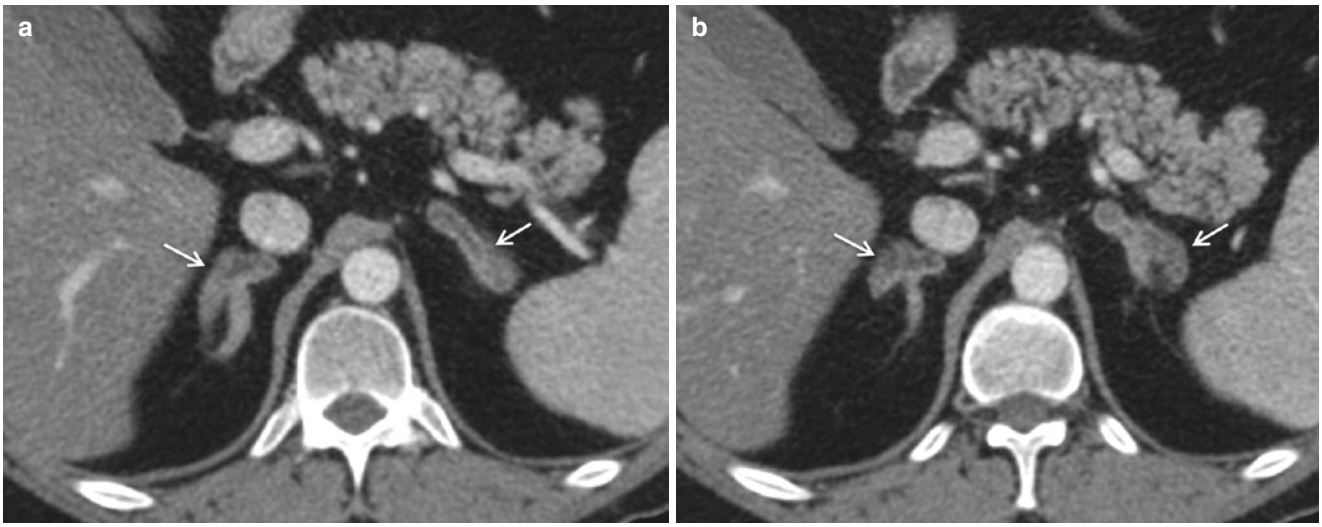

Fig. 12.4 ACTH-dependent Cushing's syndrome. Post-contrast CT images with diffuse enlargement of both adrenal glands (*white arrows*)

Fig. 12.5 ACTH-dependent Cushing's syndrome. Axial T2-weighted (**a**), out-of-phase T1-weighted (**b**), and post-gadolinium fat-suppressed T1-weighted (**c**) images showing diffuse enlargement of both adrenal glands (*white arrow* in **c**). After treatment follow-up with post-contrast CT (**d**) image showing normal adrenal glands (*white arrows*)

Non-classical Congenital Adrenal Hyperplasia in Females

Girls with any kind of 21OH-CAH may develop reproductive problems such as oligomenorrhea or amenorrhea in adolescence [4, 5]. Other problems that can occur are vaginal insufficiency with dyspareunia, and secondary polycystic ovary syndrome from adrenal-derived androgens [3]. The increased incidence of polycystic ovaries is a common finding in mild CAH, but also in the classic form, and it may contribute to infertility [5]. About 40% of patients with non-classic CAH have polycystic ovaries (Fig. 12.6). Pregnancy rates of 50% have been reported in untreated patients with non-classic CAH compared with 93–100% after treatment, but these data are mainly from studies with symptomatic women; thus, the overall rate for all 21OH-CAH women may be lower [5].

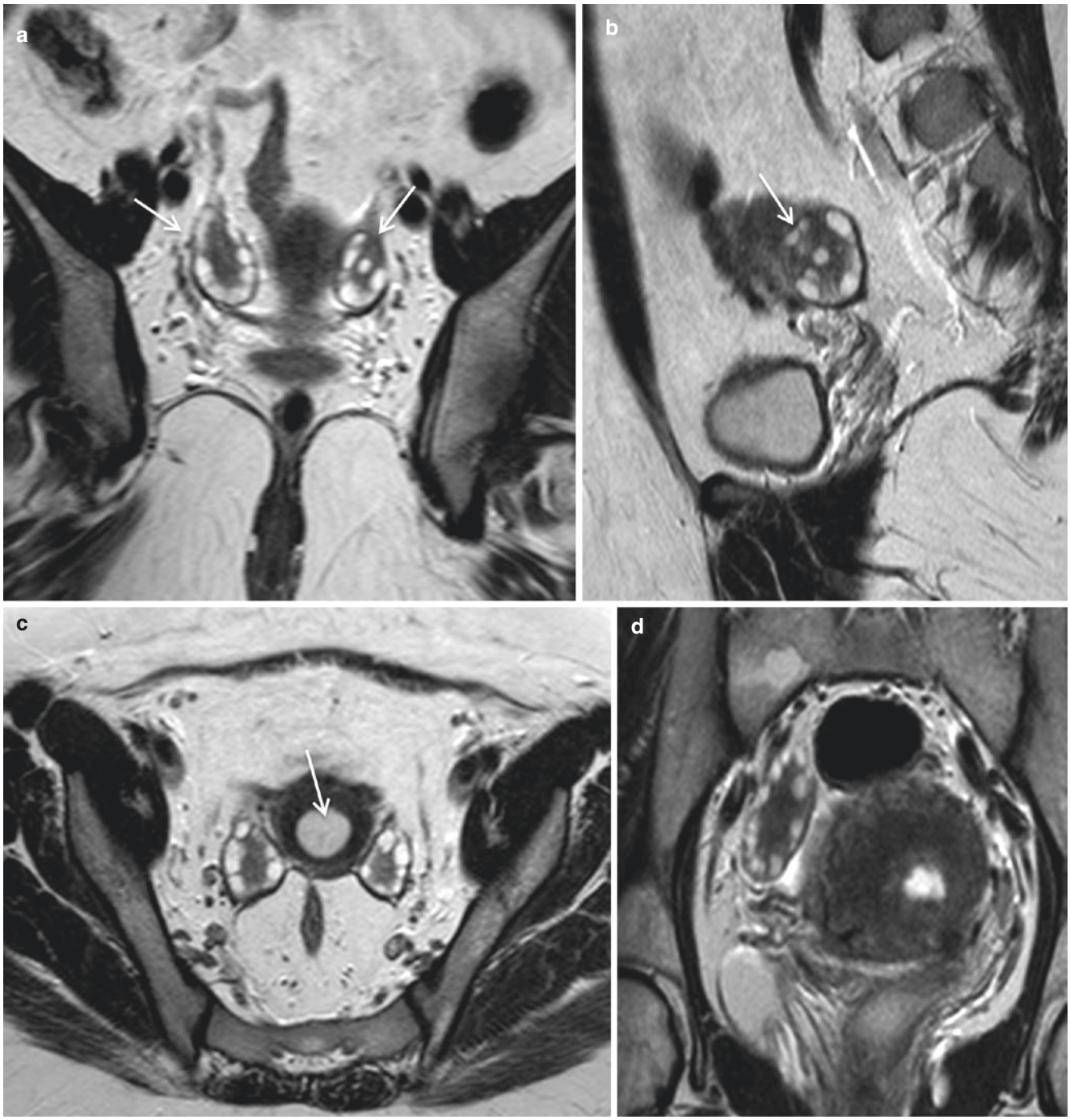

Fig. 12.6 Two different cases of polycystic ovaries. Coronal (**a**, **d**), sagittal (**b**) and axial (**c**) T2-weighted images with enlargement of both ovaries that present peripherally located small-size follicles, hypointense central stroma, and thickened capsule (*white arrows*). Endometrium in (**c**) is thickened as in the proliferative phase (*white arrows*)

Congenital Adrenal Hyperplasia in Males

Most men with CAH have no fertility-related problems, presenting with normal sperm counts and being able to father children. Nonetheless, a high incidence of testicular adrenal rest tumors (TART) have been reported in men with CAH, with a prevalence of up to 94% determined by ultrasound (US) [19]. In males with salt-wasting CAH, TART may be accompanied by deficient spermatogenesis [20, 21], and medical treatment consists of pituitary suppression with dexamethasone, since tumors are usually responsive to corticotropin. Ultrasound findings include bilateral intratesticular hypoechoic lobulated masses surrounding the mediastinal testis (Fig. 12.7) [22]. TART are mainly hypo or avascular on color Doppler ultrasound (CDUS) [23] and cause no course deviation or changes in caliber of locoregional vessels [22, 23]. In some cases, TART may appear as heterogeneous or hyperechoic nodules [22–26], which may represent fibrosis or calcifications [23]. MRI may help differentiate testicular mass lesions in selected cases where ultrasound findings are not definitive, and TART appears as a relatively hypointense lobulated mass on T2-weighted sequences located adjacent to testicular mediastinum, as in ultrasound (Fig. 12.8) [27]. On follow-up, TART can vary in size [25], but the size seems to have no correlation with hormonal control or hormonal markers [21, 25, 28]. As TART may be responsible for reduced fertility, occurring even in young children with a prevalence of 21–24% [29, 30], and with data suggesting that gonadal dysfunction is already present before puberty, the early detection of testicular lesions is advised to improve treatment and prevent longstanding gonadal impairment function [29, 31]. Moreover, it is important to note that the first major mechanism of impaired fertility in men with 21OH-CAH is gonadotropin suppression from adrenal-derived androgens, which causes testicular atrophy and impairs spermatogenesis [3].

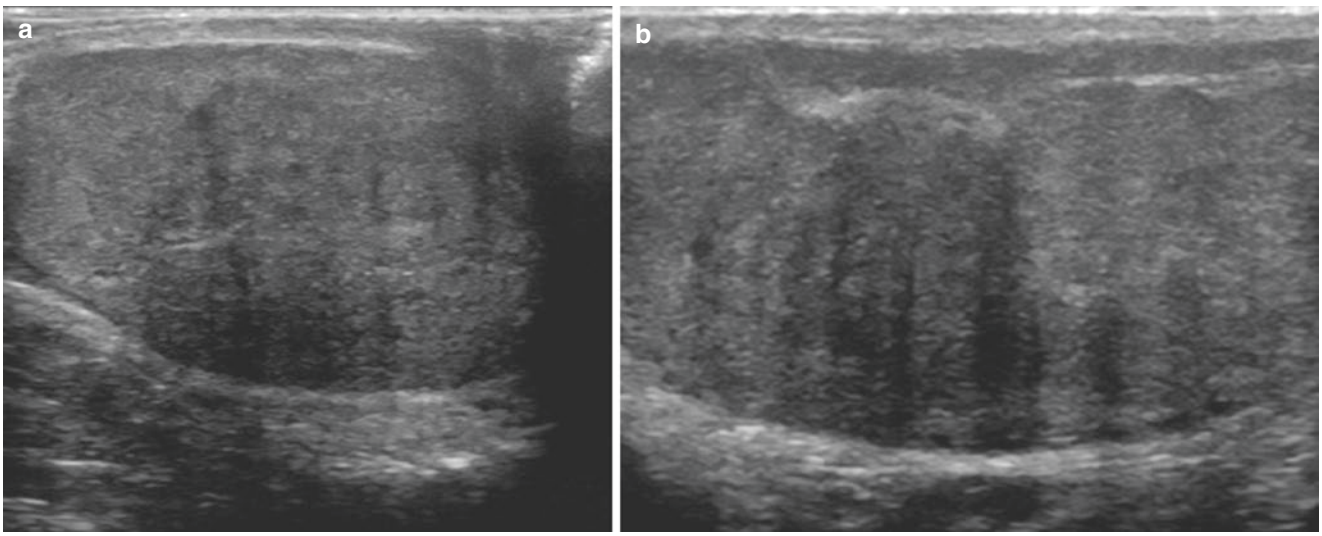

Fig. 12.7 Testicular adrenal rest tumors. Ultrasound of both testicles with ill-defined bilateral intratesticular hypoechoic lobulated masses surrounding the mediastinal testis (*white arrows*)

Fig. 12.8 Testicular adrenal rest tumors. T2-weighted MR images of both testicles with lobulated hypointense intratesticular masses occupying the testicular parenchyma (*white arrows*)

Endogenous Cushing Syndrome

Cushing's syndrome is categorized as an iatrogenic or an endogenous condition. Endogenous Cushing's syndrome is further dichotomized as ACTH-dependent or ACTH-independent. All patients with Cushing's syndrome may be infertile due to a gonadal axis blockade related to hypercortisolism. However, adrenal imaging findings may vary depending on the etiologies.

ACTH-dependent Cushing's Syndrome

The ACTH-dependent Cushing's syndrome has an abnormal production of ACTH due to, in 80% of the cases, ACTH oversecretion by a pituitary adenoma (Cushing's syndrome) and in 20% of the cases to ectopic ACTH secretion (neuroendocrine tumor of lung and pancreas, thymic tumors, and others). Cushing's syndrome is the most relevant form of endogenous hypercortisolism that impairs reproduction, and it is most frequent in women. Additionally, associated hyperandrogenism, mainly dehydroepiandrosterone sulfate production, is more commonly elevated in ACTH-dependent forms of Cushing's syndrome and may also contribute to infertility. ACTH-dependent Cushing's syndrome may present bilateral enlargement of adrenal glands due to ACTH stimulus, similarly to CAH (Figs. 12.4 and 12.5) or may have no adrenal changes on imaging.

ACTH-independent Cushing's Syndrome

Most of cases of ACTH-independent Cushing's syndrome are due to cortisol-secreting functioning adrenocortical tumors. Less frequent etiologies are macronodular adrenal hyperplasia (AIMAH) and primary pigmented nodular adrenocortical disease (PPNAD).

Adrenocortical Tumors

Overt Cushing's syndrome due to adrenocortical tumor will depend on tumor hormone secretion pattern. Thus, in pure glucorticoid-secreting tumors, clinical features of Cushing's syndrome will be present with no hyperandrogenism signs and symptoms. It is often due to small adenomas with benign behavior. However, benign adrenocortical tumors are most frequently diagnosed incidentally, when they are termed "incidentalomas." The prevalence of incidentalomas is increasing, mainly due to the widespread and increasing use of abdominal CT and MRI. Although incidentalomas are mostly asymptomatic, they prompt evaluation by laboratory hormonal tests to exclude oligosymptomatic adrenal functioning conditions. Instead, functioning adrenocortical tumors are actively sought through CT and MRI exams for diagnosis confirmation (lateralization), characterization (benign vs. malignant), and pre-operative staging (invasion, extension, distant metastases).

Adenomas are the most common adrenal masses. These are benign neoplasms, usually small (<5 cm), solitary, and well encapsulated. Typically, adrenal adenomas are hypodense on CT without intravenous contrast. Classic reported evidence shows that if the mean CT pre-contrast attenuation coefficient of an adrenal mass is less than 10 Hounsfield Units (HU), a diagnosis of adrenal adenoma can be made with high specificity (Fig. 12.9) due to lipid-rich content [32, 33]. However, up to 30% of overall adrenal adenomas are lipid-poor. Moreover, a recent report concluded that the 10 HU unenhanced CT attenuation threshold does not apply to cortisol-secreting adrenocortical adenomas, showing that only about 20% of them were lipid-rich, probably directly related to the oversecretion of cortisol [34]. Post-contrast absolute and relative washout evaluation techniques increase CT accuracy for adrenal adenomas diagnosis. Reported sensitivity and specificity of absolute washout for adenomas is 86% and 92%, respectively, and sensitivity and specificity of relative washout is 82% and 92%, respectively, even for cortisol secreting, lipid-poor adrenal adenomas [33–35]. The formulas to obtain the absolute and relative washout, using 60–75 s post-contrast phase and 15 min delayed post-contrast phase, are: absolute washout = 100 × post-contrast phase − delayed post-contrast phase/post-contrast phase − unenhanced phase and relative washout = 100 × post-contrast phase − delayed post-contrast phase/post-contrast phase. Absolute washout of 60% or higher, and relative washout of 40% or higher, are consistent with adenoma.

On MRI, the most accurate method for adrenal adenoma characterization is to demonstrate accentuated and homogeneous loss of signal intensity on out-of-phase images (Fig. 12.10) [13]. Other findings are described for adrenal adenoma characterization on MRI, as uniform enhancement of the entire lesion on immediate post-gadolinium capillary-phase images, which is reported in one series in 70% of cases [36], and rapid washout of contrast on serial postgadolinium images [37, 38]. MRI is described as a problem-solving modality in cases of indeterminate adrenal masses on CT, being able to characterize correctly up to 62% of adenomas with attenuation coefficient greater than 10 HU on CT [13, 39], but only those up to 30 HU [40].

Adrenocortical carcinoma is a rare and aggressive malignancy, with poor prognosis and bimodal age distribution,

occurring in childhood and in the fourth to fifth decades [13, 41, 42]. About 50% of these tumors are hyperfunctioning, with a predominantly androgen-secreting pattern and often presentation of virilization, with or without concomitant hypercortisolism. In this condition, gonadal blockage due to hyperandrogenism is the main cause of infertility. In children, adrenocortical carcinoma is associated with virilism, and it has a less aggressive natural history; in adults, however, the tumor more commonly presents a mixed Cushing-virilizing syndrome and has a poorer prognosis [43]. Although CT and MR imaging findings help to differentiate benign from malignant adrenal tumors, they cannot differentiate functioning from non-functioning tumors. Adrenocortical carcinomas are often large, heterogeneous, and relatively well-defined masses (Figs. 12.11, 12.12, and 12.13). They may have intracytoplasmic lipid or fatty regions as well as foci of necrosis and hemorrhage. Metastatic disease is frequently found at presentation and the tumor may invade IVC.

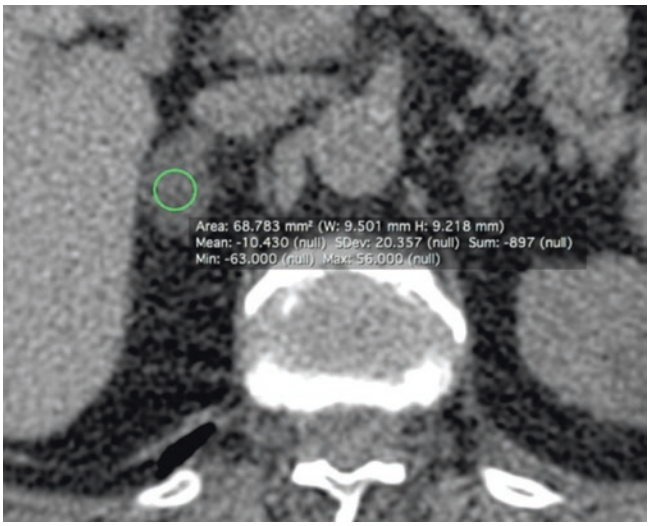

Fig. 12.9 Right adrenal adenoma. CT without IV contrast depicting an elongated hypodense adrenal mass with attenuation coefficient of −10.4 Hounsfield units

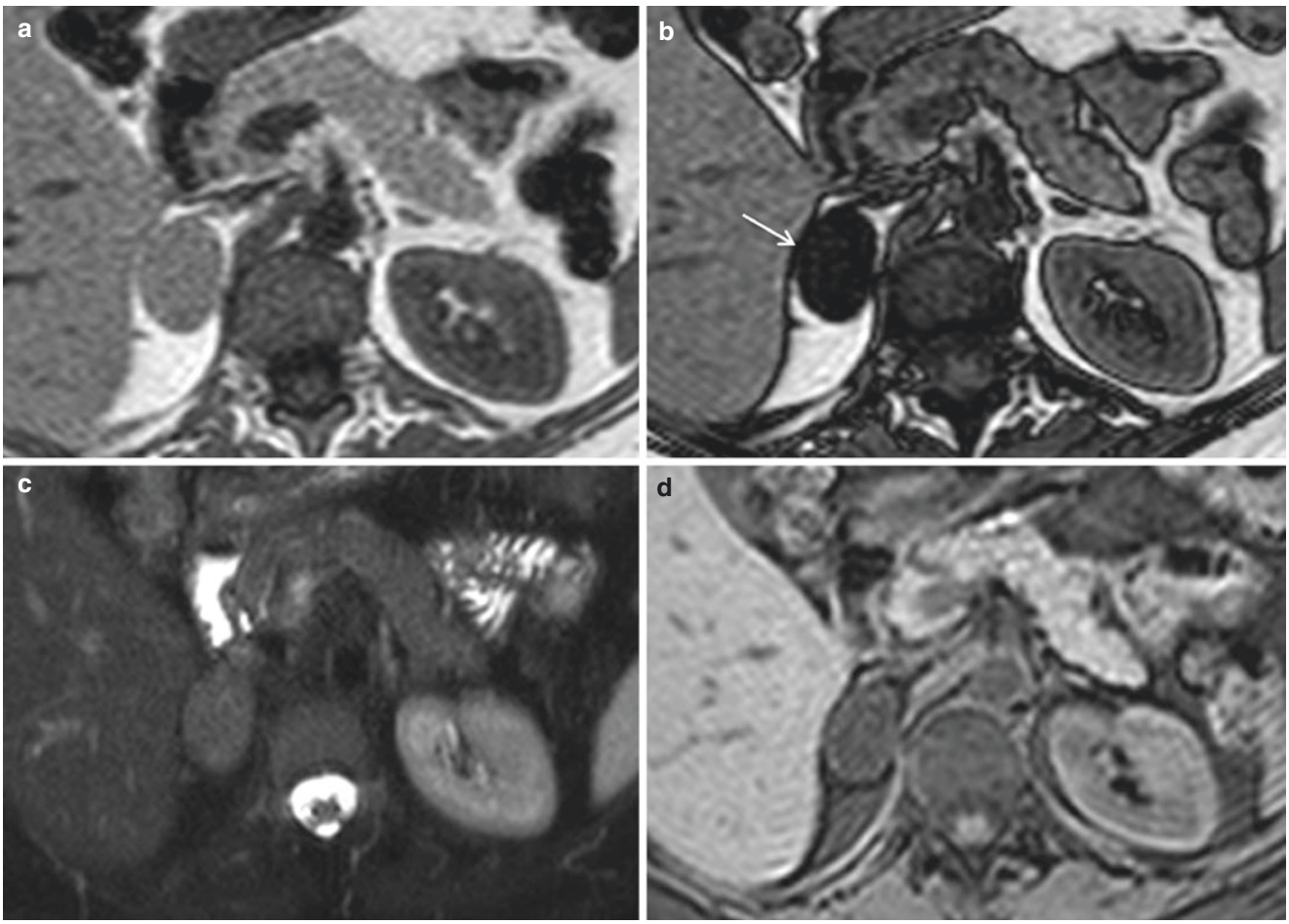

Fig. 12.10 Right adrenal adenoma. Axial in-phase (**a**) and out-of-phase T1-weighted MR images and axial fat-suppressed T2-weighted (**c**) and T1-weighted (**d**) images with accentuated and homogeneous loss of signal intensity on out-of-phase image (**b**, *white arrow*)

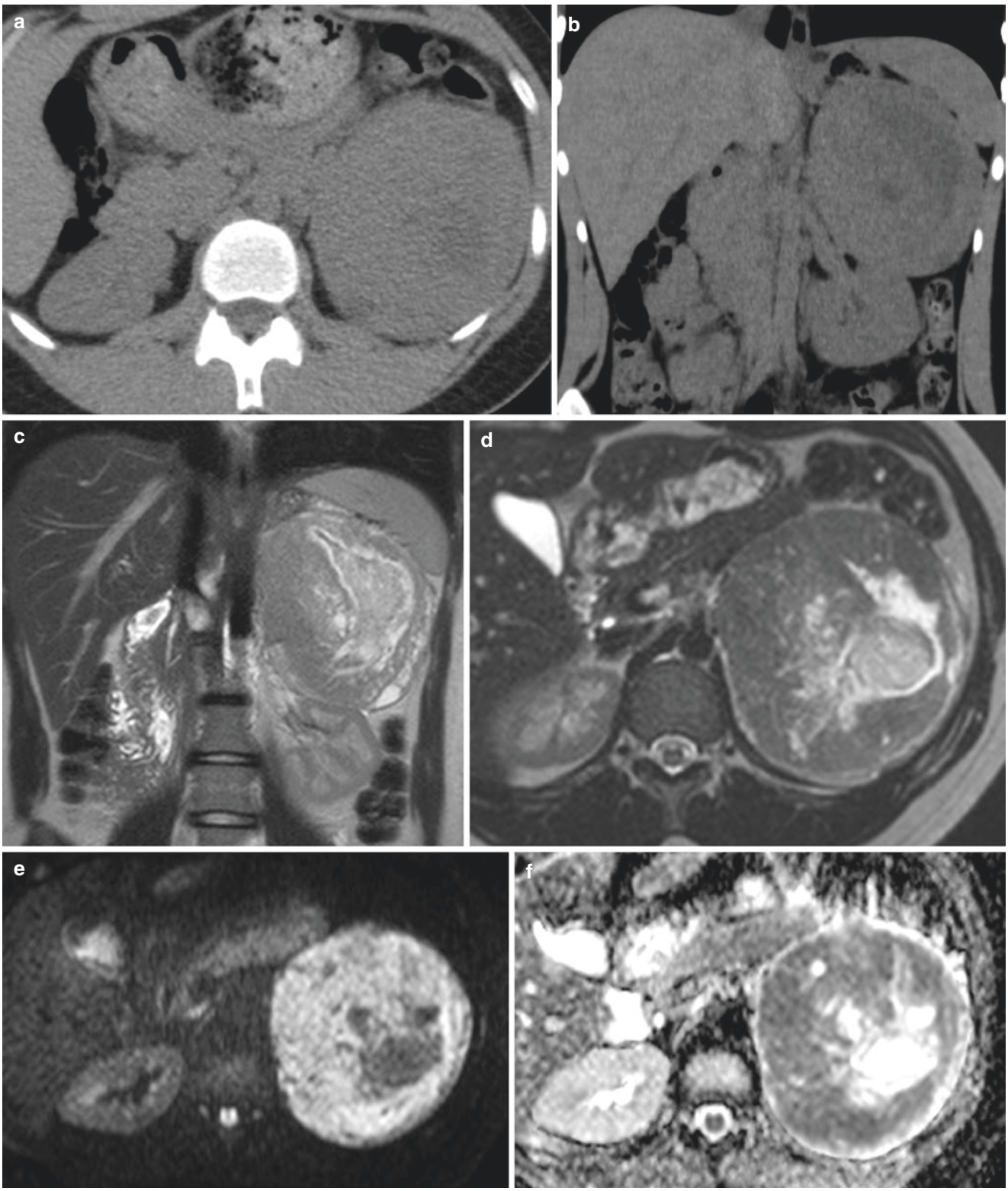

Fig. 12.11 Adrenocortical carcinoma. Axial (**a**) and coronal reconstruction (**a**) of CT without IV contrast and coronal (**c**) and axial (**a**) T2-weighted MR images with diffusion-weighted image (**e**), ADC map (**f**), and pre-(**g**) and post-gadolinium (**h**–**j**) T1-weighted MR images. Large and heterogeneous left adrenal mass with restricted diffusion (high-signal intensity on (**e**) and low-signal intensity on(**f**), and heterogeneous enhancement on post-gadolinium images

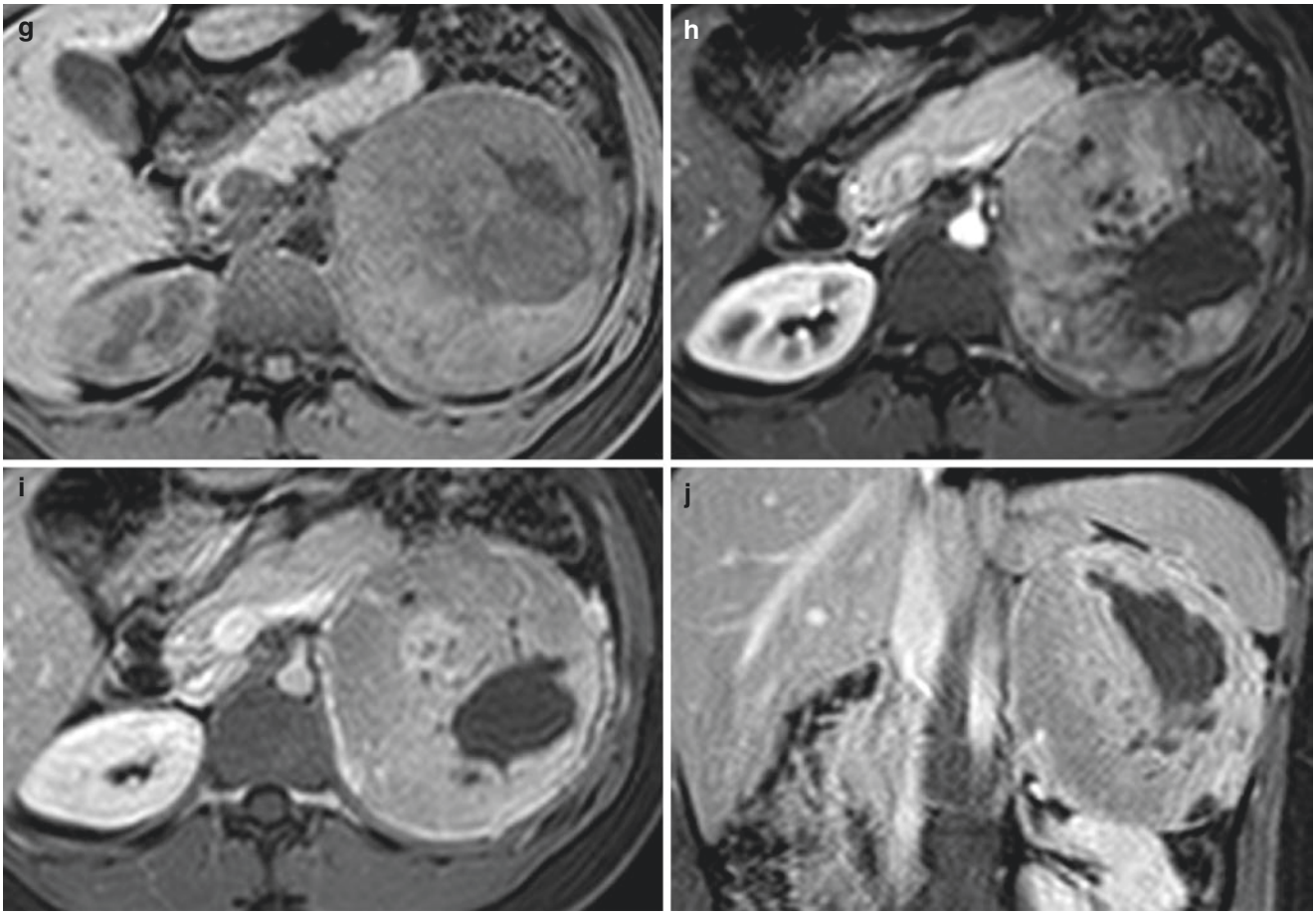

Fig. 12.11 (continued)

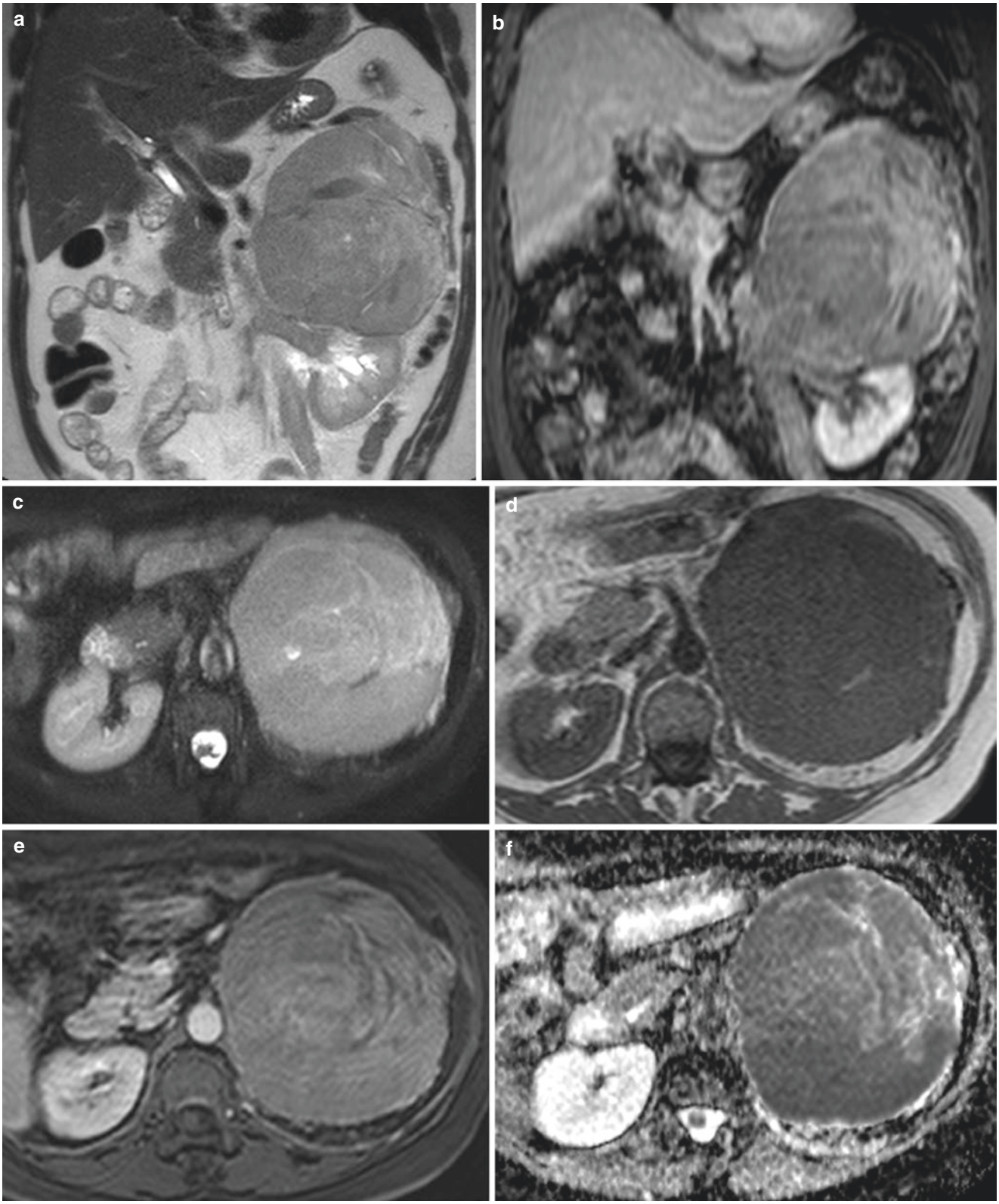

Fig. 12.12 Adrenocortical carcinoma. Coronal (**a**) and axial (C) T2-weighted and post-gadolinium T1-weighted (**b**) with axial pre-(**d**) and post-gadolinium (**e**) T1-weighted MR images, and ADC map (**f**). Large and heterogeneous left adrenal mass with restricted diffusion (low-signal intensity on **f**), and heterogeneous enhancement on post-gadolinium images. Left kidney is compressed and dislocated inferiorly by the tumor

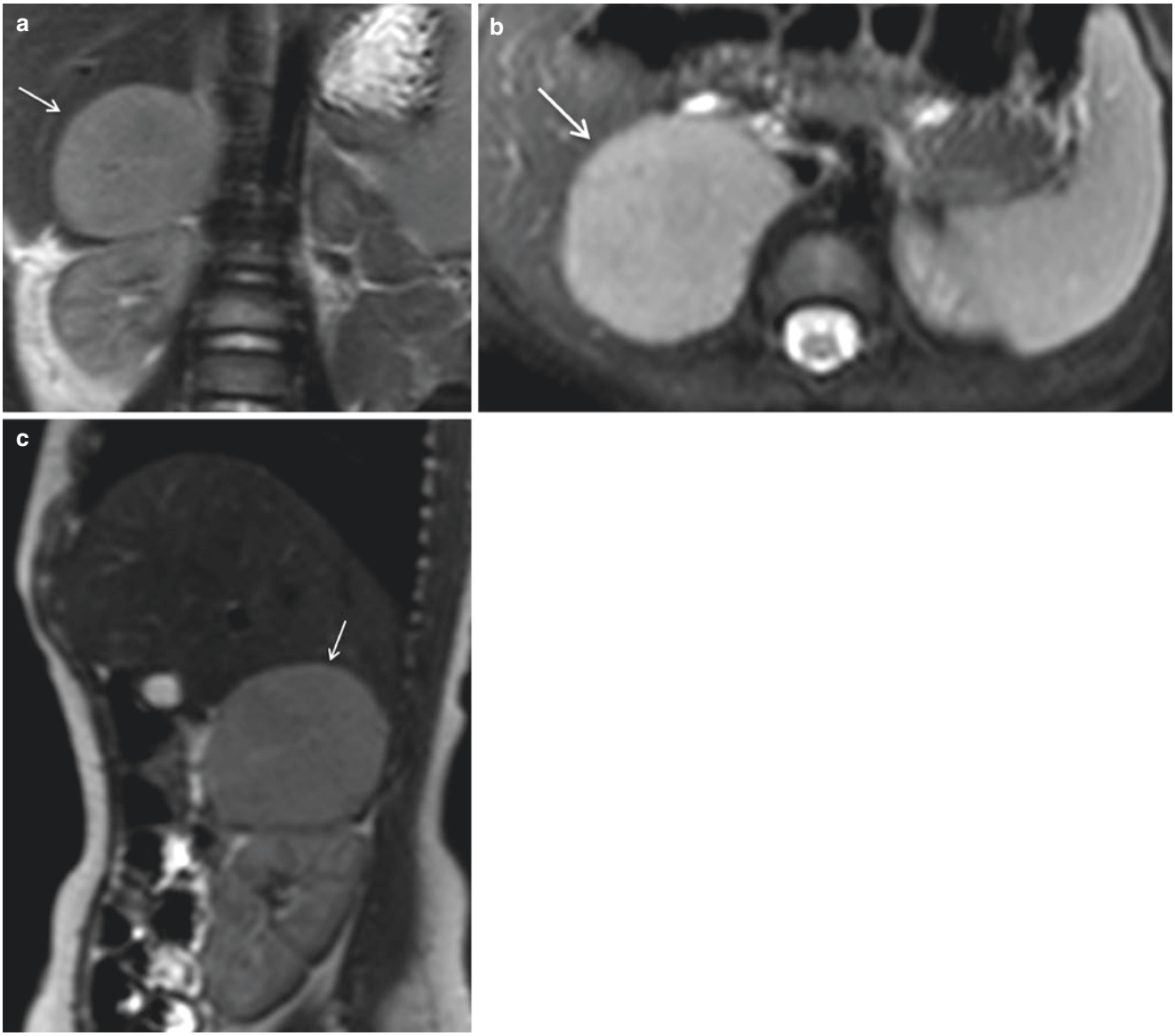

Fig. 12.13 Adrenocortical carcinoma. Coronal (**a**), axial (**b**) and sagittal (**c**) T2-weighted MR images showing a large and homogeneous right adrenal mass in a patient with hyperandrogenism (*white arrows*)

ACTH-independent Macronodular Adrenal Hyperplasia (AIMAH)

AIMAH is a rare cause of overt Cushing's syndrome. However, subclinical hypercortisolism is being more frequently detected along with bilateral adrenal incidentalomas. Characterized as the presence of bilateral adrenal nodules more than 1 cm in diameter, capable of independent cortisol secretion and suppression of pituitary ACTH, it usually occurs in older patients (fifth and sixth decades) compared to solitary adrenal tumors (Fig. 12.14) [44].

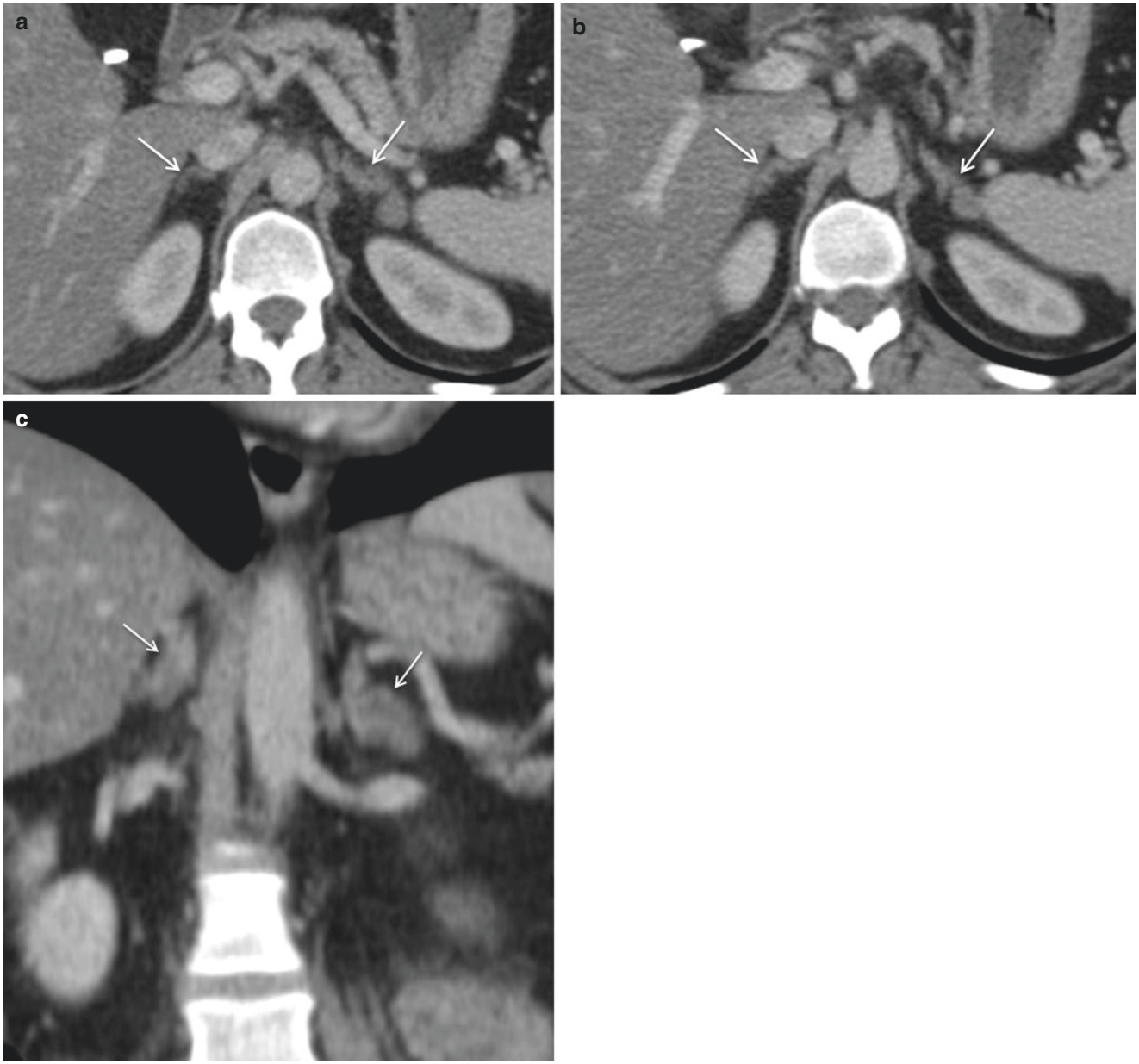

Fig. 12.14 ACTH-independent macronodular adrenal hyperplasia (AIMAH). Post-contrast CT images showing multinodular enlargement of both adrenal glands (*white arrows*)

Primary Pigmented Nodular Adrenocortical Disease (PPNAD)

PPNAD is also a rare condition that leads to endogenous hypercortisolism, but infertility is uncommonly present. It may occur sporadically, or be associated with tumors in Carney complex, such as mixoma, and testicular, pituitary and thyroid tumors [45]. About 75% of patients have some abnormality detected on imaging – usually small, irregular, micronodular hyperplasia or a "beads-on-a-string" appearance (Fig. 12.15) [46].

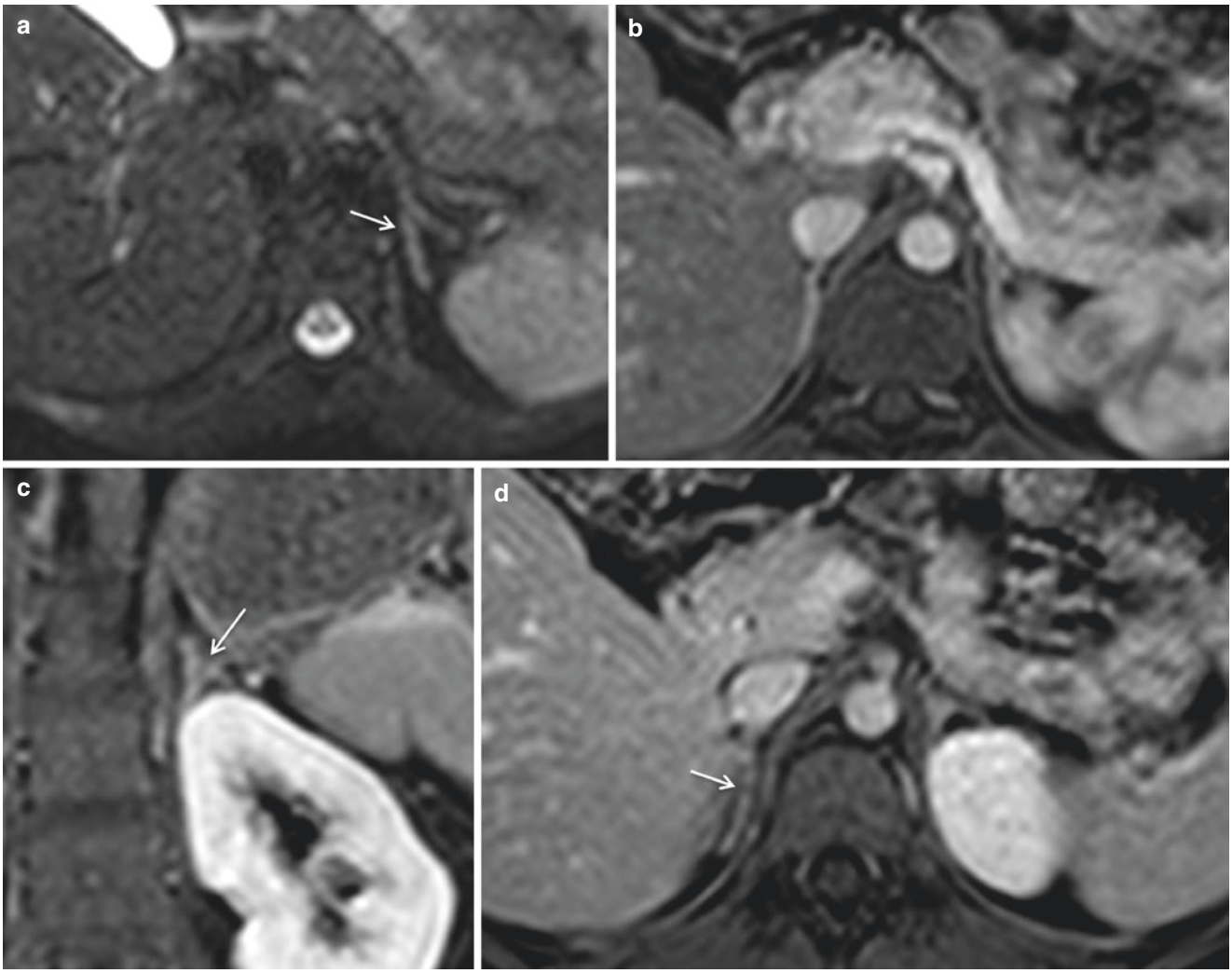

Fig. 12.15 Primary pigmented nodular adrenocortical disease (PPNAD). Axial (**a**) and post-gadolinium axial (**b**, **d**) and coronal (**c**) T1-weighted MR images. Adrenals showing a "beads-on-a-string" aspect with multiple small nodules (*white arrows*)

Primary Adrenal Insufficiency

Primary adrenal insufficiency is characterized by adrenal inability to produce cortisol, androgens, and aldosterone, due to organ atrophy that is often secondary to an autoimmune disease (Fig. 12.16) or fungal infection (Figs. 12.17 and 12.18). Reduced fertility has been described not only due to concomitant premature ovarian failure in polyglandular autoimmune syndromes, but also by autoimmune thyroid disease and inappropriate treatment of adrenal insufficiency [47]. Another rare cause of adrenal insufficiency is adrenoleukodystrophy, an X-linked metabolic disorder, which is a neurodegenerative condition characterized by the accumulation of very long-chain fatty acids in tissues such as the central nervous system, adrenal glands, and testes. As the disease progresses, hypogonadism with a decrease in testosterone levels may be present with consequent impaired fertility.

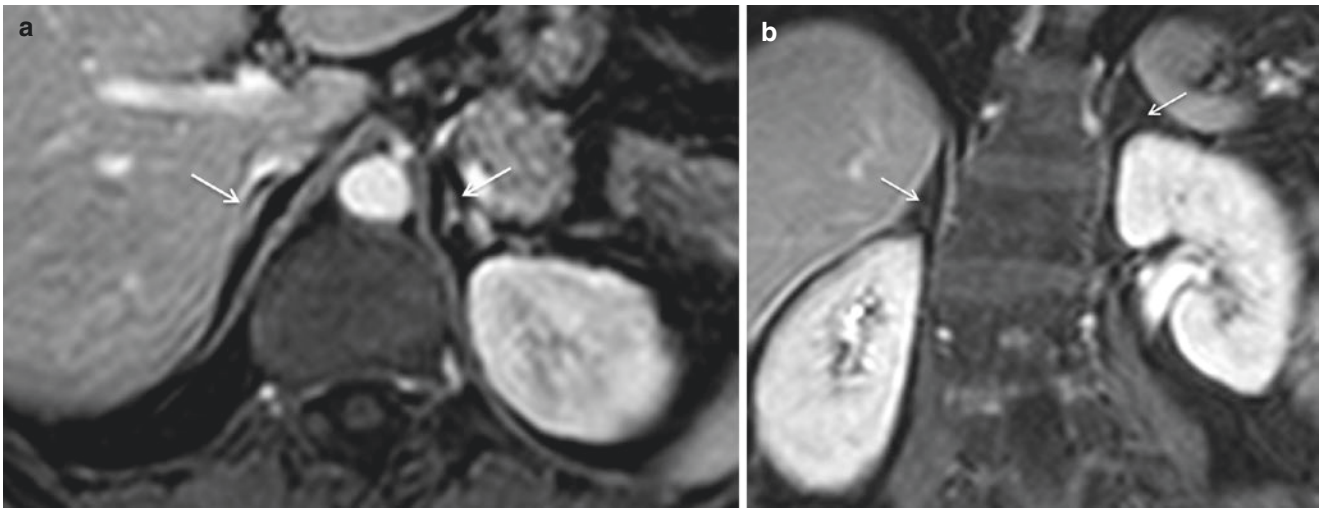

Fig. 12.16 Primary adrenal insufficiency secondary to autoimmune disease. Axial (**a**) and coronal (**b**) post-gadolinium T1-weighted images showing very small adrenal glands due to accentuated atrophy (*white arrows*)

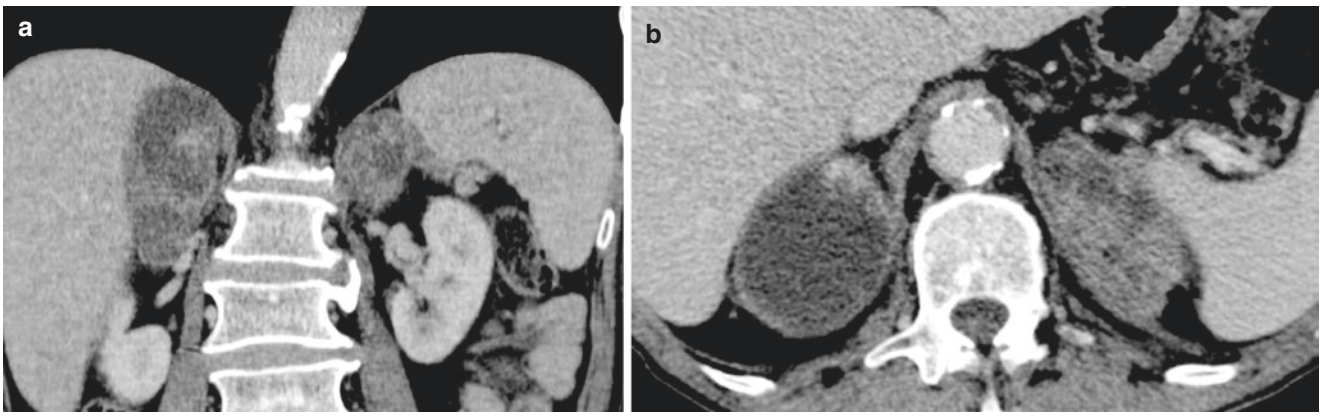

Fig. 12.17 Primary adrenal insufficiency due to fungal disease (paracoccidioidomycosis). Axial post-contrast CT with heterogeneously enhanced bilateral adrenal masses (*white arrows*)

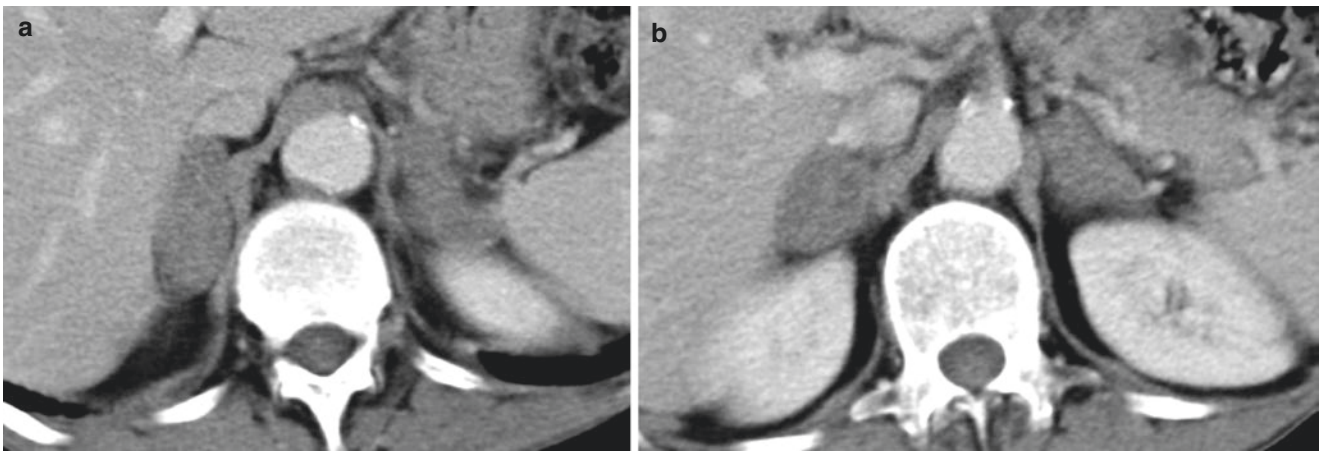

Fig. 12.18 Primary adrenal insufficiency due to fungal disease (paracoccidioidomycosis). Axial post-contrast CT showing enlargement of both adrenal glands (*white arrows*)

References

1. Teixeira SR, Elias PC, Andrade MT, Melo AF, Elias J Jr. The role of imaging in congenital adrenal hyperplasia. Arq Bras Endocrinol Metabol. 2014;58(7):701–8. PubMed PMID: 25372578.
2. Chang AY, Auchus RJ. Endocrine disturbances affecting reproduction. In: Strauss JF, Barbieri RL, editors. Yen and Jaffe's reproductive endocrinology: physiology, pathophysiology, and clinical management. 7th ed. Philadelphia: Elservier Saunders; 2014. p. 551–64.
3. Auchus RJ. Management considerations for the adult with congenital adrenal hyperplasia. Mol Cell Endocrinol. 2015;408:190–7. PubMed. PMID: 25643980.
4. Speiser PW, White PC. Congenital adrenal hyperplasia. N Engl J Med. 2003;349(8):776–88. PubMed PMID: 12930931.
5. Merke DP, Bornstein SR. Congenital adrenal hyperplasia. Lancet. 2005;365(9477):2125–36. PubMed PMID: 15964450.
6. Harinarayana CV, Renu G, Ammini AC, Khurana ML, Ved P, Karmarkar MG, et al. Computed tomography in untreated congenital adrenal hyperplasia. Pediatr Radiol. 1991;21(2):103–.5. PubMed PMID: 2027706. Epub 1991/01/01. eng.
7. Schteingart DE. The clinical spectrum of adrenocortical hyperplasia. Curr Opin Endocrinol Diabetes Obes. 2012;19(3):176–.82. PubMed PMID: 22499224. Epub 2012/04/14. eng.
8. Nandagopal R, Sinaii N, Avila NA, Van Ryzin C, Chen W, Finkielstain GP, et al. Phenotypic profiling of parents with cryptic nonclassic congenital adrenal hyperplasia: findings in 145 unrelated families. Eur J EndocrEur FedEndocr Soc. 2011;164(6):977–.84. PubMed PMID: 21444649. Pubmed Central PMCID: 3470911. Epub 2011/03/30. eng.
9. Street ME, Weber A, Camacho-Hubner C, Perry LA, Brain CE, Cotterill AM, et al. Girls with virilisation in childhood: a diagnostic protocol for investigation. J Clin Pathol. 1997;50(5):379–.83. PubMed PMID: 9215119. Pubmed Central PMCID: 499938. Epub 1997/05/01. eng.
10. Tian J, Yang G, Wang S, Zhang Y, Song G, Zheng F. Molecular diagnosis of two families with classic congenital adrenal hyperplasia. Gene. 2011;482(1–2):8–.14. PubMed PMID: 21664262. Epub 2011/06/15. eng.
11. Falke TH, vanSeters AP, Schaberg A, Moolenaar AJ. Computed tomography in untreated adults with virilizing congenital adrenal cortical hyperplasia. Clin Radiol. 1986;37(2):155–.60. PubMed PMID: 3698500. Epub 1986/03/01. eng.
12. Bachelot ARF, Rouxel A, Eiss D, Touraine P. Adrenal morphology on CT-scan in patients with congenital adrenal hyperplasia.9th European Congress of Endocrinology.Budapest; 2007. p. 654.
13. Altun E, Kelekis NL, Elias Jr J, Tannaphai P, Qureshi W, Semelka RC. Adrenal glands. In: Semelka RC, editor. Abdominal-pelvic MRI. 2. 3rd ed. Hoboken: John Wiley & Sons; 2010. p. 963–1024.
14. Barwick TD, Malhotra A, Webb JA, Savage MO, Reznek RH. Embryology of the adrenal glands and its relevance to diagnostic imaging. Clin Radiol. 2005;60(9):953–.9. PubMed PMID: 16124976. Epub 2005/08/30. eng.
15. Hernanz-Schulman M, Brock JW, 3rd, Russell W. Sonographic findings in infants with congenital adrenal hyperplasia. Pediatr Radiol. 2002;32(2):130–.7. PubMed PMID: 11819084. Epub 2002/01/31. eng.
16. Sivit CJ, Hung W, Taylor GA, Catena LM, Brown-Jones C, Kushner DC. Sonography in neonatal congenital adrenal hyperplasia. AJR Am J Roentgenol. 1991;156(1):141–.3. PubMed PMID: 1898548. Epub 1991/01/01. eng.
17. Al-Alwan I, Navarro O, Daneman D, Daneman A. Clinical utility of adrenal ultrasonography in the diagnosis of congenital adrenal hyperplasia. J Pediatr. 1999;135(1):71–.5. PubMed PMID: 10393607. Epub 1999/07/07. eng.
18. Bryan PJ, Caldamone AA, Morrison SC, Yulish BS, Owens R. Ultrasound findings in the adreno-genital syndrome (congenital adrenal hyperplasia). J Ultrasound Med. 1988;7(12):675–.9. PubMed PMID: 3070057. Epub 1988/12/01. eng.
19. Stikkelbroeck NM, Otten BJ, Pasic A, Jager GJ, Sweep CG, Noordam K, et al. High prevalence of testicular adrenal rest tumors, impaired spermatogenesis, and Leydig cell failure in adolescent and adult males with congenital adrenal hyperplasia. J Clin Endocrinol Metab. 2001;86(12):5721–.8. PubMed PMID: 11739428. Epub 2001/12/12. eng.
20. Claahsen-van der Grinten HL, Otten BJ, Hermus AR, Sweep FC, Hulsbergen-van de Kaa CA. Testicular adrenal rest tumors in patients with congenital adrenal hyperplasia can cause severe testicular damage. Fertil Steril. 2008;89(3):597–.601. PubMed PMID: 17543962. Epub 2007/06/05. eng.
21. Reisch N, Flade L, Scherr M, Rottenkolber M, Pedrosa Gil F, Bidlingmaier M, et al. High prevalence of reduced fecundity in men with congenital adrenal hyperplasia. J Clin Endocrinol Metab. 2009;94(5):1665–.70. PubMed PMID: 19258407. Epub 2009/03/05. eng.
22. Avila NA, Premkumar A, Shawker TH, Jones JV, Laue L, Cutler GB Jr. Testicular adrenal rest tissue in congenital adrenal hyperplasia: findings at Gray-scale and color Doppler US. Radiology. 1996;198(1):99–.104. PubMed PMID: 8539414. Epub 1996/01/01. eng.
23. Stikkelbroeck NM, Suliman HM, Otten BJ, Hermus AR, Blickman JG, Jager GJ. Testicular adrenal rest tumours in postpubertal males with congenital adrenal hyperplasia: sonographic and MR features. Eur Radiol. 2003;13(7):1597–.603. PubMed PMID: 12835972. Epub 2003/07/02. eng.
24. Avila NA, Premkumar A, Merke DP. Testicular adrenal rest tissue in congenital adrenal hyperplasia: comparison of MR imaging and sonographic findings. AJR Am J Roentgenol. 1999;172(4):1003–.6. PubMed PMID: 10587136. Epub 1999/12/10. eng.
25. Avila NA, Shawker TS, Jones JV, Cutler GB Jr, Merke DP. Testicular adrenal rest tissue in congenital adrenal hyperplasia: serial sonographic and clinical findings. AJR Am J Roentgenol. 1999;172(5):1235–.8. PubMed PMID: 10227495. Epub 1999/05/05. eng.
26. Delfino M, Elia J, Imbrogno N, Argese N, Mazzilli R, Toscano V, et al.Testicular adrenal rest tumors in patients with congenital adrenal hyperplasia: prevalence and sonographic, hormonal, and seminal characteristics. J Ultrasound Med. 2012;31(3):383–.8. PubMed PMID: 22368128. Epub 2012/03/01. eng.
27. Muglia V, Tucci S Jr, Elias J Jr, Trad CS, Bilbey J, Cooperberg PL. Magnetic resonance imaging of scrotal diseases: when it makes the difference. Urology. 2002;59(3):419–23. PubMed PMID: 11880084.
28. Reisch N, Scherr M, Flade L, Bidlingmaier M, Schwarz HP, Muller-Lisse U, et al. Total adrenal volume but not testicular adrenal rest tumor volume is associated with hormonal control in patients with 21-hydroxylase deficiency. J Clin Endocrinol Metab. 2010;95(5):2065–2072. PubMed PMID: 20190160. Epub 2010/03/02. eng.
29. Martinez-Aguayo A, Rocha A, Rojas N, Garcia C, Parra R, Lagos M, et al. Testicular adrenal rest tumors and Leydig and Sertoli cell function in boys with classical congenital adrenal hyperplasia. J Clin Endocrinol Metab. 2007;92(12):4583–.9. PubMed PMID: 17895312. Epub 2007/09/27. eng.
30. Claahsen-van der Grinten HL, Sweep FC, Blickman JG, Hermus AR, Otten BJ. Prevalence of testicular adrenal rest tumours in male children with congenital adrenal hyperplasia due to 21-hydroxylase deficiency. Eur JEndocrEur Fed Endocr Soc. 2007;157(3):339–.44. PubMed PMID: 17766717. Epub 2007/09/04. eng.
31. Claahsen-van der Grinten HL, Otten BJ, Stikkelbroeck MM, Sweep FC, Hermus AR. Testicular adrenal rest tumours in

congenital adrenal hyperplasia. Best Pract Res Clin Endocrinol Metab. 2009;23(2):209–.20. PubMed PMID: 19500764. Epub 2009/06/09. eng.
32. Boland GW, Lee MJ, Gazelle GS, Halpern EF, McNicholas MM, Mueller PR. Characterization of adrenal masses using unenhanced CT: an analysis of the CT literature. AJR Am J Roentgenol.1998;171(1):201–4. PubMed PMID: 9648789.
33. Johnson PT, Horton KM, Fishman EK. Adrenal mass imaging with multidetector CT: pathologic conditions, pearls, and pitfalls. RadiographicsRevPubl Radiol Soc North Am Inc. 2009;29(5):1333–51. PubMed PMID: 19755599.
34. Chambre C, McMurray E, Baudry C, Lataud M, Guignat L, Gaujoux S, et al.The 10 Hounsfield units unenhanced computed tomography attenuation threshold does not apply to cortisol secreting adrenocortical adenomas. EurJEndocr Eur FedEndocrSoc. 2015;173(3):325–32. PubMed PMID: 26243637.
35. Caoili EM, Korobkin M, Francis IR, Cohan RH, Platt JF, Dunnick NR, et alAdrenal masses: characterization with combined unenhanced and delayed enhanced CT. Radiology. 2002;222(3):629–33. PubMed PMID: 11867777.
36. Chung JJ, Semelka RC, Martin DR. Adrenal adenomas: characteristic postgadolinium capillary blush on dynamic MR imaging. J Magn Reson Imaging. 2001;13(2):242–8. PubMed PMID: 11169830.
37. Krestin GP, Steinbrich W, Friedmann G. Adrenal masses: evaluation with fast gradient-echo MR imaging and Gd-DTPA-enhanced dynamic studies. Radiology. 1989;171(3):675–80. PubMed PMID: 2717737.
38. Krestin GP, Freidmann G, Fishbach R, Neufang KF, Allolio B. Evaluation of adrenal masses in oncologic patients: dynamic contrast-enhanced MR vs CT. J Comput Assist Tomogr. 1991;15(1):104–10. PubMed PMID: 1987177.
39. Israel GM, Korobkin M, Wang C, Hecht EN, Krinsky GA. Comparison of unenhanced CT and chemical shift MRI in evaluating lipid-rich adrenal adenomas. AJR Am J Roentgenol. 2004;183(1):215–9. PubMed PMID: 15208141.
40. Sebro R, Aslam R, Muglia VF, Wang ZJ, Westphalen AC. Low yield of chemical shift MRI for characterization of adrenal lesions with high attenuation density on unenhanced CT. Abdom Imaging. 2015;40(2):318–26. PubMed PMID: 25095753.
41. Allolio B, Fassnacht M. Clinical review: adrenocortical carcinoma: clinical update. J Clin Endocrinol Metab. 2006;91(6):2027–37. PubMed PMID: 16551738.
42. Bharwani N, Rockall AG, Sahdev A, Gueorguiev M, Drake W, Grossman AB, et al. Adrenocortical carcinoma: the range of appearances on CT and MRI. AJR Am J Roentgenol. 2011;196(6):W706–14. PubMed PMID: 21606258.
43. Wajchenberg BL, Albergaria Pereira MA, Medonca BB, Latronico AC, Campos Carneiro P, Alves VA, et al. Adrenocortical carcinoma: clinical and laboratory observations. Cancer. 2000;88(4):711–36. PubMed PMID: 10679640.
44. Mermejo LM, Mazzuco TL, Grunenwald S, Fragoso MCBV, Bourdeau I, Lacroix A. ACTH-independent macronodular adrenal hyperplasia. Endocrinol Metab. 2011;26(1):1.
45. Hofland J, deHerder WW, Derks L, Hofland LJ, vanKoetsveld PM, deKrijger RR, et al.Regulation of steroidogenesis in a primary pigmented nodular adrenocortical disease-associated adenoma leading to virilization and subclinical Cushing's syndrome. Eur JEndocr Eur Fed Endocr Soc. 2013;168(1):67–74. PubMed PMID: 23065993. Pubmed Central PMCID: 4100689.
46. Powell AC, Stratakis CA, Patronas NJ, Steinberg SM, Batista D, Alexander HR, et al.Operative management of Cushing syndrome secondary to micronodular adrenal hyperplasia. Surgery. 2008;143(6):750–8. PubMed PMID: 18549891. Pubmed Central PMCID: 2601697.
47. Erichsen MM, Husebye ES, Michelsen TM, Dahl AA, Lovas K. Sexuality and fertility in women with Addison's disease. J Clin Endocrinol Metab. 2010;95(9):4354–60. PubMed PMID: 20610594.